

Performance of Layered UHPFRC under Static and Dynamic Loads

EFFECTS OF STEEL FIBERS, COARSE AGGREGATES AND LAYERED STRUCTURES

Yangyueye Cao

Bouwstenen

288

Performance of Layered UHPFRC under Static and Dynamic Loads

Effects of steel fibers, coarse aggregates and layered structures

PROEFSCHRIFT

ter verkrijging van de graad van doctor aan de Technische Universiteit Eindhoven, op
gezag van de rector magnificus prof.dr.ir. F.P.T. Baaijens,
voor een commissie aangewezen door het College voor Promoties, in het openbaar te
verdedigen op dinsdag 24 maart 2020 om 16:00 uur

door

Yangyueye Cao

geboren te Hunan, China

Dit proefschrift is goedgekeurd door de promotoren en de samenstelling van de promotiecommissie is als volgt:

Voorzitter:	prof.dr.ir. T.A.M. Salet
Promotor:	prof.dr.ir. H.J.H. Brouwers
Copromotor:	prof.dr. Q.L. Yu (Wuhan University)
Leden:	prof.dr. C. Shi (Hunan University)
	prof.dr. H. Justnes (Norwegian University of Science and Technology)
	prof.ir. S.N.M. Wijte
	prof.dr.ir. A.S.J. Suiker
Adviseur:	dr.ir. P. Spiesz (HeidelbergCement Benelux)

Het onderzoek of ontwerp dat in dit proefschrift wordt beschreven is uitgevoerd in overeenstemming met de TU/e Gedragscode Wetenschapsbeoefening.

Dedicated to dear my parents

献给我亲爱的父母

CIP-DATA LIBRARY TECHNISCHE UNIVERSITEIT EINDHOVEN

Performance of Layered UHPFRC under Static and Dynamic Loads: Effects of steel fibers, coarse aggregates and layered structures / by Yangyueye Cao

A catalogue record is available from the Eindhoven University of Technology Library

ISBN: 978-90-386-5001-2

Bouwstenen 288

Copyright © 2020 by Yangyueye Cao

Ph.D. Thesis, Eindhoven University of Technology, the Netherlands

All rights reserved. No part of this publication may be reproduced in any form or by any means without permission in writing form from the author.

Preface

This dissertation thesis presents the research work performed at Eindhoven University of Technology during my doctoral study since March 2017. The research is carried out under the funding of China Scholarship Council and supported by Eindhoven University of Technology. I appreciate the opportunities I have obtained to develop both a new coarse-aggregated layered UHPFRC and a better myself at Eindhoven University of Technology.

First and foremost, I must sincerely express my gratitude to my promotor prof.dr.ir. H.J.H. (Jos) Brouwers for giving me the opportunity to join the group of building materials, for his inspiring support throughout my PhD study, not to mention his valuable advice and broad knowledge. Moreover, I want to express my sincere gratitude to the copromotor prof.dr. Qingliang Yu for encouraging me to start this research, for guiding me with endless patience, and for giving me very constructive and sometimes even very challenging comments on the research. It is my great pleasure working under the supervisions of Jos and Qingliang, and I learnt how to be an enthusiastic, independent and responsible researcher from them.

I also wish to extend my gratefulness to the members of my committee, prof.dr. Caijun Shi (Hunan University, China), prof.dr. H. Justnes (Norwegian University of Science and Technology), prof.ir. S.N.M. Wijte (Eindhoven University of Technology), prof.dr.ir. A.S.J. Suiker (Eindhoven University of Technology), and dr.ir. P. Spiesz (HeidelbergCement Benelux) for their interests in my research, their precious time to review this thesis, and their valuable comments to improve this thesis.

Furthermore, my thanks go to my teachers in China. Particularly, prof. Wenhui Tang and prof. Zhigang Jiang are thanked for encouraging me to do my PhD research abroad, and for their continuous trust, support and guidance.

An essential part of this research is to conduct experiments under both static and dynamic loads. This would not have been possible without the supports from the technicians and engineers. Therefore, I would like to thank the technical staff in the Laboratory of Building Physics and Services and the Laboratory of Structural Design for constructing the bending and drop-weight test setups, especially ing. G.A.H. (Geert-Jan) Maas for his friendly help during my experimental work. Ing. D. Krabbenborg from the Dutch Defense Academy and the following organization are acknowledged for conducting the ballistic tests: Knowledge Center Weapon System and Ammunition from the Dutch Ministry of Defense. Thanks are also given to late Ing. Ad Verhagen for sharing his valuable experience on the pullout tests and the layered concrete.

Doing research in the Netherlands is an interesting experience. I would like to express my appreciation to my PhD colleagues at the group of building materials whoever helps me. Special thanks go to dr. Peipeng Li, Gang Liu and the master student Maarten Sluijsmans for their important help with the heavy labor work during the experimental phase of this research. In addition, my Chinese friends in the Netherlands are thanked for sharing all the wonderful moments and delicious foods with me. I will remember our precious time in the Netherlands.

Last but not the least, I would like to express my highest thank to my parents. Their unconditional love always encourage me to go forward bravely with my initial heart.



Summary

Security problems of specialized structures, e.g. nuclear power plants and high rise buildings, have become critical considerations in both civil and military fields. Having a high risk of being exposed to terrorist attacks or accidental impacts, these structures require suitable construction materials to withstand not only static but also dynamic loads. The outstanding performance of Ultra-High Performance Fiber Reinforced Concrete (UHPFRC) makes it a promising material for these specialized structures. Lowering the material costs of UHPFRC is important for promoting its application in practical constructions. Hence, cheap coarse aggregates are utilized to partially replace the expensive fine particles in UHPFRC in the present research, which also benefits the impact resistance of the UHPFRC. Moreover, the cost of steel fibers is also a dominant factor influencing the UHPFRC production. To achieve a more effective fiber distribution, an optimized layered-structure concept is applied to UHPFRC, i.e. designing UHPFRC with multi-layers. This thesis investigates the fiber effects on the coarse-aggregated layered UHPFRC subjected to static and dynamic loads, with special attention to the fiber pullout performance at mesoscale and the fiber amount distribution over the layered UHPFRC at macroscale.

The fiber-matrix interactions at mesoscale are investigated in Chapters 2 and 3 by analyzing the single fiber pullout behavior under static and dynamic pullout loads, respectively. In Chapter 2, the influences of fiber inclination angles, namely 0° , 10° , 20° and 30° , on the pullout responses of two types of hooked-end fibers from the UHPC matrix are studied. It is revealed that the effects of the fiber inclination on the pullout behavior are associated with both the snubbing effect and the matrix spalling effect. To evaluate these effects, a new analytical model for the hooked-end fiber is proposed and validated. Chapter 3 focuses on the dynamic pullout behavior of the hooked-end fiber embedded in the UHPC matrix. The pullout rate changes from 5 mm/min to 1000 mm/min, i.e. from the quasi-static to intermediate strain rates. Mechanisms contributing to the rate dependency of the pullout response, the Stefan effect and the micro inertia effect, are analyzed in this chapter. An analytical model is developed to predict the peak pullout force of the hooked-end steel fiber from the UHPC matrix under dynamic loads.

The macroscale performances of coarse-aggregated layered UHPFRC under different loading rates are presented in Chapters 4 ~ 8. Chapter 4 analyzes the static flexural behavior. Theoretical criteria for layer cracking and debonding are proposed, based on which double-layered UHPFRC beams are designed. In comparing the flexural performances of the designed double-layered UHPFRC to their single-layered counterpart with an identical total fiber amount, it is found that the double-layered UHPFRC beam composed of a 40 mm-thick top layer with 0.6% straight fibers and a 60 mm-thick bottom layer with 1.6% straight fibers achieves a 24% higher peak flexural load and a 14% higher flexural energy.

In continuation of the static flexural study in Chapter 4, Chapter 5 investigates the dynamic performance of the double-layered UHPFRC under low-velocity drop-weight impact. A 7.26 kg metal ball dropped from 2.5 m generates a dynamic load within the intermediate strain rate range. The experimental results show that in comparison to the single-layered beam, the double-layered UHPFRC achieves an improved impact resistance. For instance, a 28% enhancement of the absorbed impact energy is accomplished by the double-layered UHPFRC with 0.6% hooked-end fibers in the top layer

and 1.6% hooked-end fibers in the bottom layer. Furthermore, a model to predict the absorbed energy of the layered UHPFRC under repeated drop-weight impacts is proposed and validated.

The low-velocity impact study presented in Chapter 5 is followed by the study on the high-velocity impact. The ballistic resistance of the coarse-aggregated layered UHPFRC against in-service 7.62 mm × 51 AP projectile at 840 m/s is investigated in Chapters 6 ~ 8, experimentally, theoretically and numerically. Ballistic experiments on the coarse-aggregated layered UHPFRC are presented in Chapter 6, with the effects of the coarse aggregates, the steel fibers and the layered structure analyzed in detail. The improved penetration resistance of the coarse-aggregated layered UHPFRC is confirmed by the test results, showing a 32% reduction on the depth of penetration (DOP) achieved by the triple-layered UHPFRC. Chapter 7 presents models for predicting the DOP in single- and multi-layered UHPFRC, on the basis of an improved dynamic expansion theory. In addition to the experimental and theoretical studies, Chapter 8 numerically analyses the dynamic penetration performance of the UHPFRC using LS-DYNA. The numerical models coincide well with the experimental results. The simulations further confirm that the triple-layered UHPFRC consumes less cement and fiber, in comparison to the single-layered one with the same level of the ballistic resistance.

This thesis provides fundamental insights on the static and dynamic properties of coarse-aggregated layered UHPFRC. The investigations concerning the fibers pullout response and the effects of fiber amount distribution in a layered structure shed light on the fiber-matrix bond properties and inspire a more efficient fiber utilization in UHPFRC. In addition, the static and dynamic studies on the coarse-aggregated layered UHPFRC provide a comprehensive understanding on its mechanical performances under different loading rates, contributing to the state-of-the-art. Furthermore, with the incorporation of the coarse aggregates and the efficient utilization of the steel fibers, the designed UHPFRC can bring great economic benefits and can promote the future technological application of UHPFRC in the civil and military constructions.

Contents

Preface	1
Summary	3
Contents	5
Chapter 1	9
Introduction	9
1.1 Research background	10
1.1.1 Characteristics of conventional UHPFRC	10
1.1.2 UHPFRC with coarse aggregates	11
1.1.3 Fibers effects on UHPFRC performance	12
1.1.4 Rate effects on UHPFRC performance	13
1.2 Research motivation and aim	13
1.3 Outline of the thesis	14
Chapter 2	17
<i>Effect of inclination angle on the pullout performance of hooked-end steel fiber embedded in UHPC *</i>	17
2.1 Introduction	19
2.2 Single fiber pullout experiments	20
2.2.1 Steel fibers	20
2.2.2 UHPC matrix	20
2.2.3 Mixing and casting procedures	21
2.2.4 Pullout test setup and procedure	21
2.2.5 SEM observations	22
2.3 Pullout responses	22
2.3.1 Complete fiber pullout	23
2.3.2 Fiber breakage	24
2.3.3 Matrix failure	24
2.4 Parametric evaluation and mechanism analysis	26
2.4.1 Evaluation of parameters for fiber pullout performance	26
2.4.2 Snubbing and matrix spalling effect	28
2.5 Optical microscope and SEM observations	30
2.6 Conclusions	31
Chapter 3	33
<i>Effects of loading rate on the pullout performance of hooked-end steel fiber embedded in UHPC *</i>	33
3.1 Introduction	35
3.2 Materials and experiments	36
3.2.1 Steel fibers and UHPC matrix	36
3.2.2 Mixing and casting procedures	36
3.2.3 Fiber pullout test setup and procedure	37
3.3 Rate dependency of cementitious material	37

3.3.1 Rate effects on concrete tensile strength	37
3.3.2 Mechanisms behind concrete rate dependency	37
3.3.3 Rate dependency of fiber-matrix interface	38
3.4 Fiber pullout test results	39
3.4.1 Rate-dependent pullout performances	39
3.4.2 Rate effects on the pullout load and energy	40
3.4.3 Rate effects on the maximum and equivalent bond strengths	42
3.4.4 Effect of embedded length on the rate dependency.....	42
3.5 Rate-dependent model.....	45
3.5.1 Predictive model.....	45
3.5.2 Model validation.....	47
3.6 Conclusions	49
Chapter 4	51
<i>Enhancing the static flexural performance of coarse-aggregated UHPFRC by an optimized layered-structure concept*</i>	51
4.1 Introduction	53
4.2 Theoretical analysis of the first failure stage	54
4.2.1 Cracking criteria in the layered UHPFRC beam	55
4.2.2 Debonding criteria in the layered UHPFRC beam	58
4.2.3 Influences of β_E and β_h on stress distribution and critical load	59
4.3 Experimental program.....	61
4.3.1 Materials and mix design.....	61
4.3.2 Design of double-layered UHPFRC composite beams	61
4.3.3 Mixing and casting procedures.....	62
4.3.4 Testing methods.....	63
4.4 Experimental results and discussion	63
4.4.1 Mechanical and interfacial properties.....	63
4.4.2 Effects of layer thickness.....	65
4.4.3 Effects of fiber amount distribution in layered structures	67
4.4.4 Effects of fiber amount in individual layers	69
4.5 Conclusions	71
Chapter 5	73
<i>Enhancing the low-velocity impact resistance of coarse-aggregated UHPFRC by an optimized layered-structure concept*</i>	73
5.1 Introduction	75
5.2 Experimental program.....	76
5.2.1 Materials and mix design.....	76
5.2.2 UHPFRC composite beam	77
5.2.3 Mixing, casting and testing methods	77
5.3 Static mechanical properties	78
5.4 Drop-weight impact performances.....	79
5.4.1 Reaction force and deflection	79
5.4.2 Performance of single-layered UHPFRC	80

5.4.3 Performance of double-layered UHPFRC	84
5.5 Prediction of absorbed impact energy based on fiber pullout	87
5.5.1 Predicting the absorbed impact energy	87
5.5.2 Model validation and discussion	89
5.6 Conclusions	91
Chapter 6	93
<i>Enhancing the high-velocity impact resistance of coarse-aggregated UHPFRC by an optimized layered-structure concept *</i>	93
6.1 Introduction	95
6.2 Materials and experimental methods	97
6.2.1 Materials and mix design	97
6.2.2 Design of the layered UHPFRC target	97
6.2.3 Mixing, casting and testing methods	97
6.3 Experimental results	100
6.3.1 Static mechanical properties	100
6.3.2 Ballistic test results	101
6.4 Discussions	103
6.4.1 Response of single-layered UHPFRC	103
6.4.2 Response of double-layered UHPFRC	104
6.4.3 Response of triple-layered UHPFRC	106
6.5 Conclusions	110
Chapter 7	111
<i>Predicting the depth of penetration in UHPFRC under high-velocity impact using a nonlinear rate-dependent model *</i>	111
7.1 Introduction	113
7.2 Improved constitutive model for UHPFRC	114
7.2.1 Hoek-Brown criterion	114
7.2.2 Rate dependency incorporation	115
7.3 Dynamic cavity expansion model	117
7.3.1 Descriptions	117
7.3.2 Elastic-cracked-comminuted response	118
7.3.3 Elastic-comminuted response	122
7.4 DOP model for single-layered UHPFRC	123
7.4.1 DOP predictive model	123
7.4.2 Model validation	127
7.4.3 Parameter discussion	131
7.5 DOP model for multi-layered UHPFRC	137
7.5.1 Predictive model for multi-layered UHPFRC	137
7.5.2 Model validation	139
7.6 Conclusions	140
Chapter 8	143
<i>Modelling the ballistic response of coarse-aggregated layered UHPFRC under high-velocity impact *</i>	143

8.1 Introduction	145
8.2 Modelling of single- and triple-layered UHPFRC	146
8.2.1 Overview of the model	146
8.2.2 Material models	147
8.3 Model validation	152
8.4 Penetration analysis	153
8.4.1 Penetration history	153
8.4.2 Penetration process	154
8.5 Discussion	156
8.5.1 Influence of layer thickness on DOP	156
8.5.2 Influences of penetration velocity on perforation limit	158
8.6 Conclusions	161
Chapter 9	163
<i>Conclusions and recommendations</i>	163
9.1 Conclusions	164
9.1.1 Understanding the effects of the fiber inclination on the static fiber pullout performance	164
9.1.2 Understanding the effects of the pullout rate on the dynamic fiber pullout performance	165
9.1.3 Enhancing the static flexural performance of the coarse-aggregated UHPFRC using a layered structure	165
9.1.4 Enhancing the low-velocity impact resistance of the coarse-aggregated UHPFRC using a layered structure	166
9.1.5 Enhancing the high-velocity impact resistance of the coarse-aggregated UHPFRC using a layered structure	166
9.2 Recommendations	167
Bibliography	169
List of notations	183
List of publications	189
Curriculum Vitae	191

Chapter 1

Introduction



1.1 Research background

1.1.1 Characteristics of conventional UHPFRC

Ultra-High Performance Fiber Reinforced Concrete (UHPFRC) is generally characterized by its very high compressive strength, excellent energy absorption capacity and outstanding damage resistance (Yu, 2015), making it a promising material to withstand both static and dynamic loads. In general, UHPFRC is composed of cement, mineral additives, fine aggregates, water, chemical admixtures and steel fibers. The differences between an Ultra-High Performance Concrete (UHPC) matrix and normal strength concrete (NC) lie particularly in the following aspects (Shi et al., 2015): (1) the high binder amount and low water-cement ratio of UHPFRC, which results in the low porosity and significantly improved compressive strength; (2) the fine size of aggregates in UHPFRC, i.e. coarse aggregates are eliminated in UHPFRC to decrease the effects of heterogeneity and eliminate defects; (3) the use of silica fume in UHPFRC to reduce porosity and achieve a dense microstructure; (4) the large amount of superplasticizer in UHPFRC mixture to obtain sufficient workability. Examples of typical UHPC and NC mixtures are presented in Fig. 1-1. A detailed review on the raw materials and the mixture design of UHPFRC can be found in (Shi et al., 2015).

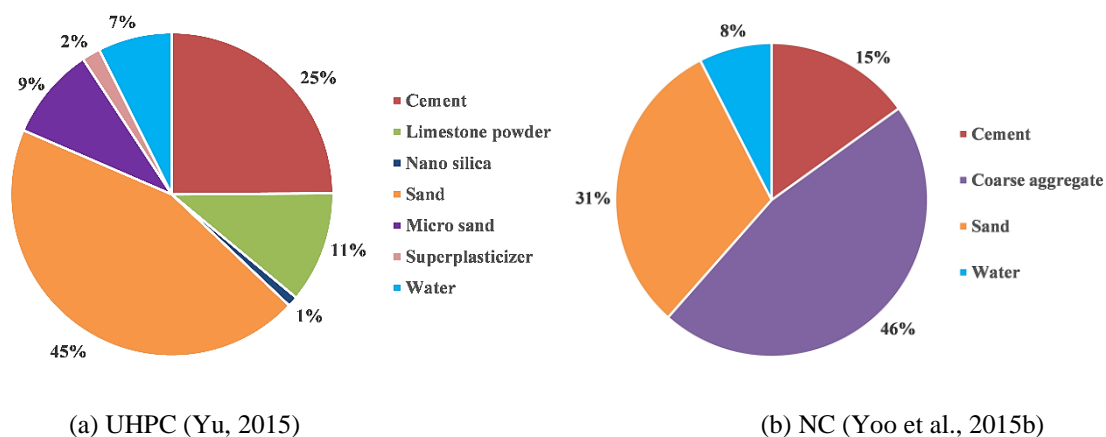


Fig. 1-1 Examples of UHPC and NC mixtures (mass %)

The fine materials and the high particle packing density of UHPFRC contribute to its superior compressive strength over other cementitious materials. As illustrated in Fig. 1-2a, the compressive stress-strain relationship of UHPFRC can be generally divided into three regimes (Spasojević, 2008): (1) Linear elastic increasing regime with an elastic modulus in the range of 50-70 GPa; (2) Nonlinear increasing regime until the compressive strength (usually over 150 MPa) is reached; (3) Post-peak softening behavior

The addition of steel fibers has been recognized to significantly enhance the tensile strength of UHPFRC. A typical tensile constitutive relationship of UHPFRC is exhibited in Fig. 1-2b (Spasojević, 2008). Similarly, three regimes can be distinguished from the curve (Spasojević, 2008):

- (1) Linear elastic regime up to the matrix tensile strength;
- (2) Strain hardening regime resulting from multi-micro cracking;
- (3) Strain softening regime with localization of cracking.

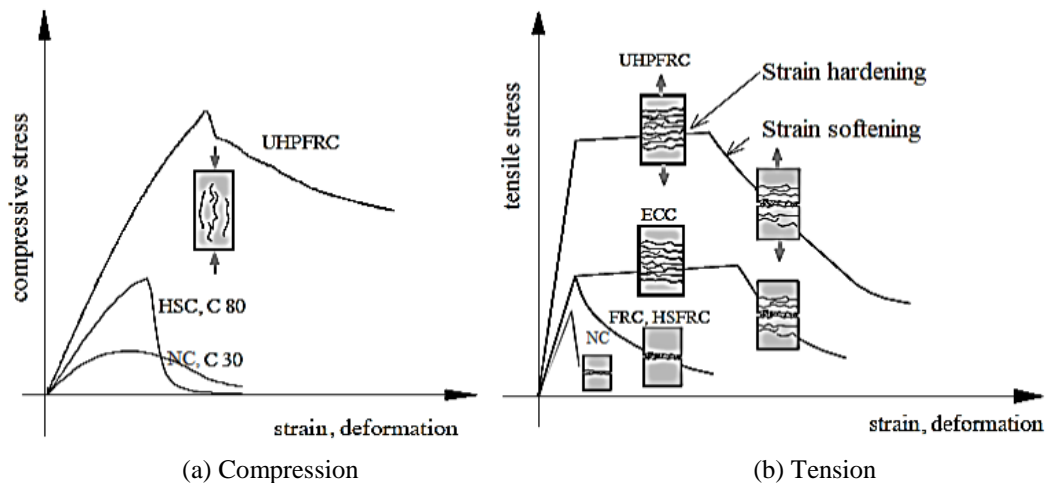


Fig. 1-2 Mechanical properties of conventional concrete and UHPFRC (Spasojević, 2008)

The low water-cement ratio of UHPFRC contributes to its superior mechanical properties. However, a too low water addition can cause fluidity problems for the fresh matrix (Li, 2019). To achieve a satisfying workability, superplasticizers are incorporated in UHPFRC, which significantly increases its flowability with a relatively small water addition (Li, 2019). Furthermore, the flowability of UHPFRC is associated with the fiber amount added into the matrix. Fiber incorporation can reduce the fresh behaviors of UHPFRC, which may be attributed to the fiber friction and the changed skeleton structure (Buttignol et al., 2017). That being the case, to guarantee a satisfying fiber dispersion and to achieve a uniform fiber distribution, the mixing procedure of UHPFRC is also important (Buttignol et al., 2017). The fine raw materials should be mixed first before the addition of water and superplasticizers, and fibers should be added until a sufficient flowability of the fresh UHPC has been obtained.

1.1.2 UHPFRC with coarse aggregates

Despite the excellent properties, the practical application of UHPFRC is still limited. This can be attributed to several reasons, e.g. technical issues concerning UHPFRC production and lack of guidelines for designing UHPFRC structure (Spiesz and Hunger, 2017a, 2017b). The high material costs of UHPFRC is also an important factor influencing its application (Shaikh et al., 2018). Replacing the fine particles in UHPFRC with cheaper coarse aggregates can be one of the solutions to lowering the material cost. Coarse aggregates are usually eliminated from conventional UHPFRC as they decrease the material homogeneity and increase the possibility of defects (Shi et al., 2015), which can lead to strength reduction of UHPFRC. Nevertheless, recent studies confirm that the strength reduction of UHPFRC due to incorporating coarse aggregates can be limited by properly packing the granular constituents (Li et al., 2018; Wille et al., 2011), and some researches even reported strength improvements with the increase of the aggregate size (Liu et al., 2016; Wille et al., 2011).

Moreover, coarse-aggregated UHPFRC possesses some benefits on e.g. binder material saving, shrinkage control and impact resistance improvement (Li et al., 2018; Peng et al., 2016a; Yoo and Banthia, 2016), which further confirms the feasibility of using coarse aggregates in UHPFRC. For instance, Ma et al. (Ma et al., 2004) compared the properties of UHPC with and without coarse aggregates, and obtained that the coarse-aggregated UHPC has a larger elastic modulus and 40% lower autogenous shrinkage. Li and Yu (Li and Yu, 2019) found that incorporating coarse basalt aggregates

in UHPFRC reduces the powder consumption from 900 kg/m^3 to 700 kg/m^3 , and the coarse-aggregated UHPFRC has a significantly enhanced ballistic resistance.

1.1.3 Fibers effects on UHPFRC performance

(1) Fiber pullout behavior

Steel fibers, e.g. straight fibers and hooked-end fibers, are commonly used in UHPFRC. The addition of steel fibers benefit the cracking control ability of UHPFRC and enhance its energy absorption capacity. Acting as stress-transfer bridges, fibers effectively prohibit cracks at both micro- and macro-levels (Banthia and Sappakittipakorn, 2007), and the performances of UHPFRC can be affected by not only the fiber amount but also the individual pullout behavior of the activated fibers crossing a crack. As a foundation to analyze the fibers effects, investigating the single fiber pullout behavior embedded in UHPC matrix promotes a comprehensive understanding on the fiber-matrix interaction at mesoscale. Considering the simplicity of the operation and the reliability of the result, single fiber pullout experiment has been widely utilized to study the fibers effects on UHPFRC (Tai et al., 2016; Xu et al., 2016). Further, the fiber pullout behavior depends on many factors, including the fiber geometry, embedded length, inclination angle and pullout rate (Markovic, 2006).

Normally, fibers are randomly distributed in UHPFRC. Fibers under different inclination angles have distinct pullout responses (Laranjeira et al., 2010). On the one hand, an inclined fiber within a certain degree has enhanced pullout performance due to the snubbing effect (Isla et al., 2015; Markovic, 2006), which invokes an additional friction resistance, promotes the increase of the pullout load, and leads to an improved load carrying capacity of the UHPFRC. On the other hand, an inclined fiber also generates a stress concentration at the matrix near the bearing point (Li et al., 1990). This concentrated stress can result in a higher probability of fiber or matrix rupture, undermining the overall performance of the UHPFRC material. Therefore, understanding the effects of fiber inclination angle is essential for analyzing the fiber pullout behavior at mesoscale and the UHPFRC mechanical performance at macroscale.

(2) Fiber amount distribution

The cost of steel fibers is one of the dominant factors influencing the UHPFRC production and limiting its widespread utilization (Wu et al., 2017b). For instance, the price of 2% straight steel fibers comprises more than 30% of the total material cost of UHPFRC (Brühwiler, 2009). This situation, therefore, makes it highly necessary to achieve a more effective utilization of the steel fibers in UHPFRC. In other words, fibers should be selectively distributed in part of the UHPFRC structure where their advantages can be fully exploited (Dias et al., 2010). This is especially true for structures that are partially in tension and partially in compression. A typical example is a bending beam. When a UHPFRC beam is subjected to bending, half of it is under compression while the other half is in tension (Shen et al., 2008). The same applies to concrete specimens under drop-weight impacts: the compressive waves generated by the drop weight in the impact region would propagate and reflect to be tensile waves at the distant region. Although the tensile properties of UHPFRC are significantly enhanced by the increasing the fiber amount, the contribution of fibers to the compressive performance of UHPFRC is relatively modest (Savino et al., 2018; Spasojević, 2008). Consequently, fibers in the compressive zone of the bending beam or the impacted specimen have a relatively small contribution,

whereas fibers in the tensile zone can effectively improve the load carrying capacity of the concrete by inhibiting cracking and redistributing stress in that region (Yang and Dong, 2003).

In order to obtain a more efficient utilization of the steel fibers, the concept of multi-layered concrete with different amounts of fibers distributed according to the stress distribution is proposed (Dias et al., 2010). In addition, research on multi-layered NC indicates that the application of a layered structure could be a breakthrough in enhancing its mechanical performances (Dias et al., 2010). For example, Shen et al. (Shen et al., 2008) studied the flexural behavior of a four-layered concrete beam with PVA fibers gradually distributed. Their results show that the layered beam has a 50% higher flexural strength compared to its single-layered counterpart. Accordingly, a multi-layered UHPFRC with fibers purposefully reinforced in the target region has the potential to improve the material utilization efficiency, as well as the static and dynamic properties of the composite.

1.1.4 Rate effects on UHPFRC performance

The superior performances of UHPFRC make it suitable for impact-resistant structures in both the civil and military fields (Spasojević, 2008; Yu, 2015). Due to the rate effect, the dynamic behaviors of cementitious materials differ from their static performances (Weerheijm, 2013). Concerning the dynamic tension load, the enhancement of concrete tensile strength under dynamic loading is mainly attributed to two factors: the moisture in the pores distributing in the concrete matrix, i.e. the Stefan effect; and the inertia effects associated with micro-cracking of the material (Alwan et al., 1999; Lu and Li, 2011). As with dynamic compression, there appears to be a general agreement that the dynamic enhancement of the concrete compressive strength is largely attributed to the Stefan effect and structural inertia forces, particularly the lateral inertia confinement under high loading rates (Bischoff and Perry, 1991; Li and Meng, 2003).

Understanding the response of UHPFRC under dynamic loadings is of great significance for the safe design of impact-resistant structures. According to ACI Committee Reports (ACI Committee 544, 1999), the following types of dynamic tests can be employed to evaluate the impact resistance of concrete: (1) Charpy impact test; (2) instrumented pendulum impact test, (3) drop-weight test, (4) constant strain-rate test, (5) split-Hopkinson bar test, (6) projectile impact test, and (7) blast test. Among these testing methods, the drop-weight impact test can be employed to investigate the resistance of UHPFRC against low-velocity impacts, which are common in the civil engineering field such as a vehicle collision and rock fall (Hrynyk and Vecchio, 2014). With respect to high-velocity impacts, projectile impact tests are commonly utilized to evaluate the ballistic resistance of UHPFRC, providing valuable perspective for understanding its dynamic performance and promoting the advanced design of UHPFRC protective structures.

1.2 Research motivation and aim

UHPFRC is one of the most advanced cementitious materials developed to date. Its superior performances give it the potential to be utilized for wide applications. Developing coarse-aggregated UHPFRC contributes to the environmentally sustainability and the cost efficiency, considering the reduced cement usage due to the incorporation of the coarse aggregates. Additionally, appropriate types of coarse aggregates, e.g. basalt aggregates, also possess advantages on enhancing the impact resistance of the coarse-aggregated UHPFRC.

Furthermore, the performances of UHPFRC can be influenced by the incorporated steel fibers, making studying fibers effects a highly significant issue. Understanding the effects of fiber inclination is of great importance as fibers are usually randomly distributed in UHPFRC. Moreover, fibers contribute more to the tensile properties of UHPFRC than to its compressive strength. Compared to a single-layered UHPFRC with the same amount of fibers distributed randomly in the whole structure, a multi-layered one with the fibers purposefully reinforcing the target area according to the stress distribution has the potential to increase the material utilization efficiency and to improve the performances of UHPFRC.

In addition of the static properties, the dynamic responses of UHPFRC against impacts have received increasing attentions. Low-velocity impacts are common in the civil engineering field, such as vehicle collisions and falling rock impacts. Besides, the use of ballistic weapons in conflict areas or under terrorist attacks also makes the security problem of concrete structure a critical concern. Considering that the behaviors of cementitious materials, e.g. the strength and the failure mode, are rate dependent, the performances of UHPFRC under dynamic impacts should be clearly understood prior to the design and application of impact-resistant UHPFRC structures.

Accordingly, this research aims to investigate the fibers effects on the coarse-aggregated layered UHPFRC, subjected to static and dynamic loads, with the focus on the fiber pullout performance at mesoscale and the fiber amount distribution over the layered UHPFRC at macroscale. Specific research objectives include:

- (1) To understand the effects of the fiber inclination on the static fiber pullout performance;
- (2) To understand the effects of the pullout rate on the dynamic fiber pullout performance;
- (3) To enhance the static flexural performance of the coarse-aggregated UHPFRC using a layered structure, and obtain the optimum design of layered UHPFRC;
- (4) To understand the dynamic performance of the coarse-aggregated UHPFRC subjected to drop-weight load, and enhance its low-velocity impact resistance using a layered structure;
- (5) To understand the dynamic performance of the coarse-aggregated UHPFRC subjected to projectile penetration, and enhance its high-velocity impact resistance using a layered structure.

1.3 Outline of the thesis

The research framework of this thesis is shown in Fig. 1-3. This chapter introduces briefly the background and aim of this research; whereas the detailed state-of-the-art development concerning each research objective is presented in the introduction part of each chapter. Chapters 2 and 3 exhibit the static and dynamic fiber-matrix interactions at mesoscale by analyzing the single fiber pullout performances under static and dynamic pullout loads, respectively. The following chapters focus on the performances of the layered UHPFRC at macroscale under different loading rates: Chapter 4 evaluates the static flexural properties, Chapter 5 investigates the response under low-velocity impact, while Chapters 6 to 8 account for the impact resistance against high-velocity projectile penetration. More specific explanations of these chapters are given below.

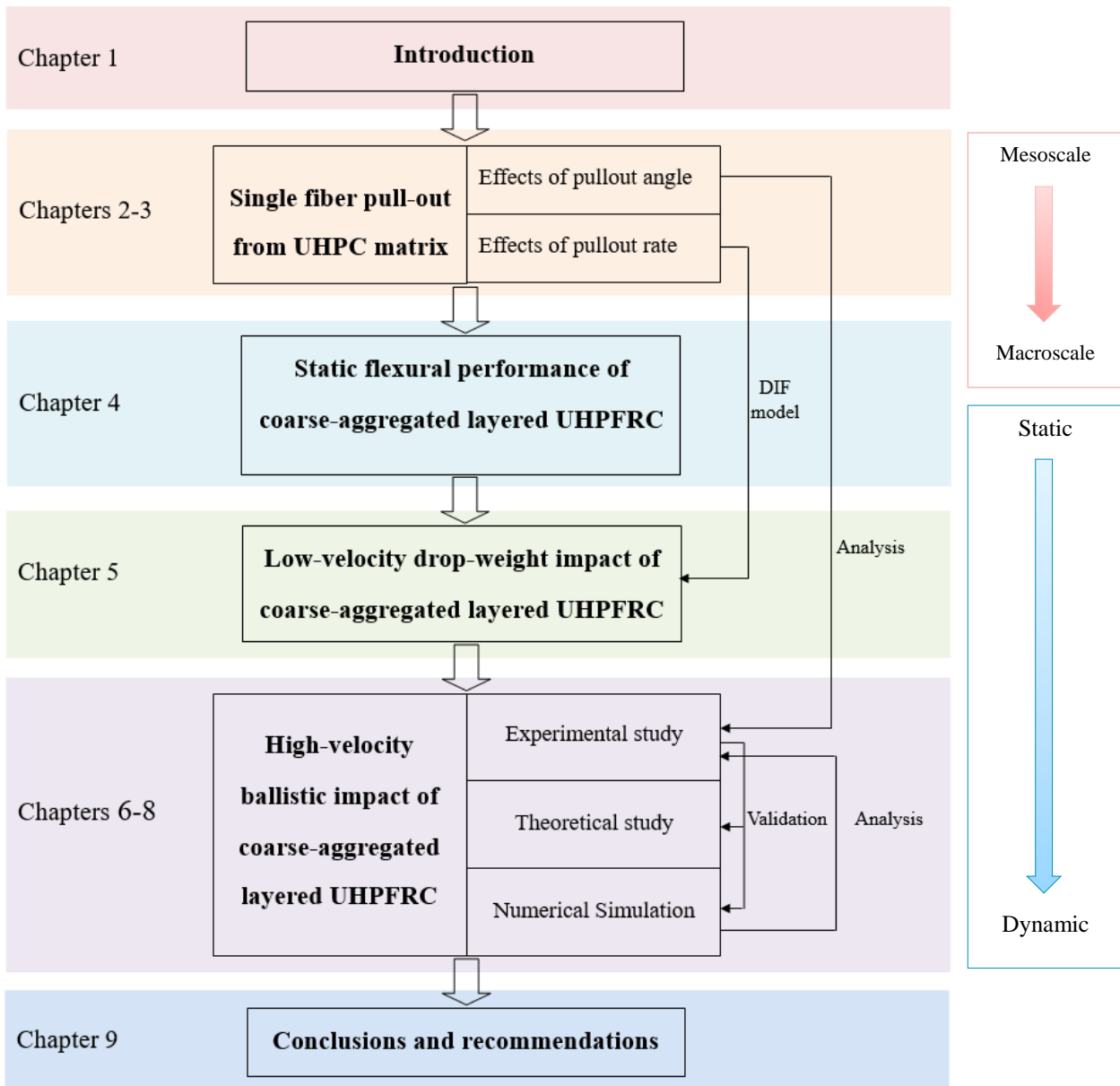


Fig. 1-3 Outline of the thesis

Chapter 2 studies the influences of fiber inclination angle on the pullout response of the hooked-end steel fiber embedded in UHPC matrix. The fiber inclination angles analyzed are 0° , 10° , 20° and 30° , the effects of which are estimated by parameter calculations and mechanism analysis. Furthermore, an analytical model for evaluating the snubbing and spalling effects of the inclined hooked-end fiber is proposed and validated.

Chapter 3 investigates the rate-dependent pullout response of the hooked-end fiber from the UHPC matrix. The pullout rate changes from 5 mm/min (0.083 mm/s) to 1000 mm/min (16.67 mm/s), i.e. from the quasi-static to intermediate strain rates. The mechanisms of the rate effect on the fiber pullout performance are revealed, and a rate-dependent model for predicting the dynamic peak pullout load of the hooked-end fiber is developed and validated.

Chapter 4 focuses on the static flexural performance of coarse-aggregated layered UHPFRC. Theoretical criteria for layer cracking and debonding are proposed, based on which double-layered UHPFRC beams with different layer thicknesses are designed and evaluated under three-point

bending. Different amounts of fibers are employed in the different layers of the UHPFRC with the aims of improving the beam flexural performance and achieving a higher fiber utilization efficiency. The optimum layer thickness and fiber amount distribution are obtained.

Chapter 5 presents the dynamic performance of the coarse-aggregated layered UHPFRC under low-velocity drop-weight impact. The optimum double-layered beam in Chapter 4 is subsequently employed in the dynamic study. A 7.26 kg metal ball dropped from 2.5 m generates dynamic load within the intermediate strain rate range, under which the resistance of the UHPFRC is analyzed. Additionally, a model to estimate the absorbed impact energy of the UHPFRC is proposed and validated. The model divides the absorbed energy into two parts: the matrix-consumed part and the fiber-consumed part, and the latter is calculated using the model from Chapter 3.

Chapter 6 experimentally analyses the dynamic performance of the coarse-aggregated layered UHPFRC under high-velocity projectile penetration impact. The in-service 7.62 mm \times 51 AP projectile impacts the UHPFRC targets at around 840 m/s. A multi-layered UHPFRC protective element with superior ballistic resistance is developed, and the influences of the aggregate size, steel fiber and layer thickness are addressed. The results in Chapter 2 concerning the inclined fiber benefit the analysis of the fibers influences in this chapter.

Chapter 7 develops models for predicting the depth of penetration (DOP) in UHPFRC subjected to high-velocity projectile impact. The penetration process inside the semi-infinite UHPFRC target is modelled as the expansion of a spherical cavity, invoking elastic-cracked-comminuted or elastic-comminuted responses in the UHPFRC. The Hoek-Brown criterion is utilized to describe the nonlinear response, and the rate effect on the UHPFRC resistance is considered. After developing the model for the single-layered UHPFRC, the DOP predictive model is further extended for the multi-layered targets with the varying mechanical properties of the layered target considered.

Chapter 8 numerically analyses the dynamic performance of the coarse-aggregated layered UHPFRC under high-velocity projectile penetration impact. LS-DYNA is utilized to simulate the ballistic experiments of the single- and triple-layered UHPFRC presented in Chapter 6, after which the effects of the target thickness and the penetration velocity on the DOP are discussed. The perforation limits of the single- and triple-layered UHPFRC at different impact velocities are estimated and compared with the results from the empirical formulae.

Chapter 9 concludes the important results from this research and recommends further studies to continue the present research.

Chapter 2

*Effect of inclination angle on the pullout performance of hooked-end steel fiber embedded in UHPC **



*This chapter is partially reproduced from: Y.Y.Y. Cao, Q.L. Yu, Effect of inclination angle on hooked-end steel fiber pullout behavior in ultra-high performance concrete, Composite Structures 201 (2018) 151–160.

Abstract

The bond relationship between the concrete matrix and steel fiber is a significant factor affecting the performance of UHPFRC. In this chapter, the pullout performances of hooked-end steel fibers embedded in Ultra-High Performance Concrete (UHPC) matrix under various inclination angles are systematically investigated. Pullout load-slip curves are obtained, and experimental observations including complete fiber pullout, fiber breakage and matrix failure are analyzed in detail. The effects of the pullout angle are studied quantitatively by parameter calculations and mechanism analysis. Moreover, a new analytical model for evaluating the snubbing and spalling effects of the hooked-end steel fiber is proposed and validated. It is shown that the influences of the inclination angle on the peak pullout load vary with different fiber diameters and embedded lengths, which are also associated with the occurrences of the fiber breakage and the matrix failure. In addition, optical microscope and scanning electron microscopy (SEM) observations at mesoscale are performed for the further analysis.

2.1 Introduction

UHPFRC is a construction material characterized by its very high compressive strength, excellent durability, energy absorption capacity and damage tolerance (Yu, 2015). Fibers play an important role in UHPFRC. The incorporation of fibers in UHPFRC significantly improves its tensile strength, post-cracking ductility and energy absorption capacity, as well as reduces the crack width and crack spacing (Tran et al., 2015). In addition to the fiber amount, individual pullout behavior of the activated fibers crossing a crack is also an important factor that affects the performances of UHPFRC composites.

As a foundation to analyze the fiber effects on cementitious composite, single fiber pullout test can provide a comprehensive understanding of the fiber-matrix interface properties as well as the stress transfer mechanisms between the fiber and the matrix (Wille and Naaman, 2010). A number of tests concerning single fiber pulled out from NC have been performed (Orange et al., 1999). However, since the quality of the matrix is one of the dominant factors influencing the pullout behavior, the performance of steel fibers embedded in UHPC matrix can differ remarkably with that in NC (Kim et al., 2012; Wille and Naaman, 2010): instead of a sudden sharp drop after reaching the peak stress as observed in the case of NC, the pullout stress of UHPC declines gradually. As indicated by SEM images, the fiber-matrix interface zone of the UHPC matrix is much denser than that of NC (Wille and Naaman, 2010). This dense interface offers a higher resistance to matrix spalling and leads to the improved pullout resistance (Li et al., 1990).

In UHPFRC, fibers are usually randomly distributed. Fibers under different inclination angles have distinct contributions (Laranjeira et al., 2010). On the one hand, fiber inclination increases the bridging force and the pullout work (Isla et al., 2015; Markovic, 2006). On the other hand, it also generates higher stresses in the fiber and the matrix, and thus arouses a higher fiber and/or concrete rupture potential (Isla et al., 2015; Markovic, 2006). The analytical model developed by Zhang and Li (Zhang and Li, 2002) exhibited that the fiber breakage load of an inclined fiber is significantly reduced compared to that of an aligned one, and this load decreases with the increasing elastic modulus of the matrix. It can be inferred from their research that an inclined steel fiber embedded in UHPC with a higher elastic modulus may have a higher chance to break during the pullout process. This indicates the importance of studying the effects of fiber inclination angle on its pullout behavior from UHPC. Nonetheless, most of the current pullout investigations regarding UHPC focus on aligned fibers while research concerning inclined fibers is inadequate. Among the limited studies, Lee et al. (Lee et al., 2010) conducted pullout tests of straight steel fibers embedded in UHPC under 0° to 60° , and reported that the largest peak load is observed at an angle between 30° and 45° . Xu et al. (Xu et al., 2016) studied the pullout behaviors of straight steel fibers from UHPC and analyzed the influences of inclination angles on the loading rate sensitivity; it was found in their research that an inclination angle of 20° leads to a more obvious rate effect.

It is noteworthy that the object of the above studies is straight steel fibers. However, recent researches have revealed that compared to the straight-fiber-reinforced UHPFRC, the UHPFRC reinforced by an appropriate content of hooked-end steel fibers endows superior properties with respect to post cracking strength, strain capacity and multiple cracking behavior (Liu et al., 2016; Park et al., 2012; Wu et al., 2016). This makes understanding the pullout behavior of inclined hooked-end fibers from UHPC matrix a significant research topic. Nevertheless, relevant study is insufficient. Tai

and El-Tawil (Tai and El-Tawil, 2017) investigated the pullout behavior of inclined deformed steel fibers from UHPC under different loading rates, and found that the pullout resistance is sensitive to both the inclination angle and the loading rate. However, their study focused more on the loading rate effect rather than the pullout angle. Furthermore, analytical models are important tools to evaluate the snubbing and spalling effects caused by the fiber inclination on its pullout response (Lee et al., 2010). Despite the numbers of models concerning straight steel fibers (Lee et al., 2010; Tai and El-Tawil, 2017), models for the inclined hooked-end fiber are still rare and require more investigations.

To fill the gap, this chapter aims to study the pullout performances of hooked-end steel fibers embedded in UHPC matrix, with the special attention paid to the effects of fiber inclination angle. Single fiber pullout tests are performed, supported by mechanical parameter calculations. Based on previous models for straight fibers, a new analytical model for hooked-end fibers to evaluate the snubbing and matrix spalling effects is developed. Additionally, mesoscale observations of the investigated fibers and the UHPC are carried out employing optical microscope and SEM.

2.2 Single fiber pullout experiments

2.2.1 Steel fibers

As shown in Fig. 2-1, two types of hooked-end steel fibers are used in the single fiber pullout tests. One is Dramix RC-80/30-BP fiber, and the other one is a one-hooked-end steel fiber cut from Dramix 5D fiber. The basic geometry and mechanical parameters of the fibers are given in Table 2-1. The identification is defined as follows: the first letter H represents the hooked-end steel fiber, the first number denotes the fiber diameter in mm, and the last number shows the fiber embedded length in mm. For example, H-0.38-10 is a hooked-end fiber with a diameter of 0.38 mm and an embedded length of 10 mm.

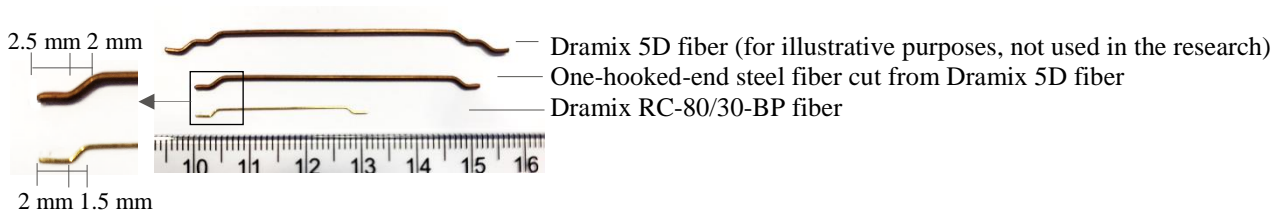


Fig. 2-1 Hooked-end steel fibers in the single fiber pullout tests

Table 2-1 Specifications of fibers

Fiber type	Dramix RC-80/30-BP fiber	One-hooked-end fiber cut from Dramix 5D fiber	
Identification	H-0.38-10	H-0.9-10	H-0.9-15
Fiber diameter d_f (mm)	0.38	0.90	0.90
Fiber length l_f (mm)	30	60	60
Embedded length l_e (mm)	10	10	15
Fiber strength σ_y (MPa)	2600	2600	2600

2.2.2 UHPC matrix

The UHPC matrix for the pullout test is based on the recipe described in (Li et al., 2018), as presented in Table 2-2. The raw materials used are Portland Cement CEM I 52.5 R (PC), micro-silica (mS), limestone powder (LP), sand 0-2 (S), basalt aggregate with sizes from 1 mm to 3 mm (BA 1-3), water (W), and PCE-type superplasticizer (SP). More detailed information about the material specific

densities, particle size distributions, and mix design of the UHPC mixture can be found in (Li et al., 2018). The 28 days compressive strength $\sigma_{c,s}$ of the UHPC is 156 MPa (measured with 100 mm cubes). The spread flow of the UHPC is around 27 cm, measured by the Hägermann cone without jolting according to EN 1015-3:2007 (DIN EN 1015-3, 2007).

Table 2-2 Recipe of UHPC matrix: CEM = Portland cement, mS = micro-silica, LP = limestone powder, S = sand, BA 1-3 = basalt aggregate with sizes of 1-3 mm, W = water, SP = superplasticizer.

Materials	CEM (kg/m ³)	mS (kg/m ³)	LP (kg/m ³)	S (kg/m ³)	BA 1-3 (kg/m ³)	W ^a (kg/m ³)	SP ^b (kg/m ³)
Quantity	675	45	180	864.5	576.3	180	10.8

a: Water from SP is included.

b: The solid content is 35%.

2.2.3 Mixing and casting procedures

The following mixing procedure is adopted for the preparation of the UHPC matrix: dry mixing for 2 minutes with all powder, sand and basalt aggregate; adding 75% water and mixing for 2 minutes; sequentially adding the remaining water with the superplasticizer incorporated and mixing for another 2 minutes at a low speed and then 4 minutes at a high speed. The mixing procedure is conducted at room temperature of about 20 ± 1 °C.

Dog-bone shaped mould (Fig. 2-2) is used for casting the specimen. The thickness of the mould is 20 mm. As presented in Figs. 2-2a and b, two pieces of hard foam with dimensions of $10 \times 10 \times 25$ mm³ are applied to hold the hooked-end steel fiber. The fiber is carefully placed on one piece of the hard foam with the desired embedded length and inclination angle, after which the fiber is fixed on the hard foam with a thin strip of scotch tape. Next, the other piece of the hard foam is put on it, sandwiching the fiber in between. The two pieces of hard foam are then wrapped together by tape and put inside the mold.

The fresh UHPC is poured without vibration into a half dog-bone shape mould. After casting, the specimens are covered with plastic sheets to prevent moisture evaporation and stored at room temperature for 24 hours. Then they are demolded and cured in water under room temperature for additional 27 days. All specimens are tested in surface dry condition at the age of 28 days, and the hard foam is removed before testing. The fiber inclination angles applied in this study are 0°, 10°, 20° and 30°.

2.2.4 Pullout test setup and procedure

The pullout test is conducted using an Instron 5967 universal testing machine (Fig. 2-2c). A round concrete grip is applied to hold the half dog-bone shaped specimen in order to reduce the confining effect of the grip on the concrete. The fiber grip is specially designed such that the free end of the fiber is tightly held without significant slip in the grip. By assuming that the elastic deformation of the steel fiber and the grips are small enough (Tai et al., 2016; Xu et al., 2016; Yoo et al., 2017b), the fiber slip is measured according to the vertical movement of the grip system. The pullout load is measured by a load cell with a capacity of 30 kN. A preload of 10 N was added to remove slack in the system. The tests are performed under the displacement control and the pullout rate adopted is 0.5 mm/min. At least five specimens are tested in each category.

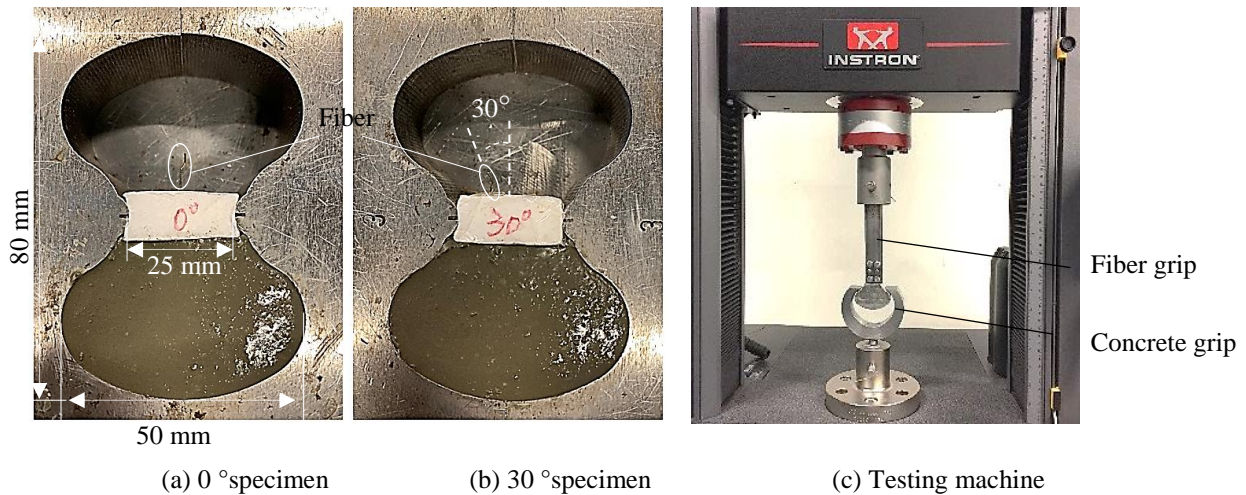


Fig. 2-2 Pullout specimens and test setup

2.2.5 SEM observations

SEM analysis is performed to investigate the mesoscopic interface structure between the steel fiber and the UHPC matrix. The sample preparation process for the SEM analysis can be briefly described as follows: (1) Cutting. The observed regions are cut into small pieces from the air-dried specimens. (2) Epoxy resin coating. The samples are put in cylindrical rubber containers with the desired face parallel in the horizontal direction, and then impregnated with epoxy. (3) Polishing. After the epoxy is hardened, i.e. approximately 6 hours, the samples are polished using an auto polisher for 5 min with a 600 grit silicon carbide sand paper, and for another 5 min with an 800 grit silicon carbide sand paper.

2.3 Pullout responses

During the pullout tests three distinct responses are observed, namely complete fiber pullout, fiber breakage and matrix failure. The first one is usually observed under small pullout angles for the three categories. On the contrary, the second and third ones occur more frequently under larger inclination angles in the cases of the H-0.38-10 and H-0.9-10 categories, respectively.

In most cases, at least 5 specimens are used to obtain the averaged pullout load-slip curve. However, for the H-0.38-10 category at 30°, only 3 specimens are used due to the fiber breakage of the other specimens (Table 2-3). For the H-0.9-10 category, the average process is based on 3 or 4 specimens for each pullout angle, which is because of the matrix failure problem (Table 2-4). The commercial data analysis software Origin is adopted for the averaging procedure. An example of the averaged pullout load-slip curve is given in Fig. 2-3. Scatterings of the curves are observed in spite of the efforts dedicated for careful specimen preparation and experiment execution.

Table 2-3 Number of fiber breakage specimen and total tested specimens

Angle (°)	0	10	20	30
H-0.38-10	0 out of 5	2 out of 7	2 out of 7	7 out of 10

Table 2-4 Number of matrix damaged specimens

Angle (°)	0	10	20	30
H-0.9-10	1 out of 5	2 out of 5	3 out of 6	6 out of 6

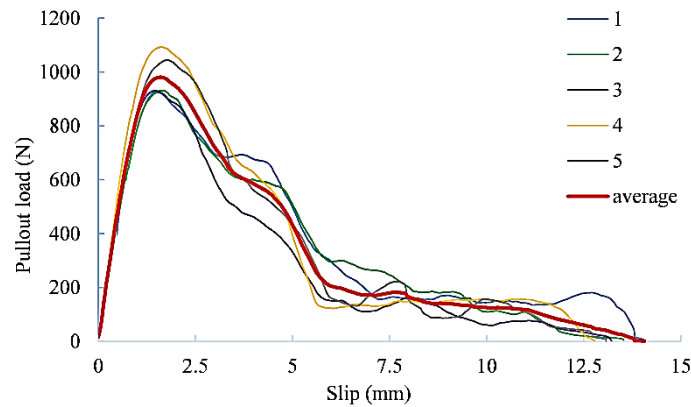


Fig. 2-3 Averaged pullout load-slip curve of H-0.9-15 fiber under 20°

2.3.1 Complete fiber pullout

Typical pullout load-slip relationships for the H-0.38-10 fiber under different angles are plotted in Fig. 2-4. As can be observed in the figure, these curves have resemble shapes, suggesting a similar pullout process under different inclination angles. In the initial elastic stage of the pullout test, the response is almost linear until the initiation of debonding (point A), after which fiber-matrix interface failure begins. The pullout load then increases at a slower rate. The contribution of the hook is activated after the complete debonding of the fiber and it reaches the peak at point B. Through the pullout process at this stage, the hook part of the steel fiber undergoes large deformations, i.e. plastic hinges are formed in the two curved sections of the fiber hook where plastic bending occurs. In the post-peak stage, the hook undergoes a straightening procedure, during which the plastic hinges play an important role. The fluctuations of the curve after point B are associated with the deformation of the hook. When the hook is fully straightened and slips along the straight tunnel (point C), the plastic hinges are deactivated and the fiber-matrix friction becomes the dominant mechanism. The pullout load decreases gradually due to the reduction of the remaining embedded length until the end of the pullout process (point D).

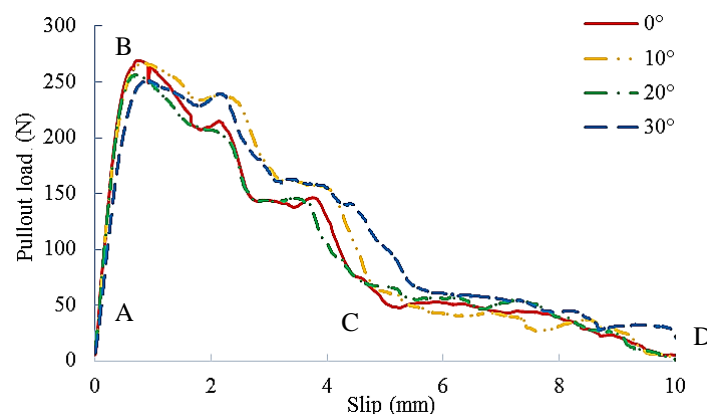


Fig. 2-4 Pullout load-slip curves of H-0.38-10 fiber

Fig. 2-4 also exhibits the effect of the inclination angle on the peak pullout load P_{max} . The P_{max} at 0° and 10° are close to each other and they are slightly higher than those at 20° and 30°. This is primarily due to the small concrete pieces spalling off from the pullout surface at 20° and 30°, resulting

in a smaller embedded length of the steel fiber and thus a reduced pullout load. An example of the matrix spalling zone on the pullout surface at 30° is shown in Fig. 2-5a. The tendency in Fig. 2-4 is in accordance with the finding in (Banthia and Trottier, 1994) that P_{max} of the hooked-end fiber remained nearly unchanged at angles from 0° to 60° when it is pulled out from high-strength concrete matrix ($\sigma_{c,s} = 85$ MPa). Nonetheless, contradictory results can be found in other studies. For example, Tai and El-Tawil (Tai and El-Tawil, 2017) tested the pullout behavior of a hooked-end steel fiber from UHPC ($\sigma_{c,s} = 184$ MPa) at $0^\circ \sim 45^\circ$ and found that the P_{max} was maximized at approximately 30° . The difference may be ascribed to the following reasons. Firstly, the enhanced strength of the matrix in (Tai and El-Tawil, 2017) can lead to an improved frictional resistance between the fiber and the matrix, generating a more remarkable snubbing effect that increases P_{max} with the inclination angle (Robins et al., 2002). Secondly, in their test matrix spalling is only observed at 45° , which means the resistance loss due to the reduced embedded length is only occurred at 45° rather than at 20° and 30° as observed in this study.

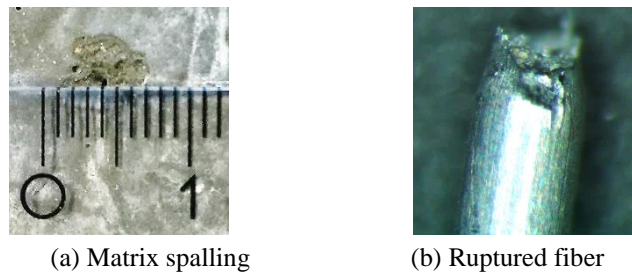


Fig. 2-5 Matrix spalling and fiber breakage

2.3.2 Fiber breakage

One common problem for pulling out an inclined fiber is its breakage. In this study, the majority of the H-0.38-10 fibers broke inside the matrix near the pullout surface when the inclination angle is 30° . The numbers of specimens experienced fiber breakage are given in Table 2-3. An example of the ruptured H-0.38-10 fiber is shown in Fig. 2-5b, in which the irregular break surface and the reduced local cross-section area due to Poisson effect, i.e. necking, can be clearly observed.

During the pullout process, the fiber breaks when the localized strain is higher than its limit value or when the pullout resistance exceeds the ultimate tensile strength of the steel material. As suggested in (Robins et al., 2002), the yield of the steel fiber is the consequence of inter-crystal slip in metal caused by atomic-level dislocation movements. In the case of the inclined fibers, additional shear stress is imposed on the fiber where it enters the matrix. This additional stress considerably accelerates the inter-crystal slip within the crystal system of the fiber by lowering both its yield and ultimate strengths (Robins et al., 2002). As a consequence, the inclined fiber would reach the ultimate conditions under a lower applied load. In other words, the fiber breakage load of an inclined fiber is reduced compared to its aligned counterpart, i.e. fiber apparent strength degradation occurs (Zhang and Li, 2002). Since the degradation is more pronounced under a larger angle, a highly inclined fiber exhibit a higher possibility to break during the pullout process.

2.3.3 Matrix failure

The pullout behavior of the H-0.9-10 fiber is illustrated in Fig. 2-6a. For this category, 20° is the optimum pullout direction to achieve the largest P_{max} . The curve corresponding to 30° drops suddenly

at a slip of about 1.8 mm. This is because all the specimens tested at 30° experience serious matrix failure, leading to a rapid pullout of the fibers. Fig. 2-7 shows examples of a failed matrix specimen and the H-0.9-10 fiber after the test at 30° . As the figure presents, the matrix is cracked from a location near the hooked-end and the cracks propagate to the pullout surface, forming a crater inside the concrete. The depth of the crater is approximately the same as the embedded length of the fiber. As can be seen, the H-0.9-10 fiber is pulled out from the cracked matrix before the hook is straightened, which manifests that the contribution of the hook is not fully utilized. This matrix failure occurs more frequently with the increase of the pullout angle (see Table 2-4).

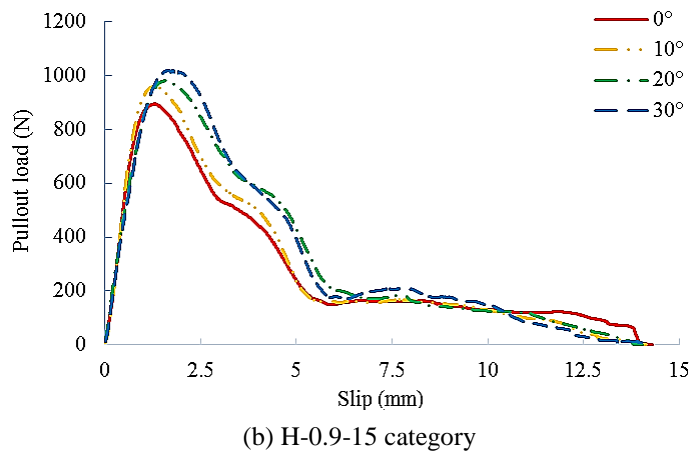
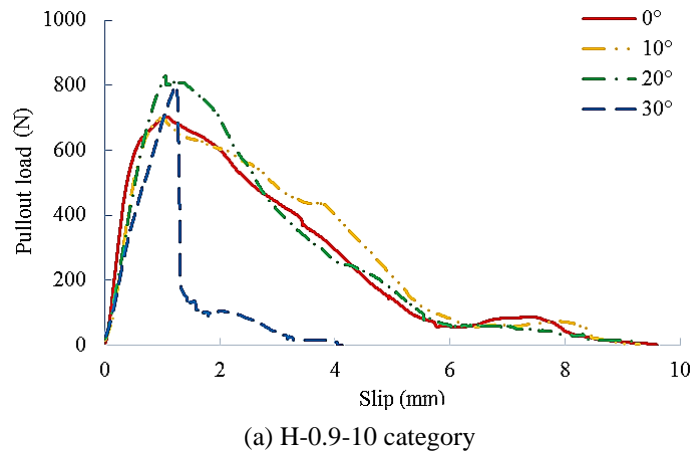


Fig. 2-6 Pullout load-slip curves

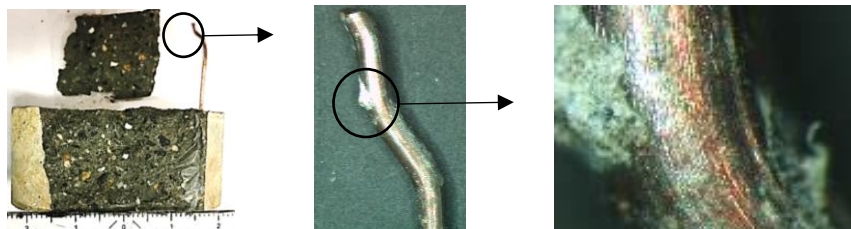


Fig. 2-7 Example of matrix failure and the fiber under 30°

The prominent anchorage force provided by the hook and the relatively small embedded length in the matrix may conduce to the matrix failure. Firstly, the stress at the bending regions of the hook due to slip shear initiates the fracture of the matrix, making the matrix near the hook a weak region.

Secondly, the surrounding concrete matrix that covers the hook is too thin to resist the large anchorage force when the fiber embedded length is insufficient. This inappropriate combination of the large hook and the small embedded length thus results in the matrix failure.

Increasing the fiber embedded length or adding micro fibers in the matrix are two potential methods to prevent the matrix failure. In this study, the former is utilized considering its simplification. The embedded length l_e is increased from 10 mm to 15 mm, viz. the H-0.9-15 category. With this enlarged l_e , only one specimen has the matrix failure problem when it is pulled-out at 30° , none of the rest specimens encounters this problem. The pullout load-slip relationships for the H-0.9-15 category are plotted in Fig. 2-6b, in which increase of the peak pullout load is observed with the increase of the inclination angle. Moreover, the pullout slip under the peak load increases with the inclination angle, while the slope of the pre-peak branch of the curve decreases. Additionally, the P_{max} of the H-0.9-15 category is also higher compared with that in the H-0.9-10 category, thanks to the longer l_e .

2.4 Parametric evaluation and mechanism analysis

2.4.1 Evaluation of parameters for fiber pullout performance

To study the influences of the inclination angle, the following mechanical parameters are calculated. The maximum fiber stress σ_{max} is an important parameter to estimate the fiber utilization efficiency and to predict fiber pullout modes, i.e. pullout or rupture. It also gives reference to determine the minimum fiber strength needed to avoid fiber fracture. Furthermore, the maximum bond strength τ_{max} , related to the peak pullout load, is often used to evaluate the pullout resistances of fibers with different geometries (Yoo et al., 2017b). Moreover, assuming the bond strength is constant along the entire fiber embedded length, the equivalent bond strength τ_{eq} can be defined based on the pullout energy dissipation, and it is associated with matrix cracking behaviors (Park et al., 2014; Yoo et al., 2017b). Equations for calculating these parameters are:

$$\text{Maximum fiber stress: } \sigma_{max} = \frac{4P_{max}}{\pi d_f^2} \quad (2-1)$$

$$\text{Maximum bond strength: } \tau_{max} = \frac{P_{max}}{\pi d_f l} \quad (2-2)$$

$$\text{Equivalent bond strength: } \tau_{eq} = \frac{2E_p}{\pi d_f l^2} \quad (2-3)$$

where P_{max} is the peak pullout load (MPa); E_p is the pullout energy dissipation, and it is defined geometrically by the area below the pullout load-slip curve (N·mm); d_f is the diameter of the fiber (mm); and l is the actual fiber embedded length obtained from the pullout load-slip curves (mm).

Fig. 2-8 presents the effects of the inclination angle on these parameters. P_{max} , τ_{max} and τ_{eq} of the H-0.9-10 category at 30° are not given because of the serious matrix failure making the results incomparable. It can be seen from Fig. 2-8 that the inclination angle barely affects the results of the H-0.38-10 category. For example, σ_{max} of the H-0.38-10 category decreases slightly with the pullout angle (Fig. 2-8c), showing that the aligned fiber or fiber with a small inclination angle achieves a slightly higher fiber efficiency. This is quite different from the H-0.9-15 category, where improving the pullout angle leads to the increases of these parameters. In addition, no clear trend can be obtained for E_p and τ_{eq} of the H-0.9-10 category, while P_{max} , σ_{max} and τ_{max} achieve their maximum values at 20° .

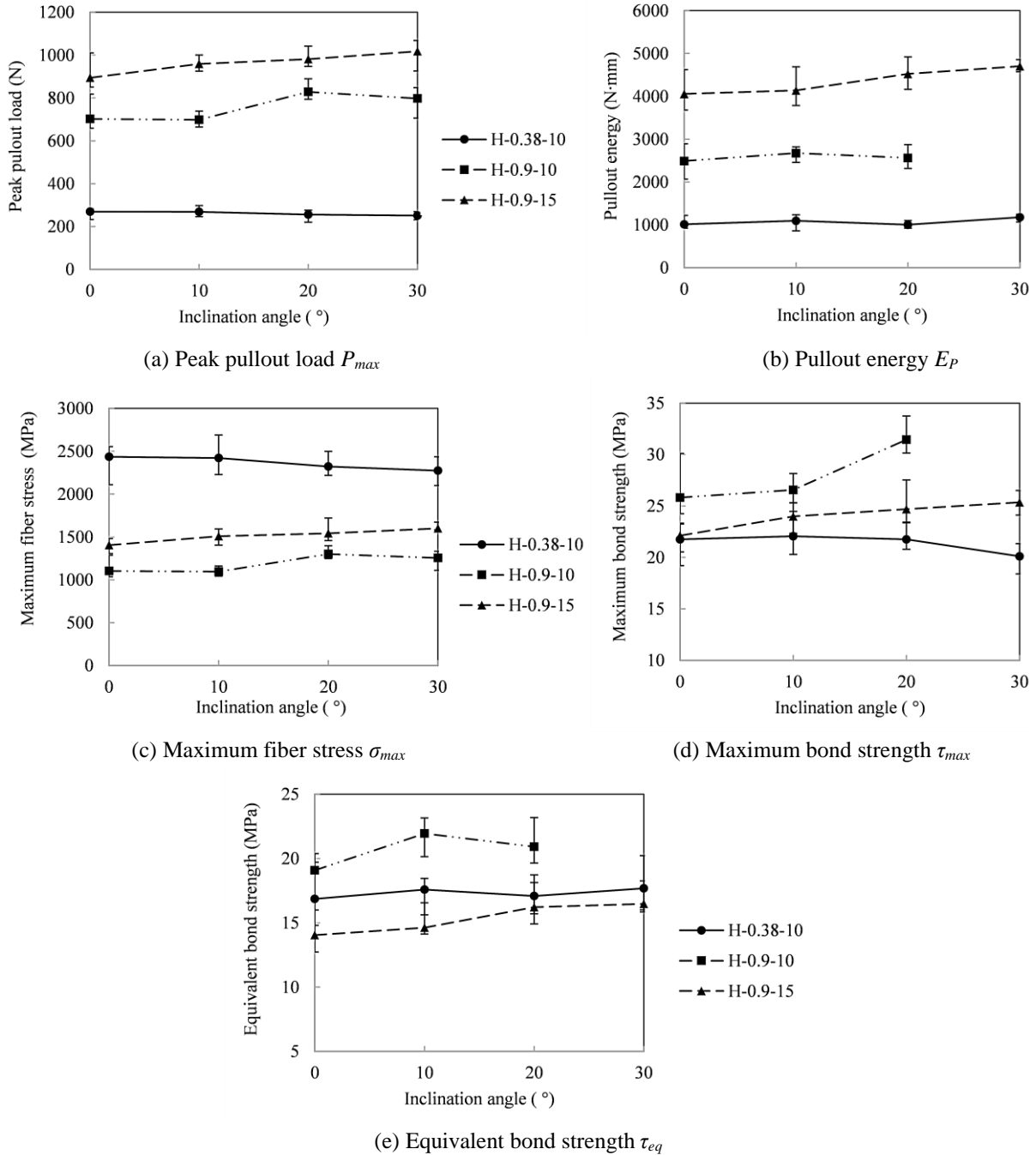


Fig. 2-8 Influences of angle on mechanical parameters

In comparing these parameters for the H-0.38-10 and H-0.9-10 categories, P_{max} , E_p , τ_{max} and τ_{eq} are improved with the increasing of the fiber size. Since τ_{eq} is related with matrix cracking behaviors, the higher τ_{eq} of the H-0.9-10 category is in line with its more frequent matrix failure occurrence during the pullout tests. In contrast, σ_{max} of the H-0.38-10 category is about twice larger than that of the H-0.9-10 category, and it is close to the fiber strength $\sigma_y = 2600$ MPa. This larger σ_{max} , on the one hand, indicates a higher utilization efficiency of the smaller fiber; on the other hand, it also explains the higher fiber breakage occurrence of the H-0.38-10 fiber in the pullout tests.

Furthermore, comparisons between the H-0.9-10 and H-0.9-15 categories demonstrate that increasing the embedded length l_e can efficiently improve P_{max} and E_p . To specify, approximately 28% and 65% increases are obtained for P_{max} and E_p , respectively, when l_e increases from 10 mm to 15 mm.

However, τ_{eq} and τ_{max} tend to be higher when l_e is shorter, i.e. the averaged τ_{eq} and τ_{max} of the H-0.9-10 category are approximately 38% and 18% higher than those of the H-0.9-15 category. This higher τ_{eq} and τ_{max} with smaller l_e of the hooked-end fiber in turn indicates the more prominent contribution of the hook than the straight part of the fiber.

2.4.2 Snubbing and matrix spalling effect

The influences of fiber inclination on the pullout performance are associated with both the snubbing effect and the matrix spalling effect. The phenomenon that the pullout load increases with the increase of the inclination angle is related to the “snubbing effect”, owing to snubbing friction forces invoked by fiber bending. As illustrated in Fig. 2-9a, when a straight fiber is being pulled out with an inclination θ under a force P , a snubbing friction force F will be generated by the normal force N and the relative slip between the fiber and matrix. In assumption that the matrix has the same deformation with the bending fiber in the curvature part, the friction system can then be illustrated as a tensioned fiber snubbed to a virtual cylinder (Li et al., 1991). This invoked snubbing friction force only exists in the curvature region and it can promote enhancements of the pullout resistance and the overall composite toughness (Li et al., 1991; Robins et al., 2002). On the contrary, the “matrix spalling effect” will lead to the decrease of pullout load with the increasing angle. Fiber inclination can cause a stress concentration at the matrix pullout surface, and consequently, local failure of the supporting matrix near the bearing point, i.e. matrix spalling, occurs (Li et al., 1990). As the inclination angle increases, the stress concentration is also enhanced, leading to a more considerable portion of the concrete to crush at the pullout surface and a longer freed embedded length, thus a lower pullout load (Lee et al., 2010).

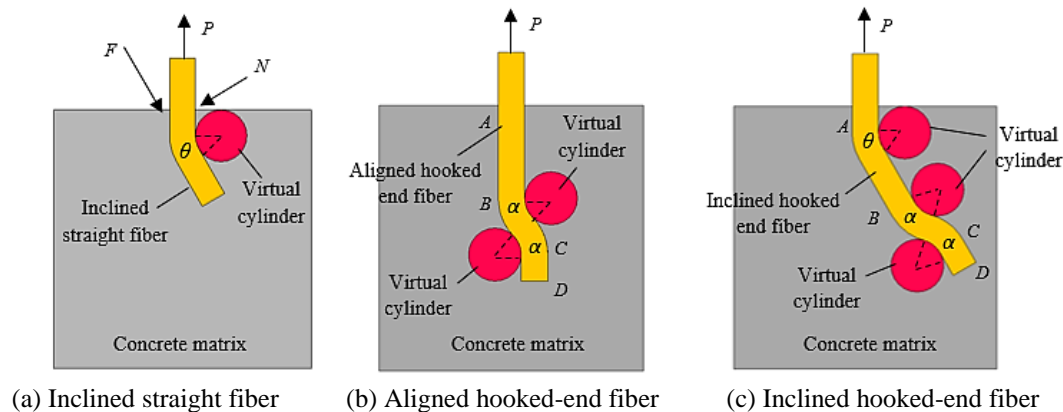


Fig. 2-9 Illustrations of snubbing effects

To study the snubbing effect and the matrix spalling effect, the corresponding evaluation coefficients, i.e. snubbing friction coefficient f_p and spalling coefficient k_p , are calculated. It should be noted that previously proposed models for calculating f_p were developed only for straight fibers without mechanical anchorage (Lee et al., 2010; Li et al., 1990; Tai and El-Tawil, 2017). This study expands these models, and proposes a new analytical model for hooked-end fibers.

Firstly, a normalized load P_n is defined as the ratio of the peak load to the pullout length at a given angle θ , normalized with the ratio at the pullout angle of 0° (Li et al., 1990):

$$P_n = \frac{P_{max,\theta} / L_\theta}{P_{max,0} / L_0} \quad (2-4)$$

where $P_{max,\theta}$ and $P_{max,0}$ are the peak pullout loads at θ and 0° (MPa); L_θ and L_0 are the corresponding actual fiber embedded length (mm).

As suggested in (Lee et al., 2010; Li et al., 1990; Yang et al., 2008), the following equation is used to represent the snubbing effect on a straight fiber:

$$P_{n,s} = \frac{P_{max,s,\theta} / L_\theta}{P_{max,s,0} / L_0} = e^{f_p \theta} \quad (2-5)$$

where $P_{n,s}$ is the normalized load for the straight fiber; $P_{max,s,\theta}$ and $P_{max,s,0}$ are the peak pullout loads of the straight fiber at θ and 0° (MPa), respectively.

Assuming that the interfacial shear stress is uniform along the embedded fiber and increases gradually with the pullout load until it approaches the interfacial shear strength τ (Fu et al., 1993), together with Eq. 2-5, $P_{max,s,0}$ and $P_{max,s,\theta}$ can be expressed as:

$$P_{max,s,0} = \pi d_f L_0 \tau \quad (2-6)$$

$$P_{max,s,\theta} = \pi d_f L_\theta \tau e^{f_p \theta} \quad (2-7)$$

Next, the above equations are expanded for hooked-end fibers. The snubbing effects of a hooked-end fiber at 0° and θ are shown in Figs. 2-9b and c, where α is the angle of the hook. As can be observed, even when the hooked-end fiber is aligned, snubbing friction forces will be generated during the pullout process because of the curvatures of the hook (the virtual cylinders in Fig. 2-9b). This denotes similar snubbing effects as the inclined straight fiber in Fig. 2-9a. Consequently, the peak pullout forces for the hooked-end fiber at 0° and θ (MPa) can be expressed as Eqs. 2-8 and 2-9. It is worth mentioning that for the hooked-end fiber, τ is an equivalent value with both the frictional effect (due to the straight part of the fiber) and part of the anchorage effect (due to the hook) included.

$$P_{max,h,0} = \pi d_f \left[L_{AB,0} + (L_{BC,0} + L_{CD,0}) e^{f_p \alpha} \right] \tau \quad (2-8)$$

$$P_{max,h,\theta} = \pi d_f \left[L_{AB,\theta} e^{f_p \theta} + (L_{BC,\theta} + L_{CD,\theta}) e^{f_p \alpha} \right] \tau \quad (2-9)$$

Substituting Eqs. 2-8 and 2-9 into Eq. 2-4, the normalized load for the hooked-end fiber considering the snubbing effect is obtained:

$$P_{n,h,1} = \frac{P_{max,h,\theta} / L_\theta}{P_{max,h,0} / L_0} = \frac{\left[L_{AB,\theta} e^{f_p \theta} + (L_{BC,\theta} + L_{CD,\theta}) e^{f_p \alpha} \right] L_0}{\left[L_{AB,0} + (L_{BC,0} + L_{CD,0}) e^{f_p \alpha} \right] L_\theta} \quad (2-10)$$

Moreover, supposing that the pullout load does not reduce in the case of the aligned fiber and that the pullout load does not act on the fiber when the load direction is perpendicular to the fiber axial, an equation to account for the spalling effect is presented (Lee et al., 2010; Tai and El-Tawil, 2017):

$$P_{n,h,2} = (\cos \theta)^{k_p} \quad (2-11)$$

Combining the above two effects, an analytical model for the hooked-end fiber is proposed:

$$P_{n,h} = \frac{\left[L_{AB,\theta} e^{f_p \theta} + (L_{BC,\theta} + L_{CD,\theta}) e^{f_p \alpha} \right] L_0}{\left[L_{AB,0} + (L_{BC,0} + L_{CD,0}) e^{f_p \alpha} \right] L_\theta} (\cos \theta)^{k_p} \quad (2-12)$$

The results of the H-0.9-10 and H-0.9-15 categories are applied for validating the proposed model, with the angle of the hook $\alpha = 45^\circ$; hook length $L_{BC} = 2.83$ mm and $L_{CD} = 2.5$ mm; $L_{AB} = l_e - L_{BC} \sin \alpha - L_{CD}$. The snubbing friction coefficient and the spalling coefficient are obtained as $f_p = 1.25$ and $k_p = 1.0$. Fig. 2-10 plots the comparison between the test results and the calculated normalized loads for the two tested categories, as well as for the pullout tests results in (Tai and El-Tawil, 2017) with the above obtained f_p and k_p . The good match indicates the validity of the proposed model. It is noteworthy that for the analytical results of (Tai and El-Tawil, 2017), k_p is only used at 45° , in which case concrete spalling was observed (Tai and El-Tawil, 2017). Besides, one should be aware that the obtained f_p and k_p in the present study are different from the ones in (Lee et al., 2010) with straight steel fiber, i.e. $f_p = 1.6$, $k_p = 1.8$. This can be explained by the following reasons. Firstly, the fiber types in the two studies are different, which can induce distinct snubbing and matrix spalling effects. Secondly, the test specimen in (Lee et al., 2010) includes 32 steel fibers, and the pullout behavior is examined using the average value relative to one fiber. This measurement of the pullout load can differ with the result from the single fiber pullout test due to the group effect, which may reduce the fiber efficiency as well as the matrix's capability to resist the bond (Wille and Naaman, 2012). Hence, the snubbing friction force has a distinct distribution along the fiber and the spalling of the matrix is also different.

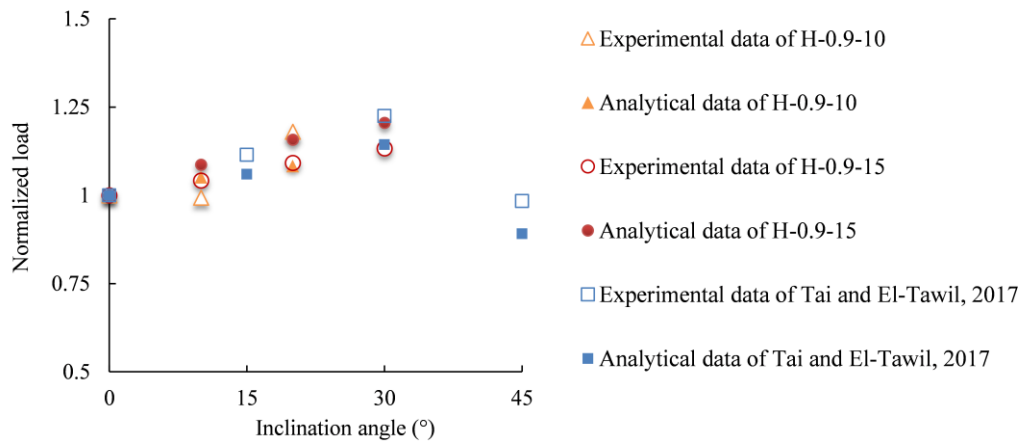


Fig. 2-10 Comparison between experimental data and analytical modelling

2.5 Optical microscope and SEM observations

After the pullout tests, the fibers are carefully checked using an optical microscope to further investigate the effects of the inclination angle on the fiber-matrix bond. The H-0.38-10 and the H-0.9-15 fibers before and after the pullout tests are compared and shown in Figs. 2-11 and 2-12. It is evident

that the brass coating of the H-0.38-10 fiber is almost completely delaminated from the steel surface after the pullout test. This is different from the H-0.9-15 category, in which most of the coated brass still remains on the fiber surface and only a few longitudinal scratches due to matrix abrasion are observed. Furthermore, insignificant difference exists between the fiber surfaces at 0° and 30° : slightly more matrix remnants are observed adhering to the fiber at 30° , e.g. Fig. 2-11c. These cementitious materials sticking to the fiber accumulate near the fiber end, which may confine the fiber more tightly. This is in line with the slightly larger post-peak load for the H-0.38-10 fiber at 30° (see Fig. 2-4).

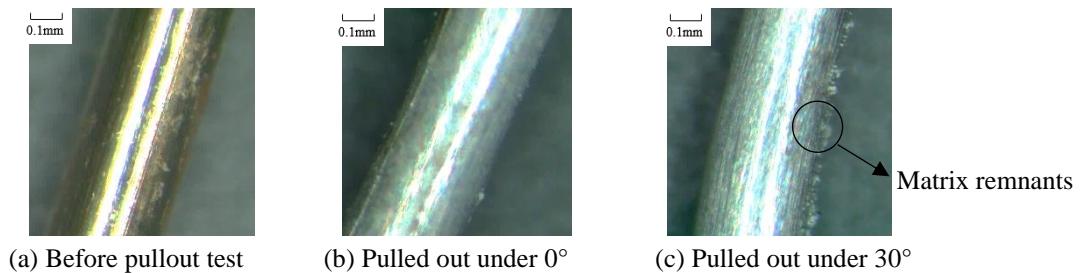


Fig. 2-11 H-0.38-10 fiber under optical microscope observation

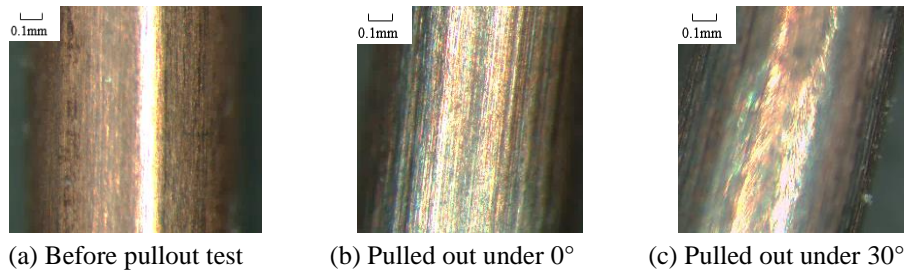


Fig. 2-12 H-0.9-15 fiber under optical microscope observation

The fiber-matrix interfaces are observed using SEM. The images of the microstructures around the H-0.38-10 fiber at 0° and 30° are presented in Fig. 2-13. Only a few pores are revealed in the interfacial transition zones (ITZ) around the fiber, implying a dense microstructure and a strong bond between the fiber and the UHPC matrix. This dense ITZ induces the delamination of the brass coating from the fiber surface during the pullout process and agrees well with the observations in Fig. 2-11. In addition, the similar ITZ for the 0° and 30° fibers indicates that the microstructure densification of ITZ is not sensitive to the inclination angle. According to (Wille, 2012), the fiber-matrix bond is dependent on both the matrix packing density and fiber surface properties. The alike ITZ quality in Fig. 2-13 under different inclination angles reveals a similar bond, which also helps to explain the similar initial ascending slop of the pullout curves in Fig. 2-4 that is associated with the fiber-matrix adhesive bonding and debonding process.

2.6 Conclusions

The pullout performances of the hooked-end steel fibers embedded in UHPC matrix are systematically investigated in this chapter. Two types of hooked-end fibers with different fiber diameters and embedded lengths are tested and discussed. The effects of the inclination angle (0° , 10° , 20° and 30°) on the pullout response are analyzed. The following conclusions can be drawn:

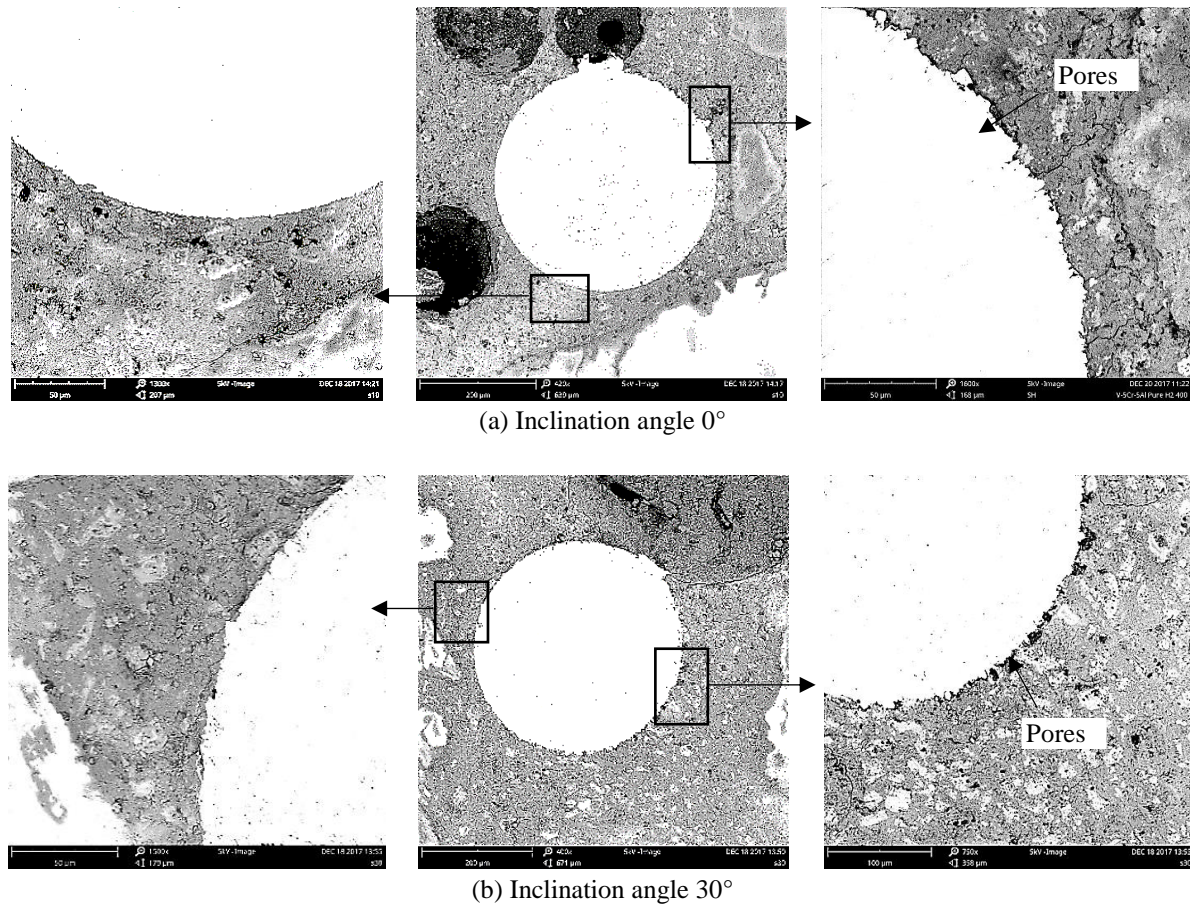


Fig. 2-13 SEM images of microstructures around H-0.38-10 fiber

- (1) Due to the strong bond and anchorage in the UHPC matrix, the small hooked-end fiber, viz. the H-0.38-10 fiber, breaks under a large inclination angle. In contrast, the large fiber with an appropriate embedded length, viz. the H-0.9-15 fiber, shows a complete pullout behavior and exhibits a more ductile response under the tested angles.
- (2) Embedded length is an important factor affecting the pullout response of the large hooked-end fiber. In the H-0.9-10 category, the relatively small embedded length results in a serious matrix failure problem, which tremendously reduces the energy absorption capacity of the specimen.
- (3) In the H-0.38-10 category, the peak pullout loads P_{max} at 0° and 10° are close to each other and they are slightly higher than those at 20° and 30° . In contrast, the optimum angles to achieve the maximum P_{max} are at 20° and 30° for the H-0.9-10 category and the H-0.9-15 category, respectively.
- (4) Regarding the fiber efficiency, the small hooked-end fiber, viz. the H-0.38-10 fiber, has a higher utilization level and it is the highest at the pullout angle of 0° . The utilization efficiencies of the H-0.9-10 and H-0.9-15 categories are approximately half that of the H-0.38-10 category, and they reach their maximum values at 20° and 30° , respectively.
- (5) To effectively evaluate the combined effects of snubbing and matrix spalling, a new analytical model for the hooked-end fiber is proposed and validated. The corresponding snubbing friction coefficient $f_p = 1.25$ and matrix spalling coefficient $k_p = 1.0$ are obtained.
- (6) The SEM images of the fiber-matrix interface confirm the dense microstructure of the ITZ in the designed UHPC matrix. The SEM of the H-0.38-10 fiber demonstrates that the fiber inclination barely affects the ITZ quality, thus no obvious difference of the fiber-matrix bond is observed under different fiber inclinations.

Chapter 3

*Effects of loading rate on the pullout performance of hooked-end steel fiber embedded in UHPC **



*This chapter is partially reproduced from: Y.Y.Y. Cao, Q.L. Yu, H.J.H. Brouwers, W. Chen, Predicting the rate effects on hooked-end fiber pullout performance from UHPC, Cement and Concrete Research 120 (2019) 164–175.

Abstract

The rate-dependent pullout performances of a hooked-end fiber embedded in UHPC matrix are investigated in this chapter. Pullout load-slip relationships under loading rates from 5 mm/min to 1000 mm/min, and the corresponding dynamic pullout responses are analyzed. The results show that the pullout energy is more rate sensitive than the peak pullout load, e.g. with an embedded length of 15 mm, the dynamic increase factors (DIFs) of the fiber pullout energy and the peak pullout load under 1000 mm/min are 1.46 and 1.22, respectively. Moreover, the rate effect on the pullout load is more prominent with a smaller embedded length due to the higher matrix cracking potential associated with the smaller concrete confinement. Further, a new analytical model to predict the dynamic peak pullout loads covering the loading rates from quasi-static to intermediate levels is proposed and validated. The present findings disclose that the inertial effects related to the crack initiation and propagation in the fiber-matrix interface have a significant influence on the rate dependent pullout behavior.

3.1 Introduction

UHPFRC is an advanced development in concrete industry. The very low water to binder ratio and the high particle packing density of the matrix result in its extremely high compressive strength, and the addition of steel fibers contributes to its excellent energy absorption capacity. Such superior mechanical properties of UHPFRC overcome the brittle nature of conventional concrete that causes an inherent poor behavior under dynamic loads (Yoo and Banthia, 2016), therefore, making UHPFRC a promising material for impact and blast resistant constructions (Yu, 2015). As a result of the strain rate effect, the behavior of cementitious materials subjected to dynamic loadings usually differs from that under static loadings, e.g. the strength, failure mode, and crack development velocity can be affected by the external loading rate (Weerheijm, 2013). Strain rate regime divisions and the corresponding loading scenarios are given in Fig. 3-1 (Tai, 2009a).

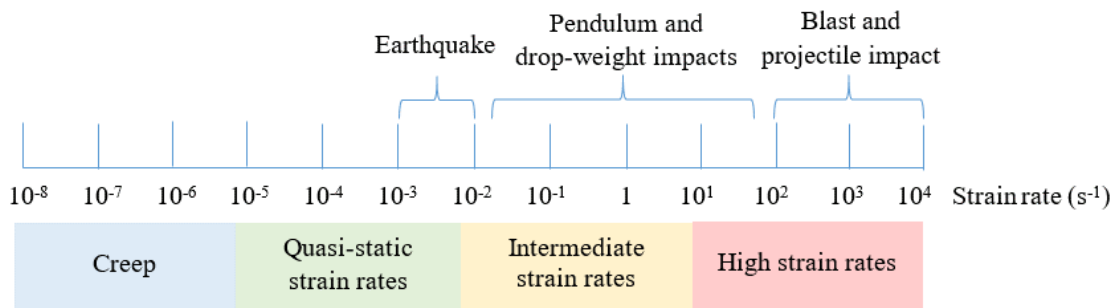


Fig. 3-1 Strain rate regimes and corresponding loading scenarios (Tai, 2009a)

Recent research reveals that UHPFRC reinforced with hooked-end fibers has an improved capacity in resisting pendulum impacts (Yoo and Banthia, 2016), indicating its potential to withstand dynamic loadings at intermediate strain rates. Given that steel fibers, UHPC matrix and the interface in between are rate sensitive, the pullout performances of the hooked-end fiber embedded in UHPC are thus expected to be rate dependent (Banthia and Trottier, 1991). Understanding this rate-dependent pullout behavior is necessary for developing impact-resistant UHPFRC with hooked-end fibers. However, contradictions exist about the dynamic pullout performances of hooked-end fibers. For instance, Xu et al. (Xu et al., 2016) found that the half-hooked fiber has the strongest rate dependency compared to the smooth and twisted fibers. On the contrary, Tai et al. (Tai et al., 2016) obtained similar rate sensitivities for the hooked-end fiber and the straight fiber. Conversely, a following study in (Tai and El-Tawil, 2017) demonstrated that the hooked-end fiber is less rate sensitive than the straight one. This discrepancy indicates the unclearness concerning the mechanisms behind the dynamic pullout behavior. By comparing the test results of hooked-end fibers with different embedded lengths in several studies, Xu et al. (Xu et al., 2016) supposed that the fiber embedded length may be a significant influencing factor on the rate effect. Nonetheless, this supposition is derived by summarizing independent studies with different concrete matrices. Aub-Lebdeh et al. (Aub-Lebdeh et al., 2010) investigated the rate sensitivities of fiber pullout behaviors with different embedded lengths, and their study confirmed that the rate dependency of the hooked-end fiber varies with the embedded length. However, only two pullout rates, i.e. 1.26 mm/min and 1524 mm/min, were involved in their study

whereas the pullout behaviors at the in-between loading rates were unclear and the mechanisms leading to the influences of the embedded length were not addressed.

Apart from these experimental investigations, little attention has been paid to developing analytical models to predict the dynamic response. To the best of the authors' knowledge, there is yet no analytical model available to predict the pullout resistance of hooked-end steel fibers embedded in UHPC under dynamic loadings, i.e. previous analytical models for hooked-end fibers can only be applied for quasi-static loading conditions. For instance, Alwan et al. (Alwan et al., 1999) developed a model to predict the quasi-static pullout performance of hooked-end steel fibers by applying a frictional pulley to simulate the hook action. Sujivorakul et al. (Sujivorakul et al., 2000) considered the mechanical anchorage of the hook as a nonlinear spring at the end of the fiber and proposed a quasi-static model for hooked-end fibers by extending the one for straight fibers. Laranjeira et al. (Laranjeira et al., 2010) experimentally evaluated the contribution of the hook under quasi-static loads and developed an analytical model for inclined hooked-end steel fibers based on the experimental data. By considering the repetitive bending and unbending of deformed fibers during the pullout process, Zile and Zile (Zile and Zile, 2013) proposed a model to investigate the influence of fiber geometry on quasi-static pullout performances, a good agreement was observed between their model prediction and the experimental results.

The study in this chapter is motivated by the insufficient understanding of the relationship between the rate-effect and the pullout performance of hooked-end fibers embedded in UHPC, as well as the lack of dynamic predictive models. Firstly, single fiber pullout tests of a hooked-end steel fiber with different embedded lengths under dynamic loading rates from 5 mm/min to 1000 mm/min are conducted, the rate range of which includes a broad band of frequencies that are excited by earthquakes and some typical impacts in reality. Together with the detailed background knowledge concerning the rate effect of cementitious materials, mechanisms affecting the rate sensitivity of the fiber-matrix bond are analyzed and the influences of the embedded length on the rate dependency are explained. Subsequently, a new analytical model to predict the dynamic pullout resistance of the hooked-end steel fiber in UHPC matrix at quasi-static to intermediate rates is proposed and validated.

3.2 Materials and experiments

3.2.1 Steel fibers and UHPC matrix

Dramix RC-80/30-BP fiber is used for the dynamic single fiber pullout tests, and it is aligned to the pullout direction. The basic geometry and mechanical parameters of the fiber can be found in Chapter 2 (Table 2-1). Two embedded lengths are investigated, i.e. $l_e = 10$ mm and 15 mm. The UHPC matrix for the pullout test is based on the recipe described in Chapter 2 (Table 2-2).

3.2.2 Mixing and casting procedures

The mixing of the UHPC matrix follows the procedure described in of Chapter 2 (Section 2.2.3). After mixing, the self-compacting UHPC mixture is poured into one half of the dog-bone shaped molds (Fig. 3-2a), in which a single hooked-end steel fiber is carefully held in place by two pieces of hard foam with the desired embedded length. Water curing method at room temperature is employed, which is the same as that in Chapter 2.

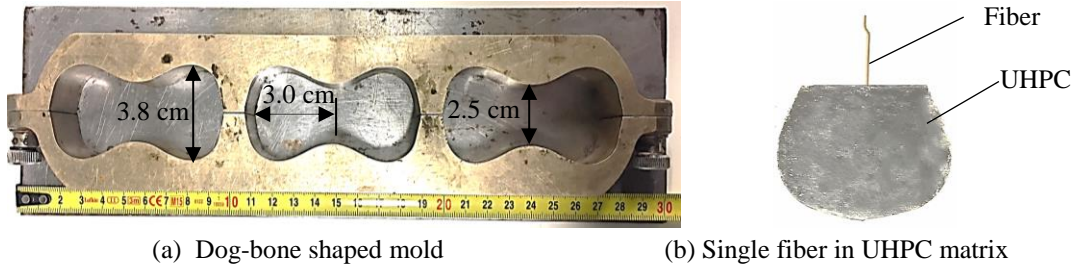


Fig. 3-2 Mold and specimen

3.2.3 Fiber pullout test setup and procedure

The single fiber pullout test is conducted at the age of 28 days using the same devices in Chapter 2 (Section 2.2.4). The pullout rates adopted are 5 mm/min, 50 mm/min, 500 mm/min and 1000 mm/min, and the corresponding strain rates are around 0.003 s^{-1} , 0.03 s^{-1} , 0.3 s^{-1} and 0.6 s^{-1} based on the dimension of the specimen. As suggested by the strain rate regimes plotted in Fig. 3-1, the smallest pullout rate in this study represents the quasi-static condition while the largest one belongs to the intermediate level. To obtain reliable data, at least five specimens are tested to calculate the average value under each loading rate category.

3.3 Rate dependency of cementitious material

3.3.1 Rate effects on concrete tensile strength

The rate dependent behavior of concrete has been the subject of intensive investigations. Dynamic increase factor (DIF), i.e. the ratio of dynamic strength to static strength, is commonly used to gauge the nominal strength enhancement for engineering applications. The results from extensive tests have shown that concrete exhibits a strong rate sensitivity under tensile loads over a wide range of strain rates (Weerheijm, 2013). The determination of the tensile strength DIF is recommended by the CEB-FIP Model Code 1990 (CEB-FIP, 1990) as:

$$\text{DIF} = \frac{f_{ct,d}}{f_{cm}} = \left(\frac{\dot{\epsilon}_t}{\dot{\epsilon}_{t0}} \right)^{1.016\delta_t} \quad \text{for } \dot{\epsilon}_t \leq 30\text{s}^{-1} \quad (3-1a)$$

$$\text{DIF} = \frac{f_{ct,d}}{f_{cm}} = \beta_t \left(\frac{\dot{\epsilon}_t}{\dot{\epsilon}_{t0}} \right)^{1/3} \quad \text{for } \dot{\epsilon}_t > 30\text{s}^{-1} \quad (3-1b)$$

where $f_{ct,d}$ is the dynamic tensile strength and f_{cm} is the mean value of the static tensile strength. $\dot{\epsilon}_t$ is the tensile strain rate; the static reference rate $\dot{\epsilon}_{t0} = 3 \times 10^{-6} \text{ s}^{-1}$. Parameters $\delta_t = 1/(10+3\sigma_{c,s}/5)$, and $\log\beta_t = 7.112\delta_t - 2.33$. $\sigma_{c,s}$ is the static compressive strength (in MPa).

3.3.2 Mechanisms behind concrete rate dependency

Concerning the dynamic tension, the enhancement of the concrete tensile strength may be mainly attributed to the two factors as explained below.

- **Stefan effect**

The free water in the pores of concrete is assumed to exhibit the Stefan effect, which can be explained by considering the cohesive force between two plates separated by an incompressible water film. Most researchers consider the Stefan effect to be one of the vital factors contributing to the rate effect on concrete material. According to Weerheijm et al. (Weerheijm, 2013) and Vegt et al. (Vegt, 2016), the amount, dimension and distribution of pores, as well as the saturation degree of the pores in concrete play an important role on the Stefan effect.

- **Micro inertia effect**

Inertia at micro-level can affect the stress fields around the concrete defects and delay the damage initiation of cracks, resulting in an enhancement in the maximum strength (Reinhardt and Weerheijm, 1991). The inertial effects can induce limitations in both crack initiation and propagation at micro-levels. When concrete material is under static loading, the rate of fracture energy dissipation is in balance with the rate of the external energy supply. At higher loading rates, however, the energy supply rate is so high that the external power cannot be absorbed in the fracture process. Hence, a major part of the supplied external power is stored as kinetic and deformation energies around cracks, changing the stress distribution around crack tips and reducing the stress intensity factor (Weerheijm, 2013). A smaller stress intensity means lower energy flux into the fracture zone in concrete, which then results in a decrease of the crack develop velocity (Reinhardt and Weerheijm, 1991). As a consequence, the crack propagation is limited and the concrete tensile strength increases with the loading rate (Ožbolt et al., 2013; Weerheijm, 2013).

3.3.3 Rate dependency of fiber-matrix interface

Fig. 3-3a is the SEM image of the fiber-matrix interface before the pullout tests. The interfacial zone between the steel fiber and the UHPC matrix has a relatively larger amount of pores than the matrix itself. Considering that the Stefan effect is associated with the amount and saturation degree of the pores in the concrete matrix (Vegt, 2016; Weerheijm, 2013), the influences of the strain rate due to the Stefan effect should be more obvious for the concrete containing more pores and a higher internal humidity. One example is that the tensile strength DIF tends to be higher for the concrete with a lower strength, which usually has a higher porosity (Othman, 2016; Thomas and Sorensen, 2017). In addition, the fiber-matrix interface is usually the weakest part in UHPFRC and has a higher potential to crack more seriously than the matrix itself. Hence, the micro-inertia effect associated with cracking would also be more significant. Consequently, the fiber-matrix interface is expected to have a more prominent rate sensitivity than the UHPC matrix itself, i.e. the DIF of the pullout load can be larger compared to the UHPC tensile strength DIF.

Moreover, when a hooked-end steel fiber is pulled from the UHPC matrix, stress localization will be induced in the matrix surrounding the hook. Micro-cracking will be generated if the localized stresses exceed the matrix tensile strength. Further, the amount of cracks is associated with the level of the matrix confinement, therefore the fiber embedded length (Xu et al., 2016). During the pullout process, micro-cracking continuously initiates along the fiber tunnel and then further propagates in the UHPC matrix. Some micro-cracks are visually observed in the SEM image of the fiber-matrix tunnel after the pullout test at 1000 mm/min (Fig. 3-3b). Since the micro inertial effects on both the crack initiation and propagation contribute to the rate sensitivity of cementitious materials (Weerheijm,

2013), the occurrence and development of these micro-cracks may result in the rate dependency of the fiber-matrix bond. Furthermore, the amount of the rate sensitivity is expected to be associated with the matrix strength, fiber geometry and embedment length, which influence the micro-cracking process (Xu et al., 2016).

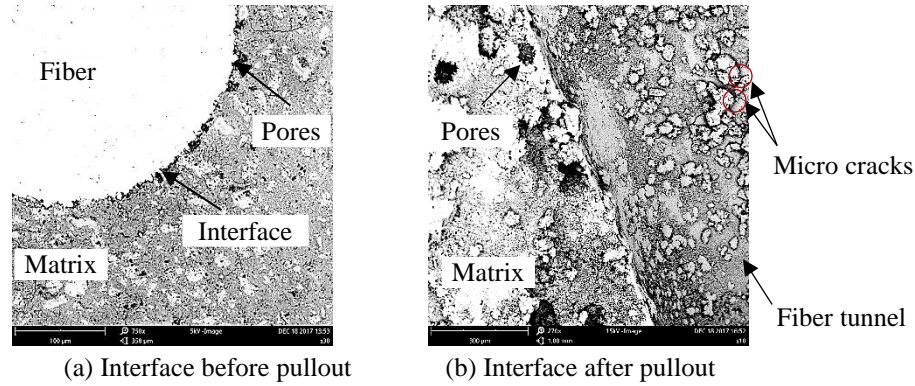


Fig. 3-3 SEM images of microstructures in fiber-matrix interface

It is worth mentioning that in the single fiber pullout experiments presented in this study, all samples have the same recipe and curing condition, and all of them are tested under a surface-dry condition. Thus, the pore structures and the moisture content in the fiber-matrix interface are assumed to be similar for all the tested samples. Consequently, the rate effect caused by the Stefan effect is presumed to contribute comparably in this study, and more attention is paid to the contributions of the micro inertial effects when analyzing the rate-dependent pullout behaviors.

3.4 Fiber pullout test results

3.4.1 Rate-dependent pullout performances

The pullout load-slip relationships for the hooked-end steel fiber with an embedded length $l_e = 15$ mm at different loading rates are plotted in Fig. 3-4. Analysis of the pullout process can be found in Chapter 2 (Section 2.3.1). The curves in Fig. 3-4 at different loading rates confirm the rate sensitivity of the pullout performance. Insignificant rate effect is observed in the initial elastic Stage O-A since the strain rates have negligible effects on the elastic moduli of steel and concrete in tension (Filiatrault and Holleran, 2001). On the contrary, Stage A-B exhibits a rate sensitivity as the slope of the curve increases slightly with the increase of the rate. The peak pullout load and the corresponding slip at Point B are significantly enhanced at higher loading rates and the fluctuations of the curves at Stage B-C become less obvious.

Since the pullout performance in Stage C-D is primarily dependent on the fiber-matrix friction, it can be inferred that the frictional force is rate dependent, which is in line with the findings in (Tai et al., 2016; Xu et al., 2016). However, this trend differs with the observation in (Gokoz and Naaman, 1981), which investigated the pullout behavior of NC. In that study, the descending part of the pullout load-slip curve is found to be insensitive to the loading rate, leading to the conclusion that the frictional force is not rate dependent. The rate dependent behavior at Stage C-D in the present study may be attributed to the stronger bond between the fiber and the UHPC matrix. More efforts are needed to debond the fiber from the UHPC than that from the NC; and the pullout process may induce more micro-cracks in the UHPC matrix, the initiation and propagation of which in turn amplify the rate

effect. In addition, comparisons of the curves at Stage B-C suggest that the mechanical anchorage due to the hook is also rate sensitive. The peaks and drops at Stage B-C due to the anchorage become less obvious at higher loading rates, indicating a less significant contribution of the hook under dynamic conditions compared to that under static loads.

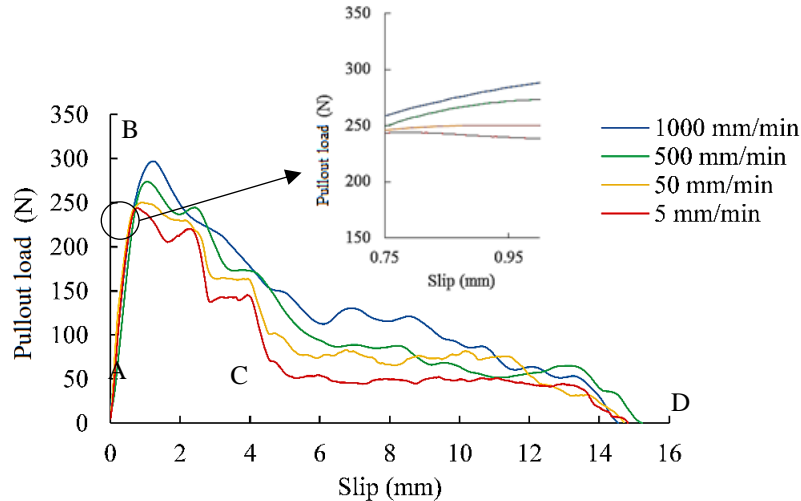
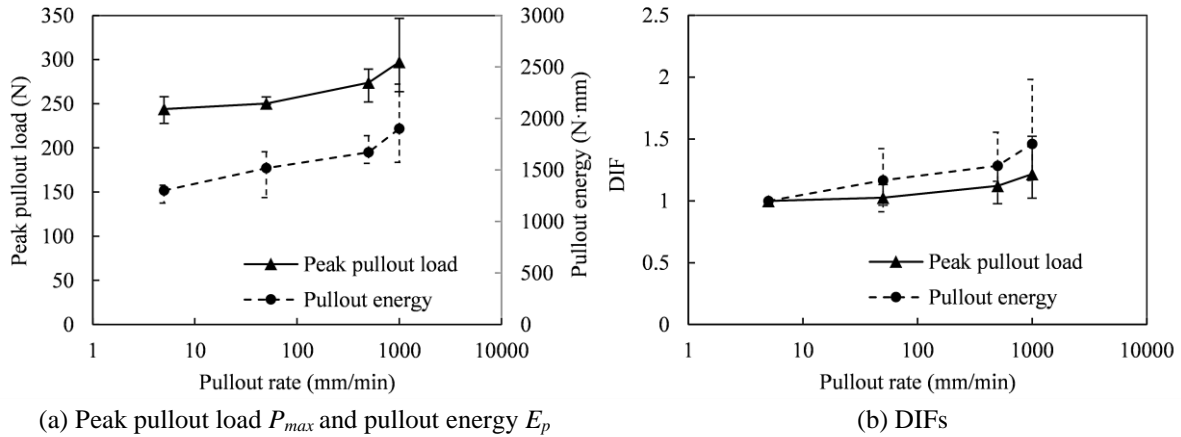


Fig. 3-4 Pullout performances at different loading rates ($l_e = 15$ mm)

3.4.2 Rate effects on the pullout load and energy

Fig. 3-5 plots the influences of the loading rate on the peak pullout load P_{max} and energy E_p in the case of $l_e = 15$ mm. The energy dissipation is defined by the area below the pullout load-slip curve (Fig. 3-4). The points illustrated in the figures are the averaged results of each group and the error bars indicate the minimum and maximum values. As shown in Fig. 3-5a, P_{max} increases from 244.1 N at 5 mm/min to 297.1 N at 1000 mm/min. E_p undergoes a similar trend, increasing from 1301.3 N·mm to 1901.3 N·mm at the corresponding loading rates. Additionally, for both P_{max} and E_p , more apparent improvements are observed in the intermediate loading rate range than in the quasi-static one. For example, P_{max} has a 3% increase when the loading rate increases from 5 mm/min to 50 mm/min (a fold of ten), while the enhancement is 9% when the rate changes from 500 mm/min to 1000 mm/min (a fold of two). Moreover, scattering of experimental results is observed, as shown by the error bars in Fig. 3-5a. The maximum scatterings of both P_{max} and E_p occur at 1000 mm/min, the variation coefficients of which reach 16% and 22%, respectively. A similar trend was reported in (Ranade et al., 2015) which studied the dynamic pullout behavior of PE fibers.

(a) Peak pullout load P_{max} and pullout energy E_p

(b) DIFs

Fig. 3-5 Rate effects on peak pullout load P_{max} and pullout energy E_p ($l_e = 15$ mm)

The relationships between the loading rates and the DIFs of P_{max} and E_p are summarized in Fig. 3-5b. The DIFs of P_{max} at 50 mm/min, 500 mm/min and 1000 mm/min are 1.03, 1.12 and 1.22, while the corresponding values of E_p are 1.17, 1.28 and 1.46, respectively. These strong rate dependencies were also observed in a previous research (Abu-Lebdeh et al., 2010), which analyzed the dynamic pullout responses of the same hooked-end steel fiber with $l_e = 12.7$ mm embedded in UHPC ($\sigma_{c,s} = 175$ MPa). The DIFs of P_{max} and E_p at 1524 mm/min in their study were 1.28 and 1.49, which are close to the values at 1000 mm/min in the present study, viz. 1.22 and 1.46. It should be noted that (Abu-Lebdeh et al., 2010) only investigated the pullout performances at 1.26 mm/min and 1524 mm/min, and the former was taken as the static rate to calculate the DIFs.

At the tested loading rates, E_p tends to be more rate sensitive than P_{max} , i.e. the DIF of E_p is always larger than that of P_{max} . This is in accordance with the findings in (Xu et al., 2016), which studied the pullout behaviors of half-hook fibers, although the causes were not addressed in their study. The more obvious rate effect on E_p may be correlated to the additional micro-cracking and the additional resistance due to the micro-inertia effects at both the fiber debonding and slip stages (Weerheijm, 2013). Firstly, the debonding process at the early pullout stages and the hook deformations at the fiber end generate micro cracks in the matrix, the inertia effects of which contribute to the rate dependency. Secondly, with the slip of the fiber at the later stages of the pullout process, some UHPC matrix particles adhere to the fiber surface (Cao and Yu, 2018), causing more damage to the surrounding matrix and accelerating the cracks developments. In the case of E_p , the micro inertia effect play a role at both the fiber debonding and slip stages, whereas the rate effect on P_{max} is more related to the debonding process. Therefore, the DIF of E_p is enhanced.

Furthermore, the DIF of the peak pullout load is higher comparing to that of the UHPC tensile strength. As plotted in Fig. 3-6, the DIFs of concrete tensile strength calculated by Eq. 3-1a are compared with the pullout test results in the present study. It is shown that the pullout load DIF at a low loading rate, e.g. 50 mm/min, is similar to the corresponding DIF of the UHPC tensile strength, whereas at intermediate strain rates the pullout load is more rate sensitive than the matrix tensile strength. These higher DIFs of the pullout behavior may be attributed to the more porous interface between the fiber and the matrix as well as its relatively lower strength than the matrix itself. As mentioned in Section 3.3.3, the Stefan effect is more prominent on the concrete containing more pores, and the micro inertia effect plays a more crucial role on the weaker matrix that is more susceptible to cracking. These, therefore, result in the higher DIF of the pullout load.

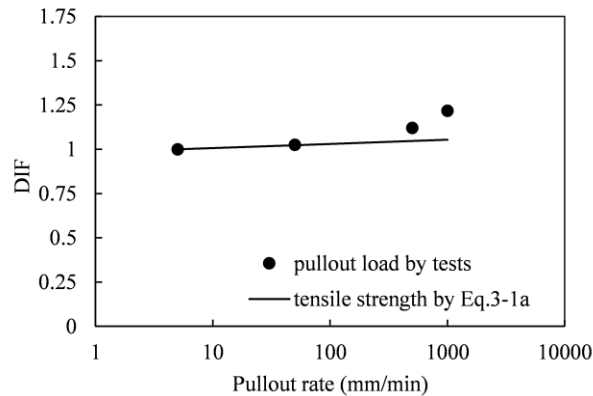
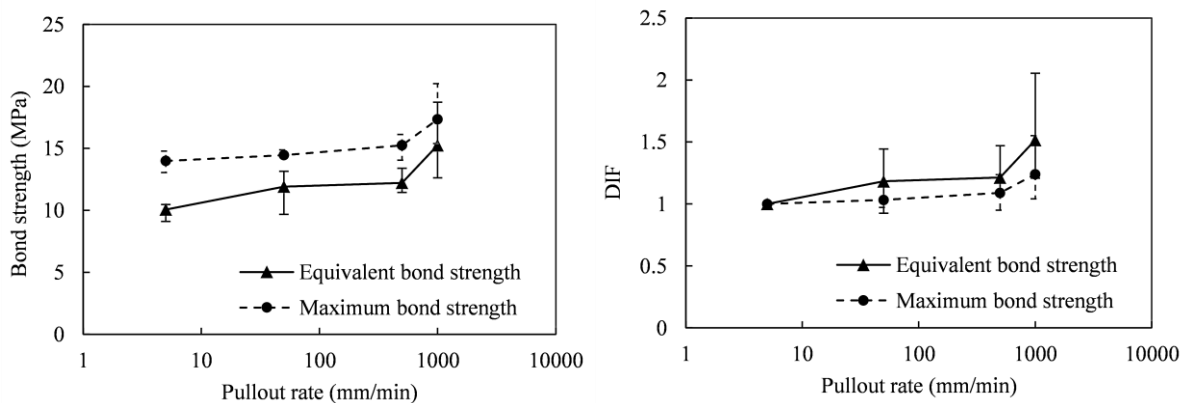


Fig. 3-6 DIFs of pullout load and UHPC tensile strength

3.4.3 Rate effects on the maximum and equivalent bond strengths

To provide a quantitative evaluation of the rate effects on the fiber-matrix interfacial bond properties, the maximum bond strength τ_{max} and equivalent bond strength τ_{eq} are calculated. Their expressions can be found in Chapter 2 (Section 2.4.1). Fig. 3-7 plots the influences of the strain rate on τ_{max} and τ_{eq} with $l_e = 15$ mm. At the quasi-static loading rate (5 mm/min), τ_{max} and τ_{eq} are 14.0 MPa and 10.1 MPa, respectively; while at the intermediate loading rate of 500 mm/min, the values increase to 15.3 MPa and 12.2 MPa, i.e. 9% and 22% enhancements, respectively. With the further increase of the loading rate, τ_{max} and τ_{eq} at 1000 mm/min experience noticeable growths, i.e. the values reach to 17.3 MPa and 15.3 MPa, respectively. As depicted in Fig. 3-7b, DIFs of τ_{eq} are higher than those of τ_{max} at the tested loading rates, indicating a more obvious rate sensitivity of the former. For instance, the DIFs for τ_{max} at 50 mm/min, 500 mm/min and 1000 mm/min are 1.03, 1.09 and 1.24, respectively; whereas the corresponding values for τ_{eq} are 1.18, 1.21 and 1.52, which are approximately 15%, 11% and 23% higher, respectively.

(a) Maximum bond strength τ_{max} and equivalent bond strength τ_{eq}

(b) DIFs

Fig. 3-7 Rate effects on maximum bond strength τ_{max} and equivalent bond strength τ_{eq} ($l_e = 15$ mm)

3.4.4 Effect of embedded length on the rate dependency

To investigate the effect of fiber embedded length on the rate dependency of the hooked-end fiber, a series of single fiber pullout tests are conducted with a smaller embedded length. Fig. 3-8

illustrates the pullout load-slip curves at various loading rates with $l_e = 10$ mm, in which similar trend can be observed as the $l_e = 15$ mm case (Fig. 3-4). It is also interesting to mention that the pullout load under 5 mm/min in Fig. 3-8 is smaller than that of the aligned fiber (0°) in Fig. 2-4 in Chapter 2. These two cases have the same fiber embedded length and the same matrix compositions, and both of them are tested under the quasi-static rates. The different pullout loads may be attributed to the different specimen dimensions in Chapters 2 and 3, leading to different clamp confinements and therefore different pullout behaviors. The comparisons of the specimens are shown in Fig. 3-9.

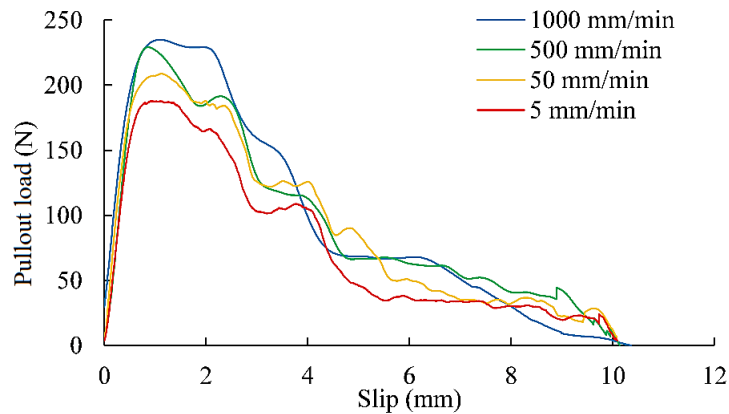
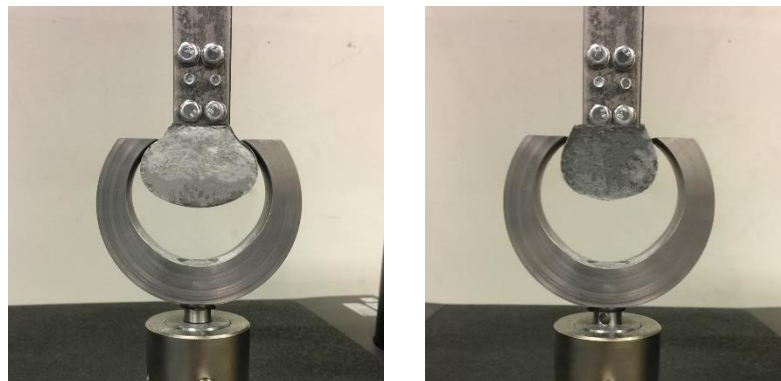


Fig. 3-8 Pullout load-slip curves at different loading rates ($l_e = 10$ mm)



(a) Specimen in Chapter 2 (b) Specimen in Chapter 3

Fig. 3-9 Comparison of pullout specimens

Comparisons of the test results between the $l_e = 10$ mm and 15 mm categories are plotted in Fig. 3-10. As depicted in the figures, P_{max} and E_p are enhanced with the increase of the embedded length at the tested loading rates. For example, P_{max} and E_p at 1000 mm/min are 27% and 89% higher for the $l_e = 15$ mm category than for the $l_e = 10$ mm counterpart. In contrast, τ_{max} and τ_{eq} tend to be smaller for a larger embedded length, e.g. τ_{max} at 500 mm/min for the $l_e = 10$ mm and 15 mm categories are 19.2 MPa and 15.3 MPa, respectively. These observations are consistent with that in Chapter 2, which analyzes the influence of the embedded length under static loadings. The higher τ_{max} and τ_{eq} with a smaller embedded length might be explained by the more remarkable contribution of the hook than the straight part of the fiber, despite of the external loading rates. Moreover, the influence of the embedded length is the most obvious on E_p , indicating a prominent influence of the fiber length on the energy absorption capacity of UHPFRC composites.

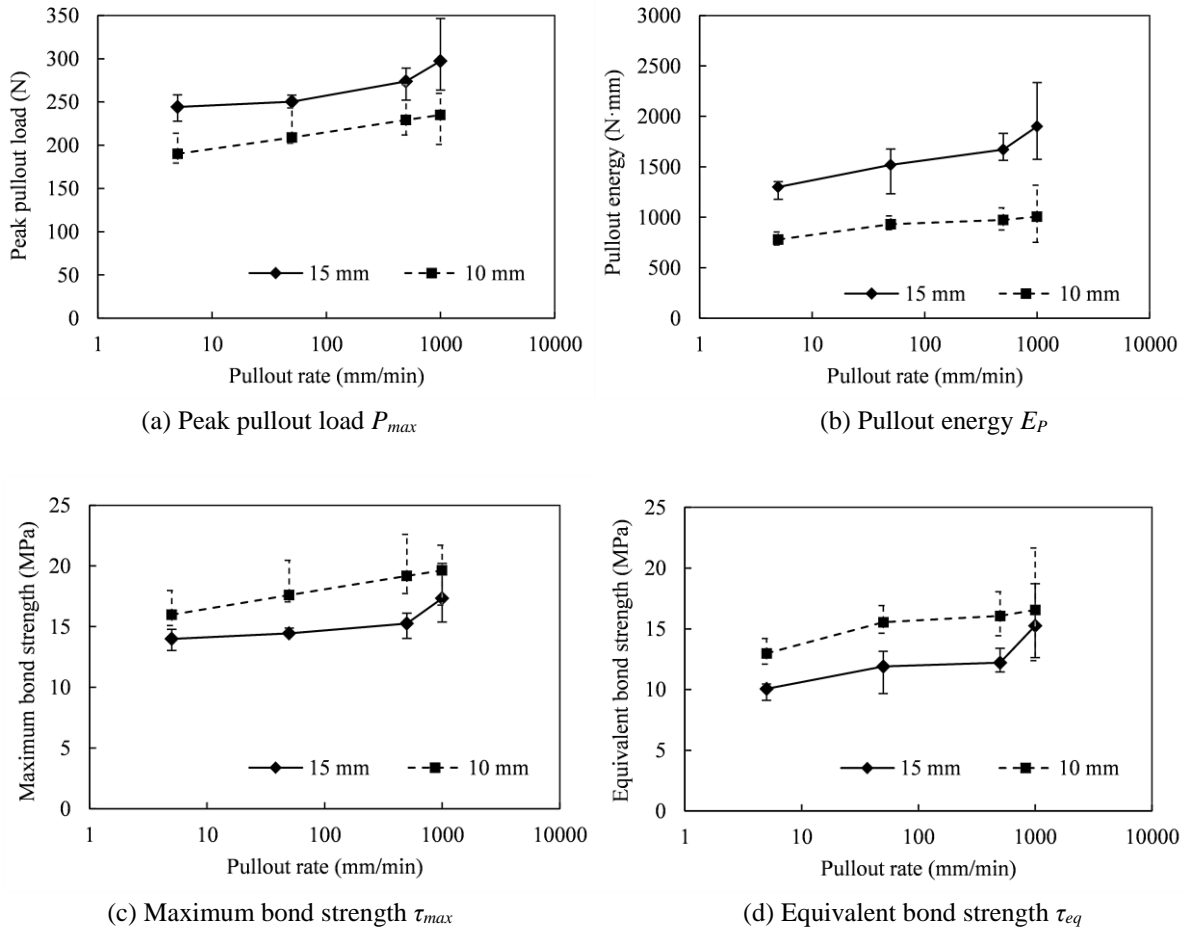


Fig. 3-10 Effects of embedded lengths

The effects of the embedded length on the DIFs of P_{max} , E_p , τ_{max} and τ_{eq} are depicted in Fig. 3-11. It is obvious that the DIFs increase with the increase of the loading rate for the two tested embedded lengths. Moreover, the DIFs of P_{max} and τ_{max} are higher in the smaller embedded length category. For instance, the DIFs of P_{max} and τ_{max} at 500 mm/min are 1.12 and 1.09 for the $l_e = 15$ mm category, while those for the $l_e = 10$ mm category increase to 1.22 and 1.21, respectively. One possible reason is the micro-cracking process in the UHPC matrix associated with the matrix confinement (Fig. 3-12) (Xu et al., 2016). At the initial stage of the pullout process, local pressure is induced into the surrounding matrix near the hooked-end, generating micro cracks in the hook bending points where stresses are localized. With a larger embedded length, the matrix confinement is higher, which offsets the split cracking and thus reduces the rate effect (Xu et al., 2016). While with a smaller embedded length, micro-cracks can occur both in plane and out of plane because of the reduced confinement, contributing to a more apparent rate effect (Xu et al., 2016). Since τ_{max} depends on P_{max} , and the latter is associated with the confinement-dependent micro-cracking process at Stage A-B, the rate effects on P_{max} and τ_{max} are thus more evident with a smaller embedded length, i.e. $l_e = 10$ mm. On the contrary, the rate dependencies of E_p and τ_{eq} are related to the micro-cracking initiation and propagation at the whole pullout stages A to D, and the rate effect induced in the later fiber slip process has more obvious influence on fibers with longer embedded lengths. Therefore, DIFs of E_p and τ_{eq} are slightly higher for the $l_e = 15$ mm category, especially at an intermediate loading rate, e.g. 1000 mm/min, at which the contribution of the hook is less prominent.

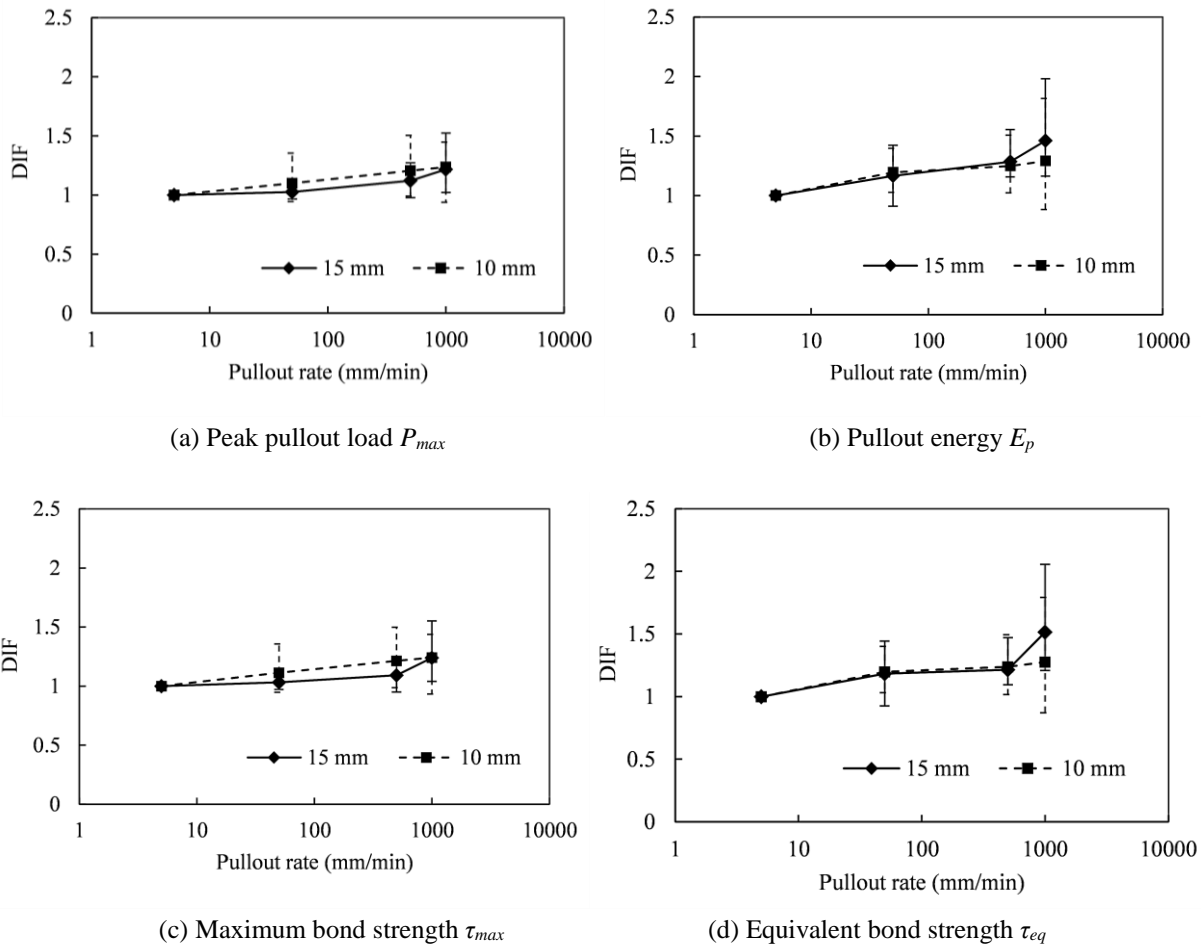


Fig. 3-11 Effects of embedded lengths on DIFs

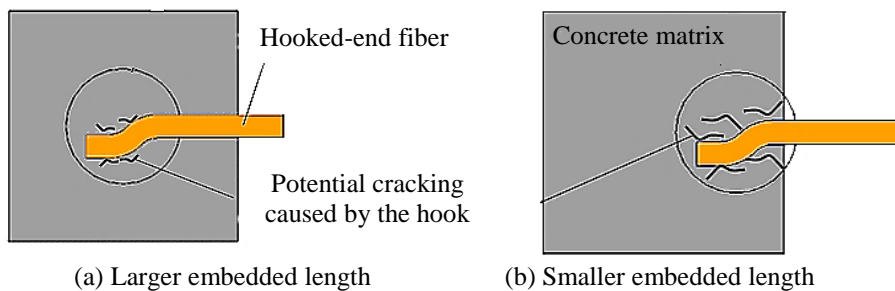


Fig. 3-12 Influence of embedded length

3.5 Rate-dependent model

3.5.1 Predictive model

A model proposed by Zile and Zile (Zile and Zile, 2013) can be used to predict the peak pullout load under the quasi-static loading. Taking it as a base, a new rate-dependent model for dynamic loading rates ranging from quasi-static to intermediate levels is developed in this section.

In order to show the rate effects on the hooked part and the straight part of the fiber, the peak pullout load P_{max} is split into two components (P_h and P_f), instead of using the general expression of P_{max} in Chapter 2 (see Eq. 2-8). P_h is the anchorage part due to the hooked-end, and P_f is the friction part due to the frictional bond between the fiber and the matrix:

$$P_{\max} = P_h + P_f \quad (3-2)$$

According to the pulley model in (Alwan et al., 1999), the pullout load caused by the mechanical anchorage of the hooked-end can be modelled as a fiber passing through two curved ducts (Fig. 3-13a). The anchorage load is given as (Alwan et al., 1999; Zile and Zile, 2013):

$$P_h = \frac{\pi d_f^2 \sigma_y}{12 \cos \alpha (1 - \mu_f \cos \beta)} \left(1 + \frac{\mu_f \cos \beta}{1 - \mu_f \cos \beta} \right) = \frac{\pi d_f^2 \sigma_y}{12 (1 - \mu_f \cos \beta)^2 \cos \alpha} \quad (3-3)$$

where d_f and σ_y are the diameter and yield strength of the hooked-end steel fiber, respectively; α and β are related to the hook geometry, as shown in Fig. 3-13a. α is the hook angle; β is the angle between the directions of the pullout force P and the reaction force R at the pulley center, i.e. $\beta = (180^\circ - \alpha)/2$.

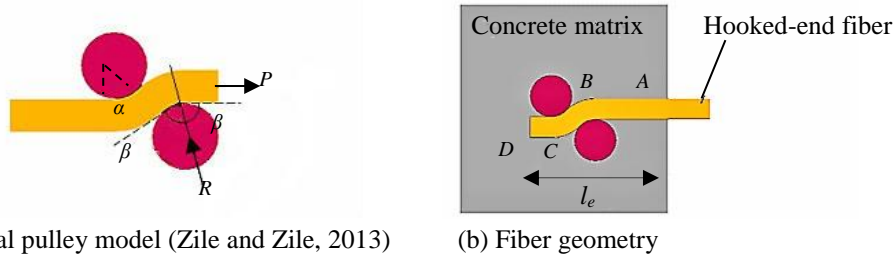


Fig. 3-13 Hooked-end fiber pullout

μ_f is the friction coefficient following:

$$\mu_f = \mu_0 + \frac{\tau_f}{\tau_0} \quad (3-4)$$

where the empirical parameters are given as $\mu_0 = 0.08$, $\tau_0 = 21.28$ MPa (Geng and Leung, 1997; Zile and Zile, 2013).

τ_f is the frictional shear stress during the fiber slip stage, the value of which can be obtained from the straight fiber pullout tests or approximately estimated with the pullout load at Stage C-D since in this stage the fiber-matrix friction is the main factor affecting the pullout load. Depending on the state of the pullout load, i.e. P_{CD} corresponds to a quasi-static or a dynamic load, τ_f can be seen as a quasi-static frictional shear stress $\tau_{f,s}$ or a dynamic one $\tau_{f,d}$. Correspondingly, μ_f can be a static or a dynamic friction coefficient. The expression of τ_f is given as:

$$\tau_f = \frac{P_{CD}}{\pi d_f (l - S_C)} \quad (3-5)$$

where P_{CD} is the average pullout load at Stage C-D (see Fig. 3-4) and S_C is the fiber slip when Stage C-D starts. l is the actual fiber embedded length obtained from the pullout load-slip curve.

The friction part P_f is calculated by:

$$P_f = \pi d_f \tau_f (L_{AB} + L_{BC} + L_{CD}) \quad (3-6)$$

where L_{BC} and L_{CD} are the lengths depending on the hook geometry (Fig. 3-13b); L_{AB} is the length of the straight part of the fiber embedded in the matrix.

Substituting Eqs. 3-3, 3-4 and 3-6 into Eq. 3-2 yields:

$$P_{\max} = \frac{\pi d_f^2 \sigma_y}{12 \left[1 - \left(\mu_0 + \frac{\tau_f}{\tau_0} \right) \cos \beta \right]^2} \cos \alpha + \pi d_f \tau_f (L_{AB} + L_{BC} + L_{CD}) \quad (3-7)$$

Under dynamic loadings, the dynamic frictional shear stress $\tau_{f,d}$ is rate dependent and the rate dependency varies with the embedded length, as discussed in Section 3.4.4. Following the expression of the concrete tensile strength DIF in Eq. 3-1, an empirical equation to account for the rate effect on τ_f at dynamic loading rates up to the intermediate level is given as:

$$\text{DIF} = \frac{\tau_{f,d}}{\tau_{f,s}} = \left(\frac{\dot{\epsilon}_d}{\dot{\epsilon}_s} \right)^{\gamma_t} \quad (3-8)$$

where $\dot{\epsilon}_s$ and $\dot{\epsilon}_d$ are the quasi-static reference rate and the dynamic loading strain rate, respectively. γ_t is an empirical parameter which has a similar expression as the parameter δ_t in Eq. 3-1. Applying nonlinear regression analysis of the experimental results in this study, γ_t is obtained as:

$$\gamma_t = e^{0.16l_e} / (5 + 0.6\sigma_{c,s}) \quad (3-9)$$

where the embedded length l_e is in mm and the matrix strength $\sigma_{c,s}$ is in MPa.

Combining Eqs. 3-7 and 3-8 results in the predicting formula for the dynamic peak pullout load of the hooked-end steel fiber embedded in the UHPC matrix:

$$P_{\max} = \frac{\pi d_f^2 \sigma_y}{12 \left[1 - \left(\mu_0 + \frac{\tau_{f,s}}{\tau_0} \left(\frac{\dot{\epsilon}_d}{\dot{\epsilon}_s} \right)^{\gamma_t} \right) \cos \beta \right]^2} \cos \alpha + \pi d_f \tau_{f,s} \left(\frac{\dot{\epsilon}_d}{\dot{\epsilon}_s} \right)^{\gamma_t} (L_{AB} + L_{BC} + L_{CD}) \quad (3-10)$$

3.5.2 Model validation

To validate the above predictive model, experimental results from this study and (Abu-Lebdeh et al., 2010) are applied. The hooked-end steel fiber used in the two researches are the same, and the fiber geometry related parameters adopted in the predictive model are $\alpha = 45^\circ$, $\beta = 67.5^\circ$, $L_{BC} = 2.12$ mm, $L_{CD} = 2$ mm and $d = 0.375$ mm. The compressive strength of the concrete matrix in this study and (Abu-Lebdeh et al., 2010) are 156 MPa and 175 MPa, respectively. The quasi-static frictional shear stresses $\tau_{f,s}$ for the two studies are taken as 3.5 MPa and 4 MPa based on the quasi-static pullout load-slip curves.

Comparisons between the experimental and the predicted peak pullout loads are illustrated in Table 3-1 and Fig. 3-14, in which variations of the experimental data in this study are also denoted by

the error bars (note that variations of the results in (Abu-Lebdeh et al., 2010) are not clear due to the lack of data). Regarding such scattering, the predictions of the dynamic pullout load by the developed model always fall within the range of experimental results. These reasonably good agreements confirm the validity of the proposed predictive model, especially at higher loading rates.

Table 3-1 Peak pullout loads from experiments and predictive model

Embedded length (mm)	Loading rate (mm/min)	Peak pullout load (N)		Error (%)
		Experimental results	Prediction results	
15	5	244.1	229.2	-6.1
	50	250.3	255.1	1.9
	500	273.8	289.2	5.6
	1000	297.1	301.5	1.5
10	5	190.1	208.6	9.7
	50	209.0	216.8	3.7
	500	229.2	226.1	-1.4
	1000	234.9	229.2	-2.4
12.7	1.26	188.1	201.0	6.9
(Abu-Lebdeh et al., 2010)	1500	211.9	212.7	0.4
6.35	1.26	164.7	172.2	4.6
(Abu-Lebdeh et al., 2010)	1500	185.1	174.1	-5.9

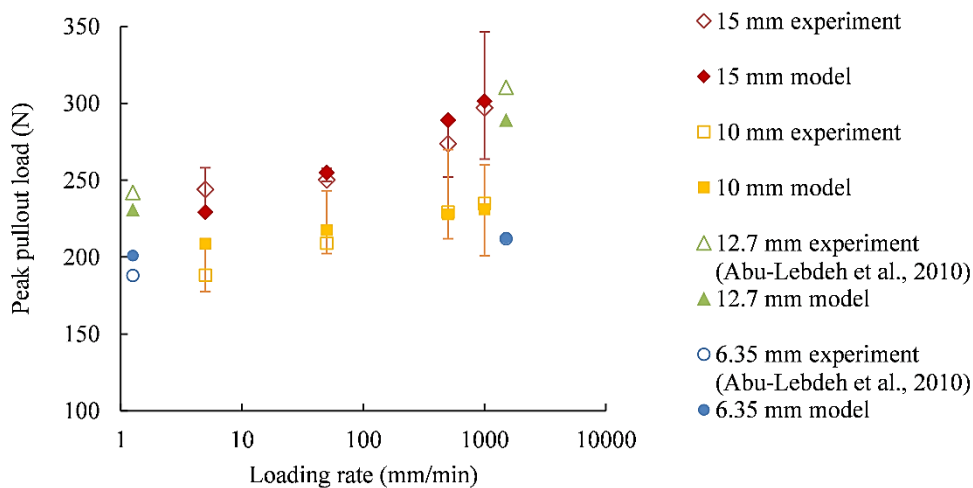


Fig. 3-14 Predictive model validation

At the quasi-static loading rate, Eq. 3-10 yields identical results as the model developed in (Zile and Zile, 2013). Corresponding values in Table 3-1 show that the accuracy of the model is slightly lower under the quasi-static condition compared with those at higher loading rates. This may be due to the fact that some empirical parameters in the quasi-static model in (Zile and Zile, 2013), e.g. τ_0 and μ_0 , are determined based on NC rather than on UHPFRC. More investigations are needed in order to improve the accuracy of the quasi-static model. Nevertheless, considering that the presented errors are acceptable, the same τ_0 and μ_0 are applied in this model as those in (Zile and Zile, 2013) and (Geng and Leung, 1997). In addition, it should be noted that the values of τ_0 and μ_0 are suggested by (Geng and Leung, 1997) using extensive experiments under quasi-static loadings; however, the value of τ_0 may be different under dynamic loadings. By assuming that its rate dependency could also be expressed in a similar format as Eq. 3-8, the presented model accounts for the rate sensitivity of τ_0 together with that of $\tau_{f,d}$ by the parameter γ_t . Furthermore, as indicated by Eq. 3-4, μ_0 represents the

intercept value of the friction coefficient when $\tau_f = 0$, which is therefore expected to remain constant under both quasi-static and dynamic loadings, i.e. without rate sensitivity. The good agreements confirm the rationality of the above hypothesis.

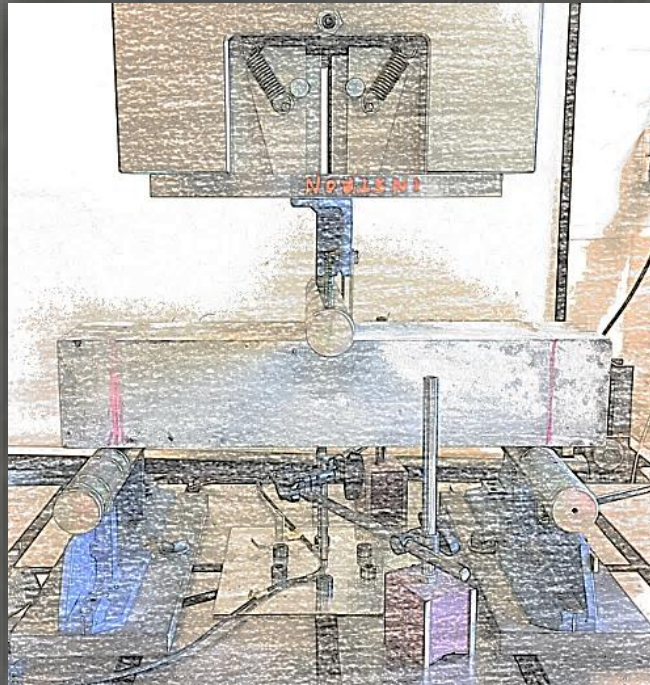
3.6 Conclusions

This chapter investigates the rate-dependent pullout performances of the hooked-end steel fiber embedded in the UHPC matrix at loading rates from 5 mm/min to 1000 mm/min. The rate sensitivity of the dynamic fiber pullout responses and the related mechanisms are analyzed. An analytical model to predict the dynamic peak pullout load covering the loading rates from quasi-static to intermediate levels is proposed and validated. The following conclusions can be drawn:

- (1) The pullout performance of the hooked-end steel fiber embedded in the UHPC matrix is rate dependent, and the loading rate affects both the mechanical anchorage and the interfacial friction during the pullout process.
- (2) The pullout energy is more rate sensitive than the peak pullout load. With an embedded length of 15 mm, the DIFs for the pullout energy at 50 mm/min, 500 mm/min and 1000 mm/min are 1.17, 1.28 and 1.46, whereas the corresponding values for the peak pullout load are 1.03, 1.12 and 1.22, respectively.
- (3) Fiber embedded length affects the rate dependency of the pullout performance. The peak pullout load is more rate sensitive with a smaller embedded length, i.e. $l_e = 10$ mm. In contrast, the rate dependency of the pullout energy is slightly higher for the $l_e = 15$ mm category, especially at a higher loading rate.
- (4) The Stefan effect and the inertia effect due to micro-cracking in the interface are two main mechanisms contributing to the rate effects on the dynamic pullout responses. The more porous and weaker fiber-matrix interface has a more prominent rate sensitivity than the UHPC matrix. And the influences of the fiber embedded length are associated with the matrix confinement which affects the interfacial cracking process.
- (5) A new analytical model to predict the dynamic peak pullout loads of hooked-end steel fiber at loading rates up to the intermediate level is developed and validated. Influences of the external loading rate, concrete compressive strength, fiber properties and embedded length are considered in the model.

Chapter 4

*Enhancing the static flexural performance of coarse-aggregated UHPFRC by an optimized layered-structure concept**



*This chapter is partially reproduced from: Y.Y.Y. Cao¹, P.P. Li¹, H.J.H. Brouwers, M. Sluijsmans, Q.L. Yu, Enhancing flexural performance of ultra-high performance concrete by an optimized layered-structure concept, Composites Part B 171 (2019) 154–165 (¹ Equivalent first authors).

Abstract

The study in this chapter aims to improve the flexural behavior of UHPFRC by applying the concept of layered-structure. Deterministic criteria for layer cracking and debonding are proposed, formulae to predict the critical load at the first failure stage are developed, and effects of the layer elastic modulus and layer thickness are assessed. Subsequently, double-layered UHPFRC beams are designed and evaluated applying three-point bending tests. The influences of the bottom layer thickness on the peak flexural load and the flexural energy are investigated, presenting that a layer thickness ratio of 0.6 gives the optimum load carrying ability and flexural energy. The subsequent section discusses the effects of the fiber amount distribution on the flexural performances, revealing that the designed double-layered UHPFRC beam is able to withstand higher flexural load and energy compared to its single-layered counterpart with the same total fiber amount. Moreover, it is exhibited that the peak flexural load is dependent on the fibers in the bottom layer while the flexural energy enhancement is related to the fibers in both layers. The layered UHPFRC beam composed of a 40 mm-thick top layer with 0.6% fibers and a 60 mm-thick bottom layer with 1.6% fibers is an optimal choice leading to the superior peak flexural load and energy.

4.1 Introduction

UHPFRC is a construction material with superior mechanical and material properties (Shi et al., 2015; Wu et al., 2017a). To broaden its application, achieving lower material costs of UHPFRC is an important issue. Replacing fine particles with cheaper coarse aggregates could be one of the solutions. Typically, coarse aggregates are eliminated from conventional UHPFRC to enhance its homogeneity and thereafter its strength. Despite that, current studies confirm the potential of incorporating coarse aggregates in UHPFRC. Studies show that the strength loss of UHPFRC due to coarse aggregates can be limited by properly packing the granular constituents (Li et al., 2018; Wille et al., 2011). Furthermore, UHPFRC with an appropriate content of coarse aggregates possess advantages on respects such as binder material saving, shrinkage control and impact resistance improvement (Li et al., 2018; Peng et al., 2016a; Yoo and Banthia, 2016).

Besides the binder, another dominant factor in UHPFRC production is the cost of steel fibers (Wu et al., 2017b), which stresses the necessity of using steel fibers more efficiently. The application of steel fibers contributes significantly to the enhancement of UHPFRC tensile properties (Meng and Khayat, 2017), and a strong dependency of the tensile strength on the fiber amount is exhibited (Wille et al., 2014). Nevertheless, previous studies suggest that steel fibers have a less significant effect on improving the compressive strength of UHPFRC compared with that on the tensile strength (Savino et al., 2018; Spasojević, 2008). As a consequence, it is uneconomical to distribute steel fibers in the whole volume of UHPFRC for applications where the structure is partially in tension and partially in compression, e.g. bending beams and specimens under impact (Burlion, 1997; Shen et al., 2008). We can take the bending beam as an example. When a beam works under service situations, half of it is in tension and the other half is in compression (Shen et al., 2008); the fibers in the tensile zones could effectively improve the flexural strength of the beam while those in the compressive zone have a relatively small contribution (Yang et al., 2003).

To generate a more efficient fiber utilization, optimization is required to selectively distribute the fibers in UHPFRC where their advantages can be maximized. An innovative approach is designing layered UHPFRC with different fiber amounts at specific depths. Cyclic loading and impact studies on NC have confirmed the benefits of applying layered-structure to cementitious materials (Dias et al., 2010; Mastali et al., 2015; Naghibdehi et al., 2015). From these evidences, it is reasonable to expect that a layered UHPFRC with fibers purposefully reinforced in the targeted region would have superior mechanical properties and improved fiber efficiency in comparison to the single-layered UHPFRC with the same amount of fibers distributed randomly in the whole structure.

Load carrying ability and flexural energy absorption are two important factors for assessing the performance of cementitious materials, and three-point bending test is often conducted for the evaluations (Wu et al., 2018). Current researches on the flexural properties of concrete mainly concentrate on the single-layered one (Kim et al., 2011; Wu et al., 2016), while multi-layered cementitious composites are insufficiently studied. Among the limited researches, most of them addressed the combination of old and new concretes as layered repair systems (He et al., 2017; Kim et al., 2007; Luković et al., 2014). Only a few studies investigated the flexural performances of multi-layered concrete with freshly cast layers. For instance, Liu et al. (Liu et al., 2018) assessed the flexural strength of double-layered concrete beams ($\sigma_{c,s} < 30$ MPa), and claimed their potential applications in real construction. Shen et al. (Shen et al., 2008) studied the flexural behavior of a four-layered concrete

beam with PVA fibers gradually distributed; their results showed that the layered beam has a 50% higher flexural strength compared to its single-layered counterpart. It noteworthy that the design of these layered cementitious composites is empirical, e.g. the thickness of the layer is randomly chosen and the influences of the layer thickness are not considered. On the other hand, Xu et al. (Xu et al., 2012) and Hou et al. (Hou et al., 2015) presented theoretical and experimental investigations on steel-bar reinforced concrete with an ultra-high flexural energy concrete (UHTCC) layer, in which the effects of the layer thickness were discussed. The studies exhibited that the interface cracking and ultimate bonding strengths of the specimen are related to the thickness of the UHTCC layer. Zhang et al. (Zhang et al., 2014, 2006) developed an theoretical model for analyzing the flexural behaviors of engineered cementitious composites (ECC) with two layers. Their study confirmed that the ECC layer thickness is an important design parameter, and that the beam flexural strength increased non-linearly with the ECC thickness. Nonetheless, in the above theoretical studies, the stress–crack relationship of concrete must be obtained in advance for the analysis. Moreover, the model calculations require complex processes and massive programming efforts, which thus hinders their engineering applications. That being the case, proposing theoretical models which are simple and ready to be applied to layered-structure design is of urgent importance.

In this chapter, flexural performances of double-layered UHPFRC incorporating coarse aggregates are investigated theoretically and experimentally. In the theoretical section, critical cracking and debonding criteria of the layered beam at the first failure stage are proposed, formulae for predicting the critical load are developed, and influences of the layer thickness are analyzed. With the support of the theoretical analysis, double-layered UHPFRC beams are designed in the subsequent experimental section, in which the theoretical and experimental first cracking loads are also compared. Moreover, enhancements of the flexural performance due to the fiber amount distribution over the layered structure, the effects of the layer interface on the crack development, and the roles of steel fibers in individual layers are discussed in detail. Results from this study provide an important perspective for understanding the flexural behaviors of layered UHPFRC. Additionally, with the incorporation of coarse aggregates and the efficient utilization of steel fibers, the designed double-layered UHPFRC can bring great economic benefits and promotes the future technological application of layered UHPFRC in engineering constructions.

4.2 Theoretical analysis of the first failure stage

In this section, a double-layered UHPFRC beam subjected to three-point bending test is considered, as shown in Fig. 4-1. The height and width of the beam are H and b , correspondingly. E_1 , h_1 and A_1 are the elastic modulus, layer thickness and cross-sectional area of the top layer; E_2 , h_2 and A_2 are those of the bottom layer, respectively. h_0 is the height of the neutral axis. F_s is the shear force, which equals to half of the external load F according to the force equilibrium. M is the bending moment in the beam at point x : $M(x) = Fx / 2$, and it reaches the maximum value $M_{\max} = FL / 4$ at $x = L / 2$.

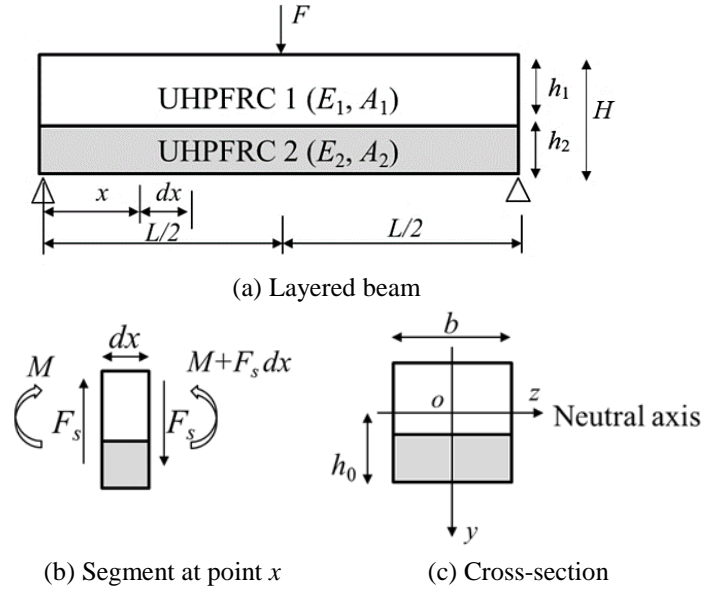


Fig. 4-1 Double-layered UHPFRC beam under bending

The failure process of the beam under bending can be generally divided into two stages: (1) a linear elastic stage until first cracking occurs and (2) a subsequent crack developing stage (Zhang et al., 2014). This section focuses on the stress distribution at the first failure stage, considering the fact that the first cracking load can be used as an indicator to evaluate the flexural capacity of UHPFRC (El-Din et al., 2016; Thomas and Sorensen, 2017), as well as the simplicity and practicality of the proposed formula to support the structure design. In addition, since stress-strain relationship of the material is not required in the analysis (only basic mechanical properties, e.g. tensile strength and elastic modulus, are necessary), formulae in this section can also be extended to general layered composite made of materials other than concrete.

4.2.1 Cracking criteria in the layered UHPFRC beam

Plane section assumption is applied in the analysis, i.e. the cross section of the double-layered UHPFRC beam is considered to remain plane (Zhang et al., 2006). The equilibrium of the forces is expressed as:

$$\int_{A_1} \sigma_1 dA_1 + \int_{A_2} \sigma_2 dA_2 = 0 \quad (4-1)$$

And it can be transformed to:

$$E_1 \int_{A_1} y dA_1 + E_2 \int_{A_2} y dA_2 = 0 \quad (4-2)$$

where σ_1 and σ_2 are the normal stress in the top and bottom layers, correspondingly. Then the height of the neutral axis h_0 could be obtained:

$$h_0 = \frac{H [1 - \beta_h^2 (1 - 1/\beta_E)]}{2 [1 - \beta_h (1 - 1/\beta_E)]} \quad (4-3)$$

where $\beta_E = E_1 / E_2$ is the layer elastic modulus ratio, and $\beta_h = h_2 / H$ is the layer thickness ratio. For a single-layered beam, i.e. $\beta_E = 1$, $\beta_h = 0$ or 1 , Eq. 4-3 reduces to $h_0 = H / 2$.

Substituting $h_2 = h_0$ to Eq. 4-3 yields the critical layer thickness ratio $\beta_{h,c}$, in which case the entire bottom UHPFRC layer is exactly in tension and the entire top layer is exactly in compression:

$$\beta_{h,c} = \frac{\sqrt{\beta_E}}{1 + \sqrt{\beta_E}} \quad (4-4)$$

When $\beta_{h,c} < \beta_h \leq 1$ is satisfied, h_2 is larger than h_0 , i.e. the neutral axis is in the bottom layer. In this situation, the layer interface is within the range of the compression zone. Otherwise, the neutral axis is in the top layer, and the interface is under tension.

Based on the plane assumption of the beam section, the normal stress distributions in the two layers can be expressed as:

$$\text{Top layer: } \sigma_{1(y)} = \frac{My}{I_0}, h_0 - H \leq y < h_0 - h_2 \quad (4-5)$$

$$\text{Bottom layer: } \sigma_{2(y)} = \frac{My}{\beta_E I_0}, h_0 - h_2 \leq y \leq h_0 \quad (4-6)$$

I_0 is the inertia moment of the layered beam, which is a function of β_E and β_h :

$$I_0 = \frac{H^3 b}{12} \left[(1 - \beta_h)^3 + \frac{\beta_h^3}{\beta_E} + \frac{3\beta_h(1 - \beta_h)}{\beta_h + \beta_E(1 - \beta_h)} \right] \quad (4-7)$$

For a given external load, the normal stress distribution along the layered beam section is plotted in Fig. 4-2a, where $\beta_E = 0.8$, $\beta_h = 0.5$ are taken as an example. It can be seen from the figure that the normal stresses, i.e. compressive and tensile stresses, reach their maximum values at the top and bottom surfaces of the beam respectively, and a jump of the compressive stress is observed at the layer interface due to the change of the material properties of the two layers.

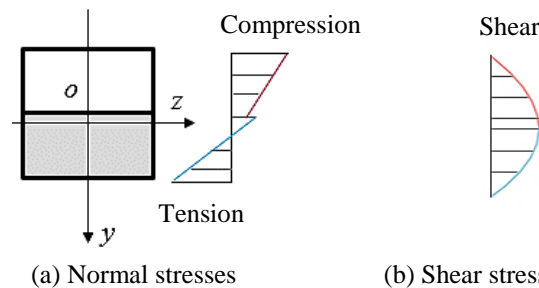


Fig. 4-2 Stress distribution along the layered beam in linear elastic stage

In general, crack initiates when the tensile stress in the UHPFRC beam exceeds its yield strength (Smarzewski, 2018; Soltani et al., 2013). If the layer interface is within the range of the compression zone ($h_2 > h_0$), cracking always starts first from the lower position of the bottom layer (Fig. 4-2a).

However, if the interface is in the tension zone ($h_0 > h_2$), the initial crack may appear first in the top layer. Assuming that the two layers reach their tensile strengths $\sigma_{t,i}$ ($i = 1, 2$) at the same time:

$$\sigma_{1(y=h_0-h_2)} = \sigma_{t,1} \quad (4-8)$$

$$\sigma_{2(y=h_0)} = \sigma_{t,2} \quad (4-9)$$

The critical first cracking condition can be obtained:

$$\frac{\sigma_{t,1}}{\sigma_{t,2}} = \left(1 - \frac{h_2}{h_0}\right) \beta_E = \frac{1 - 2\beta_h + \beta_h^2 (1 - 1/\beta_E)}{1 - \beta_h^2 (1 - 1/\beta_E)} \beta_E = \gamma_c \quad (4-10)$$

Eq. 4-10 reveals that if the tensile strength of the top layer $\sigma_{t,1}$ is smaller than the value of $\gamma_c \sigma_{t,2}$, then, in theory, the first crack would occur in the top layer near the interface at $x = L/2$. In this case, the external load to evoke the first crack is:

$$F_{c,top} = \frac{4I_0\sigma_{t,1}}{L(h_0-h_2)} = \frac{2H^2b\sigma_{t,1} \left[1 - \beta_h (1 - 1/\beta_E)\right]}{3L \left[1 - 2\beta_h + \beta_h^2 (1 - 1/\beta_E)\right]} \left[(1 - \beta_h)^3 + \frac{\beta_h^3}{\beta_E} + \frac{3\beta_h(1 - \beta_h)}{\beta_h + \beta_E(1 - \beta_h)} \right] \quad (4-11)$$

Otherwise, the bottom layer cracks earlier and the corresponding critical load is:

$$F_{c,bottom} = \frac{4\beta_E I_0 \sigma_{t,2}}{Lh_0} = \frac{2\beta_E H^2 b \sigma_{t,2} \left[1 - \beta_h (1 - 1/\beta_E)\right]}{3L \left[1 - \beta_h^2 (1 - 1/\beta_E)\right]} \left[(1 - \beta_h)^3 + \frac{\beta_h^3}{\beta_E} + \frac{3\beta_h(1 - \beta_h)}{\beta_h + \beta_E(1 - \beta_h)} \right] \quad (4-12)$$

In the specific case of a single-layered beam only composed of the UHPFRC 1 material (Fig. 4-1), i.e. $h_2 = 0$, $h_0 = H/2$, the critical load is expressed in Eq. 4-13, coinciding with the result obtained by substituting $\sigma_{1(y=H/2)} = \sigma_{t,1}$ to Eq. 4-5:

$$F_{c,top,0} = \frac{8I_0\sigma_{t,1}}{LH} \quad (4-13)$$

Similarly, when $h_2 = H$, the beam is only composed of the UHPFRC 2 material. The critical load is Eq. 4-12 with $h_2 = H$ and $h_0 = H/2$, $\beta_E = 1$, as given by:

$$F_{c,bottom,0} = \frac{8I_0\sigma_{t,2}}{LH} \quad (4-14)$$

It is identical to Eq. 4-6 with $\sigma_{2(y=H/2)} = \sigma_{t,2}$ substituted. These agreements also confirm the correctness of the proposed equations.

Furthermore, it is noteworthy that when the two layers have an equal elastic modulus ($\beta_E = 1$), the neutral axis is always at $h_0 = H/2$, and the value of I_0 as well as $F_{c,bottom}$ remain constant, i.e. changing the layer thickness h_2 has no influence under this circumstance. $F_{c,top}$ can be re-written as Eq. 4-15 when $\beta_E = 1$ is substituted, the value of which increases with the increase of β_h , viz. when the

crack initiates from the top layer ($0 < \beta_h < 0.5$ and $\sigma_{t,1} < \gamma_c \sigma_{t,2}$), the thicker the bottom layer the higher the first cracking load.

$$F_{c,top(\alpha=1)} = \frac{2H^2 b \sigma_{t,1}}{3L(1-2\beta_h)} \quad (4-15)$$

4.2.2 Debonding criteria in the layered UHPFRC beam

The shear stress distributions in the two layers can also be obtained by the equilibrium of forces in x -axis direction (see Fig. 4-1):

Top layer:

$$\int_{A1} \frac{My}{I_0} dA + \tau_1 \beta_E b dx = \int_{A1} \frac{(M + F_s dx) y}{I_0} dA \quad (4-16)$$

Bottom layer:

$$\int_{A2} \frac{My}{\beta_E I_0} dA + \tau_2 b dx = \int_{A2} \frac{(M + F_s dx) y}{\beta_E I_0} dA \quad (4-17)$$

The corresponding shear stresses in the two layers are given as:

Top layer:

$$\tau_{1(y)} = \frac{F}{4I_0} \left[(H - h_0)^2 - y^2 \right], \quad h_0 - H \leq y < h_0 - h_2 \quad (4-18)$$

Bottom layer:

$$\tau_{2(y)} = \frac{F}{4\beta_E I_0} (h_0^2 - y^2), \quad h_0 - h_2 \leq y \leq h_0 \quad (4-19)$$

It is noted that the maximum shear stress along the beam depth is at the neutral axis $y = 0$ and the value is expressed as:

$$\tau_{\max(y=0)} = \frac{F h_0^2}{4\beta_E I_0} \quad (4-20)$$

Differing with the normal stresses, the shear stress changes continuously along the beam depth (see Fig. 4-2b) and the peak is at the neutral axis, which is usually nearby the layer interface when the elastic moduli of the two layer are not very distinct, e.g. $\beta_E = 0.8$ in Fig. 4-2b. This maximum shear stress can induce the possibility of layer debonding since the interface usually presents a weak part in the composite (Zanotti et al., 2014). More specifically, debonding due to shear occurs when the interfacial shear stress reaches the bond strength σ_b :

$$\tau_{1(y=h_0-h_2)} = \tau_{2(y=h_0-h_2)} = \sigma_b \quad (4-21)$$

This leads to the critical debonding load provoked by shear:

$$F_{d, shear} = \frac{4\beta_E I_0 \sigma_b}{h_2 (2h_0 - h_2)} = \frac{\beta_E H b \sigma_b [1 - \beta_h (1 - 1/\beta_E)]}{3\beta_h (1 - \beta_h)} \left[(1 - \beta_h)^3 + \frac{\beta_h^3}{\beta_E} + \frac{3\beta_h (1 - \beta_h)}{\beta_h + \beta_E (1 - \beta_h)} \right] \quad (4-22)$$

On the other hand, when the layer interface is within the tension zone ($0 < h_2 < h_0$), the tensile stress at the interface can also procure layer debonding when

$$\sigma_{2(y=h_0-h_2)} = \sigma_b \quad (4-23)$$

Then the corresponding critical debonding load due to tension can be expressed as:

$$F_{d, tension} = \frac{4\beta_E I_0 \sigma_b}{L(h_0 - h_2)} = \frac{2\beta_E H^2 b \sigma_b [1 - \beta_h (1 - 1/\beta_E)]}{3L [1 - 2\beta_h + \beta_h^2 (1 - 1/\beta_E)]} \left[(1 - \beta_h)^3 + \frac{\beta_h^3}{\beta_E} + \frac{3\beta_h (1 - \beta_h)}{\beta_h + \beta_E (1 - \beta_h)} \right] \quad (4-24)$$

When the critical debonding load is smaller than the critical cracking load, layer debonding occurs prior to layer cracking, which will strongly affect the effectiveness of the layered composite beam. To avoid early layer debonding, the following critical condition for the bond strength should be satisfied:

(1) If $h_2 \geq h_0$, the condition is $F_{d, shear} \geq F_{c, bottom}$:

$$\sigma_b \geq \frac{2\beta_h (1 - \beta_h) H}{[1 - \beta_h^2 (1 - 1/\beta_E)] L} \sigma_{t,2} \quad (4-25)$$

(2) If $h_2 < h_0$, it turns to be $\text{Min} (F_{d, shear}, F_{d, tension}) \geq F_{c, top}$, for $\sigma_{t,1} < \gamma_c \sigma_{t,2}$:

$$\sigma_b \geq \text{Max} \left(\frac{\sigma_{t,1}}{\beta_E}, \frac{2\beta_h (1 - \beta_h) H}{[1 + \beta_h^2 (1 - 1/\beta_E) - 2\beta_h] L} \frac{\sigma_{t,1}}{\beta_E} \right) \quad (4-26)$$

or $\text{Min} (F_{d, shear}, F_{d, tension}) \geq F_{c, bottom}$, for $\sigma_{t,1} \geq \gamma_c \sigma_{t,2}$:

$$\sigma_b \geq \text{Max} \left(\frac{2\beta_h (1 - \beta_h) H}{[1 - \beta_h^2 (1 - 1/\beta_E)] L} \sigma_{t,2}, \frac{1 + \beta_h^2 (1 - 1/\beta_E) - 2\beta_h}{1 - \beta_h^2 (1 - 1/\beta_E)} \sigma_{t,2} \right) \quad (4-27)$$

4.2.3 Influences of β_E and β_h on stress distribution and critical load

Based on the above analysis, the critical load at the first stage of the failure process $F_{critical}$ and the failure modes can be concluded as follows (also given in Table 4-1):

(1) For $h_2 = 0$ ($\beta_h = 0$): $F_{critical} = F_{c, top, 0}$, the first failure stage ends with cracking of the beam (made of UHPFRC 1 material).

- (2) For $0 < h_2 < h_0$ ($0 < \beta_h < \beta_{h,c}$) and $\sigma_{t,1} < \gamma_c \sigma_{t,2}$: $F_{critical} = \text{Min}(F_{c,top}, F_{d,shear}, F_{d,tension})$, the first failure stage ends with top layer cracking or layer debonding.
- (3) For $0 < h_2 < h_0$ ($0 < \beta_h < \beta_{h,c}$) and $\sigma_{t,1} \geq \gamma_c \sigma_{t,2}$: $F_{critical} = \text{Min}(F_{c,bottom}, F_{d,shear}, F_{d,tension})$, the first failure stage ends with bottom layer cracking or layer debonding.
- (4) For $h_0 \leq h_2 < H$ ($\beta_{h,c} \leq \beta_h < 1$): $F_{critical} = \text{Min}(F_{c,bottom}, F_{d,shear})$, the first failure stage ends with bottom layer cracking or layer debonding due to shear.
- (5) For $h_2 = H$ ($\beta_h = 1$): $F_{critical} = F_{c,bottom,0}$, the first failure stage ends with cracking of the beam (made of UHPFRC 2 material).

Table 4-1 Critical load at first failure stage and the corresponding failure modes: $F_{critical}$ = critical load, β_h = layer thickness ratio, $\beta_{h,c}$ = critical layer thickness ratio, $\sigma_{t,i}$ ($i = 1, 2$) = layer tensile strength, γ_c = critical layer tensile strength ratio, $F_{c,top}$ = critical cracking load of the top layer, $F_{c,bottom}$ = critical cracking load of the bottom layer, $F_{d,shear}$ = critical debonding load by shear, $F_{d,tension}$ = critical debonding load by tension

Conditions	$F_{critical}$	First stage failure modes
$\beta_h = 0$	$F_{c,top,0}$	(Single-layered) beam cracking
$0 < \beta_h < \beta_{h,c}$ and $\sigma_{t,1} < \gamma_c \sigma_{t,2}$	$\text{Min}(F_{c,top}, F_{d,shear}, F_{d,tension})$	Top layer cracking or layer debonding
$0 < \beta_h < \beta_{h,c}$ and $\sigma_{t,1} \geq \gamma_c \sigma_{t,2}$	$\text{Min}(F_{c,bottom}, F_{d,shear}, F_{d,tension})$	Bottom layer cracking or layer debonding
$\beta_{h,c} \leq \beta_h < 1$	$\text{Min}(F_{c,bottom}, F_{d,shear})$	Bottom layer cracking or shear debonding
$\beta_h = 1$	$F_{c,bottom,0}$	(Single-layered) beam cracking

The influences of β_E and β_h on h_0 and $F_{critical}$ are plotted in Fig. 4-3, in which $H = 0.1$ m, $L = 0.4$ m, $\sigma_{t,1} = \sigma_b = 12$ MPa and $\sigma_{t,2} = 16$ MPa are taken as an example. Fig. 4-3a confirms that when the two layers have an identical elastic modulus, i.e. $\beta_E = 1$, the neutral axial is always at the middle of the beam depth regardless of the layer thickness, as expected. Consequently, the top half of the beam is always under compression while the bottom half is always in tension. On the other hand, h_0 changes with β_h when the two layers have different elastic moduli. Moreover, if the top layer has a larger elastic modulus, e.g. $\beta_E = 1.2$, then h_0 is in the top half of the composite beam, indicating a larger tension region in the composite beam; otherwise, the compression region is more dominant (see Fig. 4-2a) and it extends with the decrease of β_E .

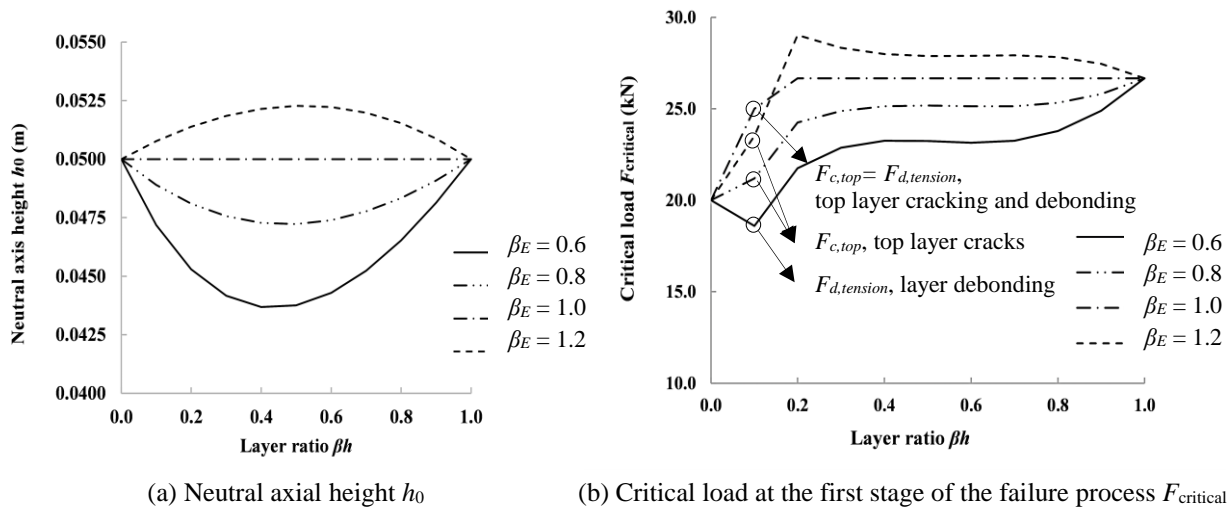


Fig. 4-3 Influences of the layer elastic modulus ratio β_E and thickness ratio β_h

The damage modes at the first failure stage are related to β_h . For $\beta_h = 0.2 \sim 1.0$, the critical debonding load is much higher than the critical cracking load, and the first failure stage always ends

with bottom layer cracking. In contrast, cases with $\beta_h = 0.1$ experience distinct damage modes (see Fig. 4-3b): (1) for $\beta_E = 0.6$, debonding due to tension occurs prior to cracking ($F_{d,tension} < F_{c,top}$), hence the failure is dominated by layer debonding; (2) for $\beta_E = 0.8$ and 1.2 , the initial crack appears in the top layer rather than in the bottom one since $\beta_h < \beta_{h,c}$ and $\sigma_{t,1} < \gamma_c \sigma_{t,2}$; (3) for $\beta_E = 1.0$, $F_{d,tension} = F_{c,top}$, i.e. debonding and cracking take place at the same time.

Furthermore, the relationship of $F_{critical}$ and β_h is also depicted in Fig. 4-3b. In the case of $\beta_E = 1.0$, $F_{critical}$ remains constant when β_h varies from 0.2 to 1.0, which is in line with the analysis in Section 4.2.1. In contrast, for $\beta_E = 0.6$ and 0.8 , $F_{critical}$ is improved when β_h increases from 0.2 to 1. The improvement is limited when β_h goes beyond 0.3, especially for $\beta_E = 0.8$. In the case of $\beta_E = 1.2$, a gradual decrease of the critical load is observed with the increase of β_h in the range of 0.2 ~ 1.0, indicating a negative effect of enhancing the bottom layer thickness despite its higher tensile strength.

4.3 Experimental program

4.3.1 Materials and mix design

The recipe of the coarse-aggregated UHPFRC is based on (Li and Yu, 2019), as presented in Table 4-2. The coarse basalt aggregates applied have two size groups namely 2-5 mm and 5-8 mm, the fraction of which are calculated applying the Brouwers mix design method (Brouwers and Radix, 2005; Wang et al., 2014). Smooth straight steel fiber Dramix OL 13/.20 (length = 13 mm, diameter = 0.2 mm, tensile strength = 2750 MPa) is utilized in the layered UHPFRC beams with different volume fractions in the individual layers. The amount of superplasticizer is adjusted according to the fiber amount until a flowability around 560 mm is achieved (measured with Abrams cone in accordance with (EN 12350-8, 2007)).

Table 4-2 Recipes of the UHPC and the UHPFRC: CEM = Portland cement, mS = micro-silica, LP = limestone powder, S = sand, BA 2-5 = basalt aggregate with sizes of 2-5 mm, BA 5-8 = basalt aggregate with sizes of 5-8 mm, W = water, SP = superplasticizer, SF = steel fiber.

Materials	CEM (kg/m ³)	mS (kg/m ³)	LP (kg/m ³)	S (kg/m ³)	BA 2-5 (kg/m ³)	BA 5-8 (kg/m ³)	W (kg/m ³)	SP (kg/m ³)	SF (%)
								5	0
								7	0.6
Quantity	588	39.2	156.8	839.9	413.2	232.3	157	9	1.2
								14	1.6
								17	2.0

4.3.2 Design of double-layered UHPFRC composite beams

Since the first cracking load can be used as an indicator to represent the maximum flexural capacity (El-Din et al., 2016; Thomas and Sorensen, 2017), thicknesses of the double-layered UHPFRC beams in this study are designed according to the theoretical first cracking load in Section 4.2. The relationship between the critical load $F_{critical}$ and the layer thickness ratio β_h is referred. As suggested in Fig. 4-3b with $\beta_E = 0.8$ and 1 (the layer elastic modulus ratios of the designed beams are within this range), the enhancement of $F_{critical}$ is prominent when β_h increases from 0.1 to 0.3, whereas further thickening the bottom layer does not generate eminent improvement, i.e. $\beta_h = 0.3$ is a threshold, below which the first cracking load still has a potential to increase. That being the case, the thickness of the bottom layer h_2 should be larger than $0.3H$, otherwise $F_{critical}$ does not achieve its maximum. Additionally, considering the crack propagation at the second stage of the failure process and to

investigate the effects of layer thickness on the composite flexural properties, three different layer thickness ratios are designed in the experimental section, namely $\beta_h = 0.4, 0.6$ and 0.8 .

Detailed information about the designed double-layered UHPFRC is given in Table 4-3. The identification is defined as follows: U indicates the beam is a UHPFRC composite, the first number denotes the fiber volume fraction V_f in the top layer, and the following one in the brackets is the layer thickness in mm; the third and the fourth numbers are those for the bottom layer, correspondingly. For instance, U0.6(40)-1.6(60) is a double-layered UHPFRC beam of which the top layer has 0.6% fibers with a thickness of 40 mm, and the bottom layer contains 1.6% fibers and its thickness is 60 mm. Three single-layered UHPFRC beams (100 mm thick) with 0%, 1.2% and 2% fibers are included as reference groups, i.e. U0(100), U1.2(100) and U2(100), respectively.

Table 4-3 Coarse-aggregated layered UHPFRC beam: For the identification, U indicates UHPFRC; the first two numbers denote the fiber volume fraction and thickness of the top layer; and the last two numbers are those for the bottom layer.

Identification	Layer thickness (mm)		Fiber volume fraction (%)		Note
	Top layer	Bottom layer	Top layer	Bottom layer	
U0(60)-2(40)	60	40	0	2.0	Double-layered beam
U0(40)-2(60)	40	60	0	2.0	
U0(20)-2(80)	20	80	0	2.0	
U0.6(40)-1.6(60)	40	60	0.6	1.6	
U0(40)-1.2(60)	40	60	0	1.2	
U0.6(40)-1.2(60)	40	60	0.6	1.2	
U0(100)	100		0		Single-layered beam
U1.2(100)	100	-	1.2	-	
U2(100)	100		2.0		

4.3.3 Mixing and casting procedures

The following mixing procedure is adopted for the UHPFRC: dry mixing for 2 minutes with all powders and sand; adding 75% of the water and mixing for 2 minutes; sequentially adding the remaining water with the superplasticizer and mixing for 4 minutes, after which the steel fibers are added sequentially. After 3 minutes, the basalt aggregates are added to the mix and stirred for 3 minutes. The mixing procedure is conducted at room temperature (20 ± 1 °C).

The dimensions of the beams are $100 \times 100 \times 500$ mm³. With regard to the double-layered UHPFRC beams, the bottom layer of the UHPFRC beam is cast in the mould with the designed thickness, and the top layer mixture is poured into the mould carefully after 45 minutes. This casting time interval is determined based on a preliminary study, considering both the experimental operability and the relationship between the bond strength and the time interval. At the time of the top layer casting, the bottom layer is sufficiently strong to support the top layer matrix, i.e. deformation of the layer interface is avoided; while the initial setting of the bottom layer matrix has not been reached (Hou et al., 2015; Li et al., 2017), resulting in a strong interfacial bond. This casting method, on the one hand, induces a sufficient layer bond strength; on the other hand, the existence of the layer interface can act as a source of micro-cracking, which consumes more fracture energy during the cracking process (this will be further explained in Section 4.4.3). The 100 mm cubic specimens are used for the compressive, splitting tensile and bond tests. The same casting method is applied for the double-layered cubes (for the bond strength test). The cast specimens are covered with plastic sheets for 24 hours. Then they are demolded and cured in water for additional 27 days.

4.3.4 Testing methods

The compressive strengths of the UHPFRC samples are measured using a DIGIMAXX C-20 universal testing machine with a maximum load capacity of 4000 kN according to EN 12390-3 (EN 12390-3, 2009). Splitting tensile tests based on EN 12390-6 (EN 12390-6, 2000) are conducted to obtain the tensile and interface bond strengths (Qian et al., 2014).

To investigate the flexural performances of the double-layered UHPFRC beams, three-point bending tests are conducted at the age of 28 days (Zhang et al., 2014). The span length is 400 mm (Corinaldesi and Nardinocchi, 2016). The beams are not notched in this study because the notch would weaken the bottom layer and lead to difficulties in comparing the fibers effects on individual layers. Displacement control under a rate of 0.2 mm/min is used in the test (RILEM TC 162-TDF, 2002). The applied load is measured by the Instron 5985 testing machine and the mid-point deflections are measured with two linear variable differential transducers (LVDTs) (Kim et al., 2014; Xu et al., 2012). Three samples are tested for each group.

4.4 Experimental results and discussion

4.4.1 Mechanical and interfacial properties

The 28-day compressive strength $\sigma_{c,s}$ and splitting tensile strength $\sigma_{t,s}$ of the individual UHPFRC layers with $V_f = 0\%$, 0.6%, 1.2%, 1.6% and 2% are given in Fig. 4-4. As expected, $\sigma_{t,s}$ increases significantly with the increasing fiber amount. For instance, a 97% enhancement of $\sigma_{t,s}$ is observed for the UHPFRC incorporating 2% fibers compared to that of the mixture without fibers. In contrast, the improvement of $\sigma_{c,s}$ is limited, i.e. $\sigma_{c,s}$ of the UHPFRC with different V_f are within the range of 140 ~ 153 MPa.

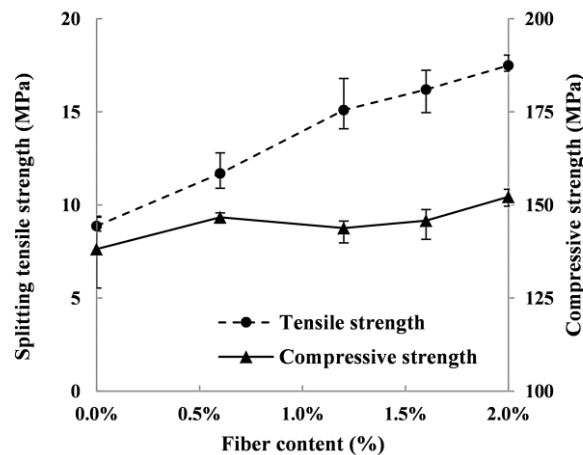


Fig. 4-4 Compressive strength $\sigma_{c,s}$ and splitting tensile strength $\sigma_{t,s}$ of mixtures

Fig. 4-5 plots the bond strengths σ_b of the tested groups. The maximum σ_b is obtained by the interface between the $V_f = 0.6\%$ and 1.6% layers (group U0.6-1.6), which is around 9.28 MPa. Fig. 4-6 shows the layer interface in the cube after the bond splitting test, in which the combination of $V_f = 0\%$ and 2% layers is taken as an example. Cohesive failure occurs in the bond splitting test, i.e. the specimen fails partially in the $V_f = 0\%$ layer and partially in the $V_f = 2\%$ layer. The failure surface is shown in Fig. 4-6. This failure pattern indicates the sufficient bond between the layers.

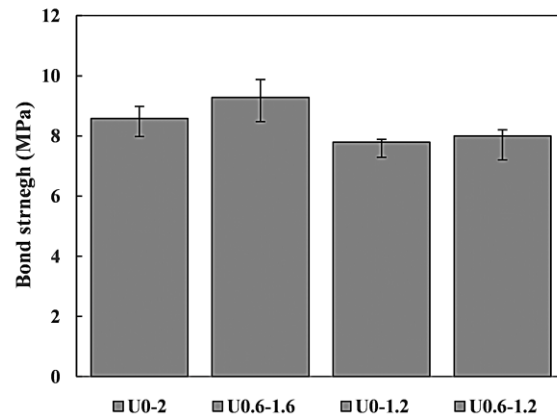
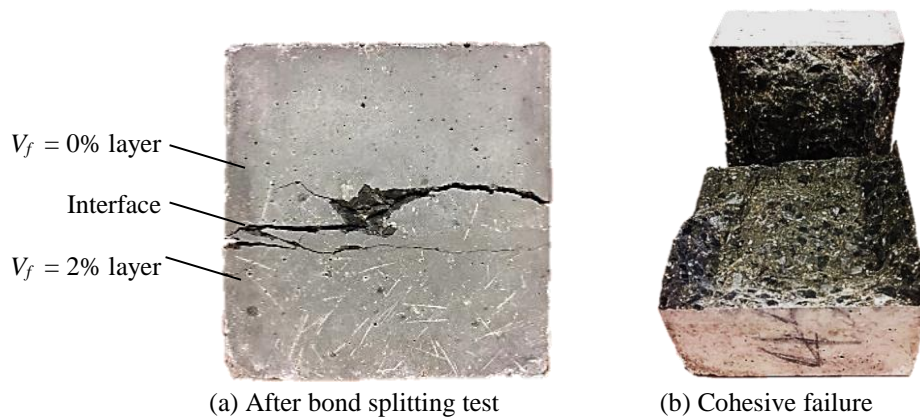
Fig. 4-5 Bond strength σ_b of the layer interface

Fig. 4-6 Bond interface and failure surface

After acquiring the basic properties, the flexural performances of the designed double-layered UHPFRC beams are investigated. During the three-point bending tests, no layer debonding is observed thanks to the sufficient interfacial bond strength. The tested beams are cut with a saw cutting machine after the bending tests to check the layer interface. Photos of half of the tested U0(40)-2(60) beam are given in Fig. 4-7 as an example. A straight layer interface is observed in the outer surface of the beam (Fig. 4-7a), and it can also be observed in the cut surface (Fig. 4-7b) where the bright dots in the bottom layer are the cross sections of the fibers. As presented in the figures, the layer interface is straight, confirming that the deformation of the bottom layer is very limited.

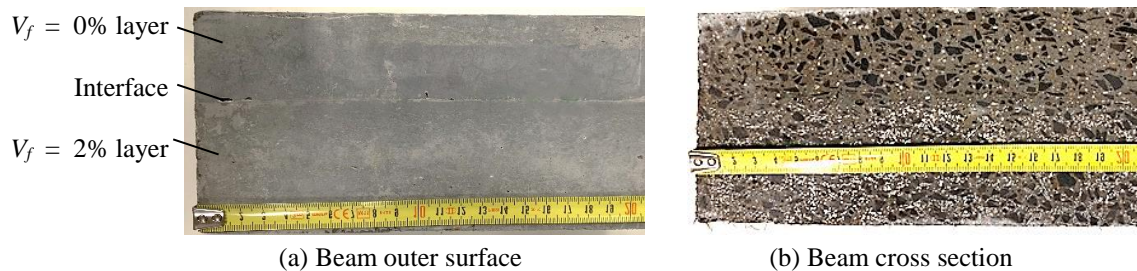


Fig. 4-7 Bond interface of the tested U0(40)-2(60) beam

4.4.2 Effects of layer thickness

Fig. 4-8 plots the flexural performances of the double-layered UHPFRC beams with different layer thicknesses, of which the bottom layers contain 2% steel fibers and the top layers are without fibers. The performances of the single-layered beams with 0% and 2% fibers are also illustrated in the figure, viz. U0(100) and U2(100). Distinct failure modes are observed for the beams with and without the fiber-reinforced layer, i.e. the plain single-layered beam experienced a catastrophic and brittle failure as opposed to the gradual failure of the composite beams reinforced with the 2% fiber layer. In addition, the first crack always initiates from the bottom layer of the UHPFRC beam, and no debonding is observed. These observations agree well with the theoretical analysis in Section 4.2.3: for $\beta_h = 0.4 \sim 0.8$, the critical debonding loads are higher than the cracking loads, and the crack condition for the bottom layer is satisfied prior to that for the top layer.

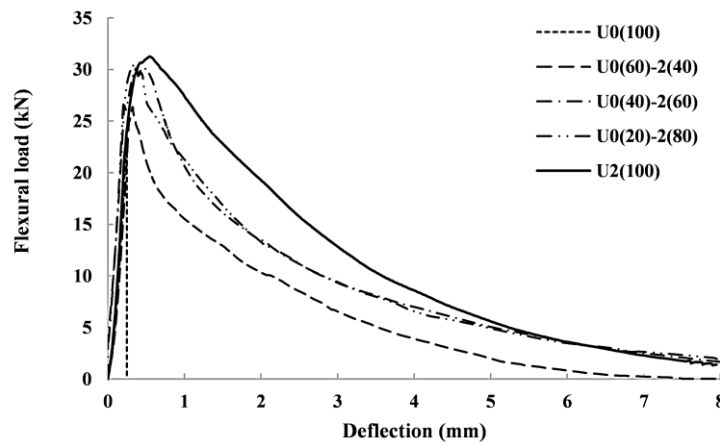


Fig. 4-8 Flexural load-deflection curve with various layer thicknesses

The relationship between the first cracking load and the layer thickness are illustrated in Fig. 4-9. It depicts that the first cracking load is insensitive to the change of β_h in the given range, corresponding with the findings in Section 4.2.3 (see Fig. 4-3b with $\beta_E = 0.8$ and 1). The calculated first cracking loads applying Eq. 4-12 are also compared with the experimental data. A reasonable agreement is achieved between the calculated and the averaged experimental results (with errors smaller than 7%, see Table 4-4), demonstrating the validity of the proposed formulae.

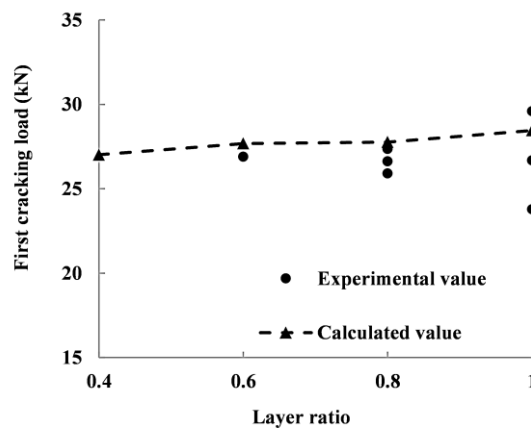
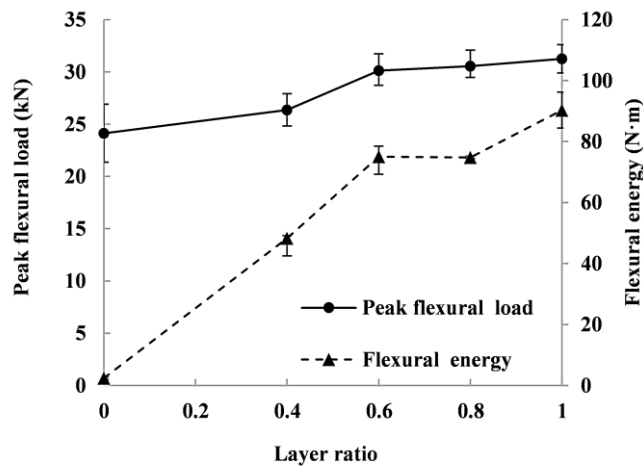


Fig. 4-9 First cracking strength with various layer thicknesses

Table 4-4 Experimental and calculated first cracking strengths

Layer thickness ratio	Averaged first cracking load (kN)		Error (%)
	Experiment	Calculation	
0.4	25.67	27.02	5.3
0.6	26.17	27.68	5.8
0.8	26.63	27.77	4.3
1	26.69	28.46	6.6

To show the effects of the layer thickness more clearly, changes of the peak flexural load $F_{s,max}$ and the flexural energy E_s (defined by the area below the flexural load-deflection curve) with the layer thickness ratio β_h are given in Fig. 4-10. With regard to $F_{s,max}$, three stages can be distinguished, i.e. the first stage ($\beta_h = 0 \sim 0.4$) has a relatively slow rate of strength increase; the second stage ($\beta_h = 0.4 \sim 0.6$) exhibits a faster increase; and the third stage ($\beta_h = 0.6 \sim 1.0$) has a slower improvement again. A similar tendency is also observed in (Zhang et al., 2006), which investigated NC beams reinforced with engineered cementitious composites. Physically, $F_{s,max}$ is associated with the aggregate governed bridging and fiber governed bridging mechanisms (Roesler et al., 2008; Zhang et al., 2006). The significant increase of $F_{s,max}$ at the transition point from the first stage to the second stage indicates that the bridging mechanism changes from the aggregate governed to the fiber governed one (Zhang et al., 2006). In other words, for a double-layered UHPFRC beam with $\beta_h < 0.4$, the fiber-reinforced bottom layer is so thin that the crack-bridging effect provided by the fibers is insufficient, and thus the peak load mainly depends on the bridging of the aggregates. Conversely, with the increase of the bottom layer thickness the fiber reinforcements can then effectively restrain the crack propagation, leading to the jump of $F_{s,max}$.

Fig. 4-10 Peak flexural strength $F_{s,max}$ and flexural energy E_s with various layer thickness ratio β_h

The flexural energy E_s is also significantly improved due to the application of the bottom UHPFRC layer. With β_h varying from 0.4 to 0.6 and 0.8, E_s increases approximately 20, 31 and 32 times than that of U0(100). Further, the improvement of E_s is more prominent within the range of $\beta_h < 0.6$, while increasing β_h to 0.8 only provides limited enhancement. To further evaluate the contribution of fibers to the flexural performances, the concept of fiber efficiency $eff_{f,s}$ is proposed, which is the ratio of the beam flexural energy to the mass of the fibers in the beam:

$$eff_{f,s} = \frac{E_s}{V_f \beta_h H b L \rho_f} \quad (4-28)$$

where the fiber density $\rho_f = 7850 \text{ kg/m}^3$.

The relationship between the fiber efficiency and layer thickness ratio is plotted in Fig. 4-11, in which the maximum $eff_{f,s}$ is reached at $\beta_h = 0.6$. Consequently, considering the tendency of the first cracking load, the improvements of the peak flexural load and the energy, as well as the fiber efficiency, $\beta_h = 0.6$ is selected for the double-layered UHPFRC beams and applied in the succeeding analysis.

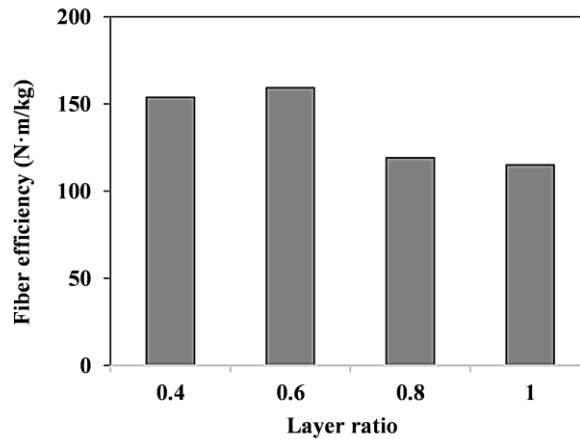


Fig. 4-11 Fiber efficiency $eff_{f,s}$ with various layer thickness ratio β_h

4.4.3 Effects of fiber amount distribution in layered structures

The flexural load-deflection curves of two double-layered UHPFRC beams and a reference single-layered beam are depicted in Fig. 4-12. The three categories, namely U1.2(100), U0(40)-2(60) and U0.6(40)-1.6(60), have the same total fiber amount (the equivalent fiber volume fraction $V_f = 1.2\%$). However, they exhibit distinct flexural capacities due to the different fiber amount distribution over the layered structure. Comparing with the single-layered UHPFRC beam, the double-layered ones achieve improved $F_{s,max}$. To specify, $F_{s,max}$ of U0(40)-2(60) and U0.6(40)-1.6(60) are approximately 30.12 kN and 32.79 kN, which are around 14% and 24% higher than that of U1.2(100), respectively. This is because in the layered beams, the fibers are more concentrated at the beam bottom. Therefore, they efficiently bridge across the lower portion of the crack and delay the opening of the crack upper portion, attributing to the increased load carrying ability of the layered beam.

The fiber amount distribution also affects E_s . Due to the lack of steel fibers in the top layer, the post-peak stage of U0(40)-2(60) shows a steeper drop than that of the single-layered beam, which leads to an approximate 10% energy reduction than that of U1.2(100). In contrast, incorporating a small amount of fibers in the top layer generates a superior energy absorption capacity, i.e. the E_s of U0.6(40)-1.6(60) is about 14% higher than that of U1.2(100). On that account, for the purpose of flexural energy enhancement, a small amount of steel fibers is required in the top layer of the UHPFRC composite beam.

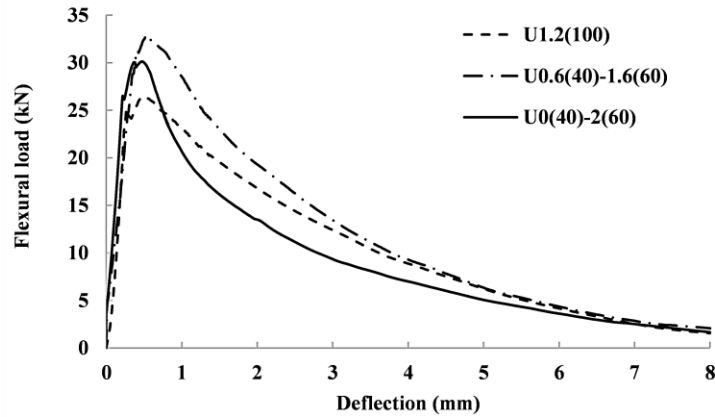


Fig. 4-12 Flexural load-deflection curve with various fiber distribution

The crack propagation is also influenced by the fiber amount distribution. For the single-layered beam U1.2(100), a single crack is observed during the flexural process, initiating from the middle of the beam bottom and gradually propagating to the beam top surface (Fig. 4-13). A different cracking process is observed for the double-layered beam U0.6(40)-1.6(60). As illustrated in Fig. 4-14, the crack first appears at the bottom of U0.6(40)-1.6(60) at around $t = 12$ min after the start of the loading. With the increase of the bending load, the crack opens more widely. At $t = 13.5$ min, a newly-developed small crack appears in the top layer near the layer interface owing to the stress concentration caused by the varying properties of the layers (Thai et al., 2014). The small crack propagates further downwards into the bottom layer as the external load increases, which interrupts the potential layer debonding (Noshiravani and Brühwiler, 2014). At $t = 16.5$ min, the small crack from the interface is connected with the previous crack at the beam bottom, creating a macro-crack. Then this macro-crack further develops upwards, during which fibers at the bottom surface of the beam are gradually pulled out from the matrix. At about $t = 35$ min, fibers near the interface are also pulled out and the failure of the beam is accelerated afterwards.

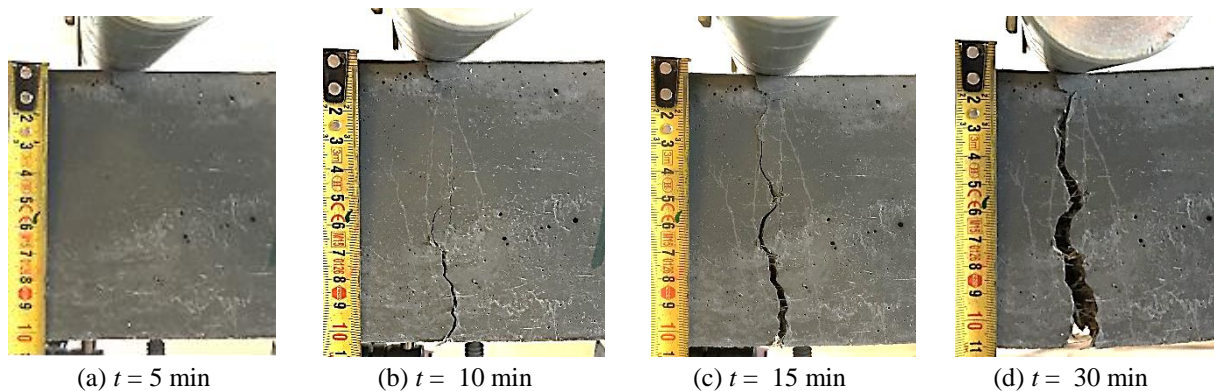


Fig. 4-13 Crack development in U1.2(100)

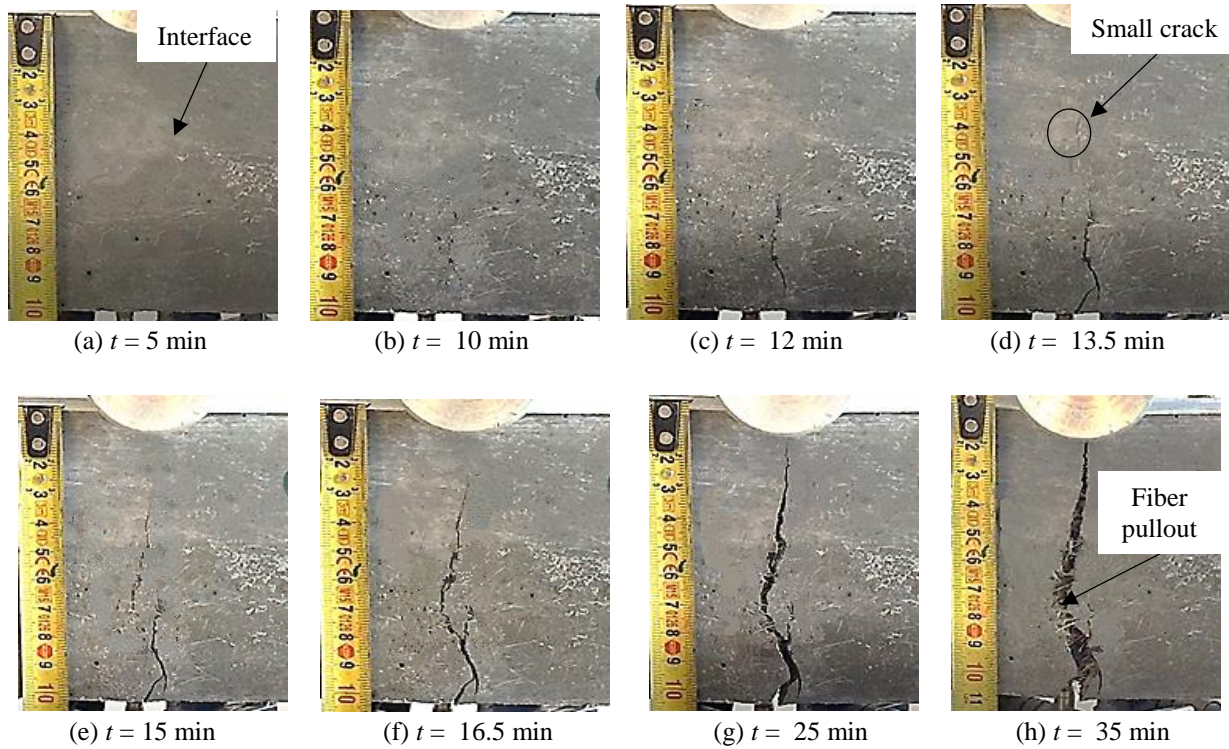


Fig. 4-14 Crack development in U0.6(40)-1.6(60)

Comparing Figs. 4-13 and 4-14 reveals that the double-layered UHPFRC beam cracks more slowly than its single-layered counterpart due to the more concentrated fibers at the beam bottom, redistributing the tensile stress and prohibiting the crack initiation. It also takes longer for the double-layered beam to reach the final failure status, i.e. being completely separated into two parts. This is attributed to the combined effects provided by the fibers in both the top and the bottom layers. Additionally, the layer interface also serves as a cracking initiator due to the stress concentration and the lack of fiber connection in the interfacial zone. Micro-cracks are observed near the interface. They connect with the macro-crack and further generate fine crack branches. These multiple micro-cracks and fine crack branches in the layered beam consume more energy during the flexural process and thus improve the flexural energy of the double-layered UHPFRC.

4.4.4 Effects of fiber amount in individual layers

The effects of the fiber amount in the individual layers of the UHPFRC composite beam are evaluated in this section. Fig. 4-15 compares the flexural responses of U0(40)-1.2(60), U0.6(40)-1.2(60) and U1.2(100). The presented beams have the same fiber amount in the bottom layer ($V_f = 1.2\%$), while the V_f in the top layer are 0%, 0.6% and 1.2%, respectively. It is obvious that the compared beams have similar $F_{s,max}$ although the V_f in their top layers differs, indicating that $F_{s,max}$ is more related to the fibers in the bottom layer. Nevertheless, improvements of E_s are observed with an increasing V_f in the top layer, which is associated with the pullout process of fibers in both the top and the bottom layers. The energy enhancement is nonlinear, which is more obvious when the V_f of the top layer increases from 0.6% to 1.2% than from 0% to 0.6%.

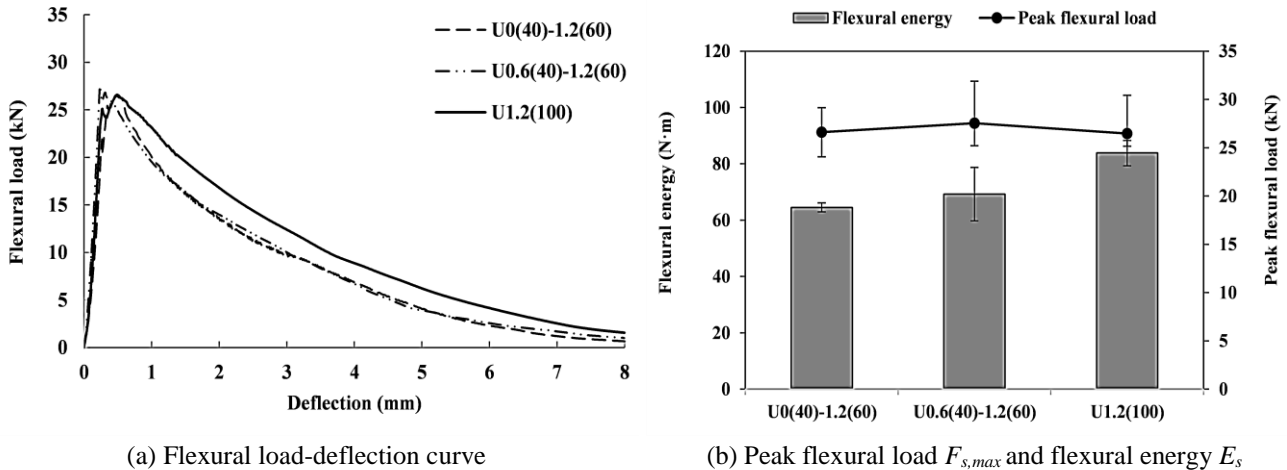


Fig. 4-15 Effects of fibers in the top layer

On the other hand, changing the V_f in the bottom layer generates more prominent effects (see Fig. 4-16). Comparing U0(40)-1.2(60) with U0(40)-2(60) reveals that when the top layer is plain UHPC, increasing the V_f of the bottom layer from 1.2% to 2% leads to 13% and 16% increases of $F_{s,max}$ and E_s , respectively. These improvements become more significant when 0.6% steel fibers are incorporated in the top layer, i.e. U0.6(40)-1.2(60) and U0.6(40)-1.6(60). Namely, 19% and 38% enhancements of $F_{s,max}$ and E_s are achieved for these beams when the V_f of the bottom layer increases from 1.2% to 1.6%.

The above analysis exhibits the different effects of steel fibers in the individual layers: (1) The enhancement of $F_{s,max}$ is more related to the fibers in the bottom layer, as they increase the stiffness of the beam. (2) Fibers in both layers contribute to the beam E_s by connecting the crack surfaces, decelerating the crack development and extending the time for the beam to reach its final failure. Furthermore, considering that the crack width in the upper section of the beam is much narrower than that in the beam bottom, incorporating a small amount of steel fibers in the top layer is sufficient to generate pronounced effects.

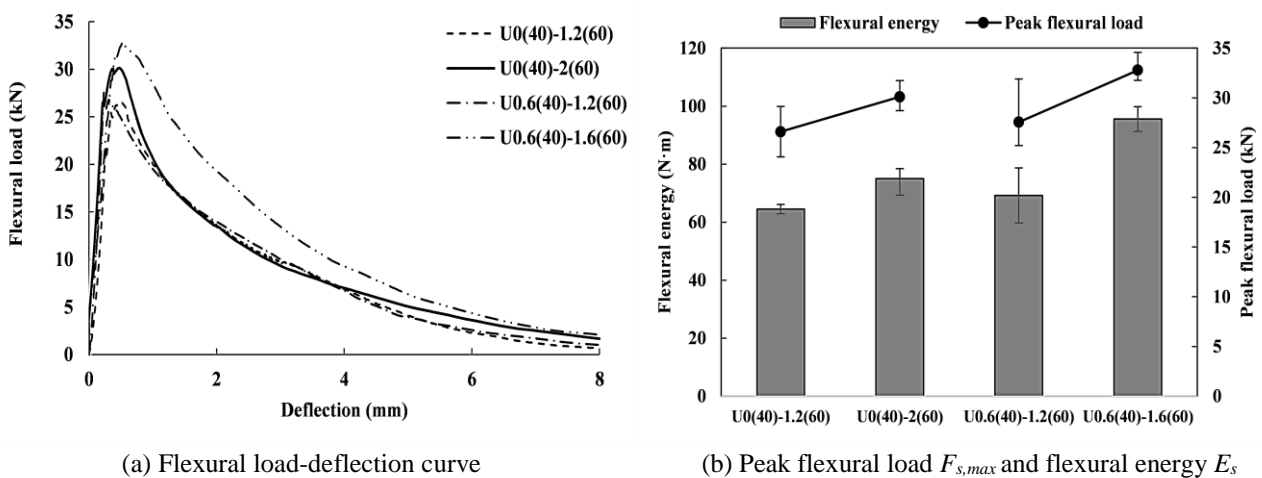


Fig. 4-16 Effects of fibers in the bottom layer

4.5 Conclusions

This chapter presents theoretical and experimental investigations on the flexural properties of the double-layered UHPFRC with coarse aggregates incorporated and fibers efficiently distributed. The cracking and debonding criteria of the double-layered beam are developed, and the critical load at the first stage of the failure process $F_{critical}$ is obtained. Based on the theoretical analysis, the double-layered beams are designed for the experimental section. Three-point bending tests are conducted to study the flexural performance of the double-layered UHPFRC. The effects of the layer thickness, fiber amount distribution over the layered structure, as well as the fiber amount of the individual layers are discussed, shedding light on the enhancement mechanisms of the layered structure. The following conclusions can be drawn:

- (1) The theoretical analysis reveals that when the top and bottom layers have comparable elastic moduli, e.g. layer elastic modulus ratio $\beta_E = 0.8 \sim 1$, increasing the layer thickness ratio β_h from 0.1 to 0.3 leads to a prominent increase of $F_{critical}$, whereas further thickening the bottom layer does not generate eminent improvement.
- (2) As confirmed by both the theoretical analysis and the experiment results, the first failure stage of the double-layered beam tends to end with bottom layer cracking rather than layer debonding in most cases (layer thickness ratio $\beta_h = 0.2 \sim 1.0$ with sufficient bond strength, e.g. $\sigma_b = \sigma_{t,1}$).
- (3) The peak flexural load $F_{s,max}$ and the flexural energy E_s are remarkably improved with the increase of the bottom layer thickness until $\beta_h = 0.6$ is reached. A jump of $F_{s,max}$ is observed at $\beta_h = 0.4$, which is associated with the transition from aggregate governed bridging to fiber governed bridging.
- (4) Fiber amount distribution over the layered structure affects $F_{s,max}$ and E_s , as well as the cracking process in the double-layered UHPFRC. Compared to the single-layered beam with an identical total fiber amount, the designed double-layered beam U0.6(40)-1.6(60) achieves a 24% higher $F_{s,max}$ and a 14% higher E_s . This also indicates the potential of utilizing layered beams containing less fiber to obtain superior flexural performances.
- (5) Fibers in the bottom layer contribute to the improvement of $F_{s,max}$ while the increase of E_s is affected by the fiber amount in both layers. Distributing a small amount of fibers in the top layer and a large amount of fibers in the bottom layer can result in the optimum flexural performance with both improved peak flexural load and energy.

Chapter 5

*Enhancing the low-velocity impact resistance of coarse-aggregated UHPFRC by an optimized layered-structure concept**



*This chapter is partially reproduced from: Y.Y.Y. Cao, G. Liu, P.P. Li, H.J.H. Brouwers, Q.L. Yu, Enhancing the low-velocity impact resistance of Ultra-High Performance Concrete by an optimized layered-structure concept (Submitted).

Abstract

Low-velocity impacts are common in the civil engineering field, and UHPFRC is a promising material to resist these impacts. This chapter investigates the dynamic resistance of coarse-aggregated layered UHPFRC under repeated low-velocity drop-weight impacts. The results show that the double-layered UHPFRC beam achieves a superior resistant capacity compared to its single-layered counterpart, e.g. an approximate 28% enhancement of the absorbed impact energy is obtained by the double-layered beam U0.6h-1.6h than that of the corresponding single-layered UHPFRC with an identical total fiber amount. Further, a new model to estimate the absorbed energy of the layered UHPFRC under multiple drop-weight impacts is developed and validated. By separating the contributions of the matrix and the fiber, the model confirms the important effects of the steel fibers on the beam absorbed impact energy, an improved fiber utilization efficiency of the double-layered beam is obtained using the model estimation. This study contributes to improving the dynamic performance of UHPFRC under low-velocity impacts, and promotes the potential utilization of layered UHPFRC composite in civil engineering.

5.1 Introduction

The resistance against low-velocity impact is of great significance for cementitious composites. Low-velocity (up to 10 m/s) impacts are common in the civil engineering field (Othman and Marzouk, 2016), typical examples of which include highway fences against vehicle collisions, bridge piers subjected to accidental ship impacts, and concrete constructions under falling rock impacts (Hrynyk and Vecchio, 2014). UHPFRC is a promising material with effective resistance against these impacts (Li and Yu, 2019; Yu, 2015). The dynamic performance of UHPFRC under low-velocity impacts should be clearly understood prior to the design and application of impact-resistant UHPFRC structures. Drop-weight experiment is widely performed to analyze the impact response of concrete. For example, Othman and Marzouk (Othman and Marzouk, 2018, 2017) experimentally and numerically investigated the behavior of straight-fiber-reinforced UHPFRC under repeated drop-weight impacts, and found that the damage level of UHPFRC is only 6 ~ 15% that of NC. Mao and Barnett (Mao and Barnett, 2017) evaluated the dynamic toughness of UHPFRC containing various amounts of straight steel fibers under drop-weight impacts; an increased resistance of the UHPFRC was observed with the increase of the fiber amount. Yoo et al. (Yoo et al., 2018, 2017a, 2015a) conducted a series of drop-weight tests on UHPFRC with straight or twisted fibers. Their studies presented that the long straight fibers provide a better resistance compared to the twisted steel fibers, and a higher reinforcement ratio leads to a lower deflection under the drop-weight impact. As can be noticed in the above studies, the drop-weight response of UHPFRC with hooked-end fibers is rarely studied, i.e. most investigated UHPFRC is reinforced with straight fibers. Therefore, there is a clear necessity to understand the dynamic responses of UHPFRC reinforced with not only straight fibers but also hooked-end fibers.

When a UHPFRC beam is under drop-weight impacts, the impact region is under compression while the distant region is in tension. This can be attributed to the wave phenomenon inside the beam: the compressive waves generated by the drop weight propagate from the top surface towards the bottom of the beam, then they are reflected to be tensile waves and invoke beam cracking. This stress distribution can also be confirmed by the damage pattern presented in previous studies (Guo et al., 2018; Willey, 2013). An example of the damage distribution in an UHPFRC sample under drop-weight impacts is illustrated in Fig. 5-1 (Guo et al., 2018), in which severe cracking on the bottom face is observed while the top face has limited damage (Guo et al., 2018; Willey, 2013). Furthermore, as mentioned in Chapter 4, steel fibers have a more prominent contribution to the tensile properties of UHPFRC (Meng and Khayat, 2017) than to the compressive ones (Abbas et al., 2015). Therefore, considering both the damage distribution and the fibers contributions, the steel fibers in the impact region of the UHPFRC beam, viz. the compression region, are not utilized as efficiently as those distributed in the distant region, viz. the tension region.

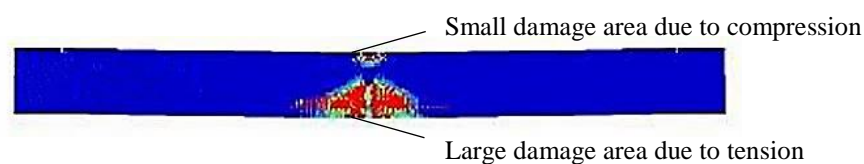


Fig. 5-1 Damage pattern of UHPFRC under impact loading (Guo et al., 2018)

The advantages of the layered UHPFRC under static loadings have been presented in Chapter 4, revealing that the deigned double-layered UHPFRC can achieve a 24% higher peak flexural load and a 14% higher flexural energy compared to the single-layered UHPFRC with an identical fiber amount. However, since the behavior of cementitious material is rate dependent and the dynamic increase factor is affected by the fiber amount (Cao and Yu, 2017; Tran and Kim, 2014), it is still questionable whether the advantageous static properties of the layered UHPFRC can be maintained at higher strain rates, e.g. under the low-velocity impacts. To the best of authors' knowledge, there is no published work presenting the impact performances of UHPFRC with a layered structure, and the influences of fiber geometry and fiber hybridization on the resistance of layered UHPFRC under drop-weight impacts have not been systematically addressed.

As a continuation of the static flexural investigation of the layered UHPFRC in Chapter 4, the study in this chapter investigates the impact resistance of the double-layered UHPFRC under low-velocity drop-weight impacts. Two types of steel fibers are utilized, namely the straight steel fiber and the hooked-end fiber. Drop-weight impacts are performed to investigate the dynamic responses, including the impact number, the reaction force, and the absorbed impact energy. Moreover, an analytical model for predicting the absorbed impact energy of the layered beam under repeated impacts is proposed. By separating the contributions of the matrix and the fiber, the model reveals the significant effects of the steel fiber on improving the absorbed impact energy, and the higher fiber efficiency of the layered beam is also confirmed. The results in this chapter contribute to a deeper understanding of the dynamic performance of UHPFRC against low-velocity impacts.

5.2 Experimental program

5.2.1 Materials and mix design

Table 5-1 gives the recipe of the UHPFRC matrix, which is based on that in Chapter 4 (Section 4.3.1). Two types of steel fibers are used in the present study: the Dramix OL 13/.20 straight steel fiber (SF) and the Dramix RC 80/30-BP hooked-end fiber (HF). The properties of the fibers can be found in Chapters 2 and 4.

Table 5-1 Recipes of the UHPC and the UHPFRC: CEM = Portland cement, LP = limestone powder, mS = micro-silica, S = sand, BA 2-5 = basalt aggregate with sizes of 2-5 mm, BA 5-8 = basalt aggregate with sizes of 5-8 mm, W = water, SP = superplasticizer, SF = straight steel fiber, HF = hooked-end steel fiber.

Materials	CEM (kg/m ³)	mS (kg/m ³)	LP (kg/m ³)	S (kg/m ³)	BA 2-5 (kg/m ³)	BA 5-8 (kg/m ³)	W (kg/m ³)	SP (kg/m ³)	SF (%)	HF (%)
									0.6	-
								7	0.3	0.3
									-	0.6
									1.2	-
Quantity	588	39.2	156.8	839.9	413.2	232.3	157	9	0.6	0.6
									0.24	0.96
									-	1.2
									1.6	-
								14	0.8	0.8
									-	1.6

5.2.2 UHPFRC composite beam

The tested UHPFRC beams are listed in Table 5-2, including both the single- and double-layered beams. The dimensions of the beams are $100 \times 100 \times 500 \text{ mm}^3$. For the double-layered UHPFRC, the thicknesses of the top and the bottom layers are 40 mm and 60 mm, respectively, which are determined based on the optimum design of the double-layered UHPFRC beam in Chapter 4. The identifications in Table 5-2 are composed of 1 or 2 phrases divided by a dash, which represents the single- or double-layered UHPFRC, respectively. The letters *s* and *h* present SF and HF, respectively, and the numbers before them are the corresponding fiber volume fractions in that layer. For example, U0.3*s*0.3*h*-0.8*s*0.8*h* is a double-layered UHPFRC beam with 0.3% SF and 0.3% HF in the top layer, and 0.8% SF and 0.8% HF in the bottom layer.

Table 5-2 Single- and double-layered UHPFRC: in the identification a dash is used to divide the layers; the numbers before *s* and *h* are the volume fractions of SF and HF, respectively.

Identification	Layer thickness (mm)		Fiber volume fraction (%)				Equivalent fiber fraction (%)		Note
	Top layer	Bottom layer	Top layer		Bottom layer		SF	HF	
			SF	HF	SF	HF			
U1.2 <i>s</i>	100	-	1.2	0	-	-	1.2	0	Single-layered beam
U0.6 <i>s</i> 0.6 <i>h</i>			0.6	0.6			0.6	0.6	
U0.24 <i>s</i> 0.96 <i>h</i>			0.24	0.96			0.24	0.96	
U1.2 <i>h</i>			0	1.2			0	1.2	
U0.6 <i>s</i> -1.6 <i>s</i>	40	60	0.6	0	1.6	0	1.2	0	Double-layered beam
U0.3 <i>s</i> 0.3 <i>h</i> -0.8 <i>s</i> 0.8 <i>h</i>			0.3	0.3	0.8	0.8	0.6	0.6	
U0.6 <i>s</i> -1.6 <i>h</i>			0.6	0	0	1.6	0.24	0.96	
U0.6 <i>h</i> -1.6 <i>h</i>			0	0.6	0	1.6	0	1.2	

5.2.3 Mixing, casting and testing methods

The concrete mixing, casting and curing methods are identical to those presented in Chapter 4 (Section 4.3.3). Tests are conducted at the age of 28 days. The compression, tension and splitting bond tests are performed with the same methods described in Chapter 4 (Section 4.3.4).

To investigate the resistance of the coarse-aggregated UHPFRC, repeated drop-weight impacts are performed with a specially designed device illustrated in Fig. 5-2. A metal ball of 7.26 kg is used as the drop weight, and it falls from a constant height of 2.5 m into a steel bucket connected with a steel roller on top of the beam. The drop height is such designed that the number of impacts would be less than 10. Hence, the beam failure would be due to the dynamic impacts, instead of material fatigue under repeated loads. Electromagnet is used to release the metal ball. Both the left and right sides of the tested beam are clamped between two steel rollers connected with springs, which prevents the uplift of the beam during rebounding after the initial impact. Free steel rollers allowing rotation are used under the beam, which minimizes the horizontal restraint (Hrynyk and Vecchio, 2014; Othman and Marzouk, 2018; Soleimani and Banthia, 2014). The span length between these two underneath support rollers is 400 mm, being the same as that in the previous static flexural test in Chapter 4. Multiple drops are required to break the UHPFRC beam to its complete fracture. After each impact, the damage on the front surface of the beam is captured using a fixed photographic setup to record the crack development. Three beams are tested for each group.

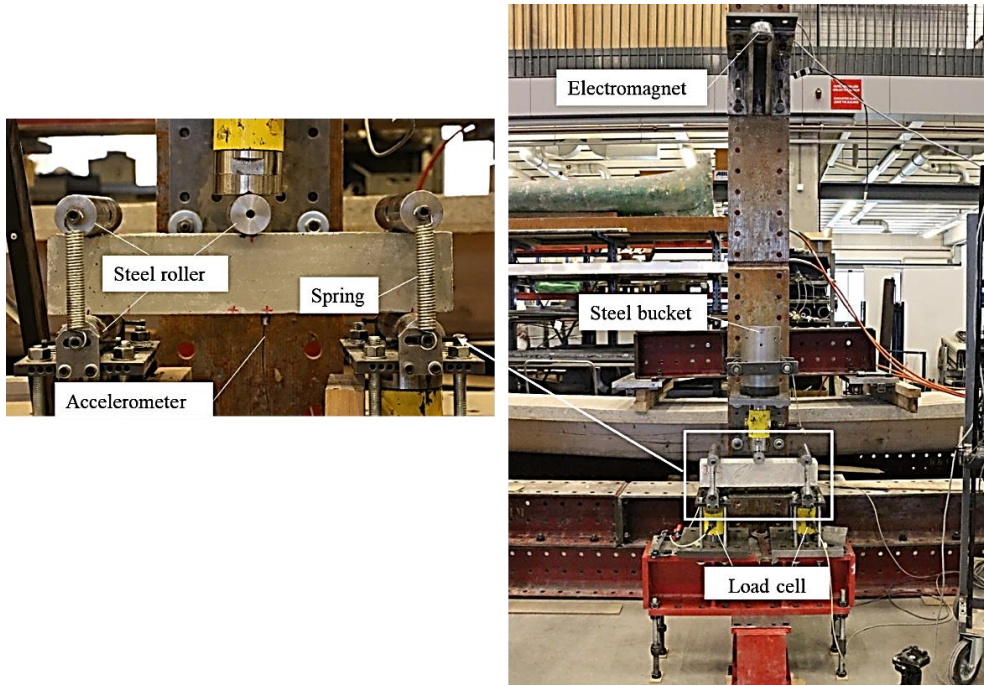


Fig. 5-2 Setup of the drop-weight test

Due to the inertial effect, the impact load generated by the drop weight is not the true dynamic flexural load acting on the beam, i.e. a large portion of the impact load is utilized to accelerate the beam from its position of rest to the direction opposite the acceleration (Yoo et al., 2016; Yoo and Banthia, 2017a). In order to obtain the pure dynamic flexural load excluding the inertial portion, two load cells are instrumented under the support steel rollers and the summation of these two reaction loads is considered as the true dynamic flexural load (Habel and Gauvreau, 2008; Soleimani and Banthia, 2014; Yoo et al., 2016). An AP 37 accelerometer, with a resonant frequency larger than 45 kHz and a maximum shock limit of 15000g (where g is the gravitational acceleration), is attached to the beam bottom surface at a point close to the center of the beam using a very high-strength epoxy (Yoo et al., 2016; Yoo and Banthia, 2017a). The measured acceleration is then double integrated to determine the mid-point deflection of the beam (M. Wu et al., 2015; Yoo and Banthia, 2017a). The load and acceleration data are recorded with a frequency of 100 kHz through a dynamic data measurement software NI LabVIEW.

5.3 Static mechanical properties

The 28-day compressive strength $\sigma_{c,s}$ and splitting tensile strength $\sigma_{t,s}$ of the individual UHPFRC layers are given in Table 5-3. In general, $\sigma_{t,s}$ increases with the increasing fiber amount whereas $\sigma_{c,s}$ is not significantly affected. Take the SF-reinforced UHPFRC as an example, the $\sigma_{t,s}$ of U1.2s and U1.6s are about 29% and 38% higher than that of U0.6s, while the $\sigma_{c,s}$ of these three groups are within a narrow range of 145.3 ~ 146.7 MPa. Moreover, UHPFRC with hybrid fibers tends to have a higher $\sigma_{t,s}$ in comparison to its single-fiber-reinforced counterpart containing the same amount of fibers. For instance, the $\sigma_{t,s}$ of the hybrid-fiber-reinforced group U0.3s0.3h is about 15% and 20% higher than that of groups U0.6s and U0.6h, respectively.

Table 5-3 28-day compressive and tensile strengths of the UHPFRC mixtures in individual layers

Identification	Compressive strength $\sigma_{c,s}$ (MPa)		Tensile strength $\sigma_{t,s}$ (MPa)	
	Avg.	St. dev.	Avg.	St. dev.
U0.6s	146.7	1.5	11.7	0.8
U0.3s0.3h	147.6	2.6	13.5	1.6
U0.6h	147.8	3.3	11.2	1.5
U1.2s	145.3	4.0	15.1	1.0
U0.6s0.6h	149.6	1.8	16.2	2.0
U0.24s0.96h	153.6	2.2	17.7	1.6
U1.2h	147.7	1.2	15.7	2.3
U1.6s	145.8	5.0	16.2	1.3
U0.8s0.8h	142.0	4.1	16.5	1.2
U1.6h	141.2	3.8	16.3	2.0

Similar to results in Chapter 4 (Section 4.4.1), cohesive failure occurred during the bond splitting tests, indicating a sufficient bond between the layers. The minimum bond strength is obtained by the interface of U0.3s0.3h-0.8s0.8h. The value is about 6.4 MPa, which is on the same order as the tensile strength of the plain UHPC matrix. The strong bond is also confirmed by the fact that no layer debonding occurred during the drop-weight tests (see the final failure pattern of a double-layered UHPFRC in Fig. 5-3).

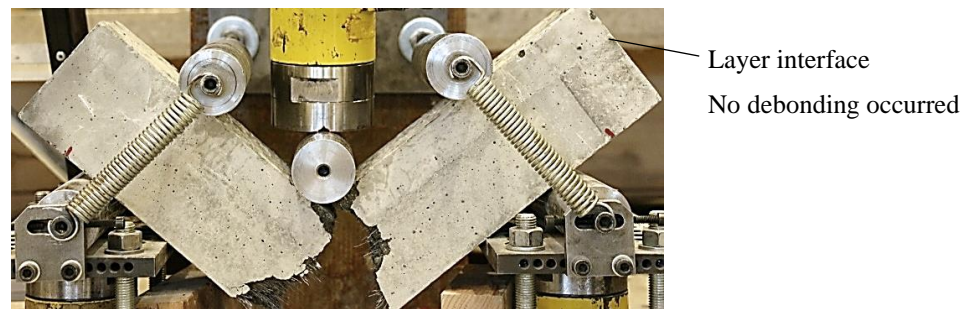


Fig. 5-3 Failure pattern of a layered beam after the drop-weight test

5.4 Drop-weight impact performances

5.4.1 Reaction force and deflection

Multiple drops are required to completely break the UHPFRC beams. Fig. 5-4 illustrates the typical reaction force-time history and mid-span deflection-time history of a tested UHPFRC beam U1.2h at its first impact. $R1$ and $R2$ are the reaction loads measured by the two load cells under the beam and their summation R is taken as the reaction force (Soleimani and Banthia, 2014; Yoo et al., 2016). δ is the deflection of the beam at its mid-span by integrating the measured acceleration twice with respect to time (Yoo et al., 2016). Similar deflection curves have been found in previous studies about the drop-weight tests on single-layered concrete (M. Wu et al., 2015; Yoo et al., 2015b). Generally, the reaction force-time curve can be divided into three stages (Ranade et al., 2017; Yoo and Banthia, 2017a):

(1) At the initial impulse stage S1, the drop weight contacts with the bottom of the steel bucket and invokes the impact force on the tested beam, which is reflected by R . The contact time is so short that the peak of the reaction force is immediately reached and then it decreases sharply. This contacting time increases with the impact number as the beam top surface becomes rougher after impact.

(2) A beam deformation stage S2 is followed after the initial impulse stage, during which the beam is sufficiently deformed and plastic deformation appears (Ranade et al., 2017). The micro-cracks initiating at stage S1 become wider while the steel fibers in the UHPFRC tend to arrest them. The reaction force at this stage is relatively low compared to the initial impulse as the beam and the drop-weight system (the metal ball, steel bucket and the top steel roller) oscillate together.

(3) The rebound stage is defined as S3. The rebound of the metal ball causes obvious oscillations of the reaction force, as shown in Fig. 5-4. These rebounds are dependent on strength and initial stiffness of the tested material, and they can be attributed to the released energy that is stored elastically in the beam (Dey et al., 2014). These rebound actions consume the kinetic energy of the impact ball, and rebounds stop until the energy is fully depleted.

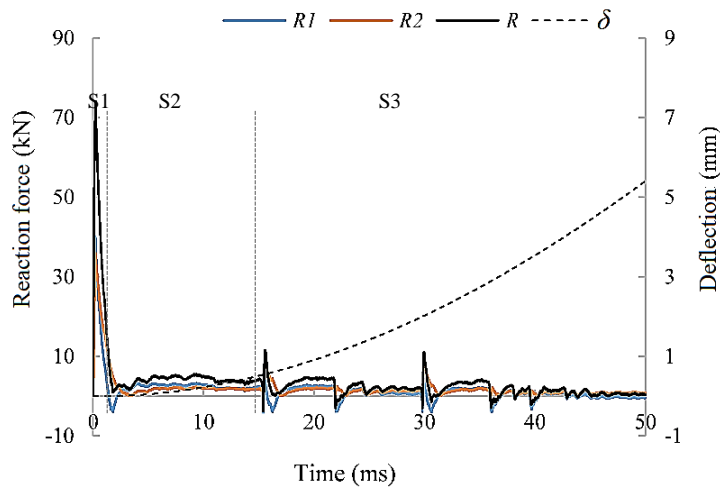


Fig. 5-4 Reaction force-time ($R-t$) and deflection-time ($\delta-t$) histories of U1.2h at the first impact

5.4.2 Performance of single-layered UHPFRC

The impact performances of the single-layered UHPFRC beams are analyzed in this section, and the influences of fiber geometry and hybridization are discussed. The solid lines in Fig. 5-5 present the peak reaction forces R_{peak} of the single-layered UHPFRC under each impact. As can be seen from the figure, the hybrid-fiber-reinforced UHPFRC beams tend to have higher peak reaction forces at the first impact $R_{peak,1}$ compared to their single-fiber-reinforced counterparts. For instance, $R_{peak,1}$ are approximately 81.1 kN and 79.7 kN for U0.6s0.6h and U0.24s0.96h, whereas they are 63.1 kN and 78.2 kN for U1.2s and U1.2h, respectively. This tendency is in accordance with the slightly higher compressive strength of the hybrid-fiber-reinforced samples (see Table 5-3), indicating that $R_{peak,1}$ may be dependent on the strength of the material. On the contrary, the peak reaction force at the last impact $R_{peak,n}$ is higher for the UHPFRC with a higher amount of HF. For example, $R_{peak,n}$ of U1.2s, U0.6s0.6h, U0.24s0.96h and U1.2h are approximately 11.4 kN, 21.0 kN, 22.7 kN and 24.5 kN, respectively.

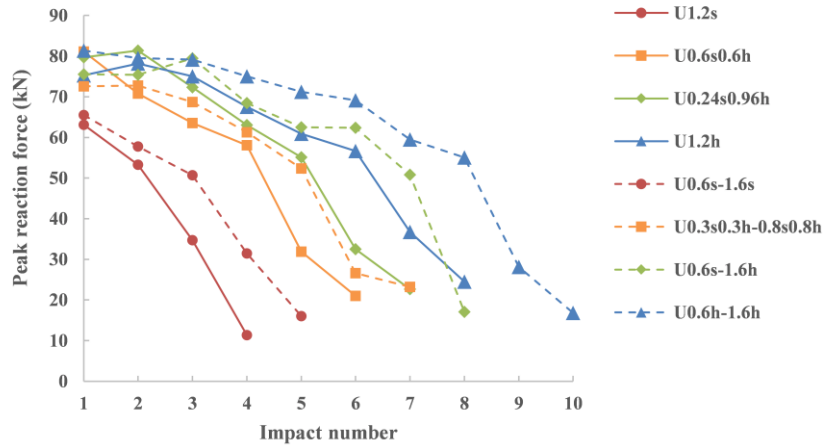


Fig. 5-5 Change of the peak reaction force R_{peak} with the impact number N

Fig. 5-6 plots the impact number N leading to the complete fracture of the tested beams and the corresponding absorbed impact energy E_a . The plotted values are the averaged results of the three tested beams in each group, together with the error bars indicating the minimum and maximum values. The averaged N is determined by the averaged data rounded off to the nearest whole number. For example, the impact numbers of the three beams in U1.2h are 8, 8 and 10, resulting in an averaged data of $(8+8+10)/3 = 8.67$, thus N is taken as 9 for this group. It is worth mentioning that the variations of N in most groups are very small, and the impact numbers are even the same for the three tested beams in some groups, e.g. U1.2s, U0.6s0.6h, and U0.24s0.96h (they hence have no error bars for N in Fig. 5-6).

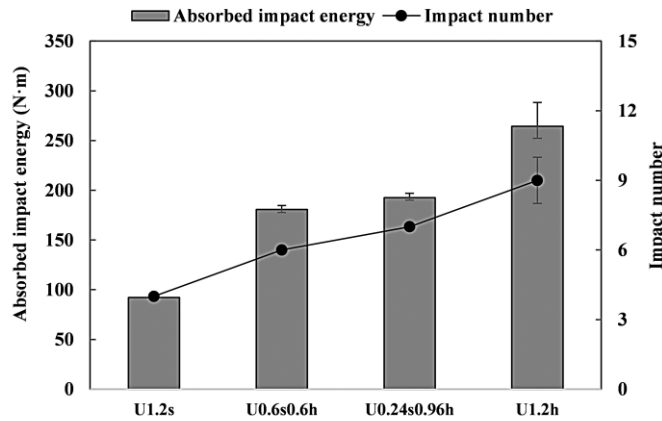


Fig. 5-6 Absorbed impact energy E_a and impact number N of single-layered UHPFRC

For each single impact, the impact energy E_i provided by the drop ball is partially absorbed by the beam E_{a0} , partially dissipated by the friction E_f during the impact event, and partially transferred to the test setup E_t , which remains in the form of elastic strains and vibrations (Dey et al., 2014; Yoo and Banthia, 2017a):

$$E_i = mgh = E_{a0} + E_f + E_t \quad (5-1)$$

The beam absorbed energy at each impact E_{a0} can be determined by the reaction load R and the beam deflection δ (Banthia et al., 1989):

$$E_{a0} = \int R_{(t)} \delta_{(t)} dt \quad (5-2)$$

And the total absorbed impact energy after multiple impacts E_a can be calculated by the sum up of E_{a0} under each impact (Yu, 2015):

$$E_a = \sum_1^{N-1} E_{a0} \quad (5-3)$$

where E_i is the input impact energy, E_f is the friction energy, and E_t is the energy transferred to the test setup. E_{a0} and E_a are the absorbed impact energy of the beam after an individual impact and multiple impacts, respectively. $R_{(t)}$ and $\delta_{(t)}$ are the reaction force and the beam deflection at time t . It should be noted that for all the tested beams, E_{a0} of their last impacts are not considered because the beams break at the last impacts and their vertical movements are too large to be measured.

As shown in Fig. 5-6, with the increase of the HF amount, both N and E_a increase. To specify, U1.2s can withstand the least impacts (4 impacts) while U1.2h achieves the largest N of 9 impacts. Further, E_a of U1.2h is more than 2.6 times higher than that of U1.2s. Additionally, U0.24s0.96h and U0.6s0.6h can withstand 2 and 3 less impacts in comparison to U1.2h, regardless of the slightly higher compressive and tensile strengths of these hybrid-fiber-reinforced UHPFRC (see Table 5-3). The E_a of U0.24s0.96h and U0.6s0.6h are approximately 27% and 32% smaller than that of U1.2h, respectively. This finding depicts that the material strength is not the dominant factor determining the impact resistance of UHPFRC. Instead, the fiber pullout response, which is associated with fiber geometry, contributes more. As shown in Fig. 5-7, fibers are observed to be pulled out from the UHPFRC matrix under the impact, leading to the significant effects of the fiber pullout performance on the impact resistance of UHPFRC. This is also confirmed by the predictive model in Section 5.5. Compared to the short SF, the HF has a longer length and its hooks can generate a mechanical anchorage during the straightening process under the impacts (see Fig. 5-7b). As a result of both the higher frictional bond force and the additional mechanical anchorage, more energy is required to pull the HF out of the UHPC matrix, which therefore leads to a higher E_a of the HF-reinforced UHPFRC.

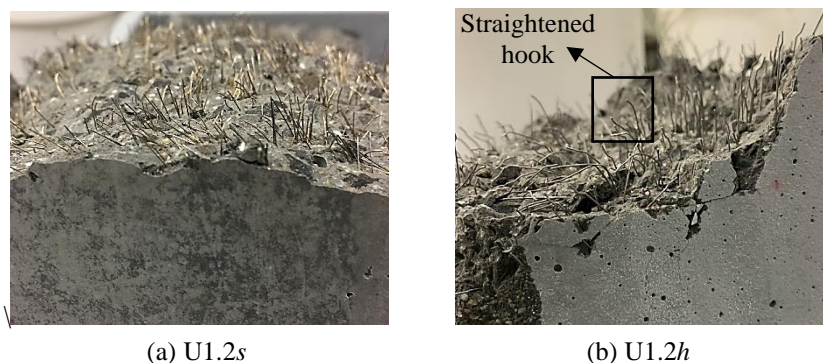


Fig. 5-7 Failure surface with fibers pulled-out after impact test

The crack development in U1.2s and U1.2h under the repeated drop-weight impacts are shown in Figs. 5-8 and 5-9, respectively. Under the first impact, visible cracks can be observed at the bottom of U1.2s, and partial concrete scabbing is observed at the top surface of the beam. Under the second and third impacts, the scabbing area has insignificant expansion; on the other hand, the dominant crack

develops wider and longer. Fibers play an important role in controlling the crack development by their bridging actions. Under the fourth impact, U1.2s breaks completely and it is separated into two pieces with fibers pulled out from the matrix at the crack surface. No single broken fiber is seen (Fig. 5-7a).

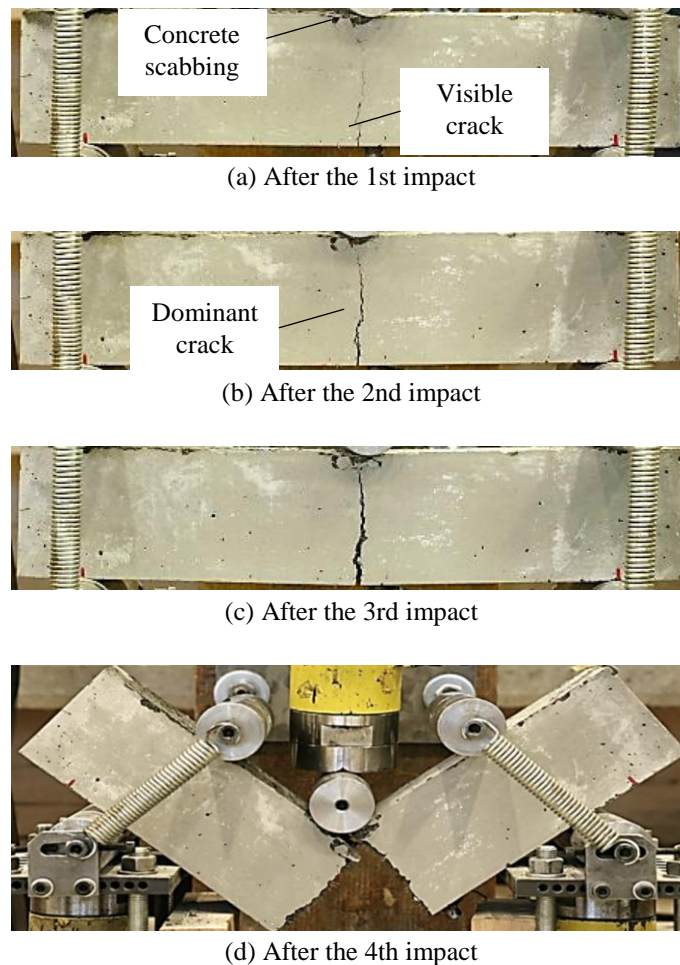


Fig. 5-8 Failure pattern of U1.2s under drop-weight impacts (failed after 4 impacts)

Compared to U1.2s, more micro cracks occur in the HF-reinforced beam U1.2h. Additionally, the dominant crack in U1.2h appears later with a zigzag path and a larger final width before the complete failure of the beam. As shown in Fig. 5-9, U1.2h has almost invisible cracking after the first impact whereas concrete scabbing is observed at the beam top surface. More hairline cracks appear at the bottom of the beam under the second impact and they develop wider with the increasing impact numbers. The scabbing area is significantly enhanced under the second impact, after which the difference becomes limited. A dominant crack is observed in U1.2h after the fifth impact and it has more branches in comparison to that in U1.2s. This dominant crack is also more torturous and wider (see Fig. 5-9d) due to the special geometry of the HF, which further contributes to the higher absorbed impact energy of U1.2h. The beam finally breaks into two pieces after the eighth impact with a failure pattern similar to that of U1.2s.

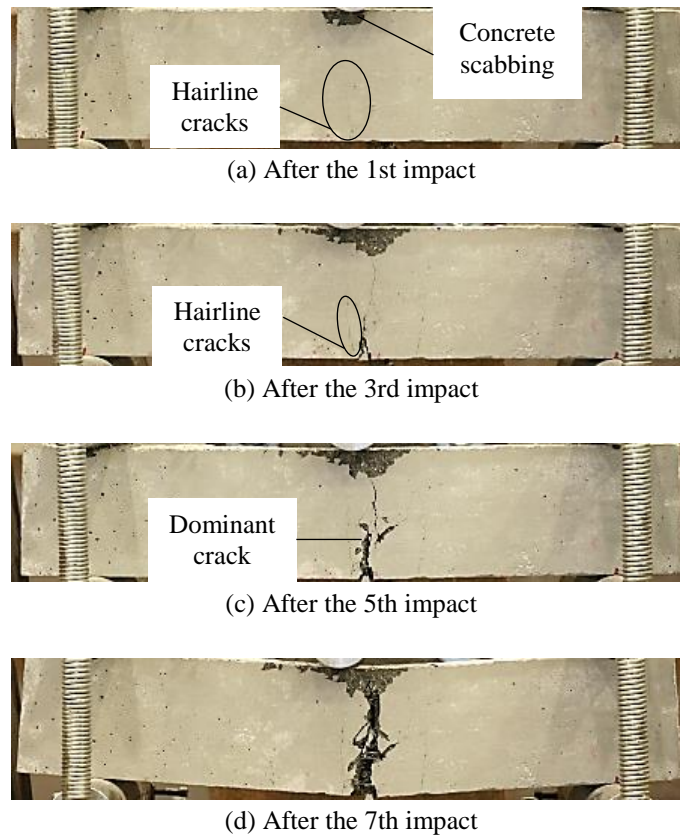


Fig. 5-9 Failure pattern of U1.2h under drop-weight impacts (failed after 8 impacts)

5.4.3 Performance of double-layered UHPFRC

The impact responses of the double-layered UHPFRC beams are analyzed in this section to exhibit the improved dynamic performance generated by optimum distributing the fibers in the layered structure. Comparing the solid lines with the dash lines in Fig. 5-5 shows the different peak reaction forces R_{peak} of the single- and the double-layered UHPFRC. Note that the equivalent fiber volumes of the double-layered beams are identical to those of the corresponding single-layered beams (see Table 5-2). As shown by Fig. 5-5, U0.6s-1.6s and U0.6h-1.6h have similar $R_{\text{peak},1}$ to their respective single-layered counterparts U1.2s and U1.2h. In contrast, the $R_{\text{peak},1}$ of U0.3s0.3h-0.8s0.8h and U0.6s-1.6h are about 11% and 5% smaller than the corresponding $R_{\text{peak},1}$ of U0.6s0.6h and U0.24s0.96h, respectively. Furthermore, Fig. 5-5 depicts that the double-layered UHPFRC, in general, have improved R_{peak} than the single-layered ones under the subsequent impacts. The R_{peak} of the double-layered beams also decreases with a lower rate, as indicated by the slopes of the dash curves in Fig. 5-5. The higher R_{peak} and its slower decline with the increasing impact numbers present the advanced impact resistance of the double-layered UHPFRC.

The N and E_a of the double-layered UHPFRC beams are analyzed in Fig. 5-10. Similar to the trend shown in Fig. 5-6, N and E_a increase with the increase of the HF amount in the double-layered UHPFRC. To be more specific, U0.6s-1.6s breaks under 4 impacts, while U0.3s0.3h-0.8s0.8h, U0.6s-1.6h and U0.6h-1.6h can withstand 2, 4 and 6 more impacts than U0.6s-1.6s, respectively. Furthermore, a prominent enhancement of E_a is obtained with the increasing HF amount. For instance, the E_a of U0.3s0.3h-0.8s0.8h, U0.6s-1.6h and U0.6h-1.6h are about 1.6, 2.2 and 2.9 times higher than that of U0.6s-1.6s.

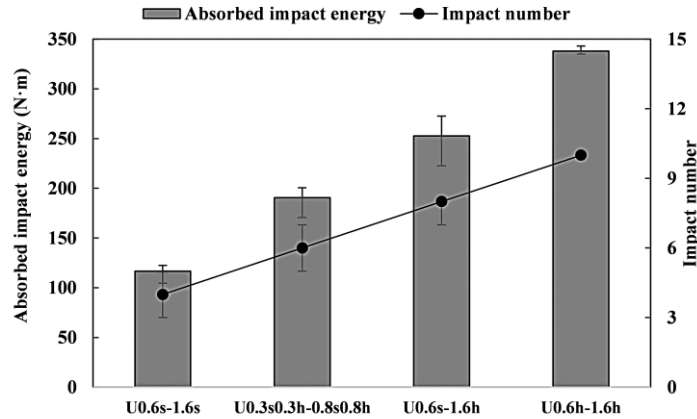


Fig. 5-10 Absorbed impact energy E_a and impact number N of double-layered UHPFRC

In comparing Fig. 5-6 with Fig. 5-10, the influences of the fiber amount distribution on the impact responses of the double-layered UHPFRC beams can be revealed. It is interesting to observe that the double-layered structure has limited influences on the N of U0.6s-1.6s and U0.3s0.3h-0.8s0.8h, but more obvious effects on their E_a . The N of these two beams have no increase compared to the corresponding single-layered beams U1.2s and U0.6s0.6h. This may be attributed to the fact that the impact number in this study is designed to be below 10 to prevent fatigue damage, making it too limited to show the difference between the double-layered beam and the single-layered one. Nevertheless, the E_a of U0.6s-1.6s and U0.3s0.3h-0.8s0.8h have 15% and 6% enhancements, respectively, showing the increased energy dissipation capacity of the double-layered UHPFRC in comparison with the single-layered ones. On the other hand, U0.6s-1.6h and U0.6h-1.6h achieve more remarkably improved impact performances. They can withstand more impacts than their single-layered counterparts, and the E_a of U0.6s-1.6h and U0.6h-1.6h are approximately 31% and 28% higher than those of U0.24s0.96h and U1.2h, respectively.

It can be concluded from the above observations that in comparison to the SF-reinforced UHPFRC, fiber amount distribution over the double-layered structure has more significant effects on the HF-reinforced UHPFRC. For instance, the difference of E_a between U0.6h-1.6h and U1.2h is about two times larger than that between U0.6s-1.6s and U1.2s. In addition, for the UHPFRC with both SF and HF, incorporating HF in the bottom layer and SF in the top layer, viz. U0.6s-1.6h, is a preferable choice. This combination can lead to a more obviously increased energy absorption capacity compared to the double-layered beam with hybrid fibers in both layers, viz. U0.3s0.3h-0.8s0.8h.

Figs. 5-11 and 12 present the failure patterns of U0.6s-1.6s and U0.6h-1.6h under the repeated drop-weight impacts, respectively. It is noteworthy that the layer interfaces in the tested beams are rather invisible due to the excellent bond between the layers. As shown in Fig. 5-11, cracking starts from the bottom of U0.6s-1.6s after the first impact. Concrete scabbing from the top of the beam is observed with a larger damage area in comparison to that in U1.2s. A new branch of crack appears on the beam after the second impact, which propagates to connect the original dominant crack and the layer interface (see Fig. 5-11b). Similar to the failure process of U1.2s, the width of the dominant crack increases with the number of impacts; however, the crack path in U0.6s-1.6s is more complex compared to the almost straight cracking in U1.2s. Although both U1.2s and U0.6s-1.6s fail after 4 impacts, a larger deflection is observed in U0.6s-1.6s (see Figs. 5-8c and 5-11c). These twisted

cracking due to the crack branch and the larger beam deflection under the impact contribute to the enhanced energy absorption capacity of U0.6s-1.6s than U1.2s.

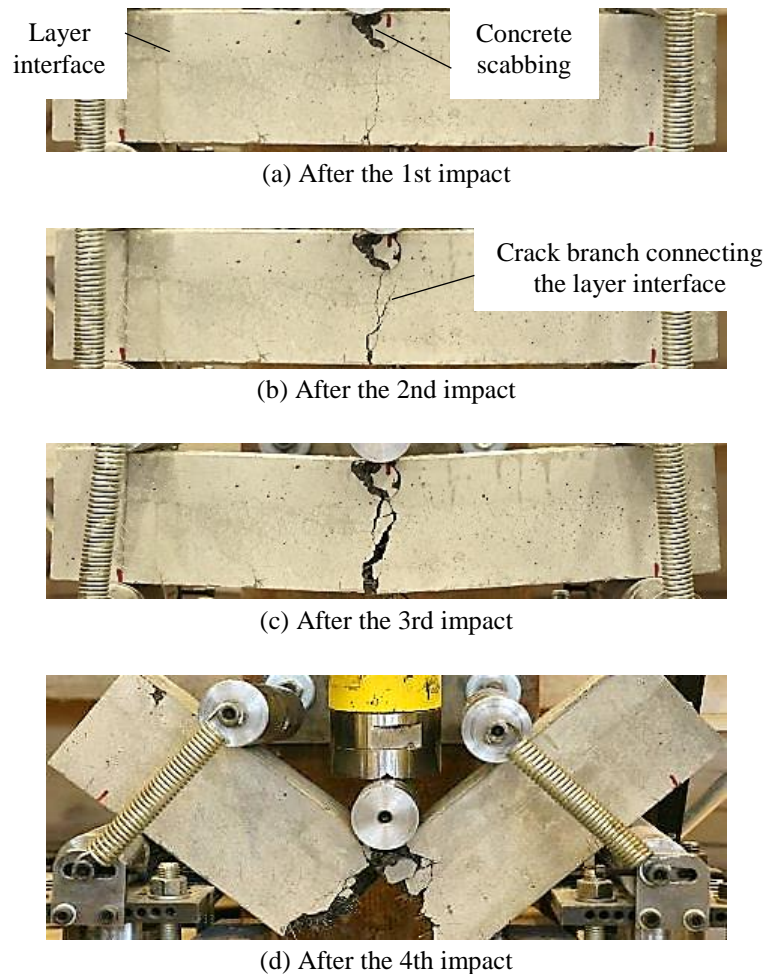


Fig. 5-11 Failure pattern of U0.6s-1.6s under drop-weight impacts (failed after 4 impacts)

U0.6h-1.6h fails completely after 10 impacts. Slight concrete scabbing occur after the first impact, as shown in Fig. 5-12a. Hairline cracking can be observed at the bottom of the beam after the third impact. The larger amount of HF in the bottom layer of U0.6s-1.6s redistributes the stress and delays the initiation of cracks. Consequently, the cracks in the double-layered beam are less obvious compared to those in the single-layered beam U1.2h after the same number of impacts. Under the fourth and fifth impacts, the initial crack widens and an almost invisible crack branch initiates from the layer interface, which can be observed with a careful check. The dominant crack is formed after 6 impacts, connecting the top and bottom surfaces of the double-layered beam. This dominant crack in U0.6h-1.6h is narrower compared to that in U1.2h because of the better crack control capacity of the double-layered beam. HFs are more concentrated at the bottom layer of U0.6h-1.6h, and they efficiently bridge the lower part of the dominant crack and inhibit the further opening of the crack at the upper part (Cao et al., 2019a). Since the width of the crack at the upper part is much smaller compared to the lower part, less fiber is required in the top layer to effectively control the crack development. As a consequence, the double-layered beam with fibers more reasonably distributed in the two layers achieves an advantageous energy absorption capacity.

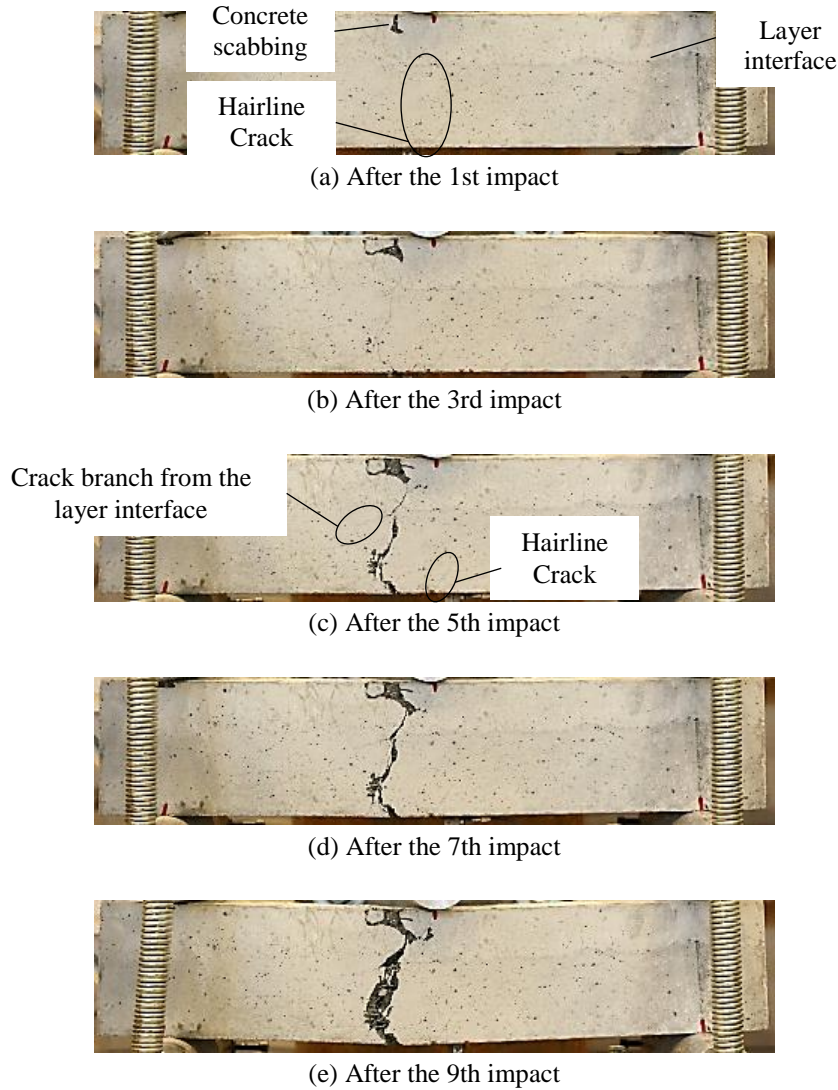


Fig. 5-12 Failure pattern of U0.6h-1.6h under drop-weight impacts (failed after 10 impacts)

5.5 Prediction of absorbed impact energy based on fiber pullout

5.5.1 Predicting the absorbed impact energy

As observed in Fig. 5-7, steel fibers are pulled out from the UHPFRC matrix during the drop-weight tests, indicating that the impact resistant capacity of the UHPFRC beam is associated closely with the dynamic fiber pullout performance. Based on a previous model characterizing the impact energy of a single-layered concrete subjected to one impact (Xu et al., 2010), a new model is developed for the double-layered UHPFRC against multiple impacts. Furthermore, the rate effects on the UHPFRC matrix and the fiber pullout responses are taken into consideration by employing the DIFs in the proposed model.

Applying the composite theory, the absorbed impact energy of the UHPFRC beam with n layers ($n = 1$ or 2 , see Fig. 5-13) can be divided into two parts: the part absorbed by the UHPC matrix (without fibers) and the part consumed by the dynamic fiber pullout (Wu et al., 2018; Xu et al., 2010; Yu, 2015):

$$E_a = \sum_{i=1}^n (E_{m,d,i} V_{m,i} + E_{f,d,i} V_{f,i}) \quad (5-4)$$

where $E_{m,d,i}$ is the impact energy absorbed by the UHPC matrix in the i^{th} layer. $E_{f,d,i}$ is the impact energy consumed by fiber pullout in the i^{th} layer. $V_{m,i}$ and $V_{f,i}$ are the volume fractions of the matrix and the fiber in the i^{th} layer, and $V_{m,i} + V_{f,i} = 1$.

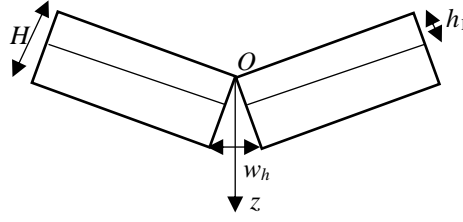


Fig. 5-13 Illustration of the beam

Taking into account the pullout energy of each single fiber, as well as the cracking characterization on the beam under multiple impacts, Eq. 5-4 can be expressed as:

$$E_a = \sum_{i=1}^n \left(E_{m,d,i} V_{m,i} + \eta_{\theta} \int_{h_{i-1}}^{h_i} \frac{\pi d_f}{2} \tau_{eq,d} w_{(z)}^2 N_{(z),i} b dz \right) \quad (5-5)$$

where η_{θ} is the fiber orientation coefficient, and it equals to 1/3 for a random 3D fiber distribution (Kang and Kim, 2011). h_i is the thickness of the i^{th} layer with $\sum_1^n h_i = H$. In the case of a single-layered beam, $h_i = H$, $h_{i-1} = 0$. b and h are the width and height of the beam, respectively. d_f is the fiber diameter. $\tau_{eq,d}$ is the equivalent bond strength under dynamic fiber pullout. $N_{(z),i}$ is the number of the fibers in an unit area on the crack plane at the depth of z . The fiber slip $w(z)$ is considered as the crack width in the UHPFRC beam before its complete failure, and it is assumed to be proportional to the depth z :

$$w_{(z)} = w_h z/H \quad \text{for } w(z) < l_f/2 \quad (5-6a)$$

$$w_{(z)} = l_f/2 \quad \text{for } w(z) \geq l_f/2 \quad (5-6b)$$

where w_h is the crack width at the beam bottom before the complete failure of the beam (after the $N-1$ impact), and l_f is the length of the fiber.

The expressions of $N_{(z),i}$ is given below (Xu et al., 2010):

$$N_{(z),i} = \frac{4V_{f,i}}{\pi d_f^2} \quad (5-7)$$

Substituting Eq. 5-7 into Eq. 5-5 yields:

$$E_a = \sum_{i=1}^n \left(E_{m,d,i} V_{m,i} + \eta_{\theta} \tau_{eq,d} \frac{2bV_{f,i}}{d_f} \int_{h_{i-1}}^{h_i} w_{(z)}^2 dz \right) \quad (5-8)$$

Then the DIF is adopted to consider the relationship between the dynamic and the static responses, and Eq. 5-8 becomes:

$$E_a = \sum_{i=1}^n \left(\text{DIF}_m E_{m,s,i} V_{m,i} + \eta_\theta \text{DIF}_{f,i} \tau_{eq,s} \frac{2bV_{f,i}}{d_f} \int_{h_{i-1}}^{h_i} w^2(z) dz \right) \quad (5-9)$$

where $E_{m,s,i}$ is the absorbed energy of the UHPC matrix in the i^{th} layer under static bending. $\tau_{eq,s}$ is the equivalent bond strength under static fiber pullout.

DIF_m presents the energy enhancement of the UHPC matrix, and the following expression (Pyo et al., 2015) is used:

$$\text{DIF}_m = 0.0967 \ln(\dot{\epsilon}_d) + 1.9012 \quad (5-10)$$

$\text{DIF}_{f,i}$ presents the pullout force increase of the single steel fiber in the i^{th} layer. For UHPFRC reinforced with hooked-end steel fibers, the $\text{DIF}_{f,i}$ from the dynamic fiber pullout study in Chapter 3 can be adopted, i.e. Eq. 3-8 from Chapter 3 with γ_t substituted is used as the $\text{DIF}_{f,i}$ in this chapter:

$$\text{DIF}_{f,i} = (\dot{\epsilon}_d)^{\frac{e^{0.08l_f}}{5+0.6\sigma_{c,s,i}}} \quad (5-11)$$

where the fiber length l_f is in mm, and $\sigma_{c,s,i}$ is the compressive strength of the UHPFRC in the i^{th} layer in MPa.

The strain rate $\dot{\epsilon}_d$ is calculated by (Yoo et al., 2018):

$$\dot{\epsilon}_d = \frac{6hV_b}{L_s^2} \quad (5-12)$$

where V_b is the beam velocity and L_s is the span length.

5.5.2 Model validation and discussion

U1.2h and U0.6h-1.6h are used to validate the proposed predictive model. The beam velocity V_b in Eq. 5-12 is obtained by integrating the acceleration data with time, and obviously, it is not constant during the drop-weight process (Yoo et al., 2018). V_b corresponding to R_{peak} is picked, and the averaged value of each impact is taken to calculate the equivalent strain rate and the corresponding DIFs. The input parameters are given in Table 5-4. The absorbed energies of the plain UHPC matrices are obtained from Chapter 4. Moreover, $\tau_{eq,s}$ is adopted according to the pullout tests in Chapter 3, and the same value is used for the two beams due to the lack of experimental data presenting the relationship between the equivalent bond stress and the matrix strength.

Table 5-4 Model inputs: $\dot{\epsilon}_d$ is the strain rate; DIF_m and $\text{DIF}_{f,i}$ are the dynamic increase factors of the matrix toughness and the fiber friction shear stress in the i^{th} layer; $E_{m,s,i}$ is the absorbed energy of the UHPC matrix in the i^{th} layer under static bending; $\tau_{eq,s}$ is the equivalent bond strength under static pullout; w_h is the crack width at the beam bottom.

	$\dot{\epsilon}_d$ (s ⁻¹)	DIF_m	$\text{DIF}_{f,1}$	$\text{DIF}_{f,2}$	$E_{m,s,1}$ (N·m)	$E_{m,s,2}$ (N·m)	$\tau_{eq,s}$ (MPa)	w_h (mm)
U1.2h	60.72	2.30	1.62	-	2.37	-	10.1	16.04
U0.6h-1.6h	66.11	2.31	1.64	1.67	0.95	1.42	10.1	15.29

Substituting these parameters into Eq. 5-9 gives the calculated absorbed impact energies of the two beams. Comparing the calculated absorbed impact energy with the experimental one (see Table 5-5) shows that the proposed model can generate satisfying predictions for the single- and the double-layered UHPFRC beams. To specify, the calculated E_a of U1.2h and U0.6h-1.6h are about 12.1% and 6.4% higher than the experimental results.

Table 5-5 Comparison between proposed model and experimental data without considering the group effect: $E_{m,d,1}V_{m,1}$ is the part of the impact energy absorbed by the UHPC matrix in the n^{th} layer under impact; $E_{f,d,i}V_{f,i}$ is the corresponding part consumed by the dynamic fiber pullout in the i^{th} layer; E_a is the absorbed impact energy of the UHPFRC beam.

	$E_{m,d,1}V_{m,1}$ (N·m)	$E_{m,d,2}V_{m,2}$ (N·m)	$E_{f,d,1}V_{f,1}$ (N·m)	$E_{f,d,2}V_{f,2}$ (N·m)	E_a (N·m)		Error (%)
					Calculation by Eq. 5-9	Experiment	
U1.2h	5.37	-	292.16	-	297.53	265.33	12.1
U0.6h-1.6h	2.17	3.22	8.68	345.69	359.76	337.98	6.4

One error source may be the different pullout energies obtained from a single-fiber pullout test and from the pullout process in an UHPFRC with multiple fibers. This difference is associated with the fiber group effect, which reduces fibers' efficiency and matrix' capacity to resist the fiber-matrix bond under the pullout load, as analyzed in Chapter 2. Consequently, the pullout energy consumed by an individual fiber in the UHPFRC should be smaller than that obtained from the single-fiber pullout test; and the proposed model hence overestimates the experimental E_a . To account for the fiber group effect, a corresponding coefficient η_g can be introduced in the model, and Eq. 5-9 further turns to:

$$E_a = \sum_{i=1}^n \left(\text{DIF}_m E_{m,s,i} V_{m,i} + \eta_\theta \eta_g \text{DIF}_{f,i} \tau_{eq,s} \frac{2bV_{f,i}}{d_f} \int_{h_{i-1}}^{h_i} w^2(z) dz \right) \quad (5-13)$$

$\eta_g = 0.9$ is determined for the utilized hooked-end steel fiber by fitting the experimental data in this study, and the corresponding error for U1.2h and U0.6h-1.6h updates to 1.1% and -4.0%, respectively (see Table 5-6).

Table 5-6 Comparison between proposed model and experimental data with the group effect

	$E_{m,d,1}V_{m,1}$ (N·m)	$E_{m,d,2}V_{m,2}$ (N·m)	$E_{f,d,1}V_{f,1}$ (N·m)	$E_{f,d,2}V_{f,2}$ (N·m)	E_a (N·m)		Error (%)
					Calculation by Eq.5-13	Experiment	
U1.2h	5.37	-	262.94	-	268.31	265.33	1.1
U0.6h-1.6h	2.17	3.22	7.81	311.11	324.32	337.98	-4.0

With regards to the double-layered UHPFRC, the model's inability to account for the extra energies dissipated by the twisted crack path and by the multiple crack branches also causes inaccuracy. As a result, the fiber slips and the number of activated fibers are underestimated, leading to a smaller fiber pullout energy. Nevertheless, this underestimation partially offsets the overestimation due to the fiber group effect, and hence U0.6h-1.6h has a smaller error than U1.2h in the original model without considering η_g , and the calculated E_a of U0.6h-1.6h is smaller than the experimental one in the modified model with η_g . Additionally, the accuracy of the proposed model can be further improved by employing more precise DIF equations for both the UHPC toughness and the fiber equivalent bond stress.

In addition, E_a absorbed by the top and bottom half of the single-layered beam U1.2h can be estimated with the proposed model in Eq. 5-13. It shows that the bottom half of the single-layered beam consumes approximately 87% of the total E_a while the top half only constitutes 13%, revealing

that the energy absorption capacity of the single-layered beam is dominated by its bottom half. Therefore, it is rational to apply a layered structure with more fibers in the bottom layer to improve the impact resistance of the UHPFRC. In the case of the double-layered beam U0.6h-1.6h, the bottom layer also consumes a higher portion of the impact energy than the top layer, as expected.

Furthermore, as shown in Table 5-6, the major part of the impact energy is consumed by the fiber pullout process, whereas the matrix cracking only constitutes an insignificant portion. This is in line with the brittle failure of plain UHPC and the remarkably improved toughness of UHPFRC under both static bending and dynamic impacts (Cao et al., 2019a; Yoo et al., 2018). It also confirms the importance of the steel fibers on enhancing the impact resistance of cementitious composites, indicating the significance of utilizing the fibers more efficiently. The dynamic fiber efficiency $eff_{f,d}$, defined as the ratio of the fiber consumed energy under the impacts and the total fiber mass in the UHPFRC beam, is adopted to further evaluate the fibers' contribution to the absorbed impact energy:

$$eff_{f,d} = \frac{\sum_{i=1}^n E_{f,d,i} V_{f,i}}{\left(\sum_{i=1}^n V_{f,i} h_i b L \rho_f \right)} \quad (5-14)$$

where L is the beam length; ρ_f is the density of the fiber ($\rho_f = 7850 \text{ kg/m}^3$).

The values of $E_{f,d,i} V_{f,i}$ are taken from Table 5-6 as calculated by the model. The obtained $eff_{f,d}$ of U1.2h and U0.6h-1.6h are approximately 558.27 N·m/kg and 677.14 N·m/kg according to Eq. 5-14. The improvement of $eff_{f,d}$ is more than 21%, which confirms the higher fiber utilization efficiency of the double-layered UHPFRC beam and further demonstrates the advantage of the layered structure.

5.6 Conclusions

The low-velocity impact performances of the coarse-aggregated UHPFRC beams with layered-structure are investigated in this chapter by the repeated drop-weight tests, and the dynamic properties, e.g. the peak reaction load, the impact number, the absorbed impact energy, and the cracking process are analyzed systematically. The influences of the fiber geometry and fiber hybridization, as well as the effects of the fiber amount distribution over the layered structure are discussed in detail. A model to estimate the absorbed impact energy of the UHPFRC beam is proposed and validated. This study sheds light on understanding the dynamic behaviors of the single- and double-layered UHPFRC under impacts, as well as promotes the potential engineering applications of layered UHPFRC composite with an improved fiber utilization efficiency. The following conclusions can be drawn:

- (1) Fiber geometry significantly affects the resistance of UHPFRC against drop-weight impacts. The peak reaction force, the impact number and the absorbed impact energy increase with the increase of the hooked-end fiber amount in both the single- and double-layered UHPFRC.
- (2) The double-layered UHPFRC has a superior impact performance than its single-layered counterpart. The double-layered beam has a higher peak reaction force and a smaller decline rate with the increasing impact number. The absorbed impact energy of the double-layered UHPFRC is also improved, and this improvement is more obvious on the UHPFRC with hooked-end fibers. Moreover, for UHPFRC with both the straight and hooked-end fibers, distributing the hooked-end fibers in the bottom layer and the straight ones in the top layer, viz. U0.6s-1.6h, generates a desirable energy absorption capacity.

- (3) No layer debonding occurs during the impact tests of the double-layered UHPFRC thanks to its sufficient bond strength. Cracking branches appear on the double-layered composite beam, connecting to or initiating from the layer interface. The dominant crack is narrower and more twisted compared to that in the corresponding single-layered beam.
- (4) A new model is developed to estimate the absorbed energy of the layered UHPFRC under repeated drop-weight impacts. The rate effects on the UHPFRC matrix and the dynamic fiber pullout responses are considered in the model. Furthermore, a coefficient accounting for the fiber group effect, viz. η_g , is proposed and it equals to 0.9 for the hooked-end steel fiber used in this study. The developed model is validated by the drop-weight test results.
- (5) The proposed model confirms that the fiber pullout process constitutes the major part of the beam absorbed impact energy while the matrix cracking only consumes an insignificant portion. Additionally, a 21% higher fiber efficiency of the double-layered beam is obtained according to the model estimation, which further confirms the advantages of the layered structure.

Chapter 6

*Enhancing the high-velocity impact resistance of coarse-aggregated UHPFRC by an optimized layered-structure concept **



* This chapter is partially reproduced from: Y.Y.Y. Cao, P.P. Li, H.J.H. Brouwers, Q.L. Yu, Resistance of Multi-Layered UHPFRC against in-service projectile: Experimental Investigation and Modelling Prediction (Submitted), and Y.Y.Y. Cao, M. Sluijsmans, H.J.H. Brouwers, Q.L. Yu, 2019. Ballistic performances of multi-layered Ultra-high Performance Fiber Reinforced Concrete, in: 2nd International Conference of Sustainable Building Materials (ICSBM 2019), Eindhoven, the Netherlands. 9 p.

Abstract

This chapter investigates the impact resistance of coarse-aggregated layered UHPFRC against in-service 7.62 mm × 51 AP projectile at 840 m/s. Coarse basalt aggregates are incorporated in the UHPFRC under the premise of reducing the cement powder consumption and taking advantages of their superior ballistic resistance. The maximum aggregate size further increases from 8 mm to 16 mm to discuss the influence of coarse aggregates on the impact resistance of UHPFRC. Thanks to the combined effects of the coarse aggregate, the layer interface, the fibers direction in the thin middle layer, and the edge confinement of the rear layer, the designed triple-layered UHPFRC U16a1s(40)-8a1s(10)-16a1s(40) achieves a superior impact resistance compared to the single-layered reference, with a 32% reduction of the depth of penetration. The results from this chapter shed light on understanding the ballistic performance of coarse-aggregated layered UHPFRC, and promote its application in protective constructions.

6.1 Introduction

Security problems of protective structures have become critical considerations. Having a potentially high risk of being exposed to ballistic weapons, e.g. in conflict areas or under terrorist attacks, these structures require suitable construction materials to withstand high-velocity impacts. The superior properties of UHPFRC make it a potential candidate for these protective structures (Li and Yu, 2019; Yu et al., 2014). The advantageous impact resistance of UHPFRC has been revealed by various studies. Yu et al. (Yu, 2015; Yu et al., 2016) evaluated the performances of a sustainable UHPFRC against projectile and claimed that the developed UHPFRC with hybrid fibers is a good choice for protective structures. Máca et al. (Máca et al., 2014) and Sovjak et al. (Sovják et al., 2015, 2013a) investigated the responses of UHPFRC under deformable and non-deformable projectile impacts; their studies presented that UHPFRC provides a better protection compared to high-strength concrete, and the UHPFRC containing 2% steel fibers achieves an optimum resistance. Liu et al. (Liu et al., 2017) experimentally and numerically evaluated the penetration responses of UHPFRC, and observed the superior performances of UHPFRC in terms of the depth of penetration (DOP), the crater diameter as well as the projectile abrasion.

Coarse aggregates are usually eliminated from conventional UHPFRC. On the one hand, using only fine aggregates in UHPFRC benefits its strength enhancement, thus reducing the DOP. On the other hand, coarse aggregates in a cementitious target improve its impact resistance by eroding the projectile and deviating the ballistic trajectory, which increase the energy dissipation of the projectile and decrease the DOP in the target (Dancygier, 2017; Peng et al., 2018; Wu et al., 2019). The above facts, therefore, promote the idea of developing coarse-aggregated UHPFRC possessing the advantages of both the ultra-high strength of the matrix and the improved resistance provided by the coarse aggregates. Insufficient studies have been conducted to explore the ballistic performance of coarse-aggregated UHPFRC. For instance, Wu et al. conducted penetration tests of UHPFRC with corundum (H. Wu et al., 2015b) and basalt (H. Wu et al., 2015a) aggregates against 25.3 mm projectile, and their studies revealed that the coarse aggregates are beneficial to reduce both the DOP and the impact crater size. It is noteworthy that their studies focus on the response of UHPFRC against large caliber projectiles (> 12.6 mm). In contrast, the resistance under small caliber arms, e.g. the 7.62 mm bullet, is not addressed, although it is a common in-service projectile in many countries (Peng et al., 2016a).

Steel fibers in UHPFRC contribute to enhancing the toughness of the specimen and reducing the damage on the impact surface, which increase the ballistic limit of the UHPFRC (Dancygier, 2017). In addition, fibers help to prevent the severe concrete spalling at the rear side of the impacted structure, which may act as further “projectiles” and amplify the devastating effect on the people and objects inside the structure (Yu, 2015). As shown in Fig. 6-1, when a UHPFRC target is under impact, three response regions can be obtained, namely the impact region, the tunnel region and the rear region (Almusallam et al., 2013; Peng et al., 2016a; Yu, 2015): (1) In the impact region, the UHPFRC is crushed by the projectile with the concrete pieces ejected off from the surface. An impact crater is generated in this region and cracking occurs around the crater as the stress waves are reflected several times inside the target. (2) The tunnel region is under compression with a confining pressure. A cylindrical tunnel is formed in this region due to the penetrating projectile. Because of the confining pressure, the diameter of the tunnel does not expand to a very large size, i.e. it is only slightly greater

than the diameter of the projectile. (3) In the rear region, the compressive waves generated by the projectile are reflected to be tensile ones, producing distributed cracks in the rear surface. Scabbing and spalling may also be observed in the rear region, and the scabbing area is usually shallower but wider than the impact crater as a result of the stronger tensile stress waves near the rear surface.

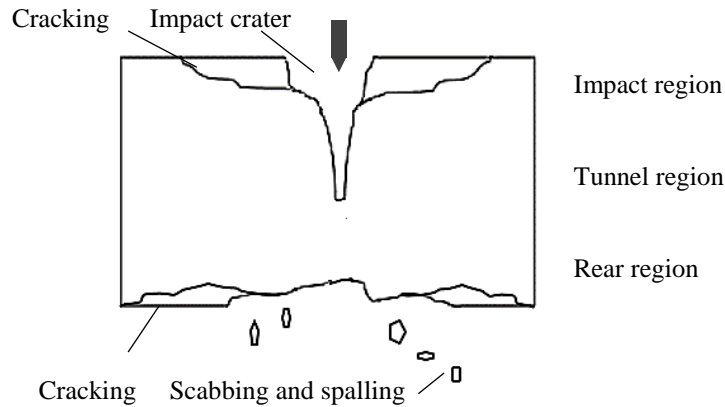


Fig. 6-1 Response regions in UHPFRC under penetration

The above response regions in Fig. 6-1 indicate that the fracture characteristic of UHPFRC changes along the projectile trajectory. That being the case, a homogeneous structure is not the most favorable option for the UHPFRC target as it cannot take the full advantages of its ingredients, e.g. the coarse aggregates and the steel fibers (Quek et al., 2010; Zhang et al., 2005). To generate a more effective ingredient utilization and to improve the overall impact resistance of the target, multi-layered UHPFRC with ingredients varying in each layer according to the response regions along the ballistic trajectory is preferred (Dancygier, 2017; Dancygier et al., 2014). Inadequate studies can be found in open literature regarding the ballistic analysis of cementitious composites with multi-layers. Among the limited studies, Quek et al. (Quek et al., 2010) designed a four-layered cementitious composite: the first and the last layers had hybrid fibers, the second layer had coarse aggregates, and the third layer was composed of plain mortar. It was found in their study that the developed layered composite has a superior ballistic resistance compared to that of the plain mortar. Lai et al. (Lai et al., 2017) developed a double-layered cementitious composite with an anti-penetration layer (containing coarse aggregates but no fiber) and a crack resistance layer (having fibers but no aggregates). By analyzing its impact response against repeated ballistic impacts, they obtained that the designed layered composite has a decreased DOP and a reduced crater area. It should be pointed out that in the above studies, the fibers and the coarse aggregates were incorporated in different layers, i.e. the combined effects of the two ingredients have not been considered.

In this chapter, coarse-aggregated layered UHPFRC is developed and tested. The ballistic resistance is evaluated by the impact test against in-service 7.62 mm × 51 AP projectile at a velocity of around 840 m/s. The effects of the fibers and coarse aggregates are exhibited using the results of the single-layered UHPFRC, while the potential enhancing mechanisms of the layered structure are revealed by analyzing the double-layered UHPFRC. Based on them, the triple-layered UHPFRC targets are designed to achieve the optimum distributions of the fiber amount and the aggregate size with the optimum layer thicknesses. The results from this chapter provide an important perspective for understanding the contributions of different ingredients on the ballistic resistance, and the developed multi-layered UHPFRC inspires the advanced design of protective structures.

6.2 Materials and experimental methods

6.2.1 Materials and mix design

The recipes of the UHPFRC are based on (Li and Yu, 2019). The basalt aggregates utilized have four size groups: 2-5 mm, 5-8 mm, 8-11 mm and 8-16 mm, as presented in Table 6-1. Two types of steel fibers are included: the Dramix OL 13/.20 straight fiber (SF) and Dramix RC 80/30-BP hooked-end fiber (HF). The properties of the fibers can be found in Chapters 2 and 4.

Table 6-1 Recipes of the UHP(FR)C: CEM = cement, mS = micro-silica, LP = limestone powder, S = sand, BA 2-5 = basalt aggregate with sizes of 2-5 mm, BA 5-8 = basalt aggregates with sizes of 5-8 mm, BA 8-11 = basalt aggregates with sizes of 8-11 mm, BA 8-16 = basalt aggregates with sizes of 8-16 mm, W = water, SP = superplasticizer, SF = straight fiber, HF = hooked-end fiber.

CEM (kg/m ³)	mS (kg/m ³)	LP (kg/m ³)	S (kg/m ³)	BA 2-5 (kg/m ³)	BA 5-8 (kg/m ³)	BA 8-11 (kg/m ³)	BA 8-16 (kg/m ³)	W (kg/m ³)	SP (kg/m ³)	SF (%)	HF (%)
								149	9.4	0	0
										1.0	0
588.0	39.2	156.8	839.9	413.2	232.3	0	0	157	8.5	0.5	0.5
										0	1.0
								157	12.5	1.5	0
										0	1.5
								154	4.9	0	0
525.0	35.0	140.0	699.3	445.2	186.9	147.8	209.6	161	4.5	1.0	0
										0	1.0
								161	6.5	1.5	0

6.2.2 Design of the layered UHPFRC target

The designed UHPFRC targets are listed in Table 6-2. The single-layered UHPFRC are labeled as S1~ S5, while the double- and the triple-layered UHPFRC are labeled as D1 ~ D4 and T1 ~ T7, respectively. The letters *a*, *s* and *h* present the aggregate, SF and HF, respectively; and the number before them are the maximum aggregate size of the layer (in mm), and the corresponding fiber volume fractions in that layer. The layer thickness (in mm) is shown by the number inside the brackets. In total 32 targets are tested, including 10 single-layered targets, 8 double-layered targets and 14 triple-layered targets.

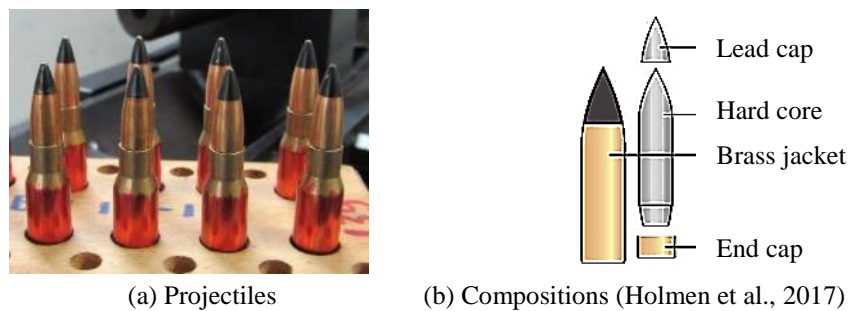
6.2.3 Mixing, casting and testing methods

The mixing and casting of the UHPFRC samples are conducted at room temperature of around 20 °C. The mixing procedure is as follows: dry mixing of all powders and sand for 2 minutes; adding 75% of the water and mixing for another 2 minutes; adding the superplasticizer with the remaining water and mixing for 4 minutes; adding the steel fibers and mixing for 3 minutes; subsequently adding the basalt aggregates and mixing for 4 to 6 minutes until they are well distributed in the mixture.

The 100 mm cubic specimens are used for the compressive, splitting tensile and bond tests, following the same methods in Chapter 4 (Section 4.3.4). Cylindrical mould with a diameter of approximately 275 mm is utilized to cast the UHPFRC targets for the ballistic tests. This diameter is more than 30 times the diameter of the projectile, hence boundary effects can be eliminated (Lai et

al., 2017; Peng et al., 2016b). For the multi-layered UHPFRC, an identical casting method is employed as described in Chapter 4 (Section 4.3.3).

The 7.62 mm \times 51 AP projectile is utilized for the ballistic tests (see Fig. 6-2). The impact velocity is around 840 m/s, as recorded by the velocity measurement system of the ballistic launch system (Fig. 6-3). The cylindrical UHPFRC target is mounted by a specially designed steel frame fixed on the ground to prevent its movement during the ballistic tests. As presented in Fig. 6-4, the top and bottom edges of the UHPFRC are clamped by two screws to simulate point supports (Máca et al., 2014). The center of the frame has a hole with a diameter slightly smaller than the size of the UHPFRC target (Fig. 6-4a), therefore, the spalling fragments from the rear face of the UHPFRC are not restrained and their traces can be observed by the damage on the white board behind the frame (Fig. 6-4b). The tests are conducted at 56 days after curing. After the ballistic tests, the targets are cut along the axial direction with a saw cutting machine to observe the internal damage.

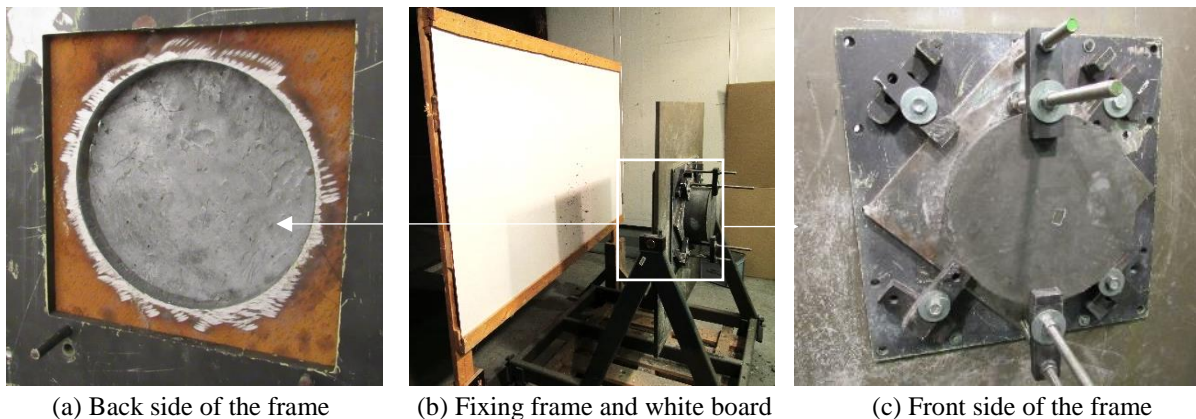


(a) Projectiles (b) Compositions (Holmen et al., 2017)

Fig. 6-2 The 7.62 mm \times 51 AP projectile (Li, 2019)



Fig. 6-3 Launch system



(a) Back side of the frame

(b) Fixing frame and white board

(c) Front side of the frame

Fig. 6-4 Penetration test set-up

Table 6-2 Multi-layered UHPFRC: In the identification a dash is used to divide the layers; U indicates UHPFRC; the number before the letter *a* is the maximum aggregate size (in mm); the numbers before *s* and *h* are the volume fractions of SF and HF; the number inside the brackets is the layer thickness (in mm).

Group	Identification	Layer thickness (mm)			Maximum aggregate size (mm)			Fiber volume fraction (%)						Equivalent fiber fraction (%)		
		1 st layer	2 nd layer	3 rd layer	1 st layer	2 nd layer	3 rd layer	1 st layer		2 nd layer		3 rd layer		SF	HF	
								SF	HF	SF	HF	SF	HF			
S1	U8a(90)	90	-	-	8	-	-	0	-	-	-	-	-	-	0	0
S2	U8a1s(90)	90	-	-	8	-	-	1	0	-	-	-	-	-	1	0
S3	U8a0.5s0.5h(90)	90	-	-	8	-	-	0.5	0.5	-	-	-	-	-	0.5	0.5
S4	U8a1h(90)	90	-	-	8	-	-	0	1	-	-	-	-	-	0	1
S5	U16a1s(90)	90	-	-	16	-	-	1	0	-	-	-	-	-	1	0
D1	U8a1s(45)-16a1s(45)	45	45	-	8	16	-	1	0	1	0	-	-	-	1	0
D2	U8a1s(45)-16a1h(45)	45	45	-	8	16	-	1	0	0	1	-	-	-	0.5	0.5
D3	U8a1h(45)-16a1s(45)	45	45	-	8	16	-	0	1	1	0	-	-	-	0.5	0.5
D4	U16a1s(45)-8a1s(45)	45	45	-	16	8	-	1	0	1	0	-	-	-	1	0
T1	U8a1.5s(30)-8a(30)-8a1.5s(30)	30	30	30	8	8	8	1.5	0	0	0	1.5	0	-	1	0
T2	U8a1.5h(30)-8a(30)-8a1.5h(30)	30	30	30	8	8	8	0	1.5	0	0	0	1.5	-	0	1
T3	U8a1.5s(30)-16a(30)-8a1.5s(30)	30	30	30	8	16	8	1.5	0	0	0	1.5	0	-	1	0
T4	U16a1.5s(30)-8a(30)-16a1.5s(30)	30	30	30	16	8	16	1.5	0	0	0	1.5	0	-	1	0
T5	U16a1s(30)-8a1s(30)-16a1s(30)	30	30	30	16	8	16	1	0	1	0	1	0	-	1	0
T6	U16a1s(20)-8a1s(50)-16a1s(20)	20	50	20	16	8	16	1.5	0	0	0	1.5	0	-	1	0
T7	U16a1s(40)-8a1s(10)-16a1s(40)	40	10	40	16	8	16	1.5	0	0	0	1.5	0	-	1	0

6.3 Experimental results

6.3.1 Static mechanical properties

The compressive strength $\sigma_{c,s}$ and the splitting tensile strength $\sigma_{t,s}$ of the designed UHPFRC mixtures (see Table 6-1) at the age of 56 days are given in Table 6-3. The UHPFRC with the hybrid fibers generates the highest σ_t . For instance, the hybrid fiber-reinforced group U8a0.5s0.5h has a 133% higher $\sigma_{t,s}$ than that of the plain UHPC U8a, whereas the corresponding enhancements are 70% and 95% for the SF reinforced group U8a1s and the HF reinforced group U8a1h. This trend is in line with that in Chapter 5 (Section 5.3).

Thanks to the dense particle size distribution resulted from the optimum mix designs, the coarse-aggregated UHPFRC achieve an ultra-high $\sigma_{c,s}$ satisfying the strength condition of UHPFRC. A slight increase of $\sigma_{c,s}$ is even observed for the UHPFRC containing the 16 mm basalt aggregates than those with the 8 mm aggregates. This may be attributed to the strengthened concrete skeleton with the larger aggregates, and the different cement amount and water/binder ratio of the 8 mm and 16 mm groups. This improved strength with the increase of the aggregate size is also reported in other studies (Liu et al., 2016; Nikbin et al., 2014; Yoo and Banthia, 2017b).

The maximum difference of $\sigma_{c,s}$ among the developed matrices is obtained between U8a and U16a1s (the difference is within 8%). As suggested by previous ballistic studies, the DOP no longer decreases remarkably when the concrete strength is higher than a certain value, e.g. 90 MPa (H. Wu et al., 2015a) ~ 100 MPa (Zhang et al., 2005). Therefore, in the ballistic performance analysis in Section 6.4, the influences of these different $\sigma_{c,s}$ on the impact resistances of the developed UHPFRC targets are ignored. More detailed information regarding the properties of the coarse-aggregated UHPFRC at the material level can be found in (Li et al., 2018).

Table 6-3 Compressive and tensile strengths of the UHPFRC mixtures in individual layers

Group	Identification	Compressive strength $\sigma_{c,s}$ (MPa)		Tensile strength $\sigma_{t,s}$ (MPa)	
		Avg.	St. dev.	Avg.	St. dev.
1	U8a	149.6	2.8	7.2	1.3
2	U8a1s	154.9	2.5	12.3	1.2
3	U8a0.5s0.5h	158.5	1.0	16.8	1.2
4	U8a1h	151.8	1.9	14.1	1.1
5	U8a1.5s	158.5	3.0	15.3	0.6
6	U8a1.5h	155.3	2.9	16.9	2.4
7	U16a	150.7	3.1	8.3	2.5
8	U16a1s	161.3	3.5	14.6	1.4
9	U16a1h	153.6	2.7	14.9	1.6
10	U16a1.5s	160.2	2.0	16.4	1.3

The interfacial bond strengths σ_b between the layers are listed in Table 6-4. The maximum σ_b is achieved by U8a1h-16a1s, which is around 8.6 MPa. The minimum σ_b is obtained by U8a-8a1.5s with a value of approximately 6.8 MPa. Similar to the failure pattern in Chapter 4 (see Fig. 4-1), cohesive failure occurs during the bond splitting tests in this chapter. Cracking is observed to propagate through both layers in each specimen. Therefore, the obtained bond strength of each specimen is associated with the properties of its two layers and the crack lengths in both layers.

Table 6-4 Bond strength of the layered UHPFRC

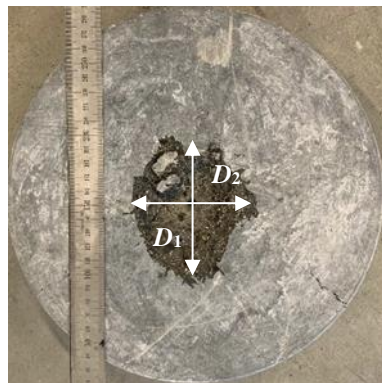
Group	Identification	Bond strength σ_b (MPa)		Corresponding to the groups in Table 6-2
		Avg.	St. dev.	
1	U8a-8a1.5s	6.8	1.8	T1
2	U8a-8a1.5h	8.1	1.8	T2
3	U8a-16a1.5s	7.2	2.6	T4
4	U8a1s-16a1s	7.0	1.6	D1, D4, T5-7
5	U8a1s-16a1h	7.0	2.4	D2
6	U8a1h-16a1s	8.6	2.4	D3
7	U8a1.5s-16a	7.5	1.7	T3

6.3.2 Ballistic test results

The resistant capacity of the designed UHPFRC is assessed by the DOP and the damage in the impact surface, i.e. the equivalent crater diameter D_{eq} . The DOP is defined as the distance from the impact surface to the deepest point in the target. D_{eq} is quantified as $D_{eq} = \sqrt{D_1 D_2}$, where D_1 and D_2 are the diameters of the impact crater measured in two perpendicular directions (see Fig. 6-5a). The damage in the rear surface is not easy to be quantified as the damage, i.e. cracks, spalling or scabbing, is not prominent in most tested targets (e.g. Fig. 6-5b). Therefore, the damage in the rear surface is used only for qualitative evaluations and it is defined as five levels (Dancygier et al., 2007; Ueno et al., 2018):

- Level 1. No visible damage to hairline cracks.
- Level 2. Visible cracks without scabbing.
- Level 3. Heavy cracking.
- Level 4. Scabbing and spalling or shear plug without perforation.
- Level 5. Perforation with a residual velocity.

DOP and D_{eq} of the tested samples are listed in Table 6-5 except for that of the UHPC target S1, viz. U8a(90), because it is perforated by the projectile and breaks into larger pieces due to the lack of fibers (see Fig. 6-6). Table 6-5 presents that DOP of the multi-layered UHPFRC are smaller than that of their single-layered counterparts. Moreover, the triple-layered target with the optimum layer thickness, viz. U16a1s(40)-8a1s(10)-16a1s(40) (T7 in Table 6-5), achieves the smallest DOP, which is approximately 32% smaller than that of the single-layered target U8a1s(90) (S2 in Table 6-5). Additionally, the cement amount utilized in T7 is about 10% less than that in S2 thanks to the incorporation of the 16 mm coarse aggregates, which contributes to the material effectiveness and the environmental sustainability. A systematical analysis of the ballistic performances of the single-, double- and triple-layered UHPFRC is presented in Section 6.4.

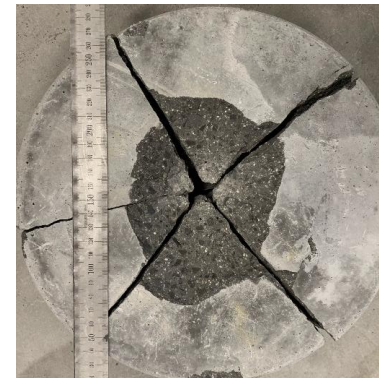


(a) Impact surface



(b) Rear surface

Fig. 6-5 Damage in the UHPFRC



(a) Impact surface



(b) Rear surface

Fig. 6-6 Perforation of the reference UHPC sample S1

Table 6-5 Penetration test results of designed UHPFRC: Level 1. No visible damage to hairline cracks; Level 2. Visible cracks without scabbing; Level 3. Heavy cracking; Level 4. Scabbing and spalling or shear plug without perforation; Level 5. Perforation with a residual velocity.

Group	Identification	Penetration velocity (m/s)		Depth of penetration (mm)			Equivalent crater diameter (mm)			Damage in the rear surface	
		1 st	2 nd	1 st	2 nd	Avg.	1 st	2 nd	Avg.	1 st	2 nd
		sample	sample	sample	sample		sample	sample		sample	sample
S1	U8a(90)	838.9	842.3	perforation						Level 5	
S2	U8a1s(90)	838.5	841.9	62.0	60.0	61.0	75.70	70.00	72.85	Level 2	
S3	U8a0.5s0.5h(90)	839.3	841.8	61.0	60.5	60.8	66.10	70.00	68.05	Level 1	
S4	U8a1h(90)	841.8	839.6	61.0	62.0	61.5	75.22	74.10	74.66	Level 1	Level 2
S5	U16a1s(90)	840.7	847.3	55.0	55.0	55.0	62.95	62.55	62.75	Level 2	
D1	U8a1s(45)-16a1s(45)	842.6	845.0	57.0	55.0	56.0	67.07	77.86	72.47	Level 3	Level 2
D2	U8a1s(45)-16a1h(45)	845.2	842.3	54.0	55.0	54.5	67.92	70.54	69.23	Level 3	Level 4
D3	U8a1h(45)-16a1s(45)	845.4	846.1	59.0	54.0	56.5	69.72	72.84	71.28	Level 2	Level 1
D4	U16a1s(45)-8a1s(45)	841.0	842.9	51.0	53.0	52.0	57.55	65.19	61.37	Level 1	Level 2
T1	U8a1.5s(30)-8a(30)-8a1.5s(30)	846.3	836.0	58.0	54.0	56.0	67.19	69.50	68.35	Level 2	
T2	U8a1.5h(30)-8a(30)-8a1.5h(30)	837.9	850.2	56.0	60.0	58.0	80.00	61.60	70.80	Level 2	
T3	U8a1.5s(30)-16a(30)-8a1.5s(30)	841.8	845.4	55.0	57.0	56.0	70.20	72.00	71.10	Level 2	
T4	U16a1.5s(30)-8a(30)-16a1.5s(30)	840.9	845.9	52.5	51.0	51.8	53.08	59.54	56.31	Level 2	
T5	U16a1s(20)-8a1s(50)-16a1s(20)	842.5	845.2	54.0	54.5	54.3	70.64	65.19	67.92	Level 1	
T6	U16a1s(30)-8a1s(30)-16a1s(30)	841.5	839.3	52.0	52.5	52.3	65.19	67.92	66.56	Level 1	Level 1
T7	U16a1s(40)-8a1s(10)-16a1s(40)	838.5	840.0	49.0	46.5	47.8	72.52	65.56	69.04	Level 1	

6.4 Discussions

6.4.1 Response of single-layered UHPFRC

In order to understand the contributions of the steel fibers and the coarse aggregates on the ballistic resistance of UHPFRC, the single-layered groups S1 ~ S5 are investigated. The plain UHPC S1 reveals the effects of fiber addition. As expected, macro-cracks split S1 into several large pieces and the projectile perforates the target with a residual velocity. Additionally, the damage in the rear surface of S1 (Fig. 6-6b) is clearly severer than that in the impact surface (Fig. 6-6a) due to the stronger tensile waves reflected at the back side of the UHPC. Other targets in this study are reinforced with steel fibers, and none of them experience such a destructive failure pattern; instead, they successfully stop the projectile inside the targets. The outstanding resistance of the fiber-reinforced targets compared to that of S1 confirms the significance of the fibers. Fibers in the UHPFRC can effectively inhibit the development of cracks. Moreover, they increase the toughness of the material as well as prevent the disintegration of the target, which further generates a supplementary confinement to the projectile and provides an additional resistance.

Fig. 6-7 shows the penetration results of S2 ~ S4, which are single-layered UHPFRC with an identical fiber amount but different fiber geometries. As can be observed in the figure, the three groups have comparable DOP of about 61 mm, indicating the insignificant effects of fiber geometry and fiber hybridization on DOP. On the contrary, fiber hybridization decreases the damage size in the UHPFRC, as confirmed by the smallest D_{eq} of S3 among the three groups. This phenomenon may be attributed to the higher tensile strength of the S3 matrix. The hybridization of the short SF and the long HF produce a synergistic cracking control ability, i.e. the short fibers effectively bridge the micro-cracks while the long fibers contribute more to the prevention of the macro-cracks (Markovic, 2006).

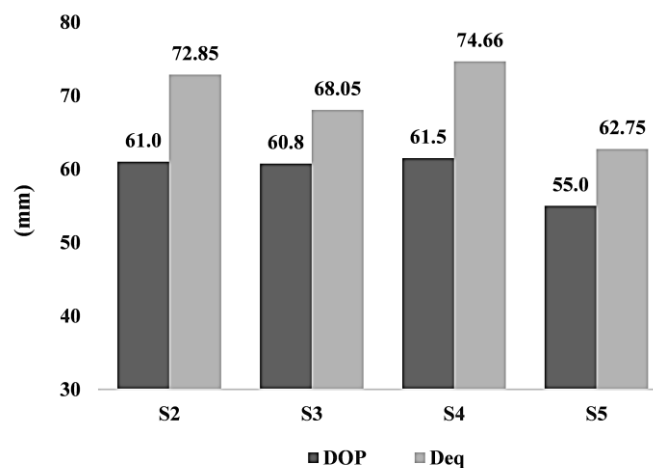


Fig. 6-7 Depth of penetration (DOP) and equivalent crater diameter (D_{eq}) of single-layered UHPFRC: S2 ~ S5 are corresponding to U8a1s(90), U8a0.5s0.5h(90), U8a1h(90), and U16a1s(90), respectively.

In comparing S2 with S5 in Fig. 6-7 demonstrates that the larger coarse aggregates promote a superior impact resistance in terms of both the DOP and the equivalent crater diameter. The DOP and D_{eq} of S5 (with the maximum aggregate size of 16 mm) are approximately 11% and 16% smaller than those of S2 (with the maximum aggregate size of 8 mm). Similar results are reported in (H. Wu et al., 2015a, 2015b), which investigated the effects of coarse aggregates in concrete targets with strengths

between 65 and 130 MPa. The contributions of these coarse aggregates are mainly associated with the following factors. When the UHPFRC is subjected to ballistic impact, the rapid pressure enhancement in the target forces the micro-cracks to propagate rapidly. The strain rate caused by the penetration is so high that the cracks are driven to develop through the aggregates instead of propagating around them. Since the coarse basalt aggregates have a higher strength and a larger hardness than the UHPC matrix, these aggregates can act as barriers to the cracks, and the resistance is consequently improved. In addition, with the increase of the aggregate size, the penetrating projectile has a higher possibility to hit the aggregate, as presented in Fig. 6-8. These aggregates not only increase the abrasion of the projectile, but also deviate its trajectory, leading to a larger loss of the projectile kinetic energy.

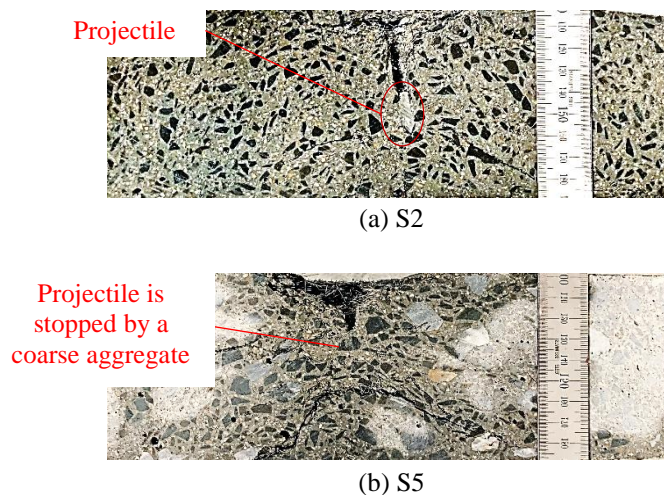


Fig. 6-8 Cross section of single-layered UHPFRC: S2 and S5 are corresponding to U8a1s(90) and U16a1s(90).

6.4.2 Response of double-layered UHPFRC

The impact resistant performances of the double-layered UHPFRC are discussed in this section. Fig. 6-9 presents the DOP and D_{eq} of the double-layered UHPFRC. As shown in the figure, D1 ~ D3 have comparable DOP despite their different fiber geometries. Similar damage level of the impact surface is also observed in these groups, showing that fiber geometry scarcely affects the damage distribution when the maximum aggregate size is 8 mm. These agree with the observations in Section 6.4.1. In contrast, the damage distribution differs with different fibers when the maximum aggregate size is 16 mm. As presented in Fig. 6-10, serious spalling of concrete pieces is observed on the rear surface of D2 (with HF in the rear layer), whereas D3 (with SF in the rear layer) has only slight damage, namely only hairline cracks appear on its back side. This distinct damage level of D2 and D3 indicates that for the UHPFRC with a maximum aggregate size of 16 mm, the short SF can provide a more effective damage control compared to the long HF. Possible reasons are illustrated in Fig. 6-11. Firstly, a larger number of short SF are added into the UHPFRC than the long HF when they have the same fiber volume fraction, resulting in the superior control on target cracking. Secondly, the distribution of the long HF in the 16 mm coarse-aggregated UHPFRC may be more inclined due to the large size of the aggregate and the long length of the HF. These inclined HF might not be able to provide a cracking resistance as efficient as the aligned fibers because of their reduced pullout resistance at large inclinations (see the pullout tests in Chapter 2). Thirdly, the longer HF generates higher stresses in the surrounding concrete and produces a larger disturbed zone, which leads to a more serious damage in the target (Zhang et al., 2007).

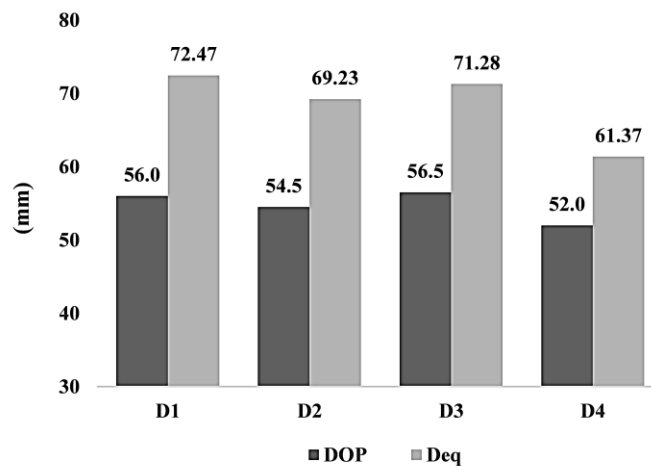


Fig. 6-9 Depth of penetration (DOP) and equivalent crater diameter (D_{eq}) of double-layered UHPFRC: D1 ~ D4 are corresponding to U8a1s(45)-16a1s(45), U8a1s(45)-16a1h(45), U8a1h(45)-16a1s(45) and U16a1s(45)-8a1s(45).

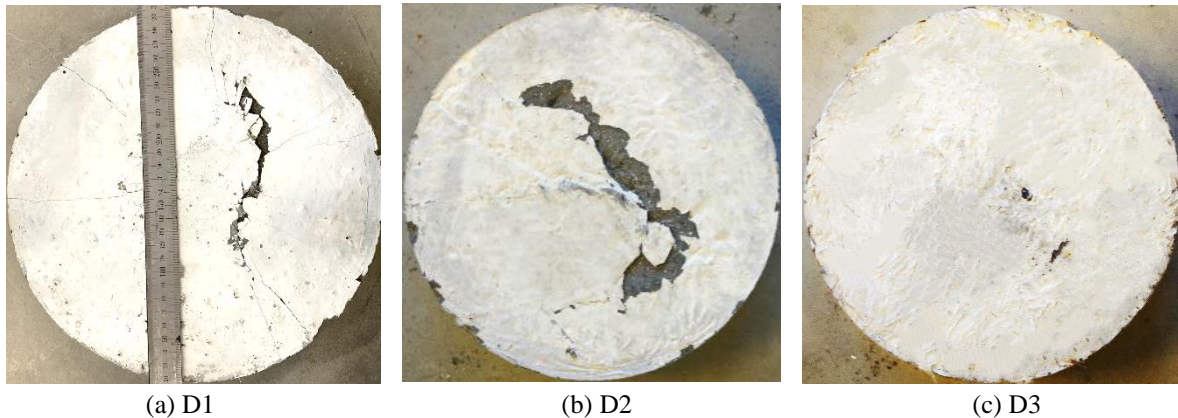


Fig. 6-10 Damage in the rear surface of double-layered UHPFRC: D1 ~ D3 are corresponding to U8a1s(45)-16a1s(45), U8a1s(45)-16a1h(45) and U8a1h(45)-16a1s(45), respectively.

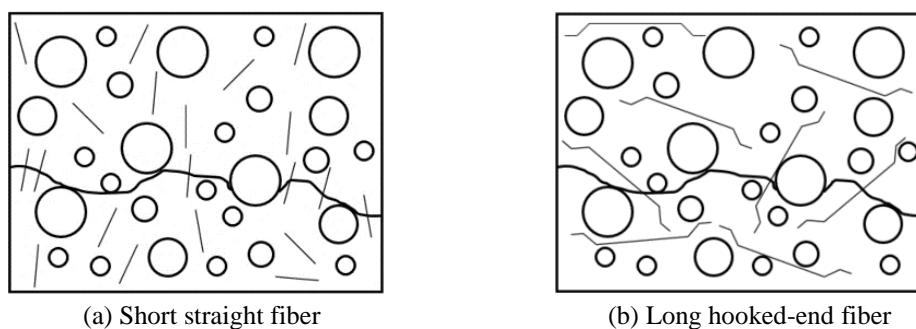


Fig. 6-11 Illustration of fibers effects on UHPFRC.

Comparing D1 and D4 with S2 further demonstrates that increasing the aggregate size in either the impact or the rear layers of the UHPFRC reduces the DOP, and this reduction is more remarkable when the large aggregates are in the impact layer, viz. D4. To be more specific, the DOP of D1 and D4 are about 9% and 20% smaller than that of S2, respectively. This is because in D1 the large coarse aggregate starts to play a role until the projectile reaches the rear layer, while in D4 its effect is activated immediately when the projectile touches the impact surface (see Fig. 6-12). With regard to

D_{eq} , increasing the maximum aggregate size of the impact layer shows a positive effect (comparing S2 in Fig. 6-7 with D4 in Fig. 6-9); however, the larger aggregates have almost no influence when they are added to the rear layer of the sample (comparing S2 in Fig. 6-7 with D1 in Fig. 6-9).

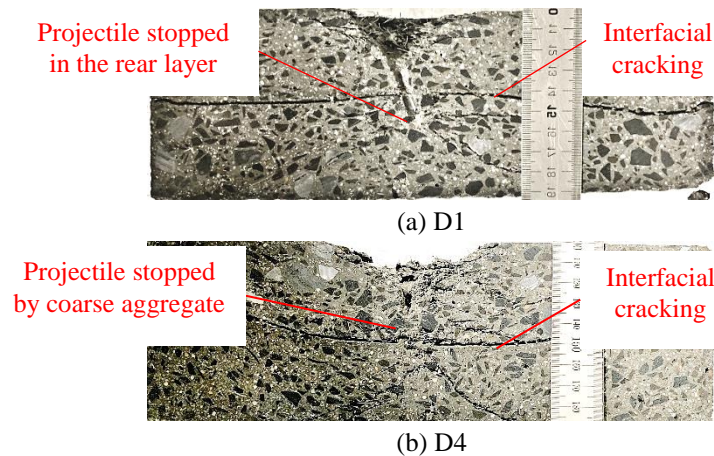


Fig. 6-12 Cross section of double-layered UHPFRC: D1 and D4 are corresponding to U8a1s(45)-16a1s(45) and U16a1s(45)-8a1s(45), respectively

Moreover, the double-layered UHPFRC D4 has a smaller DOP than the single-layered target S5, which has large aggregates in the whole volume. This may be resulted from the effects of the layered structure. Firstly, the layer interface can invoke more wave interactions in the double-layered UHPFRC and dampen the strength of the impact waves (Chen and Chandra, 2004). Secondly, the network of cracks inside the double-layered target along the layer interface, as can be observed in Fig. 6-12b, contributes to an additional absorption of the projectile kinetic energy (Quek et al., 2010). Thirdly, the interface cracking reduces the damage in the rear layer of the double-layered UHPFRC, and this stronger back side in turn provides a greater resistance to the projectile, in comparison to the single-layered UHPFRC undergoing substantial cracking in the whole target. Fourthly, the different maximum aggregate sizes in the two layers of D4 may generate varying levels of confinement on the projectile. As the projectile usually seeks a path of the least resistance during its penetration (Booker et al., 2009), this different confinement may therefore change the projectile trajectory in the layered UHPFRC and generate an improved impact performance. Furthermore, it is worth mentioning that in spite of the interfacial cracks, layer delamination did not occur in the tested multi-layered UHPFRC, i.e. the samples are able to retain their integrity rather than disintegrate into separated layers thanks to the excellent interfacial bond strength.

6.4.3 Response of triple-layered UHPFRC

In this section, triple-layered UHPFRC is designed with the optimum distributions of the fiber amount and the aggregate size in the layered structure. Based on the failure pattern illustrated in Fig. 6-1, the UHPFRC target is divided into three layers. For the group with the optimum fiber amount distribution, e.g. T1 and T2, the steel fibers are more concentrated in the outer layers while the middle layer has no fiber considering its utilization efficiency. For the group with the optimum aggregate size distributions, e.g. T5, the maximum aggregate size of the outer layers is 16 mm while that of the middle layer is 8 mm based on the knowledge gained from Section 6.4.2. Additionally, groups T6 and T7 are

set to study the effects of layer thickness, and the possible enhancing mechanisms related to the layer thickness are also analyzed.

The penetration results of T1 ~ T4 are presented in Fig. 6-13. Influences of the fiber amount distribution over the layered UHPFRC can be obtained by the comparisons of T1 with S2 or T2 with S4. As can be observed in the figure, these triple-layered targets have reduced DOP and D_{eq} , confirming that the fibers in the two outer layers are more efficiently utilized in comparison to those distributed in the middle part of the target. This is in line with the damage distribution in Fig. 6-1, as the middle tunneling region of the target is under compression with a confining pressure and the contribution of the fibers is relatively limited in this region.

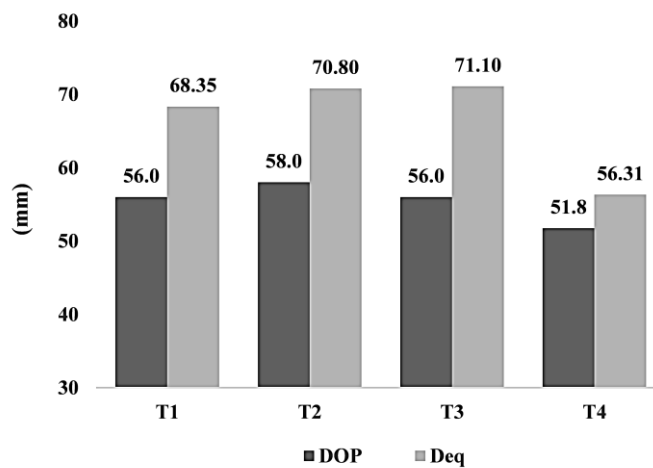


Fig. 6-13 Depth of penetration (DOP) and equivalent crater diameter (D_{eq}) of triple-layered UHPFRC: T1 ~ T4 are corresponding to U8a1.5s(30)-8a(30)-8a1.5s(30), U8a1.5h(30)-8a(30)-8a1.5h(30), U8a1.5s(30)-16a(30)-8a1.5s(30) and U16a1.5s(30)-8a(30)-16a1.5s(30), respectively.

Furthermore, the comparable DOP and D_{eq} of T1 and T3 reveal that the aggregate size in the middle layer of the target has negligible effects on its impact resistance. On the contrary, the maximum aggregate size of the outer layers plays a role. As shown in Fig. 6-13, T4 has an 8% decreased DOP than that of T1, and its D_{eq} is also remarkably reduced (approximately 21% smaller than that of T1). The rear-surface damage patterns of T1 ~ T4 are shown in Fig. 6-14. The targets have similar damage levels in their rear layers that some visible cracks appear in the distal surface, while no concrete scabbing is observed. This further presents the advantage of the triple-layered UHPFRC in preventing the second damage caused by the spalling concrete particles from the rear surface. In general, the triple-layered UHPFRC with the optimum distributions of both the fiber amount and the aggregate size, viz. T4, achieves an 18% reduced DOP and a 29% reduced D_{eq} than those of the reference group S2. Therefore, taking into account both the DOP and the damage in the two outer surfaces, the design of T4 with larger aggregates and more fibers in the outer layers is recommended.

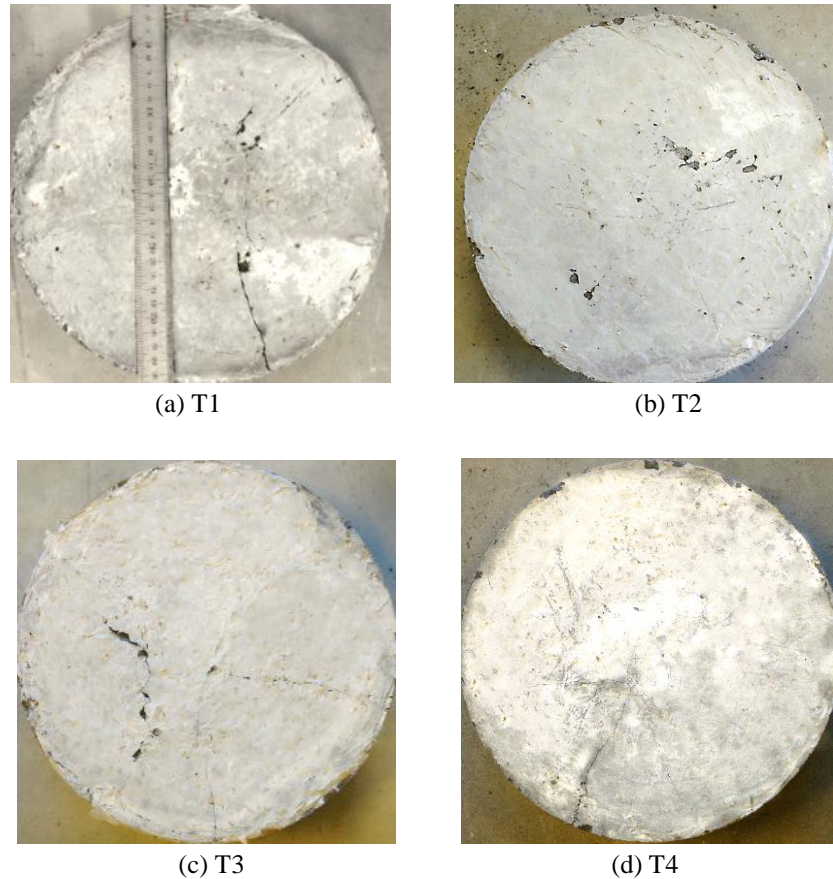


Fig. 6-14 Damage in the rear surface: T1 ~ T4 are corresponding to U8a1.5s(30)-8a(30)-8a1.5s(30), U8a1.5h(30)-8a(30)-8a1.5h(30), U8a1.5s(30)-16a(30)-8a1.5s(30) and U16a1.5s(30)-8a(30)-16a1.5s(30), respectively.

Different layer thicknesses are further considered to obtain the optimum layer design of the triple-layered UHPFRC. The results are plotted in Fig. 6-15. A clear decrease of DOP is observed with the increase of the outer layer thickness from 20, 30 to 40 mm, corresponding to T5, T6 and T7. It is noteworthy that T7 achieves the smallest DOP among all the tested targets in this study, which may be attributed to the following factors: the large aggregate, the layer interface, the direction of fibers in the thin middle layer, and the edge confinement of the thick rear layer. The effects of the coarse aggregate and the layer interface have been mentioned in previous sections. As with the contribution of the middle layer, the 10 mm thin layer of T7 restrains the randomly distribution of the 13 mm SF inside it; instead, it forces the fibers to orientate in a 2D plane and maximizes the fiber efficiency (Denarié, 2009). Since the fibers are forced to be distributed perpendicularly to the penetration direction, they work as a steel reinforcing mesh and provide an enhanced resistance to the projectile. As shown in Fig. 6-16, T7 also has smaller damage in its rear region. This almost intact rear layer of T7 further provides an enhanced edge confinement at the back side, and therefore, generates a higher resistance to the projectile.

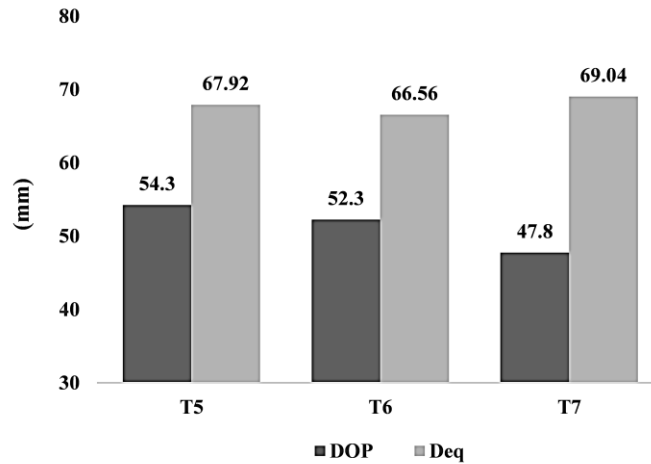


Fig. 6-15 Influences of the layer thickness on the depth of penetration (DOP) and equivalent crater diameter (D_{eq}): T5 ~ T7 are triple-layered samples corresponding to U16a1s(20)-8a1s(50)-16a1s(20), U16a1s(30)-8a1s(30)-16a1s(30) and U16a1s(40)-8a1s(10)-16a1s(40), respectively.

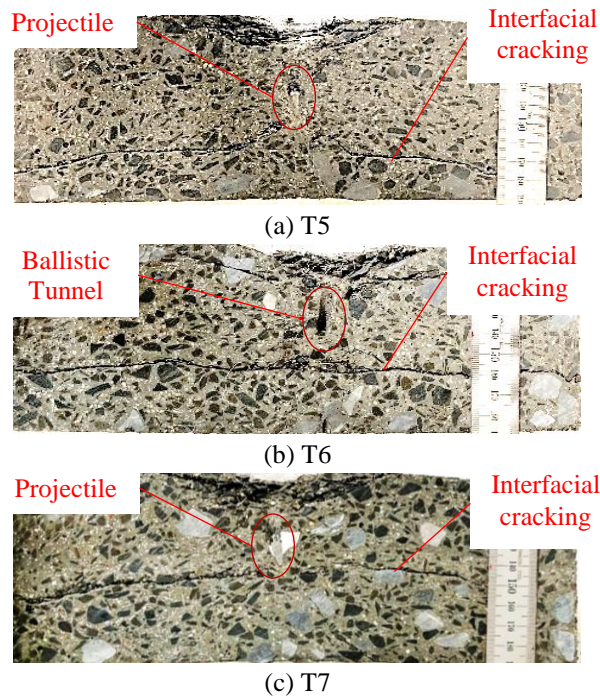


Fig. 6-16 Cross section of the UHPFRC samples: T5 ~ T7 are triple-layered samples corresponding to U16a1s(20)-8a1s(50)-16a1s(20), U16a1s(30)-8a1s(30)-16a1s(30) and U16a1s(40)-8a1s(10)-16a1s(40), respectively.

Fig. 6-17 depicts the damage on the side surface of T5 ~ T7. It is interesting to find that although these triple-layered targets have two layer interfaces in each target, only the interface between the middle and the rear layers show obvious cracks, while no crack can be observed in the other interface between the impact and the middle layers by naked eyes. This single interface cracking is associated with the stress wave phenomena inside the UHPFRC. The compressive stress wave generated by the projectile is reflected as a tensile wave upon its arrival at the rear surface of the target; then the tensile stress wave interferes with the original compressive wave, resulting in a descendingly compressive and ascendingly tensile wave (Almusallam et al., 2013; Wang et al., 2016). When the amplitude of the resulting tensile wave exceeds the bond strength between the layers, cracking would localize at the

layer interface. However, the wave propagation and the cracking at the interface between the middle and the rear layers dissipate the wave energy. Consequently, the amplitude of the reflection wave is dampened below the bond strength when it reaches the other interface between the impact and the middle layers. Therefore, no cracking occurs at the interface near the impact surface.

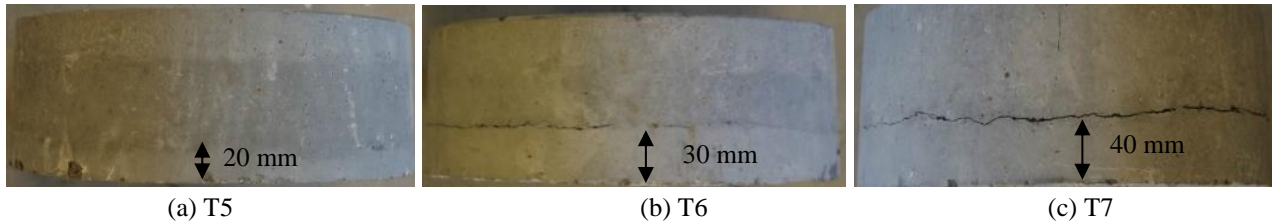


Fig. 6-17 Damage in the side surface: T5 ~ T7 are triple-layered samples corresponding to U16a1s(20)-8a1s(50)-16a1s(20), U16a1s(30)-8a1s(30)-16a1s(30) and U16a1s(40)-8a1s(10)-16a1s(40), respectively.

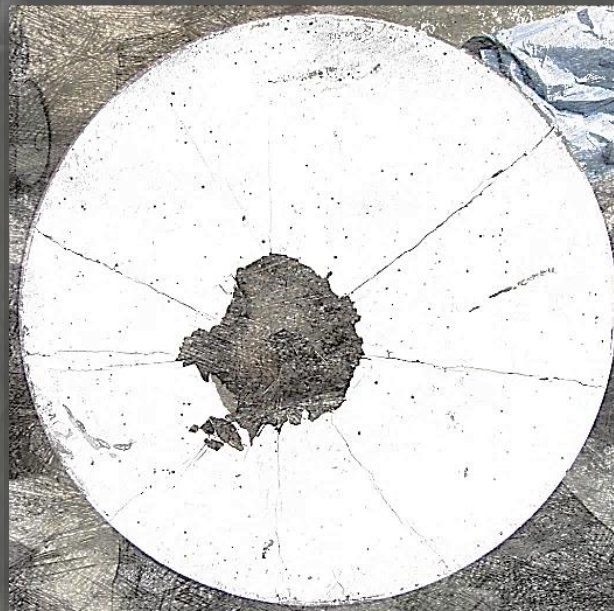
6.5 Conclusions

Multi-layered UHPFRC containing coarse basalt aggregates are developed in this chapter, and their ballistic performances are evaluated against the 7.62 mm × 51 AP projectile at a velocity of about 840 m/s. In spite of its 10% less cement dosage, the designed triple-layered UHPFRC U16a1s(40)-8a1s(10)-16a1s(40) achieves a 32% reduced DOP compared to its single-layered counterpart U8a1s(90). The following specific conclusions can be drawn:

- (1) The coarse basalt aggregates in the UHPFRC target reduce both the DOP and the equivalent crater diameter. They improve the impact resistance of UHPFRC by increasing the material hardness, eroding the projectile and deviating its trajectory, which contribute to the dissipation of the projectile kinematic energy.
- (2) Fibers improve the resistance of UHPFRC by increasing the material toughness and preventing the target disintegration. Fiber geometry insignificantly affects the ballistic performance when the maximum aggregate size of the target is 8 mm, but for the UHPFRC with a maximum aggregate size of 16 mm, the straight fiber can provide a more effective damage control compared with the hooked-end fiber. Possible reasons are related with the higher amount of the straight fiber, the reduced pullout resistance of the hooked-end fiber due to its inclination, and the smaller disturbed zone in UHPC with the short straight fiber.
- (3) For the double-layered UHPFRC, increasing the aggregate size in either layer decreases the DOP, and the effect is more obvious when the larger aggregates are applied in the impact layer. The double-layered UHPFRC with 16 mm aggregates in the impact layer and 8 mm aggregates in the rear layer has a reduced DOP than the single-layered one with 16 mm aggregates. Possible enhancing mechanisms include the layer interface that dampens the impact waves, the interfacial cracking that promotes energy consumption, the reduced damage in the rear surface that provides a higher resistance, and the different confining levels of the two layers due to the different aggregate sizes.
- (4) For the triple layered UHPFRC, fiber amount distribution over the layered structure reduces both the DOP and the equivalent crater diameter, and the design of utilizing larger aggregates and more fibers in the outer layers is recommended for the triple-layered UHPFRC. Furthermore, the optimized triple-layered UHPFRC U16a1s(40)-8a1s(10)-16a1s(40) achieves the smallest DOP, thanks to the combined effects of the coarse aggregate, the layer interface, the direction of fibers in the thin middle layer, and the edge confinement of the thick rear layer.

Chapter 7

*Predicting the depth of penetration in UHPFRC under high-velocity impact using a nonlinear rate-dependent model **



*This chapter is partially reproduced from: Y.Y.Y. Cao, Q.H. Tan, Z.G. Jiang, H.J.H. Brouwers, Q.L. Yu, A nonlinear rate-dependent model for predicting the penetration depth in UHPFRC, *Cement and Concrete Composites* 106 (2020) 103451, and Y.Y.Y. Cao, P.P. Li, H.J.H. Brouwers, Q.L. Yu, Resistance of Multi-Layered UHPFRC against in-service projectile: Experimental Investigation and Modelling Prediction (Submitted).

Abstract

UHPFRC is a promising material for constructing protective structures against ballistic impacts. Nevertheless, there is still a lack of effective models to predict the depth of penetration (DOP) in UHPFRC. This study proposes analytical predictive models for both single- and multi-layered UHPFRC, on the basis of an improved dynamic spherical cavity expansion theory. The Hoek-Brown criterion is utilized to account for the nonlinear response of UHPFRC, and its rate dependency is addressed by incorporating the dynamic increase factor (DIF). The developed predictive models for UHPFRC are validated against the penetration experimental data from literature and presented in Chapter 6. The results indicate that the proposed models can achieve reasonable DOP predictions for both the single- and multi-layered UHPFRC.

7.1 Introduction

Predicting the DOP in UHPFRC is essential for assessing its ballistic resistance. A number of DOP predictive models have been proposed for concrete (Li and Chen, 2003; Yu, 2015), and detailed reviews can be found in (Ben-Dor et al., 2015; Li et al., 2006; Yankelevsky, 2017). These models provide straightforward approaches to predict the DOP in concrete with the considerations of the impact velocity, concrete strength, projectile weight and geometry (Le, 2017). Generally, current DOP predictive models can be classified into empirical, semi-empirical and theoretical categories. The application range of empirical models normally depends on the conducted experiments, from which the formulae are derived by data-fitting. In addition, empirical models such as ACE, NDRC and UKAEA formulae are usually unit dependent, making it difficult to identify the important physical quantities in the formulae (Li and Chen, 2003). Semi-empirical models are in general developed based on theoretical analysis with some parameters determined by experimental data, for example the empirical constant S in the Forrestal semi-empirical formula (Forrestal et al., 1994; Li and Chen, 2003) and Li-Chen formula (Li et al., 2006). It is noteworthy that these empirical and semi-empirical models are mainly proposed for NC, i.e. some parameters in the models are obtained based on the properties of NC, and using them to predict the DOP in UHPFRC would lead to inaccurate results (Le, 2017). With regard to theoretical models, they calculate the impact resisting force with some physically based assumptions, e.g. the resistance on the projectile is constant (Rosenberg and Kositski, 2016) or velocity dependent (Forrestal et al., 1994; Warren and Forrestal, 1998), and then derive the DOP through the Newton's second law with the analytical resisting force (Rosenberg and Kositski, 2016). Among the existing theoretical models, the cavity expansion theory analytically calculates the resistance with definite physical meanings, and it has been successfully applied for concrete targets impacted by different projectiles under various penetration velocities (Forrestal and Tzou, 1997; Meng et al., 2018; Zhen et al., 2014).

Applying the cavity expansion theory, the penetration of the projectile in a target is modeled as the expansion of a spherical or cylindrical cavity at a constant velocity. The resistant pressure on the projectile is then computed analytically by the radial stress at the cavity surface (Macek and Duffey, 2000). Compared to the cylindrical cavity expansion theory, the spherical cavity expansion theory is more extensively used and it gives accurate results as long as proper yield criteria of the target material are adopted (Meng et al., 2018). To simplify the calculation, linear yield criteria, e.g. the Mohr-Coulomb criterion (Forrestal and Tzou, 1997; He et al., 2011; Kong et al., 2016b) and the Drucker-Prager criterion (Feng et al., 2015), are usually applied in the current cavity expansion theory. For instance, Forrestal and Tzou (Forrestal and Tzou, 1997) developed a spherical cavity expansion model for concrete targets with the assumption that the material surrounding the projectile yields according to the Mohr-Coulomb criterion with a tension cutoff. Feng et al. (Feng et al., 2015) used the modified Drucker-Prager Cap plasticity criterion to describe the concrete behavior in their dynamic cavity expansion model, which was validated by the penetration test data of NC targets with strengths of 36 MPa and 51 MPa. Nevertheless, for an UHPFRC target under high speed penetrations, its constitutive relationship exhibits nonlinear characteristics due to the extremely high pressure around the projectile-target interface (Kong et al., 2017). As a consequence, nonlinear yield criteria, such as the Hoek-Brown criterion and the Griffith criterion, can be more appropriate than their linear counterparts when applying the cavity expansion theory for UHPFRC (Kong et al., 2017). Few relevant research can be

found utilizing nonlinear yield criteria in cavity expansion models. Among the limited studies, Meng et al. (Meng et al., 2018) established a finite cavity expansion model based on the modified Griffith criterion; Kong et al. (Kong et al., 2017) introduced a hyperbolic yield criterion and Murnaghan equation of state (EOS) to describe the plastic response of concrete. It should be pointed out that the former study focused on NC targets confined in steel tubes, i.e. the boundary condition in the model cannot be applied for common UHPFRC targets without confinement; whereas the latter one had complex EOS with many parameters determined by complicated experiments, such as triaxial compression tests and flyer-plate-impact tests (Kong et al., 2017).

In addition, most of the current cavity expansion models do not take the rate dependency of the concrete material into account. However, at a high penetration velocity, the projectile produces very high strain rates in the surrounding concrete and the rate effect of the concrete material can considerably affect the ballistic resistance (CEB-FIP, 2010). Forrestal et al. (Forrestal et al., 1994; Forrestal and Tzou, 1997; Warren and Forrestal, 1998) conducted a series of investigations on the cavity expansion model for various materials. The strain rate effect was presented in their models for the aluminum target (Warren and Forrestal, 1998), but it was ignored in the models for concrete material (Forrestal and Tzou, 1997). More recently, Feng et al. (Feng et al., 2015) incorporated the concrete rate dependency into the Drucker-Prager criterion. The resistances obtained using the cavity expansion models with and without considering the rate effect were compared in their study, and the results suggested that the resistance is underestimated in the case without the rate effect, especially under high speed penetrations. This, therefore, shows the significance of catering for the rate dependency of concrete in the dynamic cavity expansion model.

In this chapter, new DOP predictive models for single- and multi-layered UHPFRC are proposed on the basis of an improved dynamic spherical cavity expansion theory. The Hoek-Brown criterion (Hoek et al., 2002) is introduced to describe the nonlinear response of the UHPFRC material, and the rate effect under projectile penetration is considered to present the enhancement of the UHPFRC resistance. Based on the obtained cavity surface stress, the DOP predicting formulae for the single- and multi-layered UHPFRC are developed and validated by the experimental data in literature and in Chapter 6. The proposed models can accurately predict the DOP of the UHPFRC, and the varying mechanical properties in the layered targets can be considered.

7.2 Improved constitutive model for UHPFRC

7.2.1 Hoek-Brown criterion

The Hoek-Brown criterion is initially introduced to describe the failure of hard rocks under confining pressures, and it has been widely used for the design of underground excavations (Hoek et al., 2002). The non-linear form distinguishes the Hoek-Brown criterion from linear failure criteria, e.g. the Mohr-Coulomb criterion (Eberhardt, 2012). Similar to the underground rocks under the confining pressure, in a UHPFRC target, the inner UHPFRC surrounding the projectile is also under high confinement generated by the outer UHPFRC layer due to the lateral inertia at high strain rates (Li et al., 2006). Considering this, the Hoek-Brown criterion is applied in the cavity expansion model for UHPFRC in this study.

The expression of the Hoek-Brown criterion is given as (Hoek et al., 2002):

$$\sigma_1 = \sigma_3 + \sigma_{c,s} \sqrt{m \frac{\sigma_3}{\sigma_{c,s}} + 1} \quad (7-1)$$

where $\sigma_{c,s}$ is the static compressive strength; σ_1 and σ_3 are the major and minor principal stresses, respectively; m is a parameter related to material properties. It is suggested that m is affected by the ratio of compressive to tensile strengths as well as the friction coefficient of the material (Meng et al., 2018).

The above equation can be transformed to:

$$\left(\frac{\sigma_1}{\sigma_{c,s}} - \frac{\sigma_3}{\sigma_{c,s}} \right)^2 - 1 = m \frac{\sigma_3}{\sigma_{c,s}} \quad (7-2)$$

Since the strength ratio of UHPFRC differs with that of NC, the values of m should also be different. To obtain the relationship between m and $\sigma_{c,s}$, triaxial compression test data of concrete with strengths from around 90 MPa to 170 MPa are collected (Farnam et al., 2010; Ren et al., 2016; Sovják et al., 2013b; Xie et al., 1995). Fitting the data gives the corresponding values of m to various $\sigma_{c,s}$, as shown in Fig. 7-1a. The equations in the figure represent the trend line of each group. An empirical equation to determine m is then proposed in Fig. 7-1b and expressed as ($\sigma_{c,s}$ in MPa):

$$m = 23.22 - 0.11\sigma_{c,s} \quad (7-3)$$

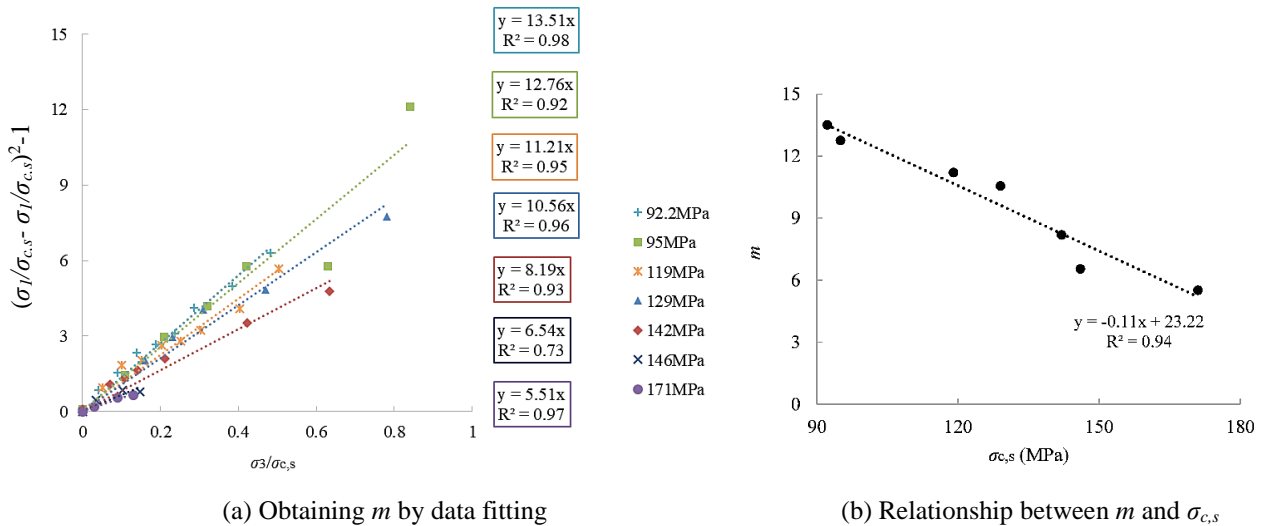


Fig. 7-1 Hoek- Brown parameter m

7.2.2 Rate dependency incorporation

The target material surrounding a penetrating projectile is under high pressure and high strain rate. As presented in literature (Li et al., 2006; Millard et al., 2010; Tran et al., 2015), the behavior of cementitious material is considerably affected by the strain rate, and the strength of concrete is significantly improved under a high loading rate. Consequently, the failure criterion of the

cementitious material differs under impact loadings and it requires modifications to address the rate effect in the case of penetration.

DIF is commonly used to gauge the strength enhancement. The DIF formulae recommended in (CEB-FIP, 2010) are most widely accepted for concrete, and they are incorporated in the constitutive relation of UHPFRC in the present study to account for the rate effects. The expressions are given as Eqs. 7-4 and 7-5:

- For tensile strength (CEB-FIP, 2010):

$$\text{DIF}_t = \left(\frac{\dot{\epsilon}_t}{\dot{\epsilon}_{t0}} \right)^{0.018} \quad \text{for } \dot{\epsilon}_t \leq 10 \text{ s}^{-1} \quad (7-4a)$$

$$\text{DIF}_t = 0.0062 \left(\frac{\dot{\epsilon}_t}{\dot{\epsilon}_{t0}} \right)^{1/3} \quad \text{for } \dot{\epsilon}_t > 10 \text{ s}^{-1} \quad (7-4b)$$

where $\dot{\epsilon}_t$ is the tensile strain rate, the static reference rate $\dot{\epsilon}_{t0} = 1 \times 10^{-6} \text{ s}^{-1}$.

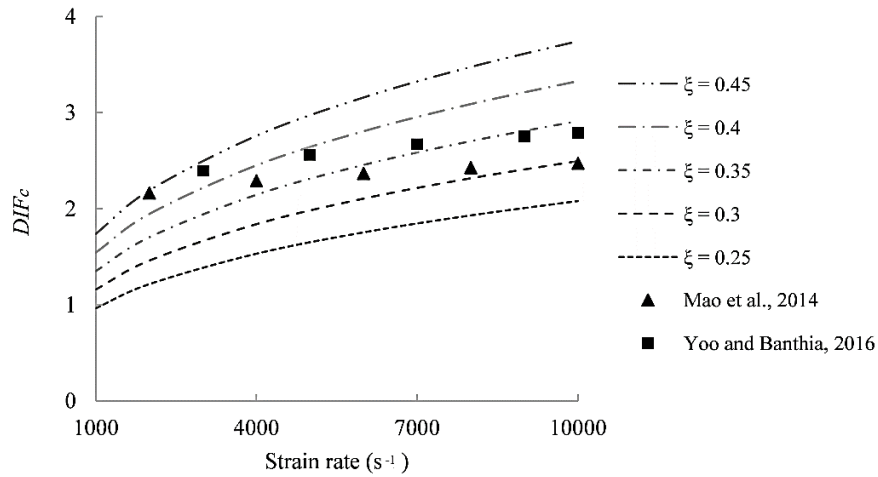
- For compressive strength (CEB-FIP, 2010):

$$\text{DIF}_c = \left(\frac{\dot{\epsilon}_c}{\dot{\epsilon}_{c0}} \right)^{0.014} \quad \text{for } \dot{\epsilon}_c \leq 30 \text{ s}^{-1} \quad (7-5a)$$

$$\text{DIF}_c = 0.012 \left(\frac{\dot{\epsilon}_c}{\dot{\epsilon}_{c0}} \right)^{1/3} \quad \text{for } \dot{\epsilon}_c > 30 \text{ s}^{-1} \quad (7-5b)$$

where $\dot{\epsilon}_c$ is the compressive strain rate, the static reference rate $\dot{\epsilon}_{c0} = 30 \times 10^{-6} \text{ s}^{-1}$.

It should be noted that these DIF formulae are developed based on dynamic tests of NC, applying them directly for UHPFRC would overestimate its rate effect. On the one hand, the compressive strength enhancement of concrete material at a high strain rate, e.g. at the order of $10^3 \sim 10^4 \text{ s}^{-1}$, is mainly attributed to the lateral inertia and the lateral confinement (Li et al., 2006). That is to say, the obtained DIF is not a material property and the true strength increase is much less than the prediction in CEB-FIP Model Code 2010. On the other hand, the DIF of concrete material tends to decrease as its strength increases, i.e. UHPFRC should have smaller DIFs compared to NC (Hassan and Wille, 2017; Hou et al., 2018; Ngo et al., 2007). Nonetheless, since current DIF formulae for UHPFRC are mainly established with small amounts of data, most studies still employ the CEB-FIP Model Code to predict the DIFs of UHPFRC (Yoo and Banthia, 2017b). In the present study, these recommended DIF formulae in (CEB-FIP, 2010) are also adopted, but the obtained cavity surface stress is then corrected with a reduction factor ζ when using it in the DOP predictive model (see Section 7.4.1). By comparing the literature-given DIFs of UHPFRC (Mao et al., 2014; Yoo and Banthia, 2016) and those given in CEB-FIP Model Code 2010 at strain rates between $10^3 \sim 10^4 \text{ s}^{-1}$, $\zeta = 0.35$ is determined in the present study for both compression and tension (an example of the rate effect on $\sigma_{c,s}$ is shown in Fig. 7-2). More discussion on ζ is presented in Section 7.4.3.

Fig. 7-2 DIF reduction factor ξ

7.3 Dynamic cavity expansion model

7.3.1 Descriptions

The following assumptions are proposed in this study for the dynamic cavity expansion model:

- The projectile penetration process in a semi-infinite UHPFRC target is treated as a spherical cavity expanding from zero to a radius r_c at a constant velocity \dot{r}_c . Since the cavity is expanded from zero initial radius, a steady-state is immediately reached and the cavity keeps expanding under a constant pressure (Rubin et al., 2016; Salgado and Prezzi, 2007). Consequently, the acceleration term \ddot{r}_c and other higher order terms equal to zero.
- Similar to previous studies concerning NC (Fang et al., 2014; Feng et al., 2015; Meng et al., 2018), the UHPFRC target is assumed to be incompressible to simplify the problem with possible analytical solutions. The assumption is acceptable since the micro structure of UHPFRC is much denser than that of NC (Cao et al., 2019a; Cao and Yu, 2018). Nevertheless, the negligence of material compressibility may lead to the overestimation of the cavity surface stress to a certain degree (Forrestal and Tzou, 1997), and this should be kept in mind in the error analysis of DOP models.
- For an incompressible material, no density change occurs during the deformation; and the radial stress, displacement and velocity at the interfaces of different response regions should be continuous according to the Hugoniot interface conditions (Warren and Forrestal, 1998).
- In the comminuted region, the UHPFRC material obeys the Hoek-Brown criterion described in Section 7.2.1. The principal stress components satisfy the conditions $\sigma_1 = \sigma_r$, $\sigma_3 = \sigma_\theta$ in the spherical coordinates (Meng et al., 2018).

Based on the above assumptions, the schematic diagram of the cavity expansion model is illustrated in Fig. 7-3. Two possible response modes could be invoked in the surrounding material depending on the expansion velocity \dot{r}_c : (1) at a relatively small \dot{r}_c , three response regions are presented in the target, namely a comminuted region ($r_c < r \leq r_p$), a cracked region ($r_p < r \leq r_{cr}$) and an elastic region ($r_{cr} < r \leq r_e$). r_c , r_p , r_{cr} and r_e are the radii of the cavity and the above corresponding regions (Fig. 7-3a); (2) as the expansion velocity \dot{r}_c increases and exceeds a critical value \dot{r}_i , the comminuted region reaches and surpasses the cracked region, viz. $r_p \geq r_{cr}$, then the response of the target turns to an elastic-comminuted mode as shown in Fig. 7-3b.

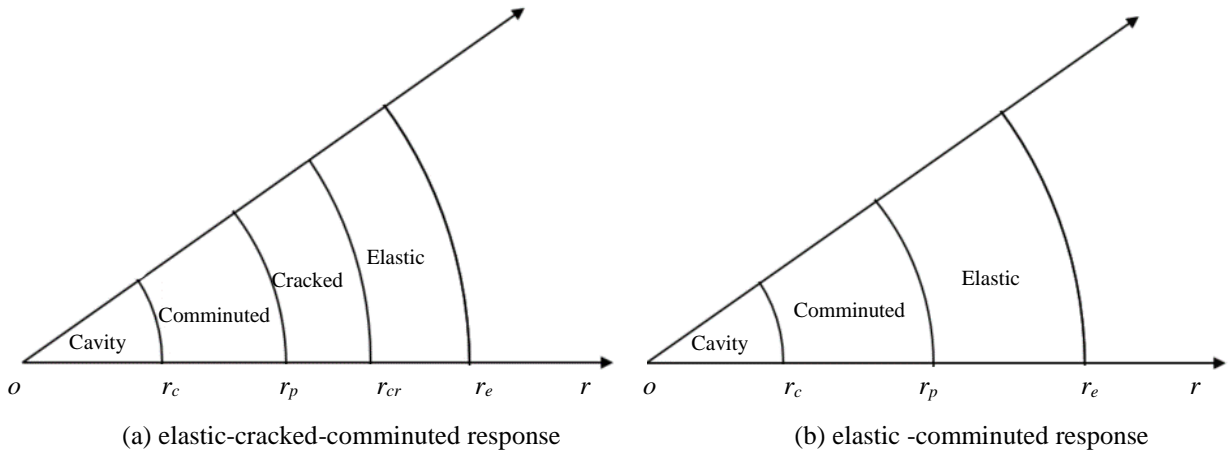


Fig. 7-3 Response regions in UHPFRC target

7.3.2 Elastic-cracked-comminuted response

The conservation equations of momentum and mass are (Warren and Forrestal, 1998):

$$\frac{\partial \sigma_r}{\partial r} + 2 \frac{\sigma_r - \sigma_\theta}{r} = -\rho \left(\frac{\partial v}{\partial t} + v \frac{\partial v}{\partial r} \right) \quad (7-6)$$

$$\rho_0 \frac{\partial}{\partial r} \left[(r-u)^3 \right] = 3\rho r^2 \quad (7-7)$$

where σ_r and σ_θ are the radial and circumferential Cauchy stress components, measured positive in compression; r is the radius; v is the particle velocity in the radial direction at time t , and u is the particle displacement (both measured positive outward); ρ_0 and ρ are the densities in the un-deformed and deformed states. For an incompressible material, $\rho = \rho_0$ (Warren and Forrestal, 1998).

The steady state expansion assumption leads to the boundary condition that the displacement at the cavity boundary must equal to its radius (Salgado and Prezzi, 2007). Therefore, Eq. 7-7 can be integrated with $u(r=r_c) = r_c$ (Meng et al., 2018), and it yields

$$u = r - (r^3 - r_c^3)^{1/3} \quad (7-8)$$

The particle displacement and velocity are related by (Warren and Forrestal, 1998):

$$\frac{\partial u}{\partial t} = v \left(1 - \frac{\partial u}{\partial r} \right) \quad (7-9)$$

Eqs. 7-8 and 7-9 then result in the expression of v (Warren and Forrestal, 1998):

$$v = \left(\frac{r_c}{r} \right)^2 \dot{r}_c \quad (7-10)$$

The strain rates at the radial and the circumferential directions are then obtained as (Warren and Forrestal, 1998):

$$\dot{\varepsilon}_r = -\frac{\partial v}{\partial r} = 2 \frac{r_c^2 \dot{r}_c}{r^3} \quad (7-11)$$

$$\dot{\varepsilon}_\theta = \frac{v}{r} = \frac{r_c^2 \dot{r}_c}{r^3} \quad (7-12)$$

Substituting Eqs. 7-11 and 7-12 into Eq. 7-6 gives the new form of the momentum conservation equation; and letting the acceleration term $\ddot{r}_c = 0$ leads to:

$$\frac{\partial \sigma_r}{\partial r} + 2 \frac{\sigma_r - \sigma_\theta}{r} = -2\rho \dot{r}_c^2 \left(\frac{r_c}{r^2} - \frac{r_c^4}{r^5} \right) \quad (7-13)$$

- Elastic region

The response equations in the elastic region is presented in (Warren and Forrestal, 1998). The particle displacement and velocity are (Warren and Forrestal, 1998):

$$u = \frac{r_c^3}{3r^2} \quad (7-14)$$

$$v = \left(\frac{r_c}{r} \right)^2 \dot{r}_c \quad (7-15)$$

Thus the elastic strains at the radial and the circumferential directions are

$$\varepsilon_r = -\frac{\partial u}{\partial r} = \frac{2}{3} \left(\frac{r_c}{r} \right)^3 \quad (7-16)$$

$$\varepsilon_\theta = -\frac{u}{r} = -\frac{1}{3} \left(\frac{r_c}{r} \right)^3 \quad (7-17)$$

The elastic strains and the Hook's law lead to the relationship between the elastic stresses:

$$\sigma_r - \sigma_\theta = \frac{E}{1+\mu} (\varepsilon_r - \varepsilon_\theta) = \frac{E}{1+\mu} \left(\frac{r_c}{r} \right)^3 \quad (7-18)$$

where E is the elastic modulus; μ is the Poisson's ratio and it equals to 0.5 for incompressible materials. Integration of Eq. 7-13 with Eq. 7-18 yields the expressions of the elastic stresses:

$$\sigma_r = \frac{2}{3} \frac{E}{1+\mu} \left(\frac{r_c}{r} \right)^3 + 2\rho \dot{r}_c^2 \left(\frac{r_c}{r} - \frac{1}{4} \left(\frac{r_c}{r} \right)^4 \right) \quad (7-19)$$

$$\sigma_\theta = -\frac{1}{3} \frac{E}{1+\mu} \left(\frac{r_c}{r} \right)^3 + 2\rho \dot{r}_c^2 \left(\frac{r_c}{r} - \frac{1}{4} \left(\frac{r_c}{r} \right)^4 \right) \quad (7-20)$$

At the elastic-cracked region interface $r = r_{cr}$, the circumferential stress reaches the dynamic tensile strength $\sigma_{t,d}$ of the material, viz. $\sigma_{\theta}(r = r_{cr}) = -\sigma_{t,d}(r = r_{cr})$. The dynamic tensile strength can be obtained by

$$\sigma_{t,d}(r=r_{cr}) = \text{DIF}_{t(r=r_{cr})} \times \sigma_{t,s} \quad (7-21)$$

where $\sigma_{t,s}$ is the static tensile strength of UHPFRC, and $\text{DIF}_{t(r=r_{cr})}$ can be calculated by Eq. 7-4 with

$$\dot{\varepsilon}_t = \dot{\varepsilon}_{\theta}(r=r_{cr}) = \frac{r_c^2 \dot{r}_c}{r_{cr}^3} \quad (7-22)$$

By combining Eqs. 7-20 ~ 7-22 and the boundary condition $\sigma_{\theta}(r = r_{cr}) = -\sigma_{t,d}(r = r_{cr})$, one gets the equations to determine the location of the elastic-cracked region interface, viz. r_{cr} :

$$2\rho\dot{r}_c^2 \left(\frac{r_c}{r_{cr}} - \frac{1}{4} \left(\frac{r_c}{r_{cr}} \right)^4 \right) - \frac{1}{3} \frac{E}{1+\mu} \left(\frac{r_c}{r_{cr}} \right)^3 = -\sigma_{t,s} \left(\frac{r_c^2 \dot{r}_c}{r_{cr}^3 \dot{\varepsilon}_{t0}} \right)^{1.016\delta} \quad \text{for } \dot{\varepsilon}_t \leq 30 \text{ s}^{-1} \quad (7-23a)$$

$$2\rho\dot{r}_c^2 \left(\frac{r_c}{r_{cr}} - \frac{1}{4} \left(\frac{r_c}{r_{cr}} \right)^4 \right) - \frac{1}{3} \frac{E}{1+\mu} \left(\frac{r_c}{r_{cr}} \right)^3 = -\sigma_{t,s} \beta \left(\frac{r_c^2 \dot{r}_c}{r_{cr}^3 \dot{\varepsilon}_{t0}} \right)^{\frac{1}{3}} \quad \text{for } \dot{\varepsilon}_t > 30 \text{ s}^{-1} \quad (7-23b)$$

- **Cracked region**

In the cracked region, the circumferential stress $\sigma_{\theta} = 0$, and Eq. 7-13 turns into

$$\frac{\partial \sigma_r}{\partial r} + 2 \frac{\sigma_r}{r} = -2\rho\dot{r}_c^2 \left(\frac{r_c}{r^2} - \frac{r_c^4}{r^5} \right) \quad (7-24)$$

Integrating Eq. 7-24 yields the expression of the radial stress in the cracked region:

$$\sigma_r = \frac{C_0}{r^2} - 2\rho\dot{r}_c^2 \left(\frac{r_c}{r} + \frac{1}{4} \left(\frac{r_c}{r} \right)^4 \right) \quad (7-25)$$

where C_0 is a constant that needs to be solved by considering the continuous condition at r_{cr} , i.e. the radial stress $\sigma_r(r = r_{cr})$ solved by Eq. 7-25 equals to the solution of Eq. 7-19. Therefore, C_0 can be obtained and the radial stress in the cracked region is

$$\sigma_r = \left(4\rho\dot{r}_c^2 \frac{r_c}{r_{cr}} + \frac{2}{3} \frac{E}{1+\mu} \left(\frac{r_c}{r_{cr}} \right)^3 \right) \left(\frac{r_{cr}}{r} \right)^2 - 2\rho\dot{r}_c^2 \left(\frac{r_c}{r} + \frac{1}{4} \left(\frac{r_c}{r} \right)^4 \right) \quad (7-26)$$

Similarly, the location of the cracked-comminuted regions interface, viz. r_p , can be determined by the boundary condition that the radial stress reaches the dynamic compressive strength $\sigma_{c,d}$ at r_p :

$$\sigma_{r(r=r_p)} = \sigma_{c,d(r=r_p)} \quad (7-27)$$

The dynamic compressive strength $\sigma_{c,d}(r = r_p)$ can be obtained by

$$\sigma_{c,d(r=r_p)} = \text{DIF}_{c(r=r_p)} \times \sigma_{c,s} \quad (7-28)$$

where $\text{DIF}_{c(r=r_p)}$ is calculated by Eq. 7-5 with

$$\dot{\epsilon}_c = \dot{\epsilon}_{r(r=r_p)} = \frac{2r_c^2 \dot{r}_c}{r_p^3} \quad (7-29)$$

Then r_p is solved by:

$$-\frac{1}{2} \rho \dot{r}_c^2 \left(\frac{r_c}{r_p} \right)^4 + \left(4 \rho \dot{r}_c^2 \frac{r_c}{r_{cr}} + \frac{2}{3} \frac{E}{1+\mu} \left(\frac{r_c}{r_{cr}} \right)^3 \right) \left(\frac{r_{cr}}{r_p} \right)^2 - 2 \rho \dot{r}_c^2 \left(\frac{r_c}{r_p} \right) = \sigma_{c,s} \left(\frac{2r_c^2 \dot{r}_c}{r_p^3 \dot{\epsilon}_{c,0}} \right)^{1.026\alpha} \quad \text{for } \dot{\epsilon}_c \leq 30 \text{ s}^{-1} \quad (7-30a)$$

$$-\frac{1}{2} \rho \dot{r}_c^2 \left(\frac{r_c}{r_p} \right)^4 + \left(4 \rho \dot{r}_c^2 \frac{r_c}{r_{cr}} + \frac{2}{3} \frac{E}{1+\mu} \left(\frac{r_c}{r_{cr}} \right)^3 \right) \left(\frac{r_{cr}}{r_p} \right)^2 - 2 \rho \dot{r}_c^2 \left(\frac{r_c}{r_p} \right) = \sigma_{c,s} \gamma \left(\frac{2r_c^2 \dot{r}_c}{r_p^3 \dot{\epsilon}_{c,0}} \right)^{1/3} \quad \text{for } \dot{\epsilon}_c > 30 \text{ s}^{-1} \quad (7-30b)$$

- **Comminuted region**

The UHPFRC material in the comminuted region yields according to the nonlinear Hoek-Brown criterion. Substituting Eq. 7-1 to the momentum conservation equation Eq. 7-13 with $\sigma_1 = \sigma_r$, $\sigma_3 = \sigma_\theta$ and replacing $\sigma_{c,s}$ by $\sigma_{c,d}$ lead to

$$\frac{\partial \sigma_r}{\partial r} = -\frac{2}{r} \left(\sqrt{\frac{m^2 + 4}{4} \sigma_{c,d}^2 + m \sigma_{(r)} \sigma_{c,d}} - \frac{m}{2} \sigma_{c,d} \right) - 2 \rho \dot{r}_c^2 \left(\frac{r_c}{r^2} - \frac{r_c^4}{r^5} \right) \quad (7-31)$$

Further incorporating DIF_c and the strain rate results in:

$$\frac{\partial \sigma_r}{\partial r} = -\frac{2}{r} \left(\sqrt{\frac{m^2 + 4}{4} \left(\sigma_{c,s} \left(\frac{2r_c^2 \dot{r}_c}{r^3 \dot{\epsilon}_{c,0}} \right)^{1.026\alpha} \right)^2 + m \sigma_{(r)} \sigma_{c,s} \left(\frac{2r_c^2 \dot{r}_c}{r^3 \dot{\epsilon}_{c,0}} \right)^{1.026\alpha}} - \frac{m}{2} \sigma_{c,s} \left(\frac{2r_c^2 \dot{r}_c}{r^3 \dot{\epsilon}_{c,0}} \right)^{1.026\alpha} \right) - 2 \rho \dot{r}_c^2 \left(\frac{r_c}{r^2} - \frac{r_c^4}{r^5} \right) \quad \text{for } \dot{\epsilon}_c \leq 30 \text{ s}^{-1} \quad (7-32a)$$

$$\frac{\partial \sigma_r}{\partial r} = -\frac{2}{r} \left(\sqrt{\frac{m^2 + 4}{4} \left(\sigma_{c,s} \gamma \left(\frac{2r_c^2 \dot{r}_c}{r^3 \dot{\epsilon}_{c,0}} \right)^{1/3} \right)^2 + m \sigma_{(r)} \sigma_{c,s} \gamma \left(\frac{2r_c^2 \dot{r}_c}{r^3 \dot{\epsilon}_{c,0}} \right)^{1/3}} - \frac{m}{2} \sigma_{c,s} \gamma \left(\frac{2r_c^2 \dot{r}_c}{r^3 \dot{\epsilon}_{c,0}} \right)^{1/3} \right) - 2 \rho \dot{r}_c^2 \left(\frac{r_c}{r^2} - \frac{r_c^4}{r^5} \right) \quad \text{for } \dot{\epsilon}_c > 30 \text{ s}^{-1} \quad (7-32b)$$

The numerical solutions of the above nonlinear differential equations can be solved by Runge-Kutta method with the boundary conditions given in Eqs. 7-27 and 7-30. Finally, the radial stress at the cavity surface $\sigma_r(r=r_c)$ can be obtained with $r=r_c$ in the solutions.

7.3.3 Elastic-comminuted response

- **Critical expansion velocity**

At a relatively high expansion velocity $\dot{r}_c > \dot{r}_i$, the cracked region diminishes and the UHPFRC target turns into an elastic-comminuted response. The critical expansion velocity \dot{r}_i can be obtained by letting the radius of the cracked region equal to that of the comminuted region, viz. $r_{cr} = r_p = r_i$, where r_i is the critical radius for the response transfer. Substituting $r_{cr} = r_p = r_i$ into Eqs. 7-23 and 7-30 with $\dot{r}_c = \dot{r}_i$ results in the following equations:

$$2\rho\dot{r}_i^2 \left(\frac{r_c}{r_i} - \frac{1}{4} \left(\frac{r_c}{r_i} \right)^4 \right) - \frac{1}{3} \frac{E}{1+\mu} \left(\frac{r_c}{r_i} \right)^3 = -\sigma_{t,d(r=r_i)} \quad (7-33)$$

$$-\frac{1}{2} \rho \dot{r}_i^2 \left(\frac{r_c}{r_i} \right)^4 + \frac{2}{3} \frac{E}{1+\mu} \left(\frac{r_c}{r_i} \right)^3 + 2\rho\dot{r}_i^2 \frac{r_c}{r_i} = \sigma_{c,d(r=r_i)} \quad (7-34)$$

Solving the equations results in the solutions of the critical expansion velocity \dot{r}_i as well as the critical radius r_i .

- **Elastic region**

For the elastic-comminuted response, the expressions of the elastic stresses σ_r and σ_θ are the same as Eqs. 7-19 and 7-20.

Similarly, the location of the elastic-comminuted region interface r_p can be determined by substituting Eq. 7-27 to Eq. 7-19:

$$\frac{2}{3} \frac{E}{1+\mu} \left(\frac{r_c}{r_p} \right)^3 + 2\rho\dot{r}_c^2 \left(\frac{r_c}{r_p} - \frac{1}{4} \left(\frac{r_c}{r_p} \right)^4 \right) = \sigma_{c,s} \left(\frac{2r_c^2 \dot{r}_c}{r_p^3 \dot{\epsilon}_{c,0}} \right)^{1.026\alpha} \quad \text{for } \dot{\epsilon}_c \leq 30 \text{ s}^{-1} \quad (7-35a)$$

$$\frac{2}{3} \frac{E}{1+\mu} \left(\frac{r_c}{r_p} \right)^3 + 2\rho\dot{r}_c^2 \left(\frac{r_c}{r_p} - \frac{1}{4} \left(\frac{r_c}{r_p} \right)^4 \right) = \sigma_{c,s} \gamma \left(\frac{2r_c^2 \dot{r}_c}{r_p^3 \dot{\epsilon}_{c,0}} \right)^{1/3} \quad \text{for } \dot{\epsilon}_c > 30 \text{ s}^{-1} \quad (7-35b)$$

- **Comminuted region**

In the comminuted region, the UHPFRC material yields according to the Hoek-Brown criterion. The radial stress at the cavity surface r_c is still solved by Eq. 7-32 but with a different boundary condition, i.e. r_p for the elastic-comminuted response is given by the solution of Eq. 7-35 rather than by that of Eq. 7-30, which is for the elastic-cracked-comminuted response.

The general procedure to obtain the radial stress at the cavity surface $\sigma_r(r=r_c)$ is shown in Fig. 7-4. The required initial input parameters include $r_c, \dot{r}_c, \sigma_{c,s}, \sigma_{t,s}, E, \rho, m$, where r_c equals to the radius of the projectile; $\sigma_{c,s}$ and $\sigma_{t,s}$ are the static compressive and tensile strengths of the UHPFRC, respectively; E and ρ are its elastic modulus and density; m is obtained by Eq. 7-3. \dot{r}_c can represent the particle velocity ahead of the projectile, and it depends on the projectile velocity V and the shape of the projectile head (Forrestal and LuK, 1992; Longcope et al., 1999; Meng et al., 2018):

$$\dot{r}_c = V \cos \varphi \quad (7-36)$$

where φ is the angle between the axial of the projectile and the normal direction of the projectile head surface.

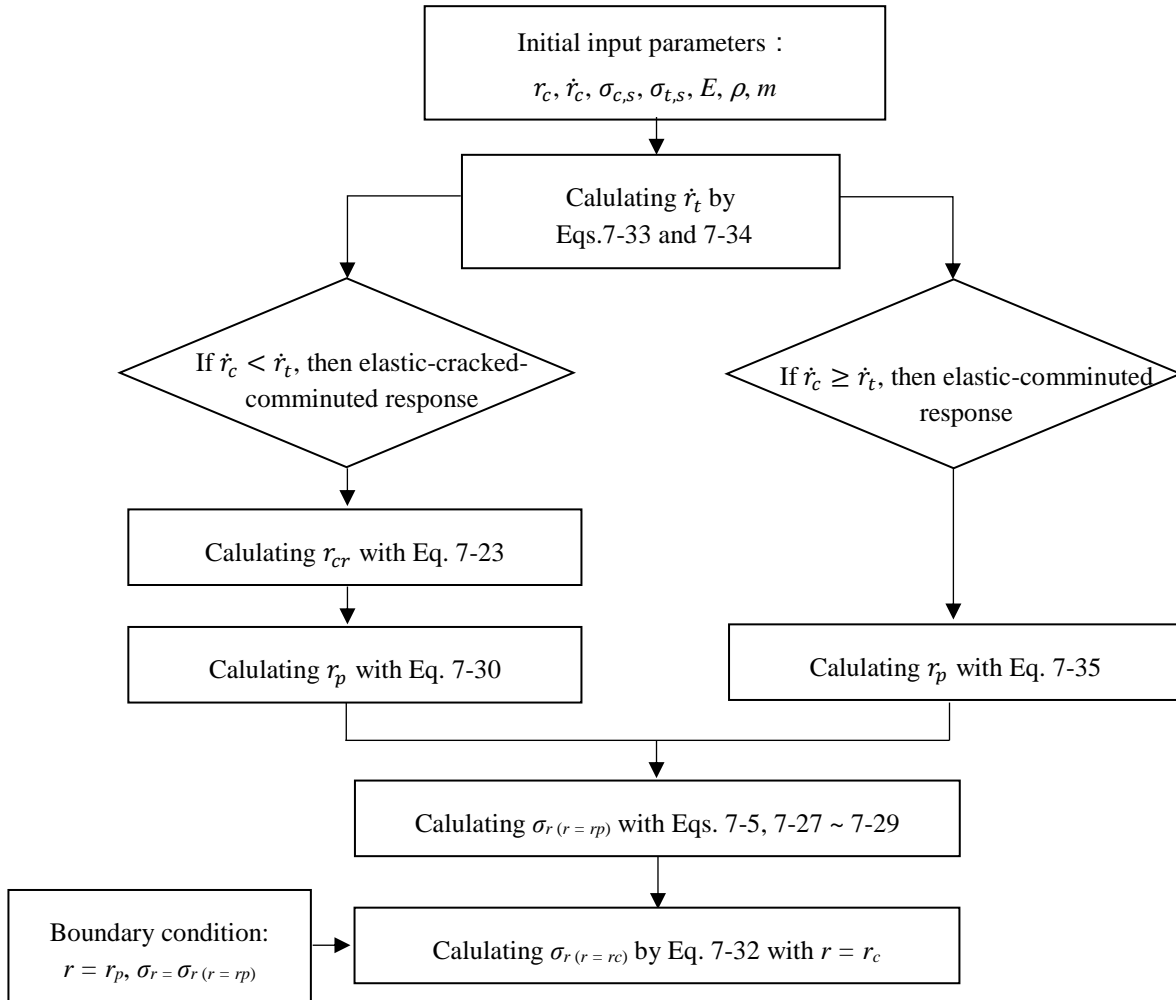


Fig. 7-4 Procedure to calculate the cavity surface stress

7.4 DOP model for single-layered UHPFRC

7.4.1 DOP predictive model

Based on the above dynamic cavity expansion theory, a model for predicting the DOP in single-layered UHPFRC target is proposed in this section. The penetration process of the projectile in the target can be divided into two stages: a cratering stage and a following tunneling stage (Forrestal et al., 1994). The cavity expansion theory is used for the tunneling stage, while the depth of the cratering

stage is assumed to be kd , where d is diameter of the projectile and $k = 0.707 + h/d$ with h being the projectile head length (Li and Chen, 2003). For simplification, only rigid projectile at normal impact is discussed in this study (Forrestal et al., 1994).

From Newton's second law of motion, one gets:

$$F = -M \frac{dV}{dt} = -MV \frac{dV}{dx} \quad (7-37)$$

where F is the axial force on the projectile head; M is the mass of the projectile. V and x are the projectile traveling velocity and the penetration depth at time t .

The axial force at the cratering stage F_1 is assumed to be proportional to the depth x , as suggested by the experimental deceleration data (Forrestal et al., 1994; Li and Chen, 2003). Thus, the expression can be presented as (Forrestal et al., 1994):

$$F_1 = C_1 x \quad \text{for } x \leq kd \quad (7-38)$$

where C_1 is a constant.

Combining Eqs. 7-37 and 7-38, and considering the initial condition of the cratering stage: $x(t=0) = 0$, $V(t=0) = V_0$, as well as its end condition: $x(t=t_1) = kd$, $V(t=t_1) = V_1$ give the expression of F_1 :

$$F_1 = \frac{M(V_0^2 - V_1^2)}{(kd)^2} x \quad \text{for } x \leq kd \quad (7-39)$$

At the tunneling stage, the axial force on the projectile head is obtained by integrating the normal stress σ_n on the projectile head surface s (Meng et al., 2018):

$$F_2 = \int \sigma_n \cos \varphi ds \quad \text{for } x > kd \quad (7-40)$$

In the presented model, the normal stress σ_n is replaced by the reduced cavity surface stress $\xi \sigma_{r(r=r_c)}$, in which $\sigma_{r(r=r_c)}$ is the radial stress at the cavity surface obtained in Section 7.3, and ξ is a reduction factor discussed in Section 7.2.2. Therefore, one gets

$$F_2 = \int \xi \sigma_{r(r=r_c)} \cos \varphi ds \quad \text{for } x > kd \quad (7-41)$$

To obtain the closed-form DOP formula, the numerical results from the dynamic cavity expansion model is curve-fitted with the following form as suggested by (Feng et al., 2015; Forrestal and Tzou, 1997):

$$\frac{\xi \sigma_{r(r=r_c)}}{\sigma_{c,s}} = A + B \left(\sqrt{\frac{\rho}{\sigma_{c,s}}} \dot{i}_c \right) + C \left(\sqrt{\frac{\rho}{\sigma_{c,s}}} \dot{i}_c \right)^2 \quad (7-42)$$

where the first term A is the radial stress at the cavity surface under the quasi-static response (Forrestal and Tzou, 1997), and it can be determined by setting $\dot{i}_c = 0$ and DIFs = 0 in the equations in Section 7.3. The second term in the right-hand side of Eq. 7-42 accounts for the rate effect, while the third

term is reported to be associated with the inertia of the target (Bornord and Hanagud, 1975; Feng et al., 2015). More detailed derivation of the inertia term can be found in (Bornord and Hanagud, 1975). The parameters B and C are determined by fitting the solutions of the cavity expansion model with $\sqrt{\rho/\sigma_{c,s}} \dot{r}_c$ being the independent variable and $\xi \sigma_{r(r=r_c)}/\sigma_{c,s}$ being the dependent variable.

Note that A , B and C are determined based on the theoretical solution of $\sigma_r(r=r_c)$ solved according to Fig. 7-4, i.e. with given conditions for the projectile and the target, the values of A , B and C can be calculated analytically. For instance, we can take the 7.62 mm projectile and the following concrete properties as the initial inputs: $r_c = d/2 = 3.81$ mm, $\sigma_{ts} = 13.5$ MPa, $E = 46.8$ GPa, $\rho = 2500$ kg/m³, then the parameters in Eq. 7-42 can be determined and the results are plotted in Table 7-1.

Table 7-1 Parameters A , B and C in an example

σ_{cs} (MPa)	Elastic-cracked-comminuted response			Elastic-comminuted response		
	A	B	C	A	B	C
105	11.83	1.05	4.07	15.48	0.35	2.91
120	10.42	1.26	4.02	14.50	0.58	2.55
135	8.89	2.02	3.49	12.61	0.83	2.46
150	8.16	1.86	3.52	11.26	1.32	2.20
165	7.17	3.39	2.30	9.92	1.10	2.35

As described in Section 7.3, the UHPFRC target has different responses depending on the cavity expansion velocity \dot{r}_c . Consequently, A , B and C also have different values under the elastic-cracked-comminuted or the elastic-comminuted responses, depending on the impact velocity and the shape of the projectile head (see Eq. 7-36 for the relationship between the impact velocity and the cavity expansion velocity). In general, the elastic-comminuted mode yields a higher A than the elastic-cracked-comminuted mode (see Table 7-1), which agrees with the trend in (Forrestal and Tzou, 1997; Kong et al., 2016c). Moreover, it is noteworthy that an extremely high impact velocity is usually required to invoke the elastic-comminuted response in UHPFRC. For example, in the case of the 135 MPa target against the 7.62 mm \times 51 AP projectile, the critical expansion velocity \dot{r}_c is around 402 m/s and the corresponding critical impact velocity is more than 1400 m/s.

Combination of Eqs. 7-36, 7-41 and 7-42 provides the axial force at the tunneling stage:

$$F_2 = \frac{\pi d^2 \sigma_{c,s}}{4} \left(A + BN_I \sqrt{\frac{\rho}{\sigma_{c,s}}} V + CN_{II} \left(\sqrt{\frac{\rho}{\sigma_{c,s}}} V \right)^2 \right) \quad \text{for } x > kd \quad (7-43)$$

where N_I and N_{II} are the shape coefficients of the projectile head, and their expressions are given below (see Fig. 7-5) (Feng et al., 2015; Kong et al., 2017):

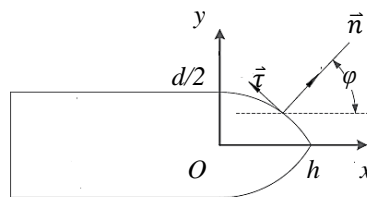


Fig. 7-5 Schematic of an arbitrary projectile (Feng et al., 2015)

$$N_I = \frac{8}{d^2} \int_0^h \frac{yy'^2}{\sqrt{1+y'^2}} dx \quad (7-44a)$$

$$N_{II} = \frac{8}{d^2} \int_0^h \frac{yy'^3}{1+y'^2} dx \quad (7-44b)$$

For an ogive-head projectile, the coefficients are (Forrestal and Tzou, 1997):

$$N_I = \frac{(4\psi-1)^{1.5}}{3\psi} + \frac{(2\psi-1)^2(4\psi-1)^{0.5}}{2\psi} - \psi(2\psi-1) \left(\pi - 2 \sin^{-1} \left(\frac{2\psi-1}{2\psi} \right) \right) \quad (7-45a)$$

$$N_{II} = \frac{8\psi-1}{24\psi^2} \quad (7-45b)$$

where ψ is the caliber-radius-head (CRH) of the projectile.

For a conical-head projectile (Kong et al., 2017):

$$N_I = \frac{1}{\sqrt{1+4\psi^2}} \quad (7-46a)$$

$$N_{II} = \frac{1}{1+4\psi^2} \quad (7-46b)$$

where ψ is the ratio between the projectile head length h and the diameter d .

For a blunt-head projectile (Kong et al., 2017):

$$N_I = \frac{8\psi^2}{3} - \frac{(4\psi^2-1)^{3/2}}{3\psi} \quad (7-47a)$$

$$N_{II} = 1 - \frac{1}{8\psi^2} \quad (7-47b)$$

where ψ is the ratio between the sphere radius and the projectile diameter.

For a flat-head projectile, $N_I = N_{II} = 1$.

The continuous condition of the axial force at the end of the cratering stage, i.e. the beginning of the tunneling stage, requires $F_1(t=t_1) = F_2(t=t_1)$. Together with the boundary condition $x(t=t_1) = kd$, $V(t=t_1) = V_1$, one obtains the initial penetration velocity at the tunneling stage V_1 :

$$\frac{M(V_0^2 - V_1^2)}{kd} = \frac{\pi d^2 \sigma_{c,s}}{4} \left(A + BN_I \sqrt{\frac{\rho}{\sigma_{c,s}}} V_1 + CN_{II} \left(\sqrt{\frac{\rho}{\sigma_{c,s}}} V_1 \right)^2 \right) \quad (7-48)$$

Furthermore, substituting Eq. 7-43 into Eq. 7-37 yields

$$\frac{\pi d^2 \sigma_{c,s}}{4} \left(A + BN_I \sqrt{\frac{\rho}{\sigma_{c,s}}} V + CN_{II} \left(\sqrt{\frac{\rho}{\sigma_{c,s}}} V \right)^2 \right) = -MV \frac{dV}{dx} \quad (7-49)$$

Integrating Eq. 7-49 and considering $x(t = t_1) = kd$, $V(t = t_1) = V_1$ with V_1 solved by Eq. 7-48 provide the relationship between x and V . Letting $V = 0$ leads to the final DOP of the projectile (Forrestal and Tzou, 1997):

$$DOP = D_I \ln \left(1 + \frac{BN_I}{A} \sqrt{\frac{\rho}{\sigma_{c,s}}} V_1 + \frac{CN_{II} \rho V_1^2}{A \sigma_{c,s}} \right) + 2D_I D_{II} \left(\tan^{-1} D_{II} - \tan^{-1} \left(\frac{2D_{II} CN_{II}}{BN_I} \sqrt{\frac{\rho}{\sigma_{c,s}}} V_1 + D_{II} \right) \right) + kd \quad (7-50)$$

where $D_I = \frac{2M}{\pi d^2 \rho CN_{II}}$, $D_{II} = BN_I / \sqrt{4ACN_{II} - (BN_I)^2}$.

7.4.2 Model validation

The UHPFRC penetration test data in (Yu et al., 2016; Zhang et al., 2005) and Chapter 6 are taken to validate the proposed DOP predictive model for single-layered UHPFRC. The quasi-static solution of the proposed model without considering the rate effect (determined by setting $\dot{\epsilon}_c = 0$ and DIFs = 0 in the equations in Section 7.3) and the calculated DOP from the following predicting formulae are also presented and compared. The listed ACE, modified NDRC and UKAEA formulae are recommended by the US Army manual, the Air force manual and the British Army manual, respectively, for evaluating the DOP in concrete (Li et al., 2006).

- ACE formula (Li et al., 2006):

$$\frac{DOP}{d} = \frac{3.5 \times 10^{-4}}{\sqrt{\sigma_{c,s}}} \left(\frac{M}{d^3} \right) d^{0.215} V_0^{1.5} + 0.5 \quad (7-51)$$

- Modified NDRC formula (Li et al., 2006):

$$G_n = 3.8 \times 10^{-5} \frac{N^* M}{d \sqrt{\sigma_{c,s}}} \left(\frac{V_0}{d} \right)^{1.8} \quad (7-52a)$$

$$\frac{DOP}{d} = 2G_n^{0.5} \quad \text{for } G_n \geq 1 \quad (7-52b)$$

$$\frac{DOP}{d} = G_n + 1 \quad \text{for } G_n < 1 \quad (7-52c)$$

where N^* is the nose shape factor, $N^* = 0.72, 0.84, 1.0$ and 1.14 for flat, blunt, spherical and sharp heads, respectively.

- UKAEA formula (Li et al., 2006):

$$\frac{DOP}{d} = 0.275 - (0.0756 - G_n)^{0.5} \quad \text{for } G_n \leq 0.0726 \quad (7-53a)$$

$$\frac{DOP}{d} = (4G_n - 0.242)^{0.5} \quad \text{for } 0.0726 < G_n < 1.0605 \quad (7-53b)$$

$$\frac{DOP}{d} = G_n + 1 \quad \text{for } G_n \geq 1.065 \quad (7-53c)$$

where G_n is the same as that given in the modified NDRC formula, viz. Eq. 7-52a.

- Forrestal semi-empirical formula (Forrestal et al., 1994; Frew et al., 1998):

$$DOP = \frac{2M}{\pi d^2 \rho N_2} \ln \left(1 + \frac{N_2 \rho V_1^2}{S_f \sigma_{c,s}} \right) + 2d \quad (7-54a)$$

$$V_1^2 = \frac{2MV_0^2 - \pi d^3 S_f \sigma_{c,s}}{2M + \pi d^3 N_2 \rho} \quad (7-54b)$$

$$S_f = 82.6 \sigma_{c,s}^{-0.544} \quad (7-54c)$$

- Li-Chen formula (Li et al., 2006; Li and Chen, 2003):

$$DOP = \frac{2dN}{\pi} \ln \left(\frac{1 + I/N}{1 + k\pi/4N} \right) + kd \quad (7-55a)$$

$$I = \frac{1}{S_{l-c}} \frac{MV_0^2}{d^3 \sigma_{c,s}} \quad (7-55b)$$

$$S_{l-c} = 72 \sigma_{c,s}^{-0.5} \quad (7-55c)$$

$$N_{l-c} = \frac{1}{N_{II}} \frac{M}{d^3 \rho} \quad \text{for an ogive-head projectile} \quad (7-55d)$$

(1) 135 MPa UHPFRC target

The penetration test in (Yu, 2015) is chosen as an example to validate the proposed DOP predictive model. The UHPFRC with hybrid fibers is impacted by the 7.62 mm \times 51 AP projectile at a velocity around 830 m/s (Yu, 2015). This impact velocity leads to a cavity expansion velocity around 230 m/s, which is smaller than the critical expansion velocity \dot{r}_c of approximately 402 m/s. Therefore, the target has the elastic-cracked-comminuted response mode in this example. The input parameters are given in Table 7-2, in which the elastic modulus is calculated by $E = 8010 \sigma_{c,s}^{0.36}$ (in MPa) (Alsaman et al., 2017). Based on Eq. 7-3, $m = 8.37$ can be obtained. More parameters related to the projectile can be found in (Holmen et al., 2017). From the quasi-static response of the cavity expansion model, $A = 8.89$ is obtained. The curve-fitting procedure for obtaining parameters B and C is shown in Fig. 7-6, and $B = 2.02$, $C = 3.49$ are determined.

Table 7-2 Model inputs for the 135 MPa target

Compressive strength $\sigma_{c,s}$ (MPa)	Tensile strength $\sigma_{t,s}$ (MPa)	Elastic modulus E (GPa)	Density ρ (kg/m ³)
135	13.5	46.8	2500
Projectile diameter d (mm)	Projectile mass M (g)	Projectile CRH ψ	
7.62	10.5	5.0	

The predicted DOP by the proposed model with the above inputs is illustrated in Fig. 7-7. It can be observed that the proposed model successfully predicts the DOP in the 135 MPa UHPFRC target, while the static solution results in the underestimation of the impact resistance, indicating the necessity of incorporating the rate effect in the predictive model. To be more precise, the experimentally

determined DOP at 827.2 m/s and 832.6 m/s are around 57 mm and 60 mm, respectively, which are about 3% lower and 1% higher than the predicted DOP. The static solutions are approximately 30% and 25% higher than the experimental DOP, indicating the necessity of considering the rate effect on the resistant pressure.

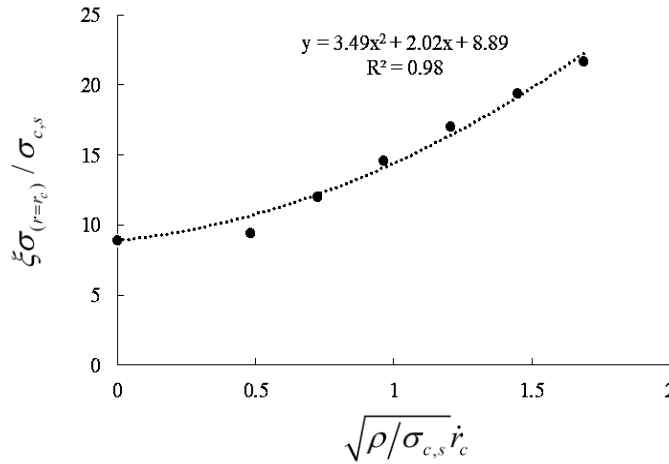


Fig. 7-6 Procedure to obtain B and C

With regards to the empirical formulae, the UKAEA formula provides results close to those of the proposed model and the errors are around 8% and 12%. Additionally, the ACE formula also gives acceptable predictions with errors smaller than 17%, whereas the other formulae fail to make appropriate estimations. Both the Forrestal formula and the Li-Chen formula underestimate the penetration resistance of the target, i.e. the given DOP are more than 60% higher than the experimental data. This may be attributed to the empirical constants S given by Eqs. 7-54c and 7-55c, as they are obtained by fitting the experimental data of concrete targets with relatively low strengths than UHPFRC (Forrestal et al., 1996, 1994; Frew et al., 1998). On the contrary, the modified NDRC formula clearly falls beneath the experimental results, indicating overestimations of the UHPFRC resistance.

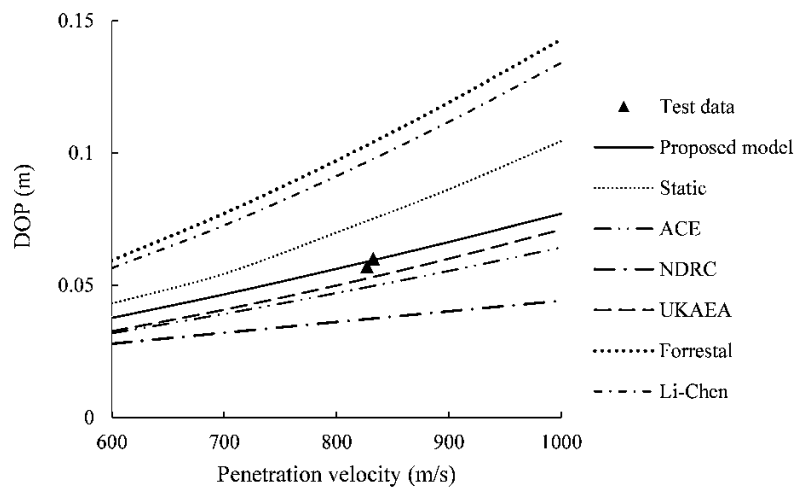


Fig. 7-7 Model validation of the 135 MPa UHPFRC

(2) 151 MPa UHPFRC target

To further validate the model, the experimental data of 151 MPa UHPFRC targets impacted by a 12.6 mm projectile at velocities between 635 ~ 685 m/s (Zhang et al., 2005) are compared with the predicted results, as shown in Fig. 7-8. The critical expansion velocity \dot{r}_i is about 391 m/s, i.e. the critical impact velocity to invoke the elastic-comminuted response is approximately 1200 m/s. Hence, the response of the UHPFRC target is again the elastic-cracked-comminuted mode. The relevant input parameters are given in Table 7-3, and $m = 6.61$ is calculated according to $\sigma_{c,s}$. The coefficients in Eq. 7-42 are determined as $A = 8.17$, $B = 0.83$ and $C = 4.30$ by applying the same curve-fitting process.

Table 7-3 Model inputs for the 151 MPa target

Compressive strength $\sigma_{c,s}$ (MPa)	Tensile strength $\sigma_{t,s}$ (MPa)	Elastic modulus E (GPa)	Density ρ (kg/m ³)
150.9	13.0	48.8	2500
Projectile diameter d (mm)	Projectile mass M (g)	Projectile CRH ψ	
12.6	15.0	2.5	

In Fig. 7-8, a good agreement can be observed between the experimental DOP and the predicted ones by the proposed model. The errors are in the range of 0.1% ~ 5%, except for one data at 634.2 m/s (the error is 16%), which may be attributed to the scatter of the test data. The static DOP reveals that ignoring the rate effect of the UHPFRC target leads to a smaller penetration resistance and therefore the overestimation of the DOP. It is noteworthy that this overestimation is smaller than that in the previous example as the penetration velocity in this example is lower, i.e. the influences of the concrete rate sensitivity are less obvious.

Furthermore, when the penetration velocity is smaller than around 800 m/s, the UKAEA formula gives a prediction similar to that of the NDRC formula, while it is getting close to the proposed model at higher velocities. The modified NDRC model presents a reasonable estimate in this example in contrast to the underestimation in the previous 135 MPa example. In addition, DOP given by the ACE formula are approximately 22% ~ 25% smaller than the test results, suggesting the instability of this formulae when used for UHPFRC targets. As with the Forrestal formula and the Li-Chen formula, they fail again to achieve accurate results by overestimating the DOP.

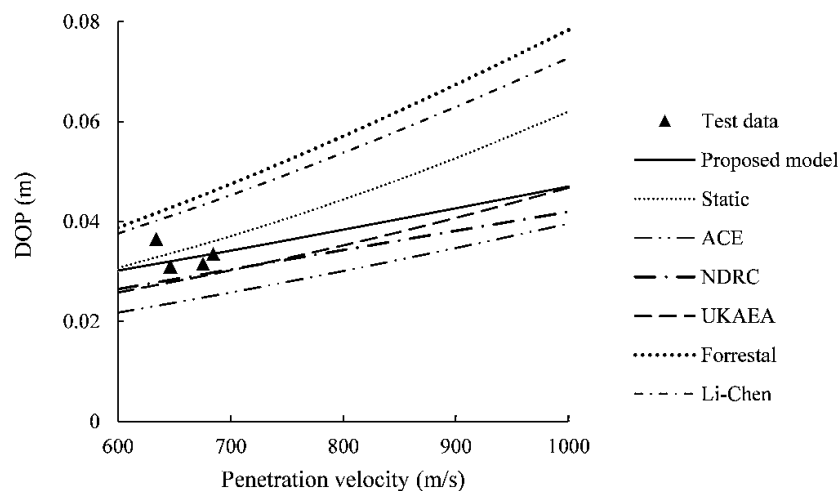


Fig. 7-8 Model validation of the 151 MPa UHPFRC

(3) 161 MPa UHPFRC target

DOP of the U16a1s(90) UHPFRC target in Chapter 6, with the compressive strength of around 161 MPa, is further used for the model validation. The relevant input parameters are given in Table 7-4. Similarly, the target shows an elastic-cracked-comminuted response mode, and $m = 5.48$, $A = 7.70$, $B = 3.96$ and $C = 1.60$ are obtained.

Table 7-4 Model inputs for the 161 MPa target

Compressive strength $\sigma_{c,s}$ (MPa)	Tensile strength $\sigma_{t,s}$ (MPa)	Elastic modulus E (GPa)	Density ρ (kg/m ³)
161.3	14.6	49.9	2500
Projectile diameter d (mm)	Projectile mass M (g)	Projectile CRH ψ	
7.62	10.5	5.0	

Fig 7-9 illustrates the comparisons of the experimental DOP and the predicted ones, exhibiting accurate predictions of the proposed model. To specify, the differences are about 1% and 2%, respectively, for the 840.7 m/s and 847.3 m/s penetration cases. Regarding to the empirical formulae, the UKAEA formula gives acceptable predictions, and the corresponding errors are approximately 8% and 7%. The ACE formula gives larger errors, which are around 16% and 15% for the 840.7 m/s and 847.3 m/s cases, respectively. The modified NDRC significantly underestimates the DOP, while the Forrestal formula and the Li-Chen formula again overestimate the DOP.

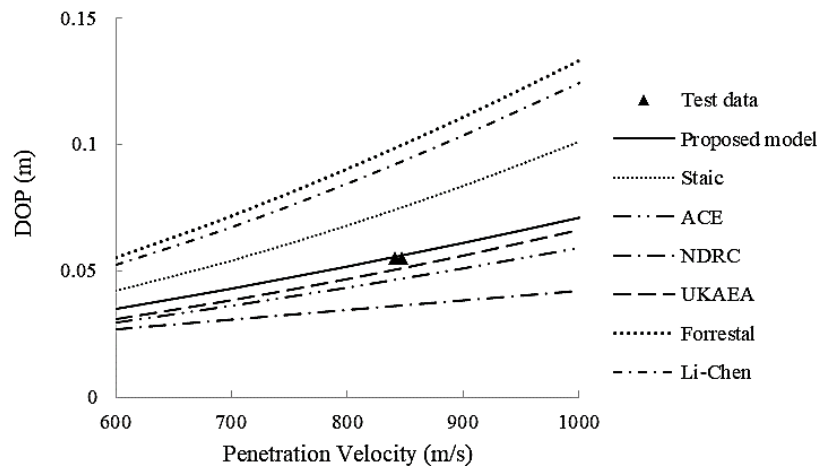


Fig. 7-9 Model validation of the 161 MPa UHPFRC

7.4.3 Parameter discussion

Section 7.4.2 confirms the reliability of the proposed model for the single-layered UHPFRC, in this section the model is applied to analyze the influences of the concrete strength and the reduction factor. The experiment of the 135 MPa UHPFRC in Section 7.4.2 is taken as a basis, and the elastic-cracked-comminuted response mode is considered in the following discussions.

(1) Influence of target compressive strength

To investigate the effects of the compressive strength $\sigma_{c,s}$, this study chooses various concrete strengths namely 75 MPa, 105 MPa, 135 MPa, and 165 MPa as inputs for the proposed DOP predictive model. The effects of $\sigma_{c,s}$ on the cracked and the comminuted regions are plotted in Fig. 7-10. It is

found that the radius of the cracked region r_{cr} in the UHPFRC target increases with the decrease of the penetration velocity V (Fig. 7-10a). In contrast, the radius of the comminuted region r_p , which suggests the area of the comminuted region, generally tends to decrease with the reduction of V at dynamic conditions. An exception exists at the ballistic end $V = 0$, which corresponds to the quasi-static expansion $\dot{\epsilon}_c = 0$. A larger r_p is observed when the projectile velocity approaches zero (Fig. 7-10b). This trend is theoretically reasonable because the static resistance is smaller than its dynamic counterpart, attributing to a larger comminuted area at $\dot{\epsilon}_c = 0$. Moreover, the difference between r_{cr} and r_p , viz. $r_{cr} - r_p$, can be used as an indicator to show the area of the cracked region; and it first increases gradually to a peak and then decreases with the reducing projectile velocity (Fig. 7-10c).

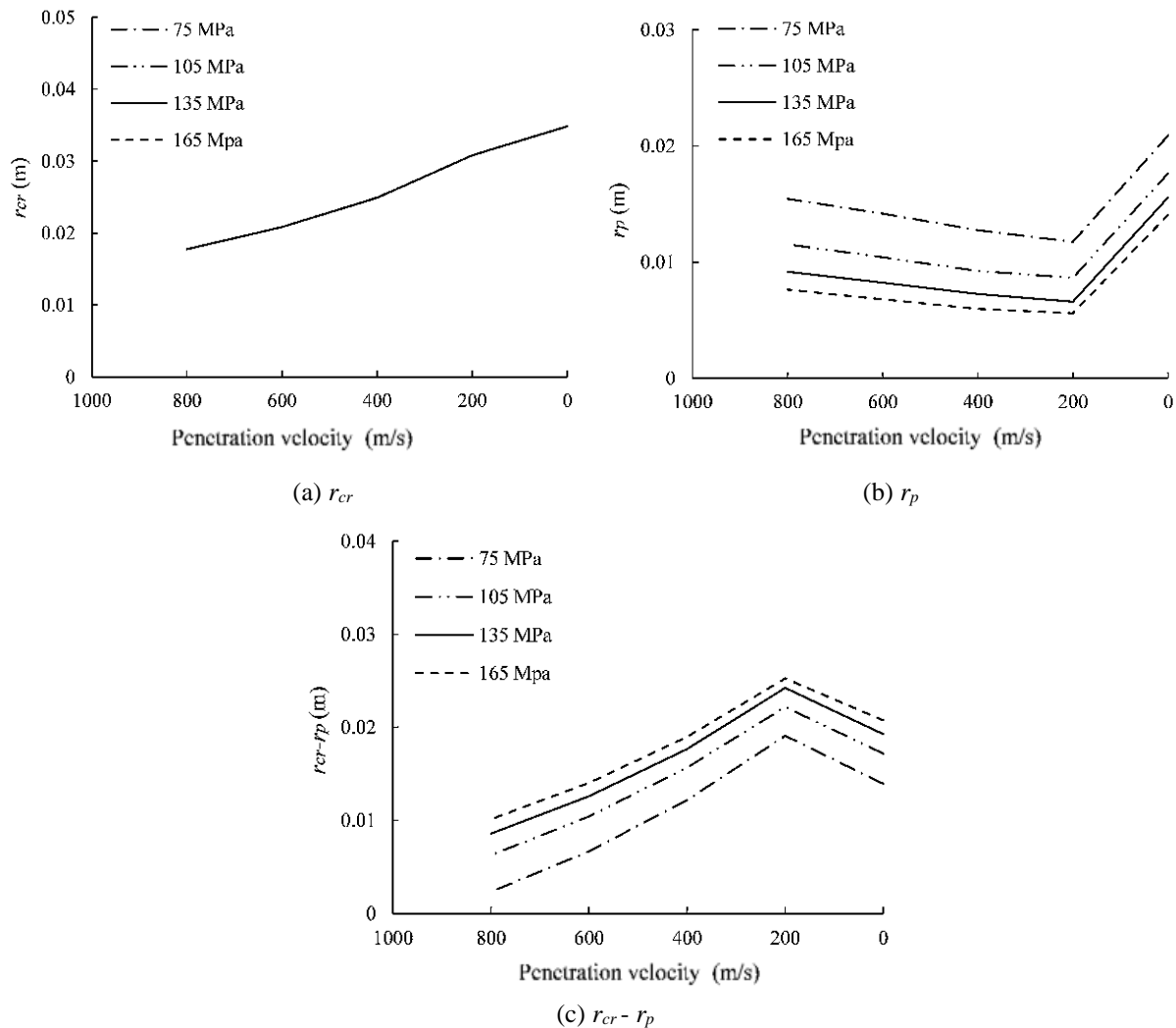


Fig. 7-10 Influence of compressive strength $\sigma_{c,s}$ on response radius

In addition, the influences of $\sigma_{c,s}$ on the distributions of the response zones are also exhibited in Fig. 7-10. Firstly, the area of the comminuted region (shown by r_p) is smaller in the concrete target with a higher $\sigma_{c,s}$. Secondly, the cracked region (shown by $r_{cr} - r_p$) increases with the increase of $\sigma_{c,s}$, reflecting the increasing brittleness of the higher strength concrete. Thirdly, $\sigma_{c,s}$ barely affects the total cracking area in the target (r_{cr} curves are overlapped in Fig. 7-10a), agreeing with the experimental observation that target cracking is more affected by the fiber amount than the concrete strength

(Almusallam et al., 2013). Furthermore, the critical expansion velocity \dot{r}_t for the target transferring from the comminuted-cracked-elastic response to the comminuted-elastic one increases with the increase of $\sigma_{c,s}$, while the corresponding radius of the comminuted region at the moment of transformation r_t decreases (see Fig. 7-11).

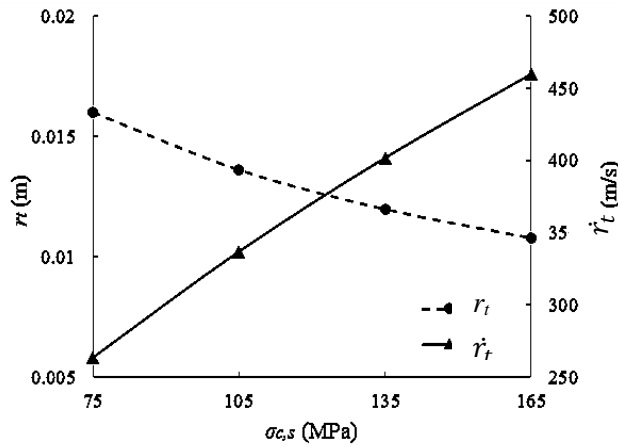
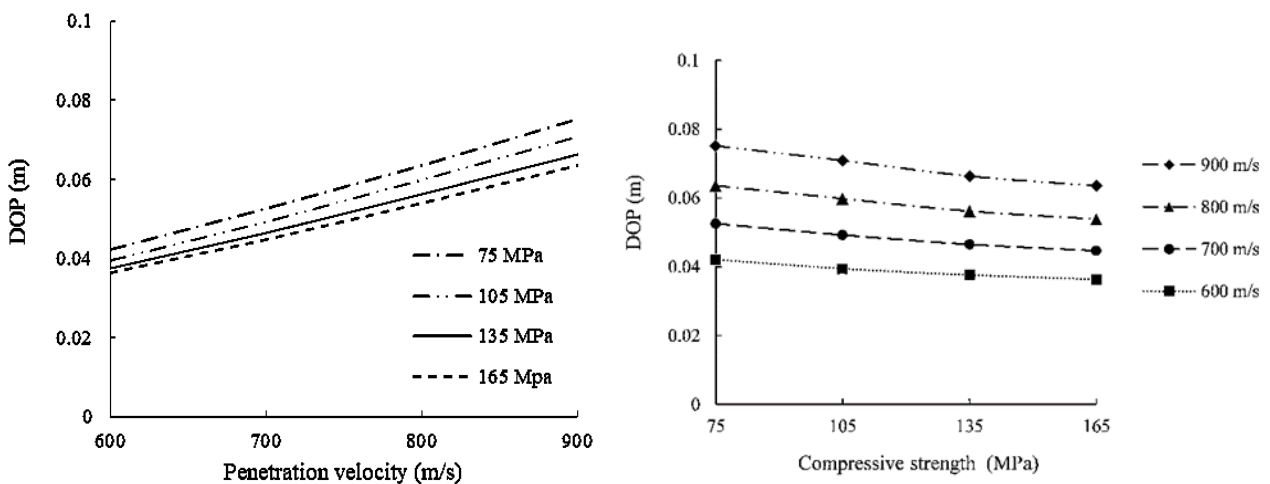


Fig. 7-11 Influence of compressive strength $\sigma_{c,s}$ on response transformation

Fig. 7-12 illustrates the DOP in the concrete targets with different $\sigma_{c,s}$. As observed, DOP decreases with the increase of $\sigma_{c,s}$. However, this decrease is not linear and it becomes very limited when $\sigma_{c,s}$ reaches a threshold, in this example the value is around 105 MPa. For instance, the DOP reduction at 600 m/s is around 7% when $\sigma_{c,s}$ increases from 75 MPa to 105 MPa, while it is about 3% when $\sigma_{c,s}$ is improved from 135 MPa to 165 MPa. This trend is also observed in some ballistic experiments in previous studies, suggesting that the DOP no longer decreases prominently when the target strength is larger than a certain value, e.g. approximately 90 MPa in (H. Wu et al., 2015a) or 100 MPa in (Zhang et al., 2005). Additionally, the decrease of DOP caused by the increasing $\sigma_{c,s}$ is more obvious at a higher penetration velocity. This can be seen by comparing the slopes of the DOP curves at 600 m/s and 900 m/s in Fig. 7-12b. The 900 m/s curve has a larger slope than its 600 m/s counterpart, indicating that increasing $\sigma_{c,s}$ has more prominent effects on the DOP when it is under a relatively high-velocity penetration.



(a) DOP versus penetration velocity

(b) DOP versus compressive strength

Fig. 7-12 Influence of compressive strength $\sigma_{c,s}$ on DOP

(2) Influence of target tensile strength

The effects of the concrete tensile strength are analyzed with $\sigma_{t,s} = 7.5$ MPa, 10.5 MPa, 13.5 MPa and 16.5 MPa. Fig. 7-13 show the changes of r_{cr} , r_p and $r_{cr} - r_p$ with $\sigma_{t,s}$ and V . Similarly, r_{cr} increases with the decreasing V . On the other hand, r_p first decreases and then increases significantly after V drops to a turning point near the ballistic end; whereas $r_{cr} - r_p$ first increases to the peak, after which it reduces remarkably. The turning points in Figs. 7-13b and 7-13c indicate that there exists a projectile velocity around 200 m/s at which the target has a minimum comminuted region and a maximum cracked region.

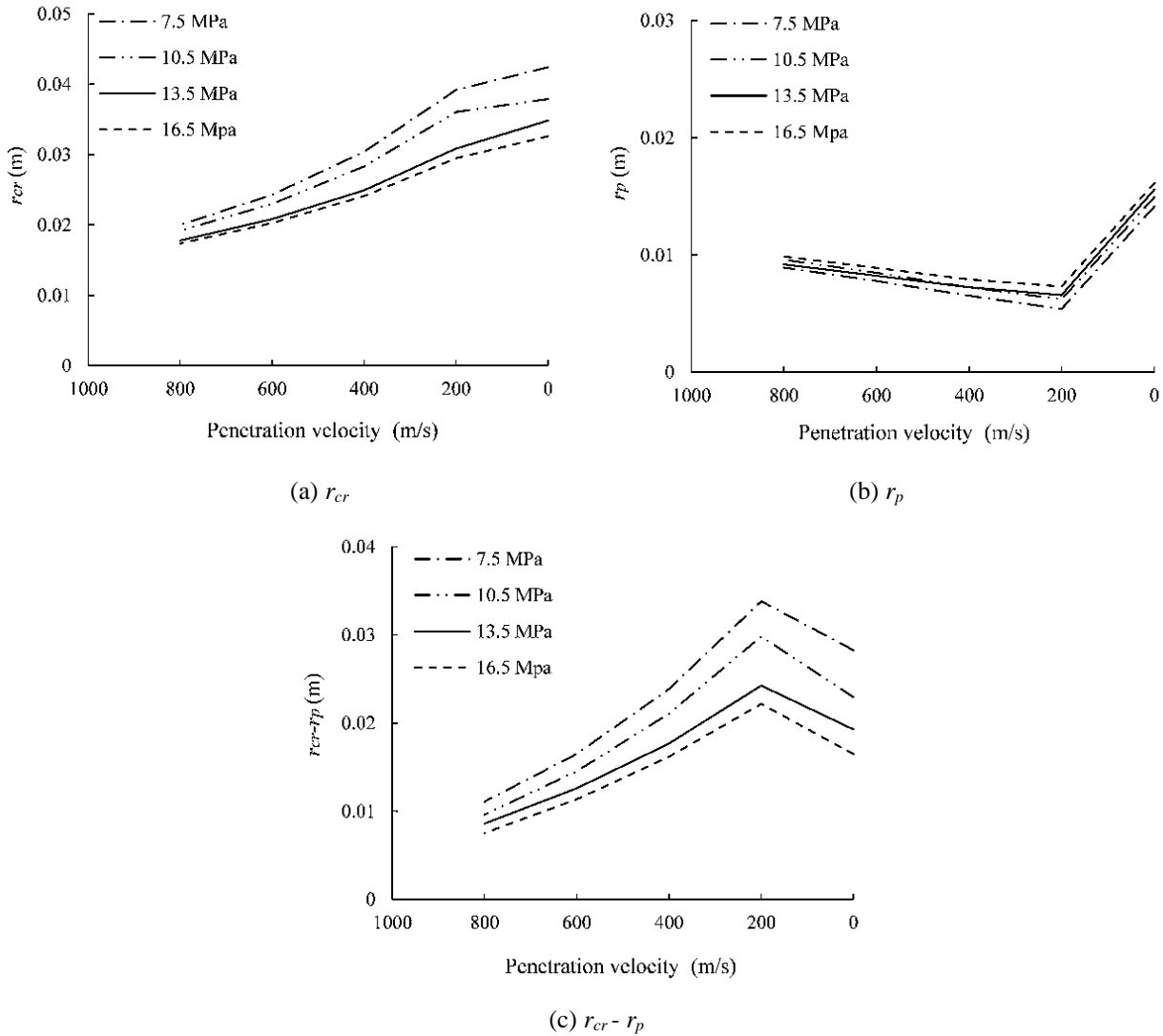


Fig. 7-13 Influence of tensile strength $\sigma_{t,s}$ on response radius

In contrast to the effects of $\sigma_{c,s}$, $\sigma_{t,s}$ has obvious influences on the total damage area r_{cr} but very limited effects on the comminuted region r_p (see Figs. 7-13a and 7-13b). In addition, increasing $\sigma_{t,s}$ significantly reduces the area of the cracked region $r_{cr} - r_p$, and the reduction is more evident at a smaller projectile velocity (see Fig. 7-13c). Moreover, as shown in Fig. 7-14, the critical transforming radius r_t seems not sensitive to the change of $\sigma_{t,s}$, whereas the critical cavity expansion velocity \dot{r}_t decreases with the increasing $\sigma_{t,s}$. Consequently, the target with a higher $\sigma_{t,s}$ transfers from the

comminuted-cracked-elastic response into the comminuted-elastic one at a lower velocity, and the corresponding radius of the comminuted region at the moment of the transfer is more dependent on the target compressive strength than on its tensile strength.

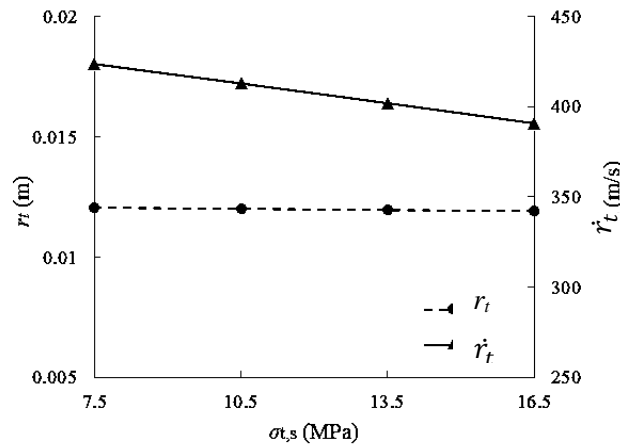
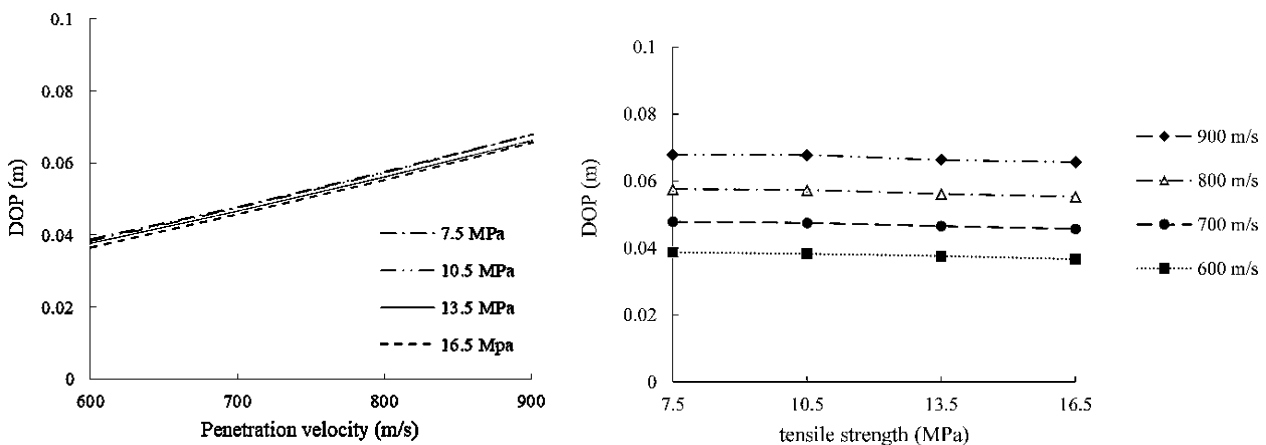


Fig. 7-14 Influence of tensile strength $\sigma_{t,s}$ on response transformation

The DOP of the targets with different $\sigma_{t,s}$ at different penetration velocities are given in Fig. 7-15. Insignificant reduction of DOP is observed with the increase of $\sigma_{t,s}$, suggesting that improving the target tensile strength, e.g. by adding fibers, is not an efficient approach to reduce the DOP in concrete target. This trend coincides with the experimental finding that increasing the fiber amount in UHPFRC has very limited contribution to the DOP although it has prominent effects on controlling the cracked area in the target surface (Almusallam et al., 2013). Furthermore, taking into consideration of both Figs. 7-13c and 7-15, it is further deduced that the proposed DOP predictive model may be able to reflect the effects of fibers on the UHPFRC resistance via $\sigma_{t,s}$, as the fibers contribute to reducing the cracked area (increasing $\sigma_{t,s}$ results in a smaller $r_{cr} - r_p$ in Fig. 7-13c) but have limited effects on the DOP (DOP is almost insensitive to $\sigma_{t,s}$ in Fig. 7-15). This may be done by establishing the relationship between the fiber amount and the target tensile strength, and incorporating it into the dynamic cavity expansion model. However, the confirmation of this point and the exact relationship between the fiber amount and the DOP require more studies and will be of interest in the further research.



(a) DOP versus penetration velocity

(b) DOP versus tensile strength

Fig. 7-15 Influence of tensile strength $\sigma_{t,s}$ on DOP

(3) Influence of the reduction factor

The reduction factor ζ is used to correct the strength overestimation of the target due to the “artificial” rate effect given in CEB-FIP Model Code 2010, and its effects are analyzed to evaluate the correctness of introducing this factor. As shown in Fig. 7-16, B increases remarkably with the increase of ζ while C experienced an insignificant drop. The prominent increase of B with a small growth of ζ shows its sensitivity, which demonstrates the importance of choosing the reduction factor appropriately. Moreover, the dependence of B on ζ is in accordance with its physical meaning, i.e. B is the dominate parameter reflecting the rate effect (Feng et al., 2015). The improvement of B , therefore, presents the enhanced rate effect on the resistant pressure with an increasing ζ .

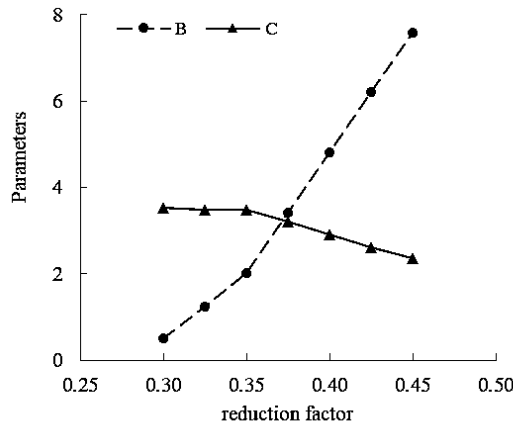


Fig. 7-16 Influence of the reduction factor ζ

The calculated DOP with different ζ are plotted in Table 7-5. The calculated DOP is observed to decrease with the increase of ζ . This trend is reasonable because with a smaller ζ , the theoretical resistant pressure on the projectile $\zeta\sigma_r(r=rc)$ is also smaller, which consequently attributes to a larger DOP in the UHPFRC targets. When $\zeta=0.30$, the rate effect is over-reduced that the dynamic resistance is underestimated. Consequently, the predicted DOP are 11.9% and 7.3% higher than the experimental data at 827.2 m/s and 832.6 m/s, respectively. On the other hand, inaccurate DOP is obtained with an error larger than 15% when $\zeta \geq 0.425$. It can be inferred that the calculated dynamic resistance would be far beyond the actual value, i.e. the DOP would be significantly underestimated, if the rate effect is fully accounted for according to Eqs. 7-4 and 7-5 (with $\zeta=1$). The trend in Table 7-5 confirms the necessity of introducing an appropriate ζ to reduce the DIFs in CEB-FIP Model Code 2010 to achieve reasonable predictions for the UHPFRC targets. The recommended range of ζ is around 0.325 ~ 0.375 for the UHPFRC targets investigated in this study.

Table 7-5 Influences of the reduction factor on the velocity and DOP

ζ	$V_0 = 827.2$ m/s, $DOP_{\text{test}} = 57$ mm (Yu, 2015)		$V_0 = 832.6$ m/s, $DOP_{\text{test}} = 60$ mm (Yu, 2015)	
	DOP_{cal} (mm)	Error (%)	DOP_{cal} (mm)	Error (%)
0.300	63.8	11.9	64.4	7.3
0.325	61.3	7.5	61.9	3.2
0.350	58.9	-3.3	59.4	1.0
0.375	55.6	-2.5	56.1	-6.5
0.400	52.7	-7.5	53.2	-11.3
0.425	48.4	-15.1	49.0	-18.3
0.450	47.9	-16.0	48.4	-19.3

7.5 DOP model for multi-layered UHPFRC

As indicated in Section 7.1, current predictive models are proposed for single-layered target with homogeneous properties. In other words, these models cannot reflect the changing properties of a multi-layered target. Moreover, the empirical parameters in the previous models are obtained from the overall responses of single-layered concrete targets, hence using them for multi-layered targets with material properties varying in each layer can lead to inaccurate results. To fill the gap, this section further extends the DOP predictive model (in Section 7.4) for multi-layered UHPFRC, and the prediction accuracy is validated by the experiments of the layered UHPFRC presented in Chapter 6.

7.5.1 Predictive model for multi-layered UHPFRC

As illustrated in Fig. 7-17, a UHPFRC target with n layers is under impact; and the projectile penetrates through the $n-1$ layers and stops inside the n layer. The penetration process in this n -layered UHPFRC can then be divided into $n+1$ stages: (1) a cratering stage with a depth of kd , which ends at time t_1 with a projectile velocity of V_1 ; (2) the 1st tunneling stage in the 1st layer with a depth of H_1 (H_i is the thickness of the i^{th} layer, $i = 1, 2, \dots, n-1$), which ends at time t_2 with a projectile velocity of V_2 ; ...; (n) the $n-1^{\text{th}}$ tunneling stage in the $n-1^{\text{th}}$ layer with a depth of $H_1 + H_2 + \dots + H_{n-1}$, which ends at time t_n with a projectile velocity V_n ; ($n+1$) and the n^{th} tunneling stage in the n^{th} layer until the projectile stops and the velocity becomes 0.

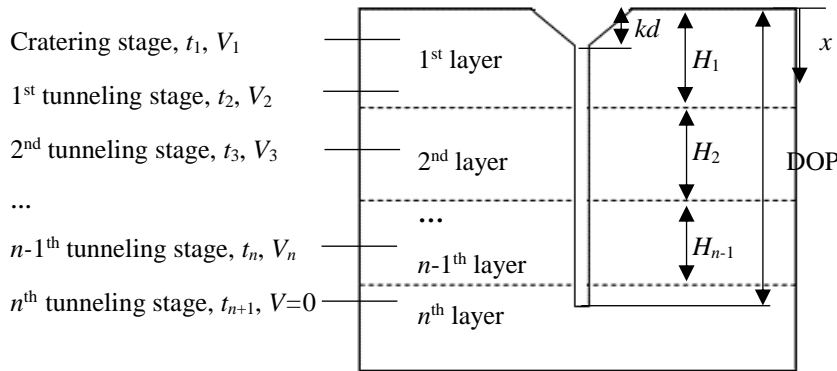


Fig. 7-17 Illustration of penetration process in an n -layered target: H_i is the thickness of the i^{th} layer ($i = 1, \dots, n-1$). kd is the crater depth. t_1 and V_1 are the time and projectile velocity at the end of the cratering stage, respectively. t_i and V_i are the time and projectile velocity at the end of the $i-1^{\text{th}}$ tunneling stage ($i = 2, n+1$), respectively.

The axial force at the cratering stage F_1 is the same as Eq. 7-39. The axial force at the 1st and the n^{th} tunneling stages are given as F_2 and F_{n+1} :

$$F_2 = \frac{\pi d^2 \sigma_{c,s,1}}{4} \left(A_1 + B_1 N_I \sqrt{\frac{\rho_1}{\sigma_{c,s,1}}} V + C_1 N_{II} \left(\sqrt{\frac{\rho_1}{\sigma_{c,s,1}}} V \right)^2 \right) \quad \text{for } kd \leq x < H_1 \quad (7-56)$$

$$F_{n+1} = \frac{\pi d^2 \sigma_{c,s,n}}{4} \left(A_n + B_n N_I \sqrt{\frac{\rho_n}{\sigma_{c,s,n}}} V + C_n N_{II} \left(\sqrt{\frac{\rho_n}{\sigma_{c,s,n}}} V \right)^2 \right) \quad \text{for } H_1 + \dots + H_{n-1} \leq x < \text{DOP} \quad (7-57)$$

where $\sigma_{c,s,n}$ and ρ_n are the compressive strength and density of the n^{th} layer. Parameters A_n , B_n and C_n are determined based on the theoretical solutions of the cavity expansion model, and they are solved according to the material properties of the n^{th} layer.

The projectile velocity at the beginning of the 1st tunneling stage V_1 can be obtained by the continuous condition of the axial force at the end of the cratering stage, i.e. $F_1(t = t_1) = F_2(t = t_1)$ and the boundary condition $V(t = t_1) = V_1$, $x(t = t_1) = kd$, resulting in:

$$\frac{M(V_0^2 - V_1^2)}{kd} = \frac{\pi d^2 \sigma_{c,s,1}}{4} \left(A_1 + B_1 N_I \sqrt{\frac{\rho_1}{\sigma_{c,s,1}}} V_1 + C_1 N_{II} \left(\sqrt{\frac{\rho_1}{\sigma_{c,s,1}}} V_1 \right)^2 \right) \quad (7-58)$$

Combining Eq. 7-56 and Newton's second law of motion Eq. 7-37 gives:

$$\frac{\pi d^2 \sigma_{c,s,1}}{4} \left(A_1 + B_1 N_I \sqrt{\frac{\rho_1}{\sigma_{c,s,1}}} V + C_1 N_{II} \left(\sqrt{\frac{\rho_1}{\sigma_{c,s,1}}} V \right)^2 \right) = -MV \frac{dV}{dx} \quad (7-59)$$

Integrating Eq. 7-59 provides the relationship between x and V in the 1st layer. Then the projectile velocity at the end of the 1st tunneling stage V_2 can be obtained by considering the initial condition $V(t = t_1) = V_1$, $x(t = t_1) = kd$ and the end condition $V(t = t_2) = V_2$, $x(t = t_2) = H_1$:

$$\begin{aligned} \frac{H_1 - kd}{D_{I,1}} = & \ln \left(1 + \frac{B_1 N_I}{A_1} \sqrt{\frac{\rho_1}{\sigma_{c,s,1}}} V_1 + \frac{C_1 N_{II} \rho_1 V_1^2}{A_1 \sigma_{c,s,1}} \right) + 2D_{II,1} \left(\tan^{-1} D_{II,1} - \tan^{-1} \left(\frac{2D_{II,1} C_1 N_{II}}{B_1 N_I} \sqrt{\frac{\rho_1}{\sigma_{c,s,1}}} V_1 + D_{II,1} \right) \right) \\ & - \ln \left(1 + \frac{B_1 N_I}{A_1} \sqrt{\frac{\rho_1}{\sigma_{c,s,1}}} V_2 + \frac{C_1 N_{II} \rho_1 V_2^2}{A_1 \sigma_{c,s,1}} \right) - 2D_{II,1} \left(\tan^{-1} D_{II,1} - \tan^{-1} \left(\frac{2D_{II,1} C_1 N_{II}}{B_1 N_I} \sqrt{\frac{\rho_1}{\sigma_{c,s,1}}} V_2 + D_{II,1} \right) \right) \end{aligned} \quad (7-60)$$

$$\text{where } D_{I,1} = \frac{2M}{\pi d^2 \rho_1 C_1 N_{II}}, \quad D_{II,1} = B_1 N_I / \sqrt{4A_1 C_1 N_{II} - (B_1 N_I)^2}.$$

With a similar process, the projectile velocity at the end of the $n-1^{\text{th}}$ tunneling stage V_n can be obtained by solving Eq. 7-61. A positive V_n indicates that the projectile penetrates through the $n-1^{\text{th}}$ layer; otherwise it stops inside the $n-1^{\text{th}}$ layer, and the problem returns to the case of an $(n-1)$ -layered target.

$$\begin{aligned} \frac{H_{n-1}}{D_{I,n-1}} = & \ln \left(1 + \frac{B_{n-1} N_I}{A_{n-1}} \sqrt{\frac{\rho_{n-1}}{\sigma_{c,s,n-1}}} V_{n-1} + \frac{C_{n-1} N_{II} \rho_{n-1} V_{n-1}^2}{A_{n-1} \sigma_{c,s,n-1}} \right) + 2D_{II,n-1} \times \\ & \left(\tan^{-1} D_{II,n-1} - \tan^{-1} \left(\frac{2D_{II,n-1} C_{n-1} N_{II}}{B_{n-1} N_I} \sqrt{\frac{\rho_{n-1}}{\sigma_{c,s,n-1}}} V_{n-1} + D_{II,n-1} \right) \right) - \ln \left(1 + \frac{B_{n-1} N_I}{A_{n-1}} \sqrt{\frac{\rho_{n-1}}{\sigma_{c,s,n-1}}} V_n + \frac{C_{n-1} N_{II} \rho_{n-1} V_n^2}{A_{n-1} \sigma_{c,s,n-1}} \right) \\ & - 2D_{II,n-1} \left(\tan^{-1} D_{II,n-1} - \tan^{-1} \left(\frac{2D_{II,n-1} C_{n-1} N_{II}}{B_{n-1} N_I} \sqrt{\frac{\rho_{n-1}}{\sigma_{c,s,n-1}}} V_n + D_{II,n-1} \right) \right) \end{aligned} \quad (7-61)$$

The relationship between x and V in the n^{th} layer can be obtained by combining Eq. 7-57 with the Newton's second law of motion, and integrating the result. Letting $V = 0$ finally leads to the DOP in the n -layered UHPFRC:

$$DOP = D_{I,n} \ln \left(1 + \frac{B_n N_I}{A_n} \sqrt{\frac{\rho_n}{\sigma_{c,s,n}}} V_n + \frac{C_n N_{II} \rho_n V_n^2}{A_n \sigma_{c,s,n}} \right) + 2D_{I,n} D_{II,n} \left(\tan^{-1} D_{II,n} - \tan^{-1} \left(\frac{2D_{II,n} C_n N_{II}}{B_n N_I} \sqrt{\frac{\rho_n}{\sigma_{c,s,n}}} V_n + D_{II,n} \right) \right) + H_1 + \dots + H_{n-1} \quad (7-62)$$

where $D_{I,n} = \frac{2M}{\pi d^2 \rho_n C_n N_{II}}$, $D_{II,n} = B_n N_I / \sqrt{4A_n C_n N_{II} - (B_n N_I)^2}$.

7.5.2 Model validation

The double- and triple-layered UHPFRC in Chapter 6: U8a1s(45)-16a1s(45) and U16a1s(20)-8a1s(50)-16a1s(20) are taken to validate the proposed predictive model. The model inputs of the U16a1s layer can be found in Table 7-4, while those for the U8a1s layer are given in Table 7-6. Similarly, $m = 6.18$, $A = 7.84$, $B = 3.91$ and $C = 1.65$ are obtained for the U8a1s layer.

Table 7-6 Model inputs for the U8a1s layer

Compressive strength $\sigma_{c,s}$ (MPa)	Tensile strength $\sigma_{t,s}$ (MPa)	Elastic modulus E (GPa)	Density ρ (kg/m ³)
154.9	12.3	49.2	2500

The DOP obtained by the experiments in Chapter 6 and the proposed model are compared in Table 7-7. In addition, the ACE, modified NDRC and UKAEA formulae (Li et al., 2006) are also presented. These empirical formulae are developed for single-layered concrete with homogeneous material properties in the whole target. Hence, equivalent material properties are taken as the inputs when using these formulae for the layered UHPFRC. For example, the equivalent compressive strength of the triple-layered target $\sigma_{c,eq}$ is determined by the composite theory (Xu et al., 2010) as:

$$\sigma_{c,eq} = (\sigma_{c,s,1} H_1 + \sigma_{c,s,2} H_2 + \sigma_{c,s,3} H_3) / (H_1 + H_2 + H_3) \quad (7-63)$$

Table 7-7 Experimental and calculated DOP of layered UHPFRC

Targets	Velocity (m/s)	DOP (mm) and error (%)				
		Test	Proposed model (error)	ACE (error)	Modified NDRC (error)	UKAEA (error)
U8a1s(45)-16a1s(45)	842.6	57.0	56.4 (-1%)	47.0 (-18%)	36.4 (-36%)	51.0 (-11%)
	845.0	55.0	56.6 (3%)	47.2 (-14%)	36.5 (-33%)	51.2 (-7%)
U16a1s(20)-8a1s(50)-16a1s(20)	842.5	54.0	56.3 (4%)	47.0 (-13%)	36.4 (-33%)	51.0 (-6%)
	845.2	54.5	56.6 (4%)	47.2 (-13%)	36.5 (-33%)	51.3 (-6%)

Table 7-7 shows that the proposed model successfully predicts the DOP in the given layered UHPFRC with an accuracy higher than 95%. To be more precise, the averaged errors of U8a1s(45)-16a1s(45) and U16a1s(20)-8a1s(50)-16a1s(20) are about 2% and 4%, respectively. Compared to the 98% accuracy for the single-layered UHPFRC U16a1s (see Fig. 7-9), the predictions are slightly less accurate for the multi-layered targets. One possible reason leads to this slightly lower accuracy may

be that the reduction of the DOP caused by the layer interface is not considered in the model. However, with more investigations on the layer interface available, e.g. the thickness, mechanical properties and fracture response, the influences of layer interface can then be incorporated and the prediction accuracy of the model can be further improved.

As with the empirical formulae, they tend to underestimate the DOP in the tested UHPFRC targets. Although it is not developed for multi-layered targets, the UKAEA formula with the composite theory provides results close to the experimentally measured DOP, and the averaged errors are around 9% and 6% for the U8a1s(45)-16a1s(45) and U16a1s(20)-8a1s(50)-16a1s(20) targets, respectively. Nonetheless, despite these acceptable predictions, the UKAEA formula with the composite theory is not able to present the effects of the layer's order, e.g. it yields a same result for U8a1s(45)-16a1s(45) and U16a1s(45)-8a1s(45) although the two targets actually have different resistances. On the other side, the ACE formula gives less accurate predictions, and the minimum errors for the double- and triple-layered UHPFRC are approximately 14% and 13%. The modified NDRC formula also fails to make appropriate estimations; and the errors are larger than 30%, indicating significant overestimation of the impact resistance of the layered UHPFRC.

7.6 Conclusions

The present study develops new DOP predictive models for both single- and multi-layered UHPFRC based on an improved cavity expansion theory. The nonlinear behavior and the rate dependency of the UHPFRC material are accounted in the models. The proposed model provides an efficient approach to design UHPFRC protective structures, and hence promotes engineering applications of the UHPFRC material in both the civil and military fields. The following conclusions are drawn and some directions for further research are also provided:

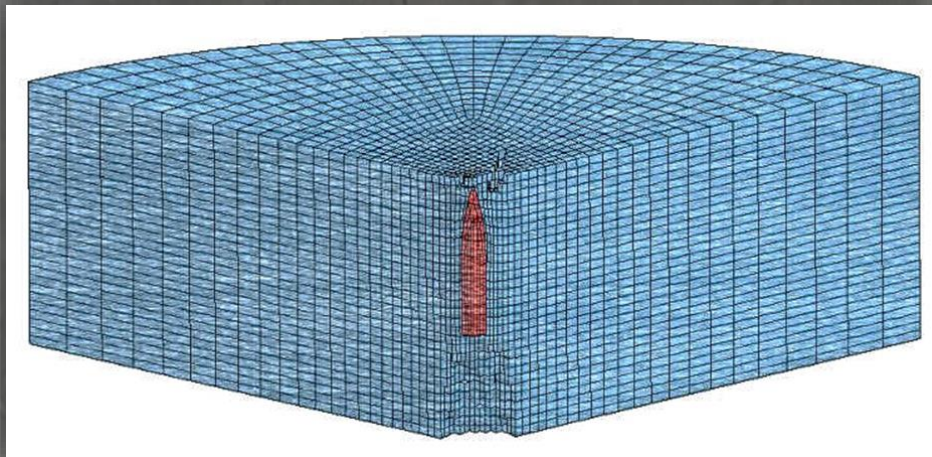
- (1) The Hoek-Brown criterion is firstly used to describe the strength feature of UHPFRC in the comminuted region in the present study, and an empirical equation for the dimensionless parameter m is derived. Despite this empirical equation, more investigations on the physical meaning of m would help to theoretically determine its value in further studies.
- (2) The inclusion of the rate effect in the dynamic cavity expansion model is essential to obtain a sufficient penetration resistance. However, directly using the DIF recommended in the CEB-FIP Model Code 2010 would overestimate the dynamic enhancement of the cavity surface stress, and a reduction factor is necessary to be adopted. The parameter sensitivity of the reduction factor is analyzed in the study, and more accurate predictions would be expected with more investigations on the rate effect of UHPFRC under high strain rates.
- (3) Parameter sensitivities are discussed with the DOP predictive model for single-layered UHPFRC. A nonlinear reduction of DOP is observed with the improvement of the target compressive strength $\sigma_{c,s}$ until it reaches around 105 MPa, higher than which the influences of $\sigma_{c,s}$ on the DOP become very limited. Moreover, increasing the target tensile strength $\sigma_{t,s}$ results in the decrease of the cracked region area $r_{cr} - r_p$; nevertheless, $\sigma_{t,s}$ has insignificant effects on the DOP, which agrees with the experimental observations that increasing the fiber amount in UHPFRC barely contributes to reducing its DOP.
- (4) The DOP predictive model for single-layered UHPFRC achieves a reasonable agreement with the experimental data, and it provides more accurate estimation than the currently extensively utilized predicting formulae. The UKAEA formula can give reasonable predictions, whereas the Forrestal

semi-empirical formula and the Li-Chen formula tend to overestimate the DOP in the single-layered UHPFRC targets; the accuracies of the ACE formulae and the modified NDRC formulae are unstable when applied to UHPFRC.

(5) The DOP predictive model for multi-layered UHPFRC is able to account for the varying mechanical properties and the layers' order in the layered targets, and it successfully predicts the DOP in the layered UHPFRC. On the contrary, the empirical formulae underestimate the DOP in the multi-layered targets. Compared to the ACE formula and the modified NDRC formula, the UKAEA formula with the composite theory provides predictions with a relatively higher accuracy, but it fails to distinguish the effects of the layers' order on the impact resistance.

Chapter 8

*Modelling the ballistic response of coarse-aggregated layered UHPFRC under high-velocity impact **



* This chapter is partially reproduced from: Y.Y.Y. Cao, Q.L. Yu, H.J.H. Brouwers, Numerical investigation on ballistic performance of coarse-aggregated layered UHPFRC (Submitted).

Abstract

Modelling the penetration process in UHPFRC by numerical simulation provides valuable information on the dynamic interaction between the projectile and the concrete. This chapter analyses the ballistic performances of the single- and triple-layered UHPFRC with LS-DYNA. The Holmquist Johnson Concrete (HJC) model is employed to describe the dynamic behavior of the UHPFRC, and the effect of the coarse aggregates is reflected in the pressure-compaction relationship in the model. The numerical models are validated by the penetration experiments in Chapter 6, after which the penetration process in the UHPFRC is analyzed. Furthermore, the effects of the target thickness on the DOP are discussed, which shows the possibility of replacing a thicker single-layered target by a thinner triple-layered one to achieve the same level of protection. Finally, the perforation limits of the single- and triple-layered UHPFRC at different impact velocities are estimated and compared with the results from the empirical formulae. The simulations reveal that the triple-layered target has a smaller perforation limit, and it requires fewer dosages of cement and steel fibers, compared to the single-layered counterpart with the same level of ballistic protection.

8.1 Introduction

The excellent properties of UHPFRC make it a promising construction material for important buildings and infrastructures against ballistic impacts. To construct reliable protective structures, the dynamic performances of UHPFRC should be understood. Ballistic experiments of UHPFRC can provide direct results; however, the expensive test facilities and the time-consuming test process put limits on experimental studies in this field (Liu et al., 2017; Tai, 2009b). Empirical and theoretical formulae have been proposed to predict some important ballistic characterizations, e.g. the depth of penetration (DOP), perforation limit and residual velocity; nevertheless, these formulae cannot reproduce the dynamic stress and the damage distribution in the impacted concrete. On the other hand, with the advancement of computer technology, numerical simulations of concrete against ballistic impacts become feasible. Numerous commercial software, such as LS-DYNA, ABAQUS and AUTODYN, can be utilized to model the response of concrete subjected to ballistic impacts, which provides valuable information on the real-time interaction between the projectile and the matrix.

Modelling the dynamic response of concrete under high-velocity ballistic impacts is challenging (Liu et al., 2017). As a result of the rate effect, the behavior of concrete subjected to dynamic load is more complicated in comparison to that under static load (Cao et al., 2019b). Furthermore, differing with the overall response of a structure exposed to normal dynamic loads, e.g. earthquake and wind, a high-velocity projectile usually generates severe local damage in the impacted object, long before the entire structure being dynamically exited (Pereira et al., 2018). This further distinguishes the high-velocity ballistic impact from other dynamic loads commonly considered in structural design. Moreover, concrete is practically idealized as a homogeneous material in macroscale simulations to improve the calculation efficiency. However, it is actually inhomogeneous and has multiple phases (e.g. matrix, aggregates and steel fibers), which makes modelling the constitutive relationship of the “homogenized” concrete rather difficult (Li et al., 2006). Consequently, choosing the appropriate material models and determining the suitable parameters to reflect the influences of concrete compositions, e.g. the coarse aggregate, are of great significance for the success of these macroscale simulations. Peng et al. (Peng et al., 2018) modelled the ballistic behaviors of concrete target at both mesoscale (with coarse aggregates explicitly presented) and macroscale. Comparing the relative DOP in their simulations exhibits that the macroscale model can give results close to that from the mesoscale model as long as appropriate material models were applied, especially for the cases where the ratio of the aggregate size to the projectile diameter is smaller than 2. This confirms the possibility of applying homogenous models to simulate the ballistic performance of concrete at macroscale.

As with UHPFRC, several studies have been conducted to simulate its ballistic response at macroscale. For example, Liu et al. (Liu et al., 2017) used the K&C model in LS-DYNA to simulate the impact responses of UHPFRC under projectile impacts from 300 to 1000 m/s. The effects of UHPFRC compressive strength, projectile velocity and nose shape on the DOP and cratering damage size were investigated in their study. Yu (Yu, 2015) developed a sustainable UHPFRC and modelled its ballistic performance using LS-DYNA. The HJC model was employed for the UHPFRC, and it was claimed that the obtained numerical simulations agreed well with the experimental results. Sovják et al. (Sovják et al., 2015) numerically evaluated the resistance of slim UHPFRC panels against an in-service projectile. The behavior of the UHPFRC was described by the RHT model in AUTODYN and the effect of fibers was incorporated in the model by increasing its fracture energy. It is noteworthy that the above numerical studies only concern conventional UHPFRC without coarse aggregates. In

other words, the influences of coarse aggregates are not addressed in these simulations although relevant experiments have shown their remarkable contributions on improving the impact resistance of cementitious targets (Dancygier, 2017; Peng et al., 2018, 2016a; Wu et al., 2019).

Based on the ballistic experiment results in Chapter 6, this chapter further investigates numerically the ballistic performances of the coarse-aggregated layered UHPFRC. LS-DYNA is employed to execute the numerical simulations, and the effect of the coarse aggregates is reflected in the crushing pressure in the HJC model. After validating the model against the experiments, the dynamic penetration processes inside the coarse-aggregated layered UHPFRC are analyzed. The influences of the target thickness on the DOP are discussed. Furthermore, the perforation limits of the single- and triple-layered UHPFRC targets at different penetration velocities are numerically evaluated. The study in this chapter advances the understanding of the ballistic performances of coarse-aggregated layered UHPFRC, and the simulation results further confirms the advantages of applying layered structure to UHPFRC targets.

8.2 Modelling of single- and triple-layered UHPFRC

8.2.1 Overview of the model

Following the ballistic experiments in Chapter 6, the performances of the single-layered targets U8a1s(90) and U16a1s(90), and the triple-layered UHPFRC U16a1s(30)-8a1s(30)-16a1s(30) subjected to in-service 7.62 mm \times 51 AP projectile at velocities of approximately 840 m/s are simulated. Three dimensional models of the ogive-nosed projectile and the targets are built in LS-DYNA, as shown in Fig. 8-1. In order to improve the computation efficiency, only one quarter of the test arrangement is modelled. Symmetric boundary conditions are imposed to the models and fixed boundary conditions are imposed on the back edge of the UHPFRC targets.

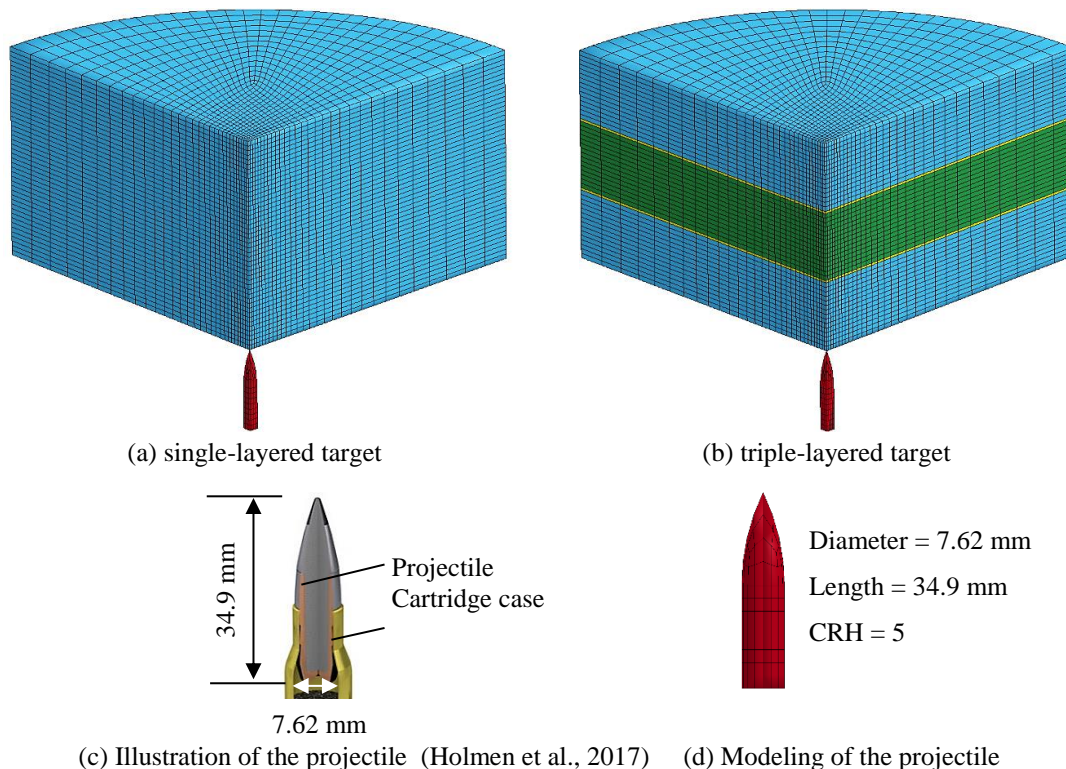


Fig. 8-1 Models of the penetration test

3D Solid 164 element is used in the simulations. As shown in Fig. 8-1a, the target is divided into 45 indices in the direction of penetration and 30 indices along its radius. The length of the element gradually increases along the target radius, and it is finer in the region where the projectile contacts the concrete. The minimum element sizes of the target and the projectile are comparable, i.e. about 1.2 mm and 1 mm, respectively. The results of mesh convergence study are presented in Fig. 8-2, in which the minimum mesh size of the target changes from 1.2 to 2.0 mm. The figure shows that 1.2 mm is sufficiently fine and the mesh is therefore adopted in the simulations. For the triple-layered target U16a1s(30)-8a1s(30)-16a1s(30), the layer bond is modelled by a thin layer of interfacial elements connecting the outer U16a1s layers and the inner U8a1s layer. The compressive strength of the interfacial element equals to the compressive strength of the plain UHPC obtained from the mechanical tests in Chapter 6, and the measured layer bond strength in Chapter 6 is taken as the tensile strength of these interfacial elements.

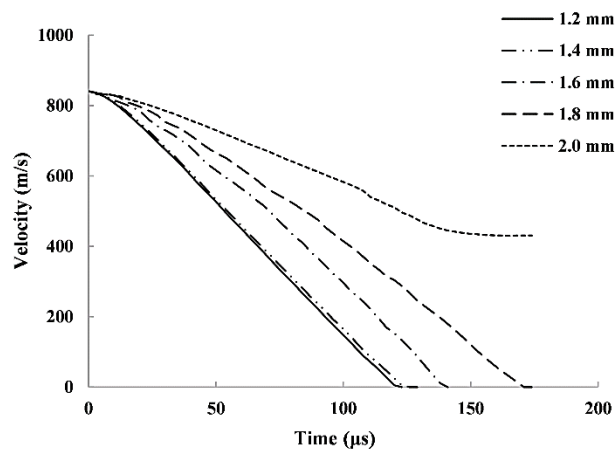


Fig. 8-2 Mesh convergence study

The penetration process is simulated based on the explicit time integration, which is suitable to solve dynamic problems such as ballistic impacts (Shaharudin Shah Zaini, 2015; Teng et al., 2008). In contrast to the implicit scheme that requires the full formation of the global stiffness matrix and updates the matrix at each step, the explicit scheme extrapolates the solution of the next time step, e.g. the nodal acceleration, velocity and displacement, based on the quantities at the current time step (Othman, 2016). Consequently, the explicit scheme is more computationally efficient as the formation of the global stiffness matrix is not required (Shaharudin Shah Zaini, 2015; Teng et al., 2008). To achieve the stability of the solution, a sufficiently small time step is necessary in the explicit time integration (Shaharudin Shah Zaini, 2015), therefore, a scale factor of 0.67 for the computed time step is applied in the impact simulations in this chapter (LSTC, 2015a).

8.2.2 Material models

The penetration velocities V_0 in the experiments are around 840 m/s, which falls within the range of non-deformable (rigid) penetration ($V_0 \leq 1000$ m/s) (Liu et al., 2017). Therefore, the deformation of the projectile is neglected in the simulation, and it is modeled as a rigid body using the material model *MAT_RIGID (MAT_020) in LS-DYNA. The input parameters for the projectile are listed in

Table 8-1. The contact between the projectile and UHPFRC is modelled by the keyword “CONTACT_ERODING_SURFACE_TO_SURFACE”.

Table 8-1 Rigid model inputs for the projectile

Parameters	Projectile
Density ρ (kg/m ³)	7850
Elastic modulus E (GPa)	206
Poisson's ratio	0.3

The HJC constitutive model *MAT_JOHNSON_HOLMQUIST_CONCRETE (MAT_111) is adopted for the UHPFRC and the layer interface. This model is suitable to describe the response of cementitious materials subjected to high strain rates, large deformations, and high hydrostatic pressures (LSTC, 2016, 2015b), and it has been widely employed to model the ballistic performance of concrete (Peng et al., 2018; Wu et al., 2019; Yu, 2015). In the HJC model, the yield surface is dependent on the pressure P , strain rate $\dot{\epsilon}$, and damage D (see Fig. 8-3) (LSTC, 2016):

$$\sigma^* = \left[A_c (1 - D_c) + B_c P^{*N_c} \right] (1 - C_c \ln \dot{\epsilon}^*) \quad (8-1)$$

where σ^* is the normalized equivalent stress, and it equals to the ratio of the actual equivalent stress σ to the static compressive strength $\sigma_{c,s}$. P^* is the normalized pressure defined as the ratio of the pressure P to $\sigma_{c,s}$. The dimensionless strain rate is $\dot{\epsilon}^* = \dot{\epsilon} / \dot{\epsilon}_0$ ($\dot{\epsilon}$ and $\dot{\epsilon}_0 = 1.0 \text{ s}^{-1}$ are the actual and reference strain rates, respectively). A_c , B_c , C_c and N_c are input parameters.

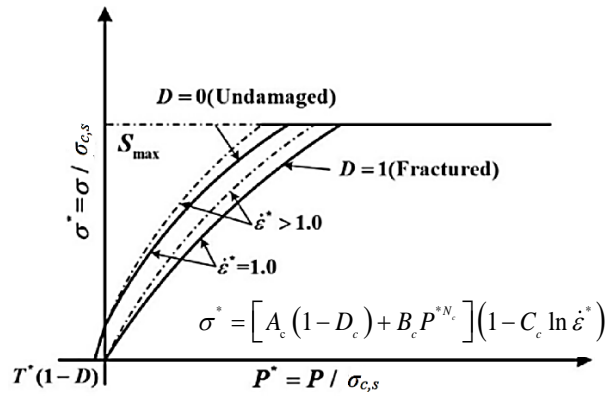


Fig. 8-3 Yield surface (Ren et al., 2017)

The damage D is accumulated as a function of the equivalent plastic strain ϵ_p , plastic volumetric strain μ_p , and the total plastic strain until fracture $\epsilon_p^f + \mu_p^f$, as illustrated in Fig. 8-4 (Ren et al., 2017):

$$D = \sum \frac{\Delta \epsilon_p + \Delta \mu_p}{\epsilon_p^f + \mu_p^f} \quad (8-2)$$

$$\epsilon_p^f + \mu_p^f = D_1 (P^* + T^*)^{D_2} \geq EFMIN \quad (8-3)$$

where D_1 and D_2 are the damage parameters. $T^* = T / \sigma_{c,s}$ is the normalized maximum tensile hydrostatic pressure and T is the maximum tensile hydrostatic pressure. $EFMIN$ is the amount of plastic strain before fracture (LSTC, 2015b; Ren et al., 2017).

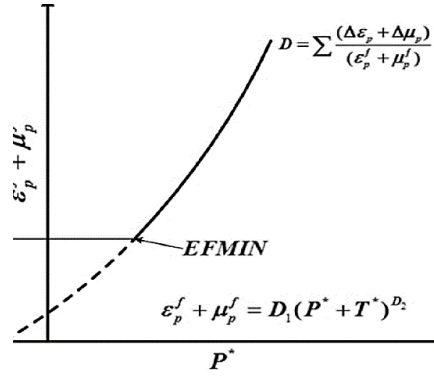


Fig. 8-4 Damage accumulation (Ren et al., 2017)

Fig. 8-5 depicts the pressure–compaction relationship of the material, i.e. the relationship between P and the volumetric strain μ_v . The curve can be separated into three response phases:

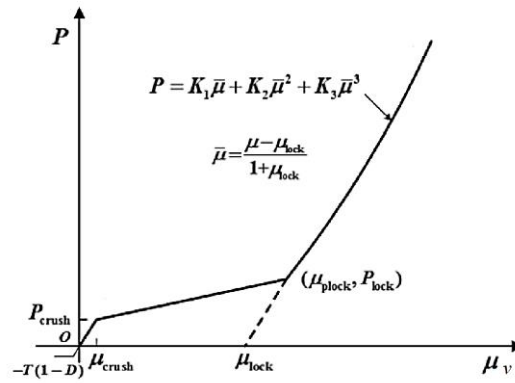


Fig. 8-5 Equation of state (Ren et al., 2017)

- The first phase is linear elastic until the crushing pressure P_{crush} and the corresponding volumetric strain μ_{crush} are reached (Ren et al., 2017):

$$P = \frac{P_{\text{crush}}}{\mu_{\text{crush}}} \mu_v \quad (8-4)$$

- The second phase corresponds to the transitional region, during which the voids in the material are gradually compressed (Ren et al., 2017):

$$P = P_{\text{crush}} + \frac{P_{\text{lock}} - P_{\text{crush}}}{\mu_{\text{lock}} - \mu_{\text{crush}}} (\mu_v - \mu_{\text{crush}}) \quad (8-5)$$

where P_{lock} and μ_{lock} are the compaction limit and the locking volumetric strain, respectively.

- The third phase describes the response of the fully densified material (Ren et al., 2017):

$$P = K_1 \bar{\mu} + K_2 \bar{\mu}^2 + K_3 \bar{\mu}^3 \quad (8-6)$$

$$\bar{\mu} = \frac{\mu_v - \mu_{\text{lock}}}{1 + \mu_{\text{lock}}} \quad (8-7)$$

where K_1 , K_2 and K_3 are material parameters, $\bar{\mu}$ is the modified volumetric strain.

The input parameters for the HJC model are listed in Table 8-2. The density ρ , uniaxial compressive strength $\sigma_{c,s}$ and the maximum tensile pressure T of the U8a1s and U16a1s mixtures are obtained from the experiments in Chapter 6. The ρ and $\sigma_{c,s}$ of the plain UHPC U8a are used for the layer interfacial element; and the tensile strength of the interface is assumed to be equal to the bond strength between the U8a1s and U16a1s layers (measured in Chapter 6). The input shear modulus in Table 8-2 is determined by $G = E/2(1+\nu)$ with E the Young's modulus and ν the Poisson's ratio.

Table 8-2 HJC model inputs in LS-DYNA for the simulated UHPFRC

parameters	UHPFRC		Layer interface
	U8a1s	U16a1s	
Density ρ (kg/m ³)	2540	2550	2540
Shear modulus G (GPa)	22.5	24.5	25.0
Normalized cohesive strength A_c	0.79	0.79	0.79
Normalized pressure hardening B_c	1.6	1.6	1.6
Strain rate coefficient C_c	0.007	0.007	0.007
Pressure hardening exponent N_c	0.61	0.61	0.61
Uniaxial compressive strength $\sigma_{c,s}$ (MPa)	154.9	161.3	149.6
Maximum tensile pressure T (MPa)	12.3	14.6	7.0
Reference strain rate $EPS0$	1.0	1.0	1.0
Plastic strain before fracture $EFMIN$	0.01	0.01	0.01
Normalized maximum strength $SFMAX$	7.0	7.0	7.0
Crushing pressure P_{crush} (MPa)	51.6	134.4	49.9
Crushing volumetric strain μ_{crush}	0.00172	0.00165	0.001497
Locking pressure P_{lock} (GPa)	1.0	1.0	1.0
Locking volumetric strain μ_{lock}	0.1	0.1	0.1
Damage constant D_1	0.04	0.04	0.04
Damage constant D_2	1.0	1.0	1.0
Pressure constant K_1 (GPa)	85	85	850
Pressure constant K_2 (GPa)	-171	-171	-1710
Pressure constant K_3 (GPa)	208	208	2080

The strength parameters A_c , B_c , N_c , $SFMAX$ can be determined by triaxial compressive tests (Ren et al., 2017). The test data in the literature (Farnam et al., 2010; Ren et al., 2016; Sovják et al., 2013b; Xie et al., 1995) concerning concrete from 92 ~ 171 MPa are given in Fig. 8-6, in which the normalized equivalent stress is $\sigma^* = (\sigma_1 - \sigma_3) / \sigma_{c,s}$ and the normalized pressure is $P^* = (\sigma_1 + 2\sigma_3) / 3\sigma_{c,s}$ (Ren et al., 2017) (σ_1 and σ_3 are the major and minor principal stresses, respectively). As presented in the figure (see the dots in Fig. 8-6), the different concrete strength does not cause significant deviations on the relationship between σ^* and P^* . Therefore, it is assumed that the developed UHPFRC in this study also possesses a similar P^* - σ^* relation. The solid curve in Fig. 8-6 is obtained from Eq. 8-1 with $A_c = 0.79$, $B_c = 1.6$, $N_c = 0.61$ and $SFMAX = 7$, which are the default values in the original HJC model (Ren et al., 2017), at a static strain rate $\dot{\epsilon} = 1.0 \text{ s}^{-1}$ and without considering damage. A fair agreement is observed between the experimental data (Farnam et al., 2010; Ren et al., 2016; Sovják et al., 2013b; Xie et al., 1995) and Eq. 8-1 with the default parameters. That being the case, these values are further used in the HJC model in the present study (see Table 8-2). Similarly, the strain rate parameter C_c , $EPS0$, and the damage parameters D_1 , D_2 , $EFMIN$ also remain the same as the default values in the original HJC model (Ren et al., 2017). These values are widely used for concrete with strengths from 12 to 200 MPa (Lai et al., 2015; Peng et al., 2018; Ren et al., 2017; Xu and Wen, 2016), and the UHPFRC developed in the present study also falls within this range.

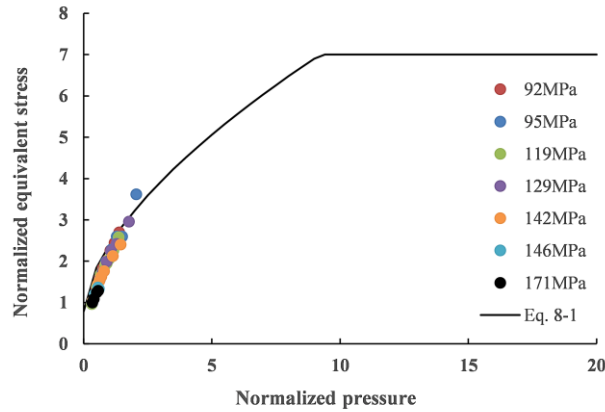


Fig. 8-6 Determination of strength parameters

Regarding the equation of state (EOS) parameters, for the layer interface and the U8a1s mixture, the crushing pressure P_{crush} and corresponding volumetric strain μ_{crush} are determined by $P_{\text{crush}} = \sigma_{c,s} / 3$ and $\mu_{\text{crush}} = P_{\text{crush}} / K$, in which the bulk modulus $K = E/3(1-2\nu)$ (Ren et al., 2017). On the other side, for the U16a1s mixture, the crushing limit and the stiffness of the material are manually enhanced to represent the influences of the large coarse aggregates. According to Chapter 6, the contributions of the coarse aggregate on improving the ballistic resistance of concrete can be mainly attributed to the following reasons: (1) the stronger coarse aggregates can act as barriers to cracking, as the cracks are driven to cut through the aggregates due to the high stress rate in the case of penetration; (2) the higher hardness of the coarse aggregates can increase the abrasion of the projectile, increasing its kinetic energy loss; (3) the direction of the projectile may be changed after it hits the coarse aggregate, which further promotes the energy consumption of the projectile. Although the third effect of the coarse aggregates, i.e. due to material heterogeneousness, cannot be reflected in a macroscale model, it is possible to represent the first two effects, i.e. the improved material strength and hardness provided by the coarse aggregates, by increasing the crushing limit and the stiffness of the material. An enhancing factor of 2.5 is applied to the crushing pressure P_{crush} of U16a1s, which is calibrated by the DOP of the U16a1s target from the ballistic tests in Chapter 6 (see Fig. 8-7). Furthermore, the erosion algorithm *MAT_ADD_EROSION is applied to remove the elements with large distortions during the penetration process. The maximum principal strain ε_{max} of 0.5 and the failure volumetric strain ε_{vol} of 0.01 are adopted as the erosion criteria, i.e. the element will be removed if ε_{max} or ε_{vol} reaches the corresponding critical values.

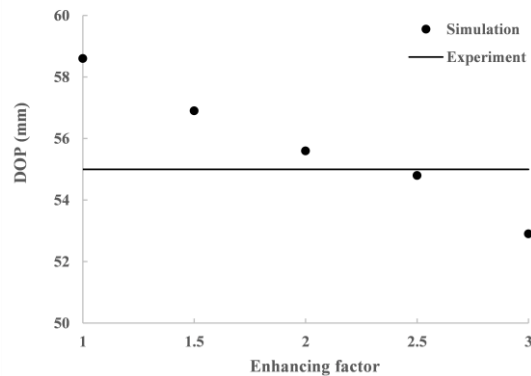


Fig. 8-7 Calibration of the enhancing factor

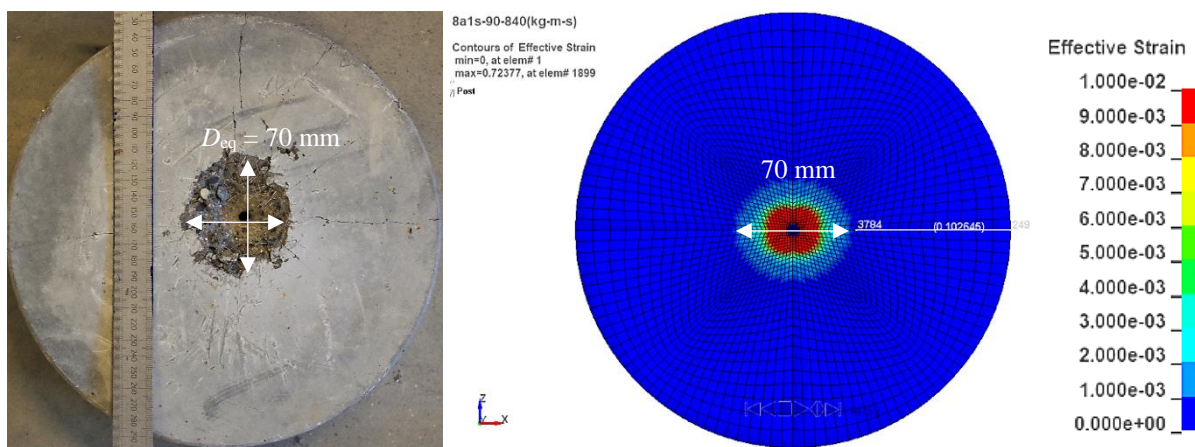
8.3 Model validation

The DOP obtained from the numerical simulations and the experiments are compared in Table 8-3. As shown in the table, the simulation results coincide well with the experimental data, i.e. the errors are less than 0.5% for both the single- and triple-layered UHPFRC targets. Furthermore, the penetration reductions caused by the 16 mm aggregates and the layered-structure are also successfully captured by the model, showing the reliability of the HJC material model and the corresponding inputs.

Table 8-3 comparison of depth of penetration

UHPFRC targets	Velocity (m/s)	DOP (mm)		Error (%)
		Experiment	Simulation	
U8a1s (90)	841.9	60.0	60.2	0.3
U16a1s (90)	840.7	55.0	54.8	-0.4
U16a1s(30)-8a1s(30)-16a1s(30)	839.3	52.5	52.6	0.2

In addition to the DOP, the damage distribution is also compared. The effective strain distribution in the impact surface of the UHPFRC is utilized to denote the crater damage of the target, and the comparisons between the experimental and the numerical results are shown in Fig. 8-8. In general, the numerical simulations are able to reproduce the major damage distribution in the targets, but it slightly underestimates the size of the impact crater in the UHPFRC and fails to reproduce the hairline cracking on the target surfaces. This can be attributed to the fact that the HJC model uses an elastic-perfectly-plastic yield surface for the tensile response of the material (see Fig. 8-5), making it less sensitive to the tension-dominated damage (Kong et al., 2016a). Nonetheless, the difference between the numerical and experimental crater size is less than 5%, and the hairline cracks in the targets are also not so severe that it is acceptable to not present them explicitly in the simulations. Additionally, comparing Figs. 8-8a and 8-8b depicts that the reduced damage region due to the larger aggregates is also successfully presented by the simulations. As demonstrated in the figures, the crater size of U16a1s(90) and its destruction level (represented by the color fringe) are more moderate compared to those of U8a1s(90), which is in line with the experimental results. In summary, with regards to both the DOP and the crater size, fair agreements are achieved by the numerical model and it is hence utilized for the further analysis.



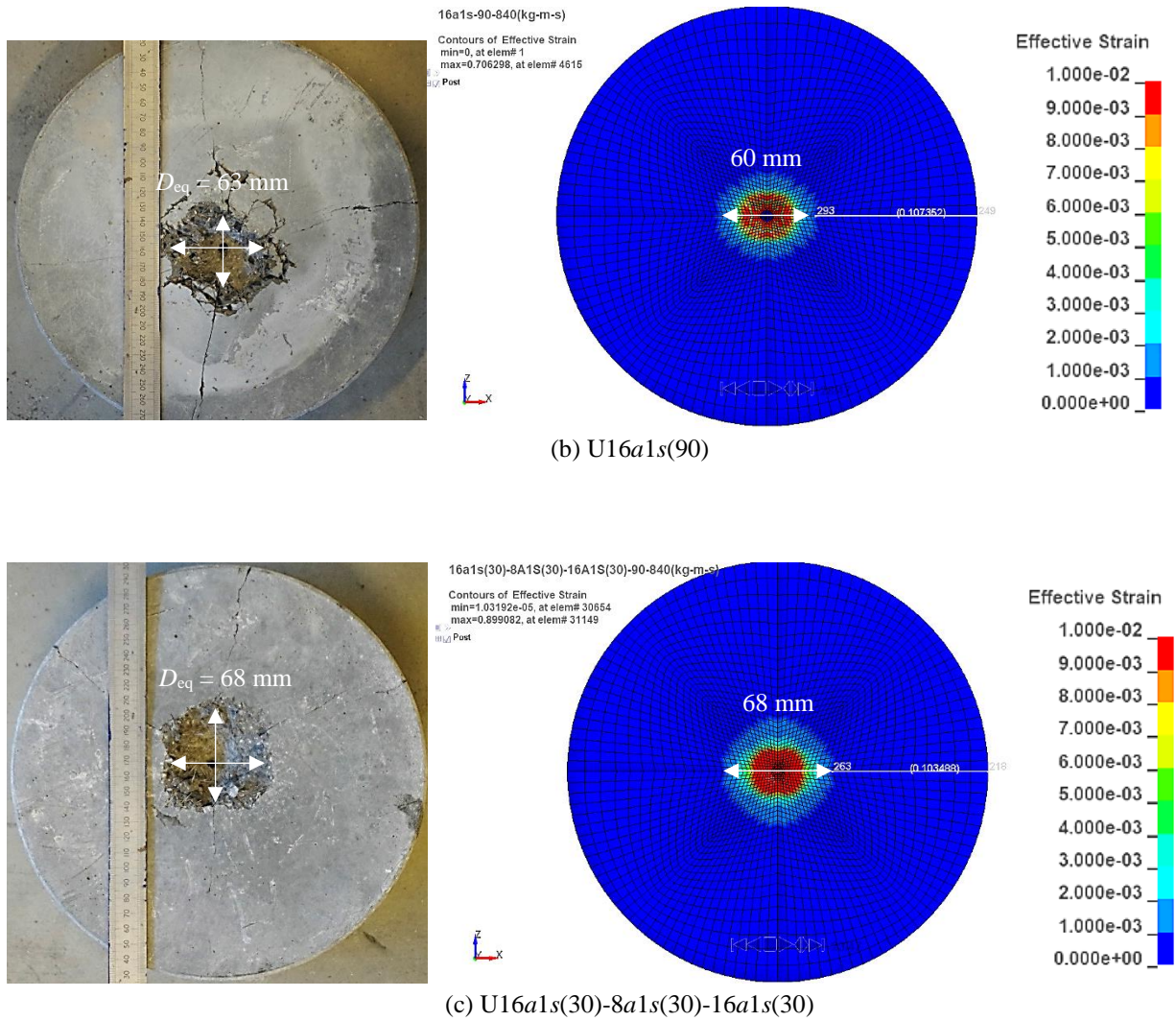


Fig. 8-8 Comparison of crater damage

8.4 Penetration analysis

8.4.1 Penetration history

Fig. 8-9 shows the displacement and velocity histories of the projectiles during the penetration process. The projectiles in U8a1s(90), U16a1s(90) and U16a1s(30)-8a1s(30)-16a1s(30) have comparable displacements at the early penetration stage (0-40 μ s after impact) because of their similar initial velocities around 840 m/s. However, with the development of the penetration process, the effects of the three targets on the projectile become increasingly obvious. Among the three targets, U16a1s(30)-8a1s(30)-16a1s(30) most effectively reduces the projectile velocity, leading to the smallest projectile displacement in the target, i.e. the simulated DOP. Moreover, the declining rate of the projectile velocity is influenced by the layer interface in U16a1s(30)-8a1s(30)-16a1s(30). Differing with the straight velocity curves of the single-layered targets, the velocity curve of the triple-layered UHPFRC bends when the projectile reaches the layer interface at around 42 μ s after impact. This may be attributed to the fact that the layer interface influences the wave propagation and reflection between the layers, affecting the force on the projectile and therefore its velocity. As with the single-layered UHPFRC, the projectile in U16a1s(90) yields a smaller velocity compared to that in U8a1s(90) at the same penetrating moment. The DOP in the U16a1s(90) target is, consequently, smaller. This

result also indicates that increasing the crushing pressure in the HJC model can efficiently reflect the increased material strength and hardness provided by the coarse aggregates, and therefore the improvement of the target resistance attributed to the coarse aggregates.

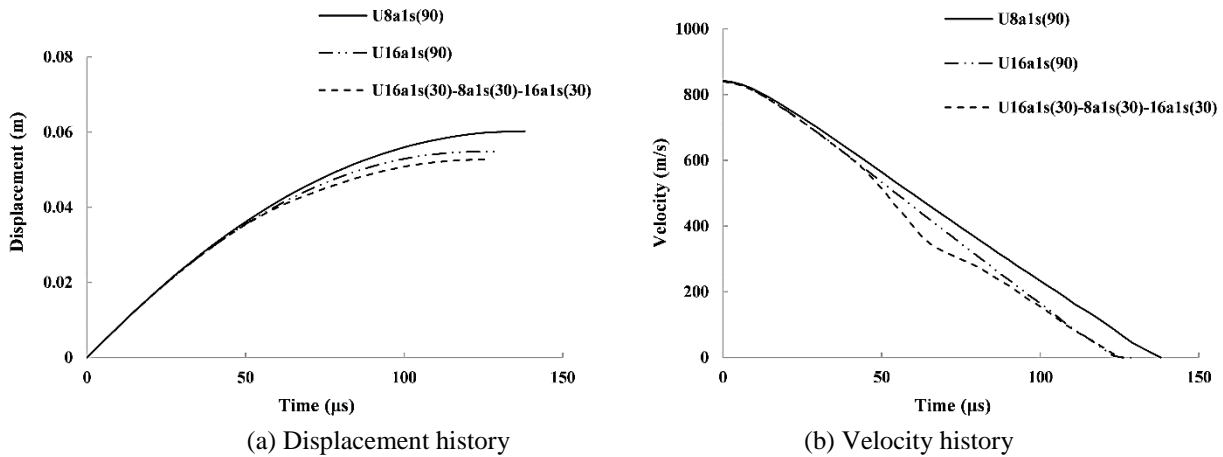


Fig. 8-9 Penetration history of the projectile (impact starts at $t = 3 \mu\text{s}$)

8.4.2 Penetration process

The penetration process in the UHPFRC is presented by the pressure development in Figs. 8-10 and 8-11. The U16a1s(90) and U16a1s(30)-8a1s(30)-16a1s(30) targets are taken as examples of the single- and triple-layered UHPFRC, respectively. As exhibited in Fig. 8-10, pressure is invoked in the U16a1s(90) target at the moment the projectile reaches the impacted surface. With the further penetrating of the projectile, the pressure develops inwards and it is localized in a region surrounding the head of the projectile (e.g. the pressure distribution at 35 μs). The affected region has an approximate spherical shape, showing that the spherical cavity expansion hypothesis in Chapter 7 is valid. The contact area between the concrete and the projectile experiences the highest pressure, as shown by the red fringe level in the figures. The pressure decreases gradually outwards in the spherical region (presented by the green fringe level), and the remote area in the target is not significantly influenced (indicated by the dark blue fringe level in the figures). The elements near the impacted surface are removed with the projectile penetrating inwards the UHPFRC, which forms the impact crater in the target. The velocity of the projectile becomes very small after 100 μs and the pressure distribution around the projectile remains almost unchanged. The velocity of the projectile finally drops to zero at approximately 135 μs .

The simulation of the triple-layered UHPFRC shows that the pressure distribution is affected by the layer interface when the stress wave reaches it, as can be observed by comparing the light blue fringe level in Figs. 8-10b and 8-11b. Furthermore, when the projectile leaves the first layer and enters the second one, e.g. at 63 μs (Fig. 8-11d), the pressure distribution varies. The distinct pressure distribution in the figure also explains the bending velocity curve of U16a1s(30)-8a1s(30)-16a1s(30) in Fig. 8-9b. As exhibited in Fig. 8-11d, the influenced region is divided into two spheres by the layer interface. This may be attributed to the complicated propagation and reflection of the stress wave near the interface, the distinct pressure bearing capacities of the interface and the layer matrix, as well as the different confining levels of the two layers. Moreover, the existence of the layer interface in the triple-layered UHPFRC can dampen the strength of the impact waves (Chen and Chandra, 2004),

contributing to the smaller DOP and reduced damage size. In addition, the affected area in the triple-layered target is larger than that in its single-layered counterpart (see the light blue area in Figs. 8-10 and 8-11), indicating a higher energy dissipation of the projectile in U16a1s(30)-8a1s(30)-16a1s(30). This, therefore, further promotes the enhanced impact resistance of the triple-layered UHPFRC.

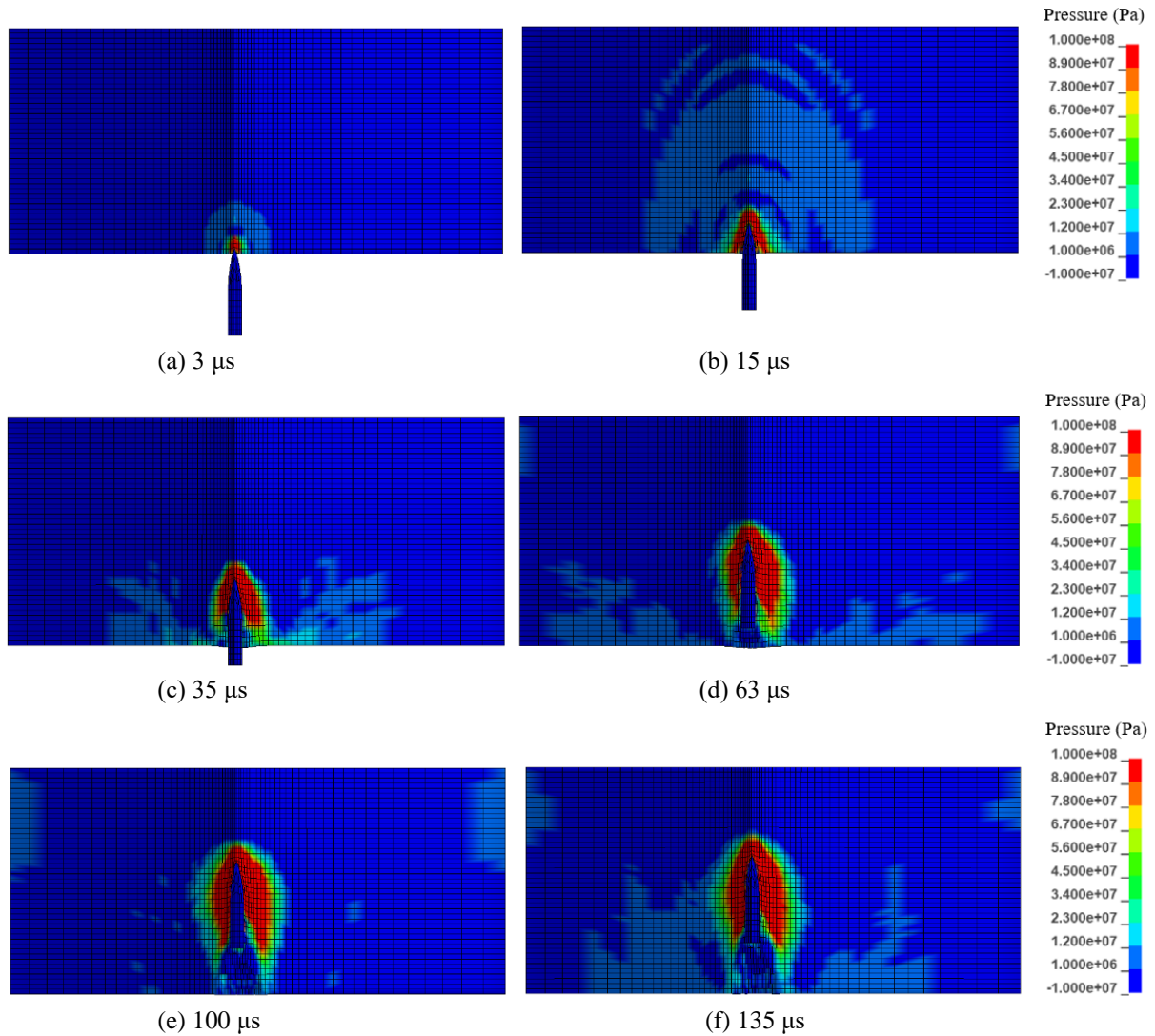
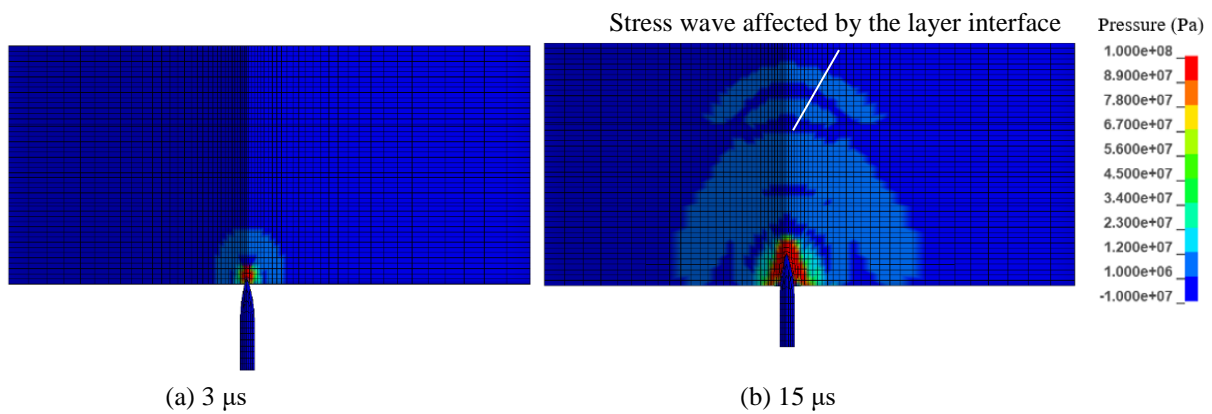


Fig. 8-10 Pressure development in U16a1s(90)



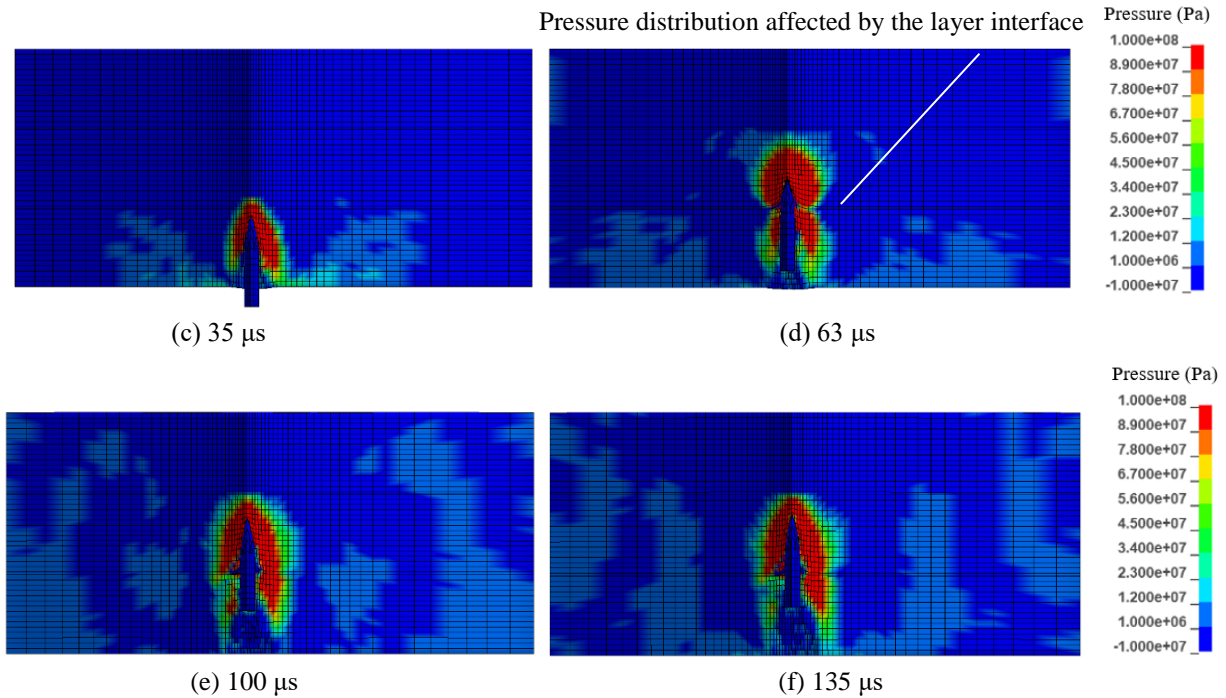


Fig. 8-11 Pressure development in U16a1s(30)-8a1s(30)-16a1s(30)

8.5 Discussion

8.5.1 Influence of layer thickness on DOP

Applying the validated models, the influences of the target thickness on the DOP are discussed. As suggested by the experimental and the simulation results, the DOP in the three targets U8a1s(90), U16a1s(90) and U16a1s(30)-8a1s(30)-16a1s(30) are less than 60 mm, indicating that the 90 mm targets are sufficient to resist the 7.62 mm \times 51 AP projectile at around 840 m/s. To achieve a more efficient utilization of the targets, their thicknesses can be reduced. Fig. 8-12 shows the DOP in the targets with their thickness decreasing from 90 to 60 mm. U8a1s and U16a1s correspond to the series of the single-layered UHPFRC targets containing maximum aggregates of 8 mm and 16 mm, respectively. U16a1s-8a1s-16a1s represents the series of the triple-layered UHPFRC, and each layer has an equal thickness. The initial velocity of the projectile remains identical to that presented in Section 8.3, i.e. approximately 840 m/s. It is noteworthy that the DOP in the U16a1s target with a thickness of 60 mm is around 60.2 mm. In other words, the tip of the projectile slightly crosses the rear surface of the target, as shown in Fig. 8-13.

Fig. 8-12 reveals that the DOP decreases with the increase of the target thickness, nonetheless, the decrease becomes insignificant after the target thickness reaches a critical value. To be more specific, an U8a1s target with a thickness of 60 mm is perforated by the projectile, hence no point corresponding to this case is shown in Fig. 8-12. However, increasing the thickness from 60 to 67.5 mm improves the ballistic resistance remarkably, i.e. the projectile is stopped inside the 67.5 mm target with a DOP of 63.1 mm. The failure pattern of this target is shown in Fig. 8-14a, in which a major crack on the rear surface of the U8a1s target caused by the reflected tensile wave is presented. Further increasing the thickness from 67.5 to 75 mm results in a 2.6 mm reduction in DOP, whereas the reduction becomes insignificant when the target thickness is further increased to 82.5 mm and 90 mm. Nevertheless, the rear surface cracking is effectively prevented in these targets thanks to their increased

thicknesses (see the failure pattern of the 82.5 mm target in Fig. 8-14b). Similar tendencies can be obtained in the cases of the U16a1s and U16a1s-8a1s-16a1s series. Moreover, the critical target thickness differs for the three target series: it is around 75 mm for the U8a1s series, while for U16a1s the value is around 67.5 mm; as with the triple-layered target, the critical target thickness is smaller than 60 mm.

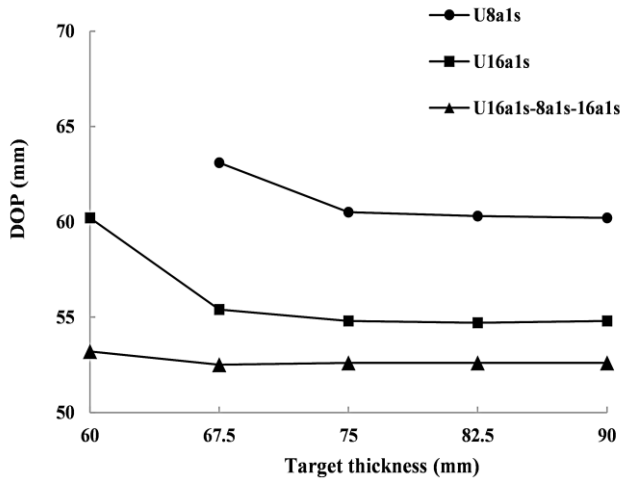


Fig. 8-12 Influence of the target thickness

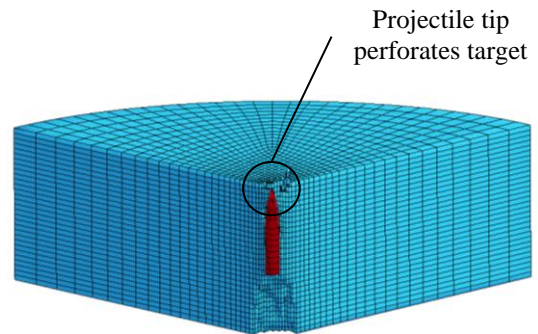
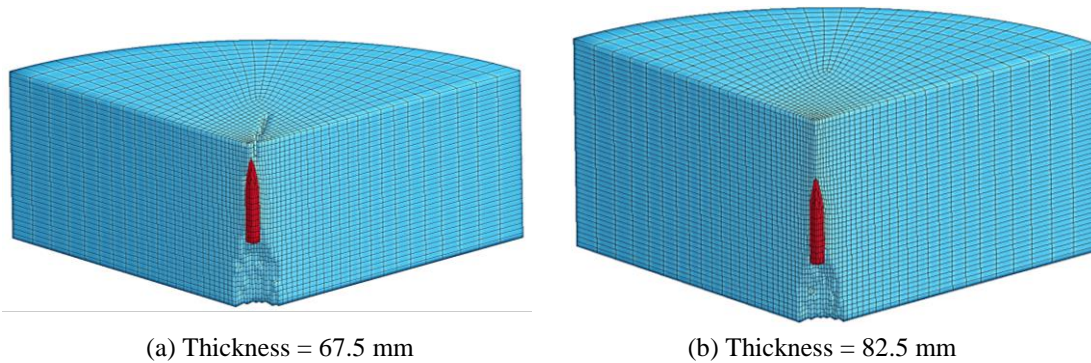


Fig. 8-13 Failure pattern of U16a1s (thickness = 60 mm)



(a) Thickness = 67.5 mm

(b) Thickness = 82.5 mm

Fig. 8-14 Failure pattern of U8a1s targets with different thicknesses

Additionally, comparing the DOP of the U8a1s and U16a1s series in Fig. 8-12 reveals that the larger aggregates play an important role on improving the ballistic resistance, and this influence is more obvious when the target is thin. For instance, the DOP in the 67.5 mm target has an approximate 12% reduction when the maximum aggregate size increases from 8 to 16 mm, while the DOP reduction is around 9% when the target thickness is 90 mm. Moreover, Fig. 8-12 shows that the U16a1s-8a1s-16a1s series has the smallest DOP among the three simulated target series with the same thickness. To be more precise, the DOP in the U8a1s, U16a1s and U16a1s-8a1s-16a1s targets with a thickness of 75 mm are about 60.5 mm, 54.8 mm and 52.6 mm, respectively. The lower DOP of the U16a1s-8a1s-16a1s series in the whole thickness range reveals that the triple-layered UHPFRC possesses an enhanced impact resistance compared to its single-layered counterparts with the same target thickness. This also indicates the possibility of using a thinner triple-layered target as an alternative to the thicker single-layered one to achieve the same level of protection, e.g. the 60 mm U16a1s-8a1s-16a1s target may be used to replace the 90 mm U16a1s target considering their comparable DOP.

8.5.2 Influences of penetration velocity on perforation limit

Perforation limit h_e is defined as the minimum target thickness required to prevent perforation (Li et al., 2006), and it is an important characterization for ballistic engineers to design safety protective structures. A number of empirical formulae have been developed to predict the perforation limit of concrete material, e.g. the BRL formula, ACE formula, modified NDRC formula and CEA-EDF formula. The expressions of these formulae are given below (Li et al., 2006), and the definitions of the parameters in these formulae can be found in Chapter 7 (Section 7.4.2).

- BRL formula (Li et al., 2006):

$$\frac{h_e}{d} = \frac{1.729 \times 10^{-3}}{\sqrt{\sigma_{c,s}}} \left(\frac{M}{d^3} \right) d^{0.2} V_0^{1.33} \quad (8-8)$$

- ACE formula (Li et al., 2006):

$$\frac{h_e}{d} = \frac{4.34 \times 10^{-4}}{\sqrt{\sigma_{c,s}}} \left(\frac{M}{d^3} \right) d^{0.215} V_0^{1.5} + 1.94 \quad (8-9)$$

- Modified NDRC formula (Li et al., 2006):

$$\frac{h_e}{d} = 3.19 \frac{DOP}{d} - 0.718 \left(\frac{DOP}{d} \right)^2 \quad \text{for } h_e/d \leq 3 \quad (8-10a)$$

$$\frac{h_e}{d} = 1.32 + 1.24 \frac{DOP}{d} \quad \text{for } 3 < h_e/d < 18 \quad (8-10b)$$

where the expression of DOP in Eq. 8-10a can be found in Chapter 7.

- CEA-EDF formula (Li et al., 2006):

$$\frac{h_e}{d} = 0.82 \frac{M^{0.5} V_0^{0.75}}{\rho^{0.125} \sigma_{c,s}^{0.375} d^{1.5}} \quad (8-11)$$

The h_e of the U8a1s, U16a1s and U16a1s-8a1s-16a1s series under different penetration velocities of 640 ~ 940 m/s are estimated approximately by the numerical models. The results are illustrated in Table 8-4, together with the calculated h_e from the above empirical formulae. It should be noted that for the triple-layered UHPFRC, the equivalent concrete compressive strength $\sigma_{c,eq}$ obtained according to the composite theory (Xu et al., 2010) is used in the empirical formulae. More information about $\sigma_{c,eq}$ can be found in Chapter 7 (Section 7.5.2).

As shown in Table 8-4, the ACE formula gives results that are closest to the numerical h_e of the U8a1s series in the whole velocity range, and predictions for the U16a1s series at high velocities namely 840 m/s and 940 m/s are also acceptable. The modified NDRC formula yields results comparable to the numerical h_e of U16a1s at 640 m/s and 740 m/s, as well as those of U16a1s-8a1s-16a1s at 640 m/s, 740 m/s and 840 m/s. In contrast, the numerical h_e of U16a1s-8a1s-16a1s at 940 m/s falls between the estimations of the modified NDRC and ACE formulae.

Table 8-4 Perforation limits at different velocities

V_0 (m/s)	Method	h_e (mm)		
		U8a1s	U16a1s	U16a1s-8a1s-16a1s
640	Simulation	48.0	45.0	42.0
	BRL	51.1	50.1	50.4
	ACE	50.6	49.8	50.1
	CEA-EDF	39.1	38.5	38.7
	Modified NDRC	45.4	45.1	45.2
740	Simulation	57.0	54.0	48.0
	BRL	62.0	60.8	61.2
	ACE	59.3	58.4	58.7
	CEA-EDF	43.6	42.9	43.1
	Modified NDRC	50.4	50.0	50.1
840	Simulation	67.5	63.0	57.0
	BRL	73.4	71.9	72.4
	ACE	68.6	67.5	67.9
	CEA-EDF	47.9	47.2	47.4
	Modified NDRC	55.2	54.8	54.9
940	Simulation	78.0	75.0	67.5
	BRL	82.3	83.5	84.1
	ACE	78.5	77.2	77.6
	CEA-EDF	52.2	51.4	51.6
	Modified NDRC	60.1	59.5	59.7

Accordingly, none of these existing empirical formulae is able to predict the h_e of the developed UHPFRC in the whole velocity range. That is because these formulae are proposed based on the regression analyses of certain types of concrete under certain impact velocities, which limits their application ranges (Li and Chen, 2003). Since UHPFRC is a relatively new material, these empirical formulae are not exactly proposed for it and their validity has not been verified against impacts on UHPFRC, not to mention the coarse-aggregated layered UHPFRC. That being the case, the ACE formula is modified to give more accurate predictions for the coarse-aggregated layered UHPFRC developed in this study. The modified ACE formulae are obtained on the basis of the simulation results in Table 8-4, and the expressions are given below:

$$\frac{h_e}{d} = \frac{4.34 \times 10^{-4}}{\sqrt{\sigma_{c,s}}} \left(\frac{M}{d^3} \right) d^{0.215} V_0^{1.5} + 1.73 \quad \text{for U8a1s} \quad (8-12a)$$

$$\frac{h_e}{d} = \frac{4.34 \times 10^{-4}}{\sqrt{\sigma_{c,s}}} \left(\frac{M}{d^3} \right) d^{0.215} V_0^{1.5} + 1.42 \quad \text{for U16a1s} \quad (8-12b)$$

$$\frac{h_e}{d} = \frac{4.34 \times 10^{-4}}{\sqrt{\sigma_{c,s}}} \left(\frac{M}{d^3} \right) d^{0.215} V_0^{1.5} + 0.63 \quad \text{for U16a1s-8a1s-16a1s} \quad (8-12c)$$

The comparisons between the h_e from the numerical simulation and the modified ACE formulae are shown in Fig. 8-15. Excellent agreements are observed. It is worth mentioning that similar to existing empirical formulae, the modified ACE formulae have their applied scopes. They are proposed for the coarse-aggregated layered UHPFRC against the 7.62 mm \times 51 AP projectile under impact velocities between 640 ~ 940 m/s. Using them for larger-caliber projectile may lead to underestimation of the

DOP due to the scaling effect, which can be attributed to the inconsistent size variations of the projectile and the aggregates (Wu et al., 2019).

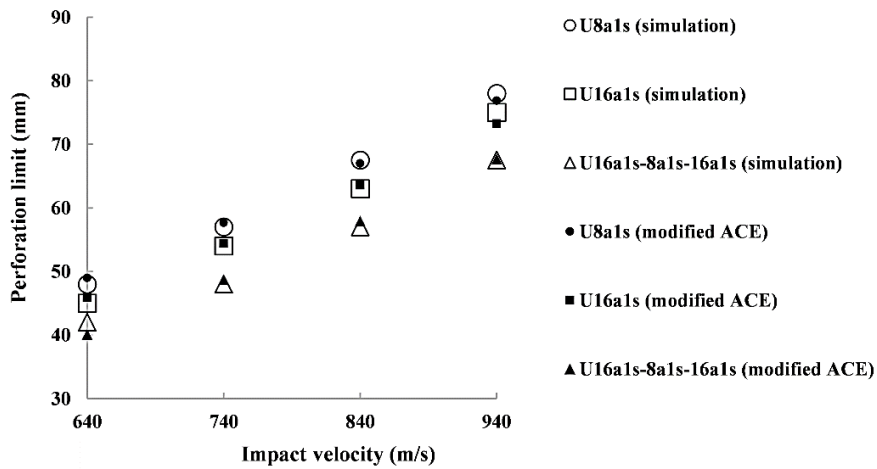


Fig. 8-15 Comparison between simulation and modified ACE formulae

Furthermore, as depicted by the numerical results in Table 8-4, h_e increases with the increase of the initial penetration velocity, and the value is the largest for the single-layered UHPFRC with smaller aggregates, viz. U8a1s, while it is the smallest for the triple-layered series, viz. U16a1s-8a1s-16a1s. For example, the simulation shows that for an U8a1s target, the smallest thicknesses to prevent perforation under 640 m/s and 940 m/s are about 48 mm and 78 mm, respectively. On the contrary, those corresponding to the U16a1s-8a1s-16a1s series are only 42 mm and 67.5 mm, decreasing 14% and 16%, respectively, compared to those of U8a1s.

The smaller h_e of the U16a1s-8a1s-16a1s series indicates the feasibility to reduce the target thickness by applying the layered-structure, which then benefits the production cost and the environmental sustainability thanks to the reduced materials used in the targets. Table 8-5 gives the cement and fiber amounts to cast a UHPFRC target with a diameter of 275 mm and a thickness of h_e (obtained from the simulations). The calculation is based on the mixture recipes given in Chapter 6 (Section 6.2.1).

Table 8-5 Cement amount to cast one UHPFRC target with a diameter of 275 mm and a thickness of h_e

Initial velocity V_0 (m/s)	Material amounts (kg)					
	U8a1s		U16a1s		U16a1s-8a1s-16a1s	
	cement	fiber	cement	fiber	cement	fiber
640	1.68	0.22	1.40	0.21	1.36	0.20
740	1.99	0.27	1.68	0.25	1.56	0.22
840	2.36	0.31	1.96	0.29	1.85	0.27
940	2.72	0.36	2.34	0.35	2.19	0.31

Thanks to the enhanced impact resistance of the triple-layered UHPFRC, the amounts of cement and fiber required to cast the U16a1s-8a1s-16a1s targets are obviously reduced compared with their single-layered counterparts. To specify, the cement amounts for the U16a1s-8a1s-16a1s targets to prevent perforation under 640 m/s, 740 m/s, 840 m/s and 940 m/s are about 19%, 22%, 22% and 20% less than those for the U8a1s targets; and the corresponding fiber amount reductions are 13%, 16%, 16% and 13%, respectively. As a consequence, with the same level of ballistic resistance, the triple-

layered UHPFRC consumes less materials than the single-layered one, making the layered target more sustainable and more economic. In addition, the lighter weight of the triple-layered UHPFRC target is also beneficial for its transportation and installation in military fields.

8.6 Conclusions

This study uses LS-DYNA to numerically investigate the ballistic performances of the single- and triple-layered UHPFRC containing coarse aggregates. The ballistic experiments of the U8a1s(90), U16a1s(90) and U16a1s(30)-8a1s(30)-16a1s(30) targets presented in Chapter 6 are utilized to validate the simulations in this chapter. The displacement and velocity histories of the projectile, as well as the dynamic penetration process in the three targets are analyzed. Furthermore, the effects of the target thickness on the DOP, and the influences of the impact velocity on the perforation limit are discussed. In addition, modified ACE formulae to accurately predict h_e of the coarse-aggregated layered UHPFRC are proposed based on the simulations. The study in this chapter benefits to better understand the responses of the single- and triple-layered UHPFRC subjected to high-velocity projectile impacts, and the advantages of applying coarse aggregates and the layered structure are further confirmed. The following conclusions can be drawn:

- (1) The numerical simulations of the U8a1s(90), U16a1s(90) and U16a1s(30)-8a1s(30)-16a1s(30) targets coincide very well with the experimental results. The difference between of the DOP and the crater size obtained from the experiments and the simulations are smaller than 0.5% and 5%, respectively.
- (2) The HJC constitutive model in LS-DYNA can well characterize the dynamic response of the coarse-aggregated UHPFRC subjected to projectile impacts; and the improved ballistic resistance provided by the coarse aggregates can be reflected by increasing the crushing pressure in the model.
- (3) The layer interface affects the pressure distribution in the triple-layered target and thus the velocity history of the projectile. This can be attributed to the complicated propagation and reflection of the stress wave near the interface, the distinct pressure bearing capacities of the interface and the layer matrix, as well as the different confining levels of the two layers.
- (4) The DOP decreases with the increase of the target thickness; however, the reduction becomes very limited when the critical target thickness is reached. The critical thickness is around 75 mm, 67.5 mm and 60 mm for the U8a1s, U16a1s and U16a1s-8a1s-16a1s targets, respectively.
- (5) The perforation limit h_e increases with the increase of the penetration velocity. Under the same velocity, U8a1s has the largest h_e while U16a1s-8a1s-16a1s achieves the smallest h_e , indicating the feasibility to make thinner targets with the layered structure concept. Consequently, the triple-layered UHPFRC consumes less amounts of cement and fiber than the single-layered one with the same level of ballistic resistance, which makes the layered target more environmentally and economically attractive.

Chapter 9

Conclusions and recommendations



9.1 Conclusions

UHPFRC is generally characterized by its very high compressive strength, excellent energy absorption capacity and outstanding damage resistance, making it a promising material to withstand both static and dynamic loads. In this research, the fibers effects on the coarse-aggregated layered UHPFRC subjected to static and dynamic loads are investigated, with the focus on the fiber pullout performance at mesoscale and the fiber amount distribution over the layered UHPFRC at macroscale. As such, the research addresses five inter-related topics:

- (1) Understanding the effects of the fiber inclination on the static fiber pullout performance;
- (2) Understanding the effects of the pullout rate on the dynamic fiber pullout performance;
- (3) Enhancing the static flexural performance of the coarse-aggregated UHPFRC using a layered structure;
- (4) Enhancing the low-velocity impact resistance of the coarse-aggregated UHPFRC using a layered structure;
- (5) Enhancing the high-velocity impact resistance of the coarse-aggregated UHPFRC using a layered structure.

Some primary conclusions concerning these topics are summarized as follows.

9.1.1 Understanding the effects of the fiber inclination on the static fiber pullout performance

Fiber inclination has different effects for different sized hooked-end steel fibers with different embedded lengths. For the small Dramix RC-80/30-BP fiber with an embedded length of 10 mm, the peak pullout loads at 0° and 10° are slightly higher than those at 20° and 30°. In contrast, for the large one-hooked-end Dramix 5D fiber, the optimum inclination angles to achieve the maximum pullout resistance are at 20° and 30° when the embedded lengths are 10 mm and 15 mm, respectively.

Regarding the fiber efficiency, the small Dramix RC-80/30-BP fiber achieves the highest utilization efficiency and the maximum value is obtained at the pullout angle of 0°. The efficiency of the one-hooked-end Dramix 5D fiber reaches its peak at 30°; however, it is only approximately half that of the Dramix RC-80/30-BP fiber, indicating that the strength of the large fiber is too superabundant to match the UHPC matrix.

Moreover, the SEM images confirm the dense microstructure of the designed UHPC, which provides a strong bond between the fiber and the matrix. Due to this strong bond and the anchorage of the fiber hook, the Dramix RC-80/30-BP fiber with an inclination angle larger than 20° has a high risk to break during its pullout from the UHPC matrix.

The effects of fiber inclination on the pullout behavior are associated with both the snubbing effect and the matrix spalling effect. The snubbing effect invokes an additional friction resistance and promotes the improvement of the pullout force at a larger inclination angle. On the one side, the matrix spalling effect reduces the fiber embedded length and results in a decreased pullout load with increased pullout angle. To effectively evaluate these effects, an analytical model for the hooked-end fiber is proposed and validated, and the corresponding snubbing friction coefficient $f_p = 1.25$ and matrix spalling coefficient $k_p = 1.0$ are obtained.

9.1.2 Understanding the effects of the pullout rate on the dynamic fiber pullout performance

The pullout performance of the hooked-end steel fiber embedded in UHPC matrix can be affected by the pullout rate. The Stefan effect and the inertia effect due to micro-cracking in the interface are the two main mechanisms contributing to the rate-dependent pullout responses. Both the peak pullout load and the pullout energy of the Dramix RC-80/30-BP fiber are enhanced under the dynamic pullout load, and the enhancement of the pullout energy is more remarkable. To be more precise, with an embedded length of 15 mm, the dynamic increase factors (DIFs) of the peak pullout load at 50 mm/min, 500 mm/min and 1000 mm/min are 1.03, 1.12 and 1.22, while those of the pullout energy are 1.17, 1.28 and 1.46, respectively.

The peak pullout load tends to be more rate sensitive with a smaller fiber embedded length. The influences of the fiber embedded length on the rate dependency of the pullout response are associated with the matrix confinement. A larger embedded length leads to a larger matrix confinement, which retards the cracking near the hook bending region and thus decreases the rate dependency caused by the micro inertia effect. In contrast, with a smaller embedded length, micro-cracks can occur both in plane and out of plane because of the reduced confinement, contributing to a more apparent rate effect.

An analytical model is developed to predict the dynamic peak pullout loads of hooked-end steel fiber embedded in UHPC matrix at loading rates up to the intermediate level. The influences of the pullout rate, concrete compressive strength, fiber properties and embedded length are considered in the model. The good correlation between the predicted peak pullout loads and the experimental results confirm the validity of the proposed model.

9.1.3 Enhancing the static flexural performance of the coarse-aggregated UHPFRC using a layered structure

The double-layered UHPFRC with coarse aggregates incorporated and fibers efficiently distributed is designed in this research, and its static flexural performance is analyzed theoretically and experimentally. In the theoretical section, the cracking and debonding criteria of the double-layered beam are developed, and the critical load at the first stage of the failure process $F_{critical}$ is obtained. The theoretical analysis reveals that when the top and bottom layers of the beam have comparable elastic moduli, e.g. layer elastic modulus ratio (the ratio of the top and bottom layers' elastic moduli) $\beta_E = 0.8 \sim 1$, increasing the layer thickness ratio β_h (the ratio of the bottom layer thickness to the total beam height) from 0.1 to 0.3 leads to a prominent increase of $F_{critical}$, whereas further thickening the bottom layer would not generate significant improvement.

Based on the theoretical analysis, the double-layered UHPFRC beams are designed for the experimental program. Three-point bending tests are conducted to evaluate the static flexural performance of the coarse-aggregated layered UHPFRC. No layer debonding is observed during the tests thanks to the strong interfacial bond between the layers. The influences of β_h on the beam flexural performance are investigated experimentally. It is found that the peak flexural load and the flexural energy are remarkably improved with the increase of the bottom layer thickness until $\beta_h = 0.6$ is reached. Moreover, the fiber efficiency, defined as the ratio of the beam flexural energy to the mass of the fiber, also reaches its maximum at $\beta_h = 0.6$. Considering the gained knowledge above, $\beta_h = 0.6$ is recommended for the double-layered UHPFRC beam.

Compared to the 100 mm single-layered UHPFRC beam with the same total fiber amount, the designed double-layered beam composed of a 40 mm-thick top layer with 0.6% straight fibers and a 60 mm-thick bottom layer with 1.6% straight fibers, viz. U0.6(40)-1.6(60), achieves a 24% higher peak flexural load and a 14% higher flexural energy. These enhancements exhibit the improved beam flexural performance by applying the layered structure, and they also indicate the potential of utilizing layered beams containing less fibers to obtain a superior flexural performance.

9.1.4 Enhancing the low-velocity impact resistance of the coarse-aggregated UHPFRC using a layered structure

In addition to the better performance under static bending, the double-layered UHPFRC has a superior resistance under the low-velocity drop-weight impact. Specifically, the double-layered UHPFRC beam has a higher peak reaction force than its single-layered counterpart. The absorbed impact energy of the double-layered UHPFRC is also improved, and this improvement is more obvious for the UHPFRC with hooked-end fibers. For instance, the double-layered beam containing straight fibers, viz. U0.6s-1.6s, achieves a 15% higher impact energy than the single-layered one; whereas the corresponding enhancement of the double-layered beam with hooked-end fibers is 28%. Moreover, for UHPFRC with both the straight and hooked-end fibers, distributing the hooked-end fibers in the bottom layer and the straight ones in the top layer, viz. U0.6s-1.6h, generates a desirable energy absorption capacity.

For both the single- and double-layered UHPFRC, the peak reaction force, impact number and absorbed impact energy increase with the increasing amount of the hooked-end fibers. This is because the resistance of the UHPFRC against low-velocity impacts is closely related to the fiber pullout response. Compared to the short straight fiber, the hooked-end fiber has a longer embedded length and its hook can generate an additional mechanical anchorage. As a consequence of both the higher frictional bond force and the mechanical anchorage, higher force and more energy are required to pull the hooked-end fiber out of the UHPC matrix, leading to a higher impact resistance of the UHPFRC reinforced with more hooked-end fibers.

A model to estimate the absorbed energy of the layered UHPFRC under repeated drop-weight impacts is developed and validated, and a fiber group effect coefficient $\eta_g = 0.9$ is proposed for the hooked-end steel fiber used in the present study. The proposed model confirms that the fiber pullout process constitutes the major part of the absorbed impact energy, while the matrix cracking only consumes an insignificant portion. Additionally, a 21% higher dynamic fiber efficiency is obtained by the double-layered beam compared to the single-layered one, which further confirms the advantages of the layered structure.

9.1.5 Enhancing the high-velocity impact resistance of the coarse-aggregated UHPFRC using a layered structure

Multi-layered UHPFRC targets containing coarse basalt aggregates are developed and tested against the 7.62 mm \times 51 AP projectile at a penetration velocity of about 840 m/s. The coarse basalt aggregates improve the impact resistance of UHPFRC by increasing the strength and hardness of the material, eroding the projectile and deviating its trajectory, which promote the dissipation of the projectile kinematic energy. Moreover, fibers in UHPFRC help to increase the material toughness and

prevent the target disintegration. Fiber geometry insignificantly affects the ballistic performance when the maximum aggregate size of the target is 8 mm, but for the UHPFRC with a maximum aggregate size of 16 mm, the straight steel fiber can provide a more effective damage control in comparison to the hooked-end fiber. This may be attributed to the following factors: the higher amount of the straight fiber, the reduced pullout resistance of the hooked-end fiber due to its inclination, and the smaller disturbed zone in the UHPFRC with the short straight fibers.

For the double-layered UHPFRC, increasing the aggregate size in either layer decreases the depth of penetration (DOP), and the effect is more obvious when the larger aggregates are in the impact layer. The double-layered UHPFRC with 16 mm aggregates in the impact layer and 8 mm aggregates in the back layer has a smaller DOP than the single-layered UHPFRC containing 16 mm aggregates in the whole target. Possible enhancing mechanisms related to the layered structure include: the layer interface that dampens the impact waves, the interfacial cracking that promotes energy consumption, the reduced damage in the back side of the target that provides a higher resistance, and the different confining levels of the two layers caused by the different aggregate sizes.

For the triple-layered UHPFRC, the fiber amount distribution over the layered structure reduces both the DOP and the equivalent crater diameter, and the design of utilizing larger aggregates and more fibers in the outer layers is recommended. Furthermore, in spite of its 10% less cement dosage, the optimized triple-layered UHPFRC U16a1s(40)-8a1s(10)-16a1s(40) achieves a 32% reduced DOP compared to U8a1s(90). This reduced DOP is associated with the effects of the coarse aggregates, the layer interface, the direction of fibers in the thin middle layer, and the edge confinement of the thick rear layer.

DOP predictive models for the single- and multi-layered UHPFRC are developed on the basis of an improved cavity expansion theory. The Hoek-Brown criterion is used in the model to describe the response of the UHPFRC material in the comminuted region. The DIF formulae in the CEB-FIP Model Code are adopted to account for the rate effect, and a reduction factor $\xi = 0.35$ to correct the dynamic resistance is obtained. The predictive model for single-layered UHPFRC is proposed and validated, and it is further extended for the multi-layered UHPFRC. The extended model is able to account for the varying mechanical properties and the layers' order in the multi-layered targets, and it successfully predicts the DOP in the layered UHPFRC with an accuracy higher than 95%.

Furthermore, the ballistic performance of the coarse-aggregated layered UHPFRC is numerically investigated using LS-DYNA. The Holmquist Johnson Concrete (HJC) constitutive model is employed for the UHPFRC, and the enhanced resistance provided by the coarse aggregates is reflected by adjusting the pressure-compaction relation in the model. The simulations coincide well with the experimental results. It is presented that the DOP decreases with the increasing target thickness until a critical thickness is reached. In addition, U16a1s-8a1s-16a1s has a smaller perforation limit than U8a1s. Consequently, the triple-layered UHPFRC consumes less cement and fiber than the single-layered one with the same level of ballistic resistance, making the layered target more environmentally and economically attractive.

9.2 Recommendations

Recommendations for future studies that stems from this research are given:

- (1) The influences of loading rate on the bond properties of the layered UHPFRC should be evaluated. It is observed in this research that no layer debonding occurs in the static flexural test and

the low-velocity drop-weight test. But obvious cracking along the interface is noticed in some layered UHPFRC targets during the high-velocity ballistic tests, which may be related to the extremely strong impact wave. These phenomena indicate that the bond properties of the layered UHPFRC are rate sensitive. That being the case, the influences of the loading rate on the layer interface properties should be clarified.

(2) For the layered UHPFRC in this research, the top layer is cast on the bottom layer without special treatment of the contact surface, i.e. the strong interfacial bond is achieved by controlling the casting time interval. To further improve the bond strength, bonding enhancement methods, e.g. applying surface treatment and using bonding agents, would be solutions. The feasibility, efficiency and influences of possible bonding enhancement methods require further investigations.

(3) The long-term performance of the layered UHPFRC is an important topic to be investigated. For example, the influences of the layer interface on the durability of the layered UHPFRC should be understood. In comparison to the UHPFRC matrix, the layer interface has a relatively larger porosity, which may affect the durability, e.g. the water permeability and chloride penetration resistance, of the layered UHPFRC at a long term.

(4) The developed drop-weight test setup in this research requires further improvement. A more accurate measurement device, e.g. contact-less laser displacement sensor, is recommended to directly measure the beam deflection with a higher accuracy. Additionally, a laser Doppler velocimetry monitoring technique is recommended to measure the rapidly changing velocity of the beam at its last impact, which can provide more complete information on the dynamic response of the UHPFRC.

(5) The impact resistance of the UHPFRC subjected to the 7.62 mm × 51 AP projectile is investigated in this research. This projectile is tested because it is a common in-service arm in many countries. Nonetheless, the developed coarse-aggregated layered UHPFRC has the potential to resist more destructive impacts caused by more powerful weapons. To fully assess the resistance of the developed UHPFRC, ballistic tests against larger-caliber projectiles should be executed.

(6) Mesoscale modelling of UHPFRC against dynamic impact is another interesting topic. Fibers and coarse aggregates are explicitly present in UHPFRC at mesoscale. Therefore, their influences on the dynamic cracking process and the wave phenomenon inside the UHPFRC can be analyzed more directly with the mesoscale model, which can promote a clearer and deeper understanding of the dynamic response of UHPFRC.

Bibliography

- Abbas, S., Soliman, A.M., Nehdi, M.L., 2015. Exploring mechanical and durability properties of ultra-high performance concrete incorporating various steel fiber lengths and dosages. *Constr. Build. Mater.* 75, 429–441. <https://doi.org/10.1016/j.conbuildmat.2014.11.017>
- Abu-Lebdeh, T., Hamoush, S., Zornig, B., 2010. Rate effect on pullout behavior of steel fibers embedded in Very-High Strength Concrete. *Am. J. Eng. Appl. Sci.* 3, 454–463. <https://doi.org/10.3844/ajeassp.2010.454.463>
- ACI Committee 544, 1999. Measurement of properties of fiber reinforced concrete, *Aci.*
- Almusallam, T.H., Siddiqui, N.A., Iqbal, R.A., Abbas, H., 2013. Response of hybrid-fiber reinforced concrete slabs to hard projectile impact. *Int. J. Impact Eng.* 58, 17–30. <https://doi.org/10.1016/j.ijimpeng.2013.02.005>
- Alsaman, A., Dang, C.N., Prinz, G.S., Hale, W.M., 2017. Evaluation of modulus of elasticity of ultra-high performance concrete. *Constr. Build. Mater.* 153, 918–928. <https://doi.org/10.1016/j.conbuildmat.2017.07.158>
- Alwan, J., Naaman, A., Guerrero, P., 1999. Effect of mechanical clamping on the pull-out response of hooked steel fibers embedded in cementitious matrices. *Concr. Sci. Eng.* 1, 15–25.
- Banthia, N., Mindess, S., Bentur, A., Pigeon, M., 1989. Impact testing of concrete using a drop-weight impact machine. *Exp. Mech.* 29, 63–69. <https://doi.org/10.1007/BF02327783>
- Banthia, N., Sappakittipakorn, M., 2007. Toughness enhancement in steel fiber reinforced concrete through fiber hybridization. *Cem. Concr. Res.* 37, 1366–1372. <https://doi.org/10.1016/j.cemconres.2007.05.005>
- Banthia, N., Trottier, J.-F., 1991. Deformed steel fiber-cementitious matrix bond under impact. *Cem. Concr. Res.* 21, 158–168.
- Banthia, N., Trottier, J., 1994. Concrete reinforced with deformed steel fibers , part I : Bond-slip mechanisms *Concrete Reinforced with Deformed Steel Fibers , Part I : Bond-Slip Mechanisms.* *Aci Mater. J.* 91, 435–446.
- Ben-Dor, G., Dubinsky, A., Elperin, T., 2015. Analytical engineering models for predicting high speed penetration of hard projectiles into concrete shields: A review. *Int. J. Damage Mech.* 24, 76–94. <https://doi.org/10.1177/1056789514521647>
- Bischoff, P.H., Perry, S.H., 1991. Compressive behaviour of concrete at high strain rates. *Mater. Struct.* 24, 425–450. <https://doi.org/10.1007/BF02472016>
- Booker, P.M., Cargile, J.D., Kistler, B.L., La Saponara, V., 2009. Investigation on the response of segmented concrete targets to projectile impacts. *Int. J. Impact Eng.* 36, 926–939. <https://doi.org/10.1016/j.ijimpeng.2008.10.006>
- Bornord, R.S., Hanagud, S. V., 1975. Development of a projectile penetration theory, Report I. Vicksburg.
- Brouwers, H.J.H., Radix, H.J., 2005. Self-compacting concrete: Theoretical and experimental study. *Cem. Concr. Res.* 35, 2116–2136. <https://doi.org/10.1016/j.cemconres.2005.06.002>
- Brühwiler, E., 2009. Improving safety and durability of civil structures, in: (eds.), A.I. and M.Z. (Ed.), *Damage Assessment and Reconstruction After War or Natural Disaster.* Springer Science+Business Media, Berlin, pp. 63–93.
- Burlion, N., 1997. *Compaction des betons: elements de modelisation et caracterisation experimentale.* LMT, ENS de Cachan, France.

- Buttignol, T.E.T., Sousa, J.L.A.O., Bittencourt, T.N., 2017. Ultra High-Performance Fiber-Reinforced Concrete (UHPFRC): a review of material properties and design procedures. *Rev. IBRACON Estruturas e Mater.* 10, 957–971. <https://doi.org/10.1590/s1983-41952017000400011>
- Cao, Y.Y.Y., Li, P.P., Brouwers, H.J.H., Sluijsmans, M., Yu, Q.L., 2019a. Enhancing flexural performance of ultra-high performance concrete by an optimized layered-structure concept. *Compos. Part B Eng.* 171, 154–165. <https://doi.org/10.1016/j.compositesb.2019.04.021>
- Cao, Y.Y.Y., Yu, Q.L., 2018. Effect of inclination angle on hooked end steel fiber pullout behavior in ultra-high performance concrete. *Compos. Struct.* 201, 151–160. <https://doi.org/10.1016/j.compstruct.2018.06.029>
- Cao, Y.Y.Y., Yu, Q.L., 2017. Numerical investigation of fibers effects in SFRC under dynamic tension, in: *The 9th International Symposium on Cement and Concrete (ISCC 2017)*. WUHAN,CHINA, pp. 1–7.
- Cao, Y.Y.Y., Yu, Q.L., Brouwers, H.J.H., Chen, W., 2019b. Predicting the rate effects on hooked-end fiber pullout performance from Ultra- High Performance Concrete. *Cem. Concr. Res.* <https://doi.org/10.1182/blood-2016-03-705590>
- CEB-FIP, 2010. Model code for concrete structures. the International Federation for Structural Concrete (fib), Lausanne, Switzerland.
- CEB-FIP, 1990. Model code for concrete structures. Thomas Telford Services Ltd, Thomas Telford House, I Heron Quay,. <https://doi.org/10.1017/CBO9781107415324.004>
- Chen, X., Chandra, N., 2004. The effect of heterogeneity on plane wave propagation through layered composites. *Compos. Sci. Technol.* 64, 1477–1493. <https://doi.org/10.1016/j.compscitech.2003.10.024>
- Corinaldesi, V., Nardinocchi, A., 2016. Mechanical characterization of Engineered Cement-based Composites prepared with hybrid fibres and expansive agent. *Compos. Part B Eng.* 98, 389–396. <https://doi.org/10.1016/j.compositesb.2016.05.051>
- Dancygier, A.N., 2017. High-performance concrete engineered for protective barriers. *Philos. Trans. R. Soc. A Math. Phys. Eng. Sci.* 375. <https://doi.org/10.1098/rsta.2016.0180>
- Dancygier, A.N., Katz, A., Benamou, D., Yankelevsky, D.Z., 2014. Resistance of double-layer reinforced HPC barriers to projectile impact. *Int. J. Impact Eng.* 67, 39–51. <https://doi.org/10.1016/j.ijimpeng.2014.01.001>
- Dancygier, A.N., Yankelevsky, D.Z., Jaegermann, C., 2007. Response of high performance concrete plates to impact of non-deforming projectiles. *Int. J. Impact Eng.* 34, 1768–1779. <https://doi.org/10.1016/j.ijimpeng.2006.09.094>
- Denarié, E., 2009. Strategic targeted research project, Recommendations for the tailoring of UHPFRC.
- Dey, V., Bonakdar, A., Mobasher, B., 2014. Low-velocity flexural impact response of fiber-reinforced aerated concrete. *Cem. Concr. Compos.* 49, 100–110. <https://doi.org/10.1016/j.cemconcomp.2013.12.006>
- Dias, C.M.R., Savastano, H., John, V.M., 2010. Exploring the potential of functionally graded materials concept for the development of fiber cement. *Constr. Build. Mater.* 24, 140–146. <https://doi.org/10.1016/j.conbuildmat.2008.01.017>
- DIN EN 1015-3, 2007. Methods of test for mortar for masonry — Part 3: Determination of consistence of fresh mortar (by flow table) Méthodes.

- Eberhardt, E., 2012. The Hoek–Brown failure criterion. *Rock Mech. Rock Eng.* 45, 981–988.
<https://doi.org/10.1007/s00603-012-0276-4>
- El-Din, H.K.S., Mohamed, H.A., Khater, M.A.E.-H., Ahmed, S., 2016. Effect of steel fibers on behavior of Ultra High Performance Concrete, in: *First International Interactive Symposium on UHPC*. Des Moines, Iowa, pp. 1–10.
- EN 12350-8, 2007. Testing fresh concrete — Part 8: Self-compacting concrete - Slump-flow test.
- EN 12390-6, 2000. Testing hardened concrete - Part 6: Tensile splitting strength of test specimens.
- EN 12390-3, 2009. Testing hardened concrete - Part 3: Compressive strength of test specimens.
- Fang, Q., Kong, X., Hong, J., Wu, H., 2014. Prediction of projectile penetration and perforation by finite cavity expansion method with the free-surface effect. *Acta Mech. Solida Sin.* 27, 597–611. [https://doi.org/10.1016/S0894-9166\(15\)60005-2](https://doi.org/10.1016/S0894-9166(15)60005-2)
- Farnam, Y., Moosavi, M., Shekarchi, M., Babanajad, S.K., Bagherzadeh, A., 2010. Behaviour of Slurry Infiltrated Fibre Concrete (SIFCON) under triaxial compression. *Cem. Concr. Res.* 40, 1571–1581. <https://doi.org/10.1016/j.cemconres.2010.06.009>
- Feng, J., Li, Wenbin, Wang, X., Song, M., Ren, H., Li, Weibing, 2015. Dynamic spherical cavity expansion analysis of rate-dependent concrete material with scale effect. *Int. J. Impact Eng.* 84, 24–37. <https://doi.org/10.1016/j.ijimpeng.2015.05.005>
- Filiatrault, A., Holleran, M., 2001. Stress-strain behavior of reinforcing steel and concrete under seismic strain rates and low temperatures. *Mater. Struct.* 34, 235–239.
<https://doi.org/10.1007/BF02480594>
- Forrestal, M.J., Altman, B.S., Cargile, J.D., Hanchak, S.J., 1994. An empirical equation for penetration depth of ogive-nose projectiles into concrete targets. *Int. J. Impact Engng* 15, 395–405.
- Forrestal, M.J., Frew, D.J., Hanchak, S.J., Brar, N.S., 1996. Penetration of grout and concrete targets with ogive-nose steel projectiles. *Int. J. Impact Eng.* 18, 465–476. [https://doi.org/10.1016/0734-743X\(95\)00048-F](https://doi.org/10.1016/0734-743X(95)00048-F)
- Forrestal, M.J., LuK, V.K., 1992. Penetration into soil targets. *Int. J. Impact Engng* 12, 427–444.
- Forrestal, M.J., Tzou, D.Y., 1997. A spherical cavity-expansion penetration model for concrete targets. *Int. J. Solids Struct.* 34, 4127–4146. [https://doi.org/10.1016/S0020-7683\(97\)00017-6](https://doi.org/10.1016/S0020-7683(97)00017-6)
- Frew, D.J., Hanchak, S.J., Green, M.L., Forrestal, M.J., 1998. Penetration of Concrete Targets with Ogive-Nose Steel Rods 21, 489–497.
- Fu, S., Zhou, B., Lung, C., 1993. On the pull-out of fibres with a branched structure and the inference of strength and fracture toughness of composites. *Compos. Sci. Technol.* 47, 245–250.
[https://doi.org/10.1016/0266-3538\(93\)90033-D](https://doi.org/10.1016/0266-3538(93)90033-D)
- Geng, Y.P., Leung, C.K.Y., 1997. Damage-based modeling of fiber pullout under variable compressive stress. *J. Eng. Mech.* 123, 342–349.
- Gokoz, U.N., Naaman, A.E., 1981. Effect of strain-rate on the pull-out behaviour of fibres in mortar. *Int. J. Cem. Compos. Light. Concr.* 3, 187–202. [https://doi.org/10.1016/0262-5075\(81\)90051-8](https://doi.org/10.1016/0262-5075(81)90051-8)
- Guo, W., Fan, W., Shao, X., Shen, D., Chen, B., 2018. Constitutive model of ultra-high-performance fiber-reinforced concrete for low-velocity impact simulations. *Compos. Struct.* 185, 307–326.
<https://doi.org/10.1016/j.compstruct.2017.11.022>
- Habel, K., Gauvreau, P., 2008. Response of ultra-high performance fiber reinforced concrete (UHPRFC) to impact and static loading. *Cem. Concr. Compos.* 30, 938–946.
<https://doi.org/10.1016/j.cemconcomp.2008.09.001>

- Hassan, M., Wille, K., 2017. Experimental impact analysis on ultra-high performance concrete (UHPC) for achieving stress equilibrium (SE) and constant strain rate (CSR) in Split Hopkinson pressure bar (SHPB) using pulse shaping technique. *Constr. Build. Mater.* 144, 747–757. <https://doi.org/10.1016/j.conbuildmat.2017.03.185>
- He, T., Wen, H.-M., Guo, X.-J., 2011. A spherical cavity expansion model for penetration of ogive-nosed projectiles into concrete targets with shear-dilatancy. *Acta Mech* 27, 1001–1012.
- He, Y., Zhang, Xiong, Hooton, R.D., Zhang, Xiaowei, 2017. Effects of interface roughness and interface adhesion on new-to-old concrete bonding. *Constr. Build. Mater.* 151, 582–590. <https://doi.org/10.1016/j.conbuildmat.2017.05.049>
- Hoek, E., Corkum, B, Carranza-torres, C., Corkum, Brent, 2002. Hoek-Brown failure criterion – 2002 Edition. NARMS-TAC Conf. Toronto 267–273.
- Holmen, J.K., Solberg, J.K., Hopperstad, O.S., Børvik, T., 2017. Ballistic impact of layered and case-hardened steel plates. *Int. J. Impact Eng.* 110, 4–14. <https://doi.org/10.1016/j.ijimpeng.2017.02.001>
- Hou, L., Xu, S., Liu, H., Chen, D., 2015. Flexural and interface behaviors of Reinforced Concrete/Ultra-high Toughness Cementitious Composite (RC/UHTCC) beams. *J. Adv. Concr. Technol.* 13, 82–93. <https://doi.org/10.3151/jact.13.82>
- Hou, X., Cao, S., Zheng, W., Rong, Q., Li, G., 2018. Experimental study on dynamic compressive properties of fiber-reinforced reactive powder concrete at high strain rates. *Eng. Struct.* 169, 119–130. <https://doi.org/10.1016/j.engstruct.2018.05.036>
- Hrynyk, T.D., Vecchio, F.J., 2014. Behavior of steel fiber-reinforced concrete slabs under impact load. *ACI Struct. J.* 111, 1213–1224. <https://doi.org/10.14359/51686923>
- Isla, F., Ruano, G., Luccioni, B., 2015. Analysis of steel fibers pull-out. Experimental study. *Constr. Build. Mater.* 100, 183–193. <https://doi.org/10.1016/j.conbuildmat.2015.09.034>
- Kang, S.T., Kim, J.K., 2011. The relation between fiber orientation and tensile behavior in an ultra high performance fiber reinforced cementitious composites (UHPFRCC). *Cem. Concr. Res.* 41, 1001–1014. <https://doi.org/10.1016/j.cemconres.2011.05.009>
- Kim, D.J., Park, S.H., Ryu, G.S., Koh, K.T., 2011. Comparative flexural behavior of Hybrid Ultra High Performance Fiber Reinforced Concrete with different macro fibers. *Constr. Build. Mater.* 25, 4144–4155. <https://doi.org/10.1016/j.conbuildmat.2011.04.051>
- Kim, J.H.J., Lim, Y.M., Won, J.P., Park, H.G., Lee, K.M., 2007. Shear capacity and failure behavior of DFRCC repaired RC beams at tensile region. *Eng. Struct.* 29, 121–131. <https://doi.org/10.1016/j.engstruct.2006.04.023>
- Kim, J.J., Kim, D.J., Kang, S.T., Lee, J.H., 2012. Influence of sand to coarse aggregate ratio on the interfacial bond strength of steel fibers in concrete for nuclear power plant. *Nucl. Eng. Des.* 252, 1–10. <https://doi.org/10.1016/j.nucengdes.2012.07.004>
- Kim, Y.Y., Lee, B.Y., Bang, J.W., Han, B.C., Feo, L., Cho, C.G., 2014. Flexural performance of reinforced concrete beams strengthened with strain-hardening cementitious composite and high strength reinforcing steel bar. *Compos. Part B Eng.* 56, 512–519. <https://doi.org/10.1016/j.compositesb.2013.08.069>
- Kong, X., Fang, Q., Wu, H., Peng, Y., 2016a. Numerical predictions of cratering and scabbing in concrete slabs subjected to projectile impact using a modified version of HJC material model. *Int. J. Impact Eng.* 95, 61–71. <https://doi.org/10.1016/j.ijimpeng.2016.04.014>
- Kong, X., Fang, Q., Wu, H., Zhang, Y., 2016b. Finite spherical cavity expansion method for layering

- effect. *Acta Mech. Solida Sin.* 29, 642–654. [https://doi.org/10.1016/S0894-9166\(16\)30334-2](https://doi.org/10.1016/S0894-9166(16)30334-2)
- Kong, X., Wu, H., Fang, Q., Peng, Y., 2017. Rigid and eroding projectile penetration into concrete targets based on an extended dynamic cavity expansion model. *Int. J. Impact Eng.* 100, 1339–1351. <https://doi.org/10.1016/j.ijimpeng.2016.10.005>
- Kong, X., Wu, H., Fang, Q., Ren, G.M., 2016c. Analyses of rigid projectile penetration into UHPCC target based on an improved dynamic cavity expansion model. *Constr. Build. Mater.* 126, 759–767. <https://doi.org/10.1016/j.conbuildmat.2016.09.093>
- Lai, J., Guo, X., Zhu, Y., 2015. Repeated penetration and different depth explosion of ultra-high performance concrete. *Int. J. Impact Eng.* 84, 1–12. <https://doi.org/10.1016/j.ijimpeng.2015.05.006>
- Lai, J., Wang, H., Yang, H., Zheng, X., Wang, Q., 2017. Dynamic properties and SPH simulation of functionally graded cementitious composite subjected to repeated penetration. *Constr. Build. Mater.* 146, 54–65. <https://doi.org/10.1016/j.conbuildmat.2017.04.023>
- Laranjeira, F., Molins, C., Aguado, A., 2010. Predicting the pullout response of inclined hooked steel fibers. *Cem. Concr. Res.* 40, 1471–1487. <https://doi.org/10.1016/j.cemconres.2010.05.005>
- Le, H.T.N., 2017. High-Strength Concrete and Fiber-Reinforced Cement Composites for Protective Structures. National University of Singapore.
- Lee, Y., Kang, S.T., Kim, J.K., 2010. Pullout behavior of inclined steel fiber in an ultra-high strength cementitious matrix. *Constr. Build. Mater.* 24, 2030–2041. <https://doi.org/10.1016/j.conbuildmat.2010.03.009>
- Li, P.P., 2019. Impact resistant ultra-high performance fibre reinforced concrete. Eindhoven University of Technology.
- Li, P.P., Yu, Q.L., 2019. Responses and post-impact properties of ultra-high performance fibre reinforced concrete under pendulum impact. *Compos. Struct.* 208, 806–815. <https://doi.org/10.1016/j.compstruct.2018.10.071>
- Li, P.P., Yu, Q.L., Brouwers, H.J.H., 2018. Effect of coarse basalt aggregates on the properties of Ultra-high Performance Concrete (UHPC). *Constr. Build. Mater.* 170, 649–659. <https://doi.org/10.1016/j.conbuildmat.2018.03.109>
- Li, P.P., Yu, Q.L., Brouwers, H.J.H., 2017. Effect of PCE-type superplasticizer on early-age behaviour of ultra-high performance concrete (UHPC). *Constr. Build. Mater.* 153, 740–750. <https://doi.org/10.1016/j.conbuildmat.2017.07.145>
- Li, Q.M., Chen, X.W., 2003. Dimensionless formulae for penetration depth of concrete target impacted by a non-deformable projectile. *Int. J. Impact Eng.* 28, 93–116. [https://doi.org/10.1016/S0734-743X\(02\)00037-4](https://doi.org/10.1016/S0734-743X(02)00037-4)
- Li, Q.M., Meng, H., 2003. About the dynamic strength enhancement of concrete-like materials in a split Hopkinson pressure bar test. *Int. J. Solids Struct.* 40, 343–360. [https://doi.org/10.1016/S0020-7683\(02\)00526-7](https://doi.org/10.1016/S0020-7683(02)00526-7)
- Li, Q.M., Reid, S.R., Wen, H.M., Telford, A.R., 2006. Local impact effects of hard missiles on concrete targets. *Int. J. Impact Eng.* 32, 224–284. <https://doi.org/10.1016/j.ijimpeng.2005.04.005>
- Li, V.C., Wang, Y., Backer, S., 1991. A micromechanical model of tension-softening and bridging toughening of short random fiber reinforced brittle matrix composites. *J. Mech. Phys. Solids* 39, 607–625.
- Li, V.C., Wang, Y., Backer, S., 1990. Effect of inclining angle, bundling and surface treatment on

- synthetic fibre pull-out from a cement matrix. *Composites* 21, 132–140.
[https://doi.org/10.1016/0010-4361\(90\)90005-H](https://doi.org/10.1016/0010-4361(90)90005-H)
- Liu, J., Han, F., Cui, G., Zhang, Q., Lv, J., Zhang, L., Yang, Z., 2016. Combined effect of coarse aggregate and fiber on tensile behavior of ultra-high performance concrete. *Constr. Build. Mater.* 121, 310–318. <https://doi.org/10.1016/j.conbuildmat.2016.05.039>
- Liu, J., Wu, C., Chen, X., 2017. Numerical study of ultra-high performance concrete under non-deformable projectile penetration. *Constr. Build. Mater.* 135, 447–458.
<https://doi.org/10.1016/j.conbuildmat.2016.12.216>
- Liu, X., Yan, M., Galobardes, I., Sikora, K., 2018. Assessing the potential of functionally graded concrete using fibre reinforced and recycled aggregate concrete. *Constr. Build. Mater.* 171, 793–801. <https://doi.org/10.1016/j.conbuildmat.2018.03.202>
- Longcope, D.B., Tabbara, JR., M.R., Jung, J., 1999. Modeling of oblique penetration into geologic targets using cavity expansion penetrator loading with target free surface effects.
- LSTC, 2016. *ls-dyna Theory Manual*, 2016th ed. Livermore Software Technology Corporation 7374, California.
- LSTC, 2015a. *LS-DYNA® Keyword User ' S Manual Volume I*. Livermore Software Technology Corporation.
- LSTC, 2015b. *LS-DYNA® Keyword User ' S Manual Volume II*. Livermore Software Technology Corporation.
- Lu, Y.B., Li, Q.M., 2011. About the dynamic uniaxial tensile strength of concrete-like materials. *Int. J. Impact Eng.* 38, 171–180. <https://doi.org/10.1016/j.ijimpeng.2010.10.028>
- Luković, M., Dong, H., Šavija, B., Schlangen, E., Ye, G., Breugel, K. Van, 2014. Tailoring strain-hardening cementitious composite repair systems through numerical experimentation. *Cem. Concr. Compos.* 53, 200–213. <https://doi.org/10.1016/j.cemconcomp.2014.06.017>
- Ma, J., Orgass, M., Dehn, F., Schmidt, D., Tue, N. V., 2004. Comparative investigations on Ultra-High Performance Concrete with or without coarse aggregates. *Proc. Int. Symp. ultra high Perform. Concr.* 205–212.
- Máca, P., Sovják, R., Konvalinka, P., 2014. Mix design of UHPFRC and its response to projectile impact. *Int. J. Impact Eng.* 63, 158–163. <https://doi.org/10.1016/j.ijimpeng.2013.08.003>
- Macek, R.W., Duffey, T.A., 2000. Finite cavity expansion method for near-surface effects and layering during Earth penetration. *Int. J. Impact Eng.* 24, 239–258.
[https://doi.org/10.1016/S0734-743X\(99\)00156-6](https://doi.org/10.1016/S0734-743X(99)00156-6)
- Mao, L., Barnett, S., Begg, D., Schleyer, G., Wight, G., 2014. Numerical simulation of ultra high performance fibre reinforced concrete panel subjected to blast loading. *Int. J. Impact Eng.* 64, 91–100. <https://doi.org/10.1016/j.ijimpeng.2013.10.003>
- Mao, L., Barnett, S.J., 2017. Investigation of toughness of ultra high performance fibre reinforced concrete (UHPFRC) beam under impact loading. *Int. J. Impact Eng.* 99, 26–38.
<https://doi.org/10.1016/j.ijimpeng.2016.09.014>
- Markovic, I., 2006. *High-Performance Hybrid-Fibre Concrete*. de Technische Universiteit Delft.
- Mastali, M., Ghasemi Naghibdehi, M., Naghipour, M., Rabiee, S.M., 2015. Experimental assessment of functionally graded reinforced concrete (FGRC) slabs under drop weight and projectile impacts. *Constr. Build. Mater.* 95, 296–311. <https://doi.org/10.1016/j.conbuildmat.2015.07.153>
- Meng, C., Tan, Q., Jiang, Z., Song, D., Liu, F., 2018. Approximate solutions of finite dynamic spherical cavity-expansion models for penetration into elastically confined concrete targets. *Int.*

- J. Impact Eng. 114, 182–193. <https://doi.org/10.1016/j.ijimpeng.2018.01.001>
- Meng, W., Khayat, K.H., 2017. Improving flexural performance of ultra-high-performance concrete by rheology control of suspending mortar. *Compos. Part B Eng.* 117, 26–34. <https://doi.org/10.1016/j.compositesb.2017.02.019>
- Millard, S.G., Molyneaux, T.C.K., Barnett, S.J., Gao, X., 2010. Dynamic enhancement of blast-resistant ultra high performance fibre-reinforced concrete under flexural and shear loading. *Int. J. Impact Eng.* 37, 405–413. <https://doi.org/10.1016/j.ijimpeng.2009.09.004>
- Naghibdehi, M.G., Naghipour, M., Rabiee, M., 2015. Behaviour of functionally graded reinforced-concrete beams under cyclic loading. *Gradjevinar* 67, 427–439. <https://doi.org/10.14256/JCE.1124.2014>
- Ngo, T., Mendis, P., Krauthammer, T., 2007. Behavior of Ultrahigh-Strength Prestressed Concrete Panels Subjected to Blast Loading. *J. Struct. Eng.* 133, 1582–1590. [https://doi.org/10.1061/\(asce\)0733-9445\(2007\)133:11\(1582\)](https://doi.org/10.1061/(asce)0733-9445(2007)133:11(1582))
- Nikbin, I.M., Beygi, M.H.A., Kazemi, M.T., Vaseghi Amiri, J., Rahmani, E., Rabbanifar, S., Eslami, M., 2014. A comprehensive investigation into the effect of aging and coarse aggregate size and volume on mechanical properties of self-compacting concrete. *Mater. Des.* 59, 199–210. <https://doi.org/10.1016/j.matdes.2014.02.054>
- Noshiravani, T., Brühwiler, E., 2014. Analytical model for predicting response and flexure-shear resistance of composite beams combining reinforced Ultrahigh Performance Fiber-Reinforced Concrete and Reinforced Concrete. *J. Struct. Eng.* 140, 04014012. [https://doi.org/10.1061/\(ASCE\)ST.1943-541X.0000902](https://doi.org/10.1061/(ASCE)ST.1943-541X.0000902)
- Orange, G., Acker, P., Vernet, C., 1999. a new generation of UHP concrete: DUCTAL damage resistance and micromechanical analysis, in: Naaman, H.W.R. and A.E. (Ed.), *Third International RILEM Workshop on High Performance Fiber Reinforced Cement Composites*. RILEM Publications SARL, pp. 101–111. <https://doi.org/2351580222>
- Othman, H., Marzouk, H., 2018. Applicability of damage plasticity constitutive model for ultra-high performance fibre-reinforced concrete under impact loads. *Int. J. Impact Eng.* 114, 20–31. <https://doi.org/10.1016/j.ijimpeng.2017.12.013>
- Othman, H., Marzouk, H., 2017. Dynamic identification of damage control characteristics of ultra-high performance fiber reinforced concrete. *Constr. Build. Mater.* 157, 899–908. <https://doi.org/10.1016/j.conbuildmat.2017.09.169>
- Othman, H., Marzouk, H., 2016. An experimental investigation on the effect of steel reinforcement on impact response of reinforced concrete plates. *Int. J. Impact Eng.* 88, 12–21. <https://doi.org/10.1016/j.ijimpeng.2015.08.015>
- Othman, H.A.B., 2016. Performance of ultra-high performance fibre reinforced concrete plates under impact loads. Ryerson University.
- Ožbolt, J., Bošnjak, J., Sola, E., 2013. Dynamic fracture of concrete compact tension specimen: Experimental and numerical study. *Int. J. Solids Struct.* 50, 4270–4278. <https://doi.org/10.1016/j.ijsolstr.2013.08.030>
- Park, S.H., Kim, D.J., Ryu, G.S., Koh, K.T., 2012. Tensile behavior of ultra high performance hybrid fiber reinforced concrete. *Cem. Concr. Compos.* 34, 172–184. <https://doi.org/10.1016/j.cemconcomp.2011.09.009>
- Park, S.H., Ryu, G.S., Koh, K.T., Kim, D.J., 2014. Effect of shrinkage reducing agent on pullout resistance of high-strength steel fibers embedded in ultra-high-performance concrete. *Cem.*

- Concr. Compos. 49, 59–69. <https://doi.org/10.1016/j.cemconcomp.2013.12.012>
- Peng, Y., Wu, H., Fang, Q., Gong, Z.M., 2018. Geometrical scaling effect for penetration depth of hard projectiles into concrete targets. *Int. J. Impact Eng.* 120, 46–59. <https://doi.org/10.1016/j.ijimpeng.2018.05.010>
- Peng, Y., Wu, H., Fang, Q., Liu, J.Z., Gong, Z.M., 2016a. Impact resistance of basalt aggregated UHP-SFRC/fabric composite panel against small caliber arm. *Int. J. Impact Eng.* 88, 201–213. <https://doi.org/10.1016/j.ijimpeng.2015.10.011>
- Peng, Y., Wu, H., Fang, Q., Liu, J.Z., Gong, Z.M., 2016b. Flat nosed projectile penetrating into UHP-SFRC target: Experiment and analysis. *Int. J. Impact Eng.* 93, 88–98. <https://doi.org/10.1016/j.ijimpeng.2016.02.012>
- Pereira, L.F., Weerheijm, J., Sluys, L.J., 2018. Simulation of compaction and crushing of concrete in ballistic impact with a new damage model. *Int. J. Impact Eng.* 111, 208–221. <https://doi.org/10.1016/j.ijimpeng.2017.09.014>
- Pyo, S., Wille, K., El-Tawil, S., Naaman, A.E., 2015. Strain rate dependent properties of ultra high performance fiber reinforced concrete (UHP-FRC) under tension. *Cem. Concr. Compos.* 56, 15–24. <https://doi.org/10.1016/j.cemconcomp.2014.10.002>
- Qian, Y., Zhang, D., Ueda, T., 2014. Tensile bond between substrate concrete and normal repairing mortar under freeze – thaw cycles, in: 4th International Conference on the Durability of Concrete Structures. Purdue University, West Lafayette, IN, USA, pp. 385–392.
- Quek, S.T., Lin, V.W.J., Maalej, M., 2010. Development of functionally-graded cementitious panel against high-velocity small projectile impact. *Int. J. Impact Eng.* 37, 928–941. <https://doi.org/10.1016/j.ijimpeng.2010.02.002>
- Ranade, R., Li, V.C., Heard, W.F., 2015. Tensile rate effects in High Strength-High Ductility Concrete. *Cem. Concr. Res.* 68, 94–104. <https://doi.org/10.1016/j.cemconres.2014.11.005>
- Ranade, R., Li, V.C., Heard, W.F., Williams, B.A., 2017. Impact resistance of high strength-high ductility concrete. *Cem. Concr. Res.* 98, 24–35. <https://doi.org/10.1016/j.cemconres.2017.03.013>
- Reinhardt, H.W., Weerheijm, J., 1991. Tensile fracture of concrete at high loading rates taking account of inertia and crack velocity effects. *Int. J. Fract.* 51, 31–42. <https://doi.org/10.1007/BF00020851>
- Ren, G.M., Wu, H., Fang, Q., Kong, X.Z., 2017. Parameters of Holmquist–Johnson–Cook model for high-strength concrete-like materials under projectile impact. *Int. J. Prot. Struct.* 8, 352–367. <https://doi.org/10.1177/2041419617721552>
- Ren, G.M., Wu, H., Fang, Q., Liu, J.Z., Gong, Z.M., 2016. Triaxial compressive behavior of UHPCC and applications in the projectile impact analyses. *Constr. Build. Mater.* 113, 1–14. <https://doi.org/10.1016/j.conbuildmat.2016.02.227>
- RILEM TC 162-TDF, 2002. Recommendations of RILEM TC 162-TDF: Test and design methods for steel fibre reinforced concrete: bending test. *Mater. Struct.* 35, 579–582. <https://doi.org/10.1617/14007>
- Robins, P., Austin, S., Jones, P., 2002. Pull-out behaviour of hooked steel fibres. *Mater. Struct.* 35, 434–442. <https://doi.org/10.1007/BF02483148>
- Roesler, J., Bordelon, A., Gaedicke, C., Park, K., Paulino, G., 2008. Fracture behavior and properties of functionally graded fiber-reinforced concrete. *AIP Conf. Proc.* 973, 513–518. <https://doi.org/10.1063/1.2896831>

- Rosenberg, Z., Kositski, R., 2016. Modeling the penetration and perforation of concrete targets by rigid projectiles. *Int. J. Prot. Struct.* 7, 157–178. <https://doi.org/10.1177/2041419616632422>
- Rubin, M.B., Kositski, R., Rosenberg, Z., 2016. Essential physics of target inertia in penetration problems missed by cavity expansion models. *Int. J. Impact Eng.* 98, 97–104. <https://doi.org/10.1016/j.ijimpeng.2016.09.002>
- Salgado, R., Prezzi, M., 2007. Computation of cavity expansion pressure and penetration resistance in sands. *Int. J. Geomech.* 7, 251–265. [https://doi.org/10.1061/\(ASCE\)1532-3641\(2007\)7:4\(251\)](https://doi.org/10.1061/(ASCE)1532-3641(2007)7:4(251))
- Savino, V., Lanzoni, L., Tarantino, A.M., Viviani, M., 2018. Simple and effective models to predict the compressive and tensile strength of HPFRC as the steel fiber content and type changes. *Compos. Part B Eng.* 137, 153–162. <https://doi.org/10.1016/j.compositesb.2017.11.003>
- Shaharudin Shah Zaini, 2015. Impact resistance of pre-damaged ultra-high performance fibre reinforced concrete (UHPFRC) slabs 308.
- Shaikh, F.U.A., Nishiwaki, T., Kwon, S., 2018. Effect of fly ash on tensile properties of ultra-high performance fiber reinforced cementitious composites (UHP-FRCC). *J. Sustain. Cem. Mater.* 7, 357–371. <https://doi.org/10.1080/21650373.2018.1514672>
- Shen, B., Hubler, M., Paulino, G.H., Struble, L.J., 2008. Functionally-graded fiber-reinforced cement composite: Processing, microstructure, and properties. *Cem. Concr. Compos.* 30, 663–673. <https://doi.org/10.1016/j.cemconcomp.2008.02.002>
- Shi, C., Wu, Z., Xiao, J., Wang, D., Huang, Z., Fang, Z., 2015. A review on ultra high performance concrete: Part I. Raw materials and mixture design. *Constr. Build. Mater.* 101, 741–751. <https://doi.org/10.1016/j.conbuildmat.2015.10.088>
- Smarzewski, P., 2018. Hybrid fibres as shear reinforcement in high-performance concrete beams with and without openings. *Appl. Sci.* 8. <https://doi.org/10.3390/app8112070>
- Soleimani, S.M., Banthia, N., 2014. A novel drop weight impact setup for testing reinforced concrete beams. *Exp. Tech.* 38, 72–79. <https://doi.org/10.1111/j.1747-1567.2012.00810.x>
- Soltani, A., Harries, K.A., Shahrooz, B.M., 2013. Crack opening behavior of concrete reinforced with high strength reinforcing steel. *Int. J. Concr. Struct. Mater.* 7, 253–264. <https://doi.org/10.1007/s40069-013-0054-z>
- Sovják, R., Vavříník, T., Máca, P., Zatloukal, J., Konvalinka, P., Song, Y., 2013a. Experimental investigation of ultra-high performance fiber reinforced concrete slabs subjected to deformable projectile impact. *Procedia Eng.* 65, 120–125. <https://doi.org/10.1016/j.proeng.2013.09.021>
- Sovják, R., Vavříník, T., Zatloukal, J., Máca, P., Mičunek, T., Frydrýn, M., 2015. Resistance of slim UHPFRC targets to projectile impact using in-service bullets. *Int. J. Impact Eng.* 76, 166–177. <https://doi.org/10.1016/j.ijimpeng.2014.10.002>
- Sovják, R., Vogel, F., Beckmann, B., 2013b. Triaxial compressive strength of ultra high performance concrete. *Acta Polytech.* 53, 901–905. <https://doi.org/10.14311/AP.2013.53.0901>
- Spasojević, A., 2008. Structural implications of Ultra-High Performance Fibre-Reinforced Concrete in bridge design. *ingénieur civil diplômée de l'Université de Niš, Serbie et.*
- Spiesz, P., Hunger, M., 2017a. Towards a more common use of Ultra-High Performance Concrete (UHPC) – development of UHPC for ready-mix and prefabrication concrete plants, in: *Proceedings of the 11th High Performance Concrete Conference, HPC Tromsø 2017.* pp. 1–10.
- Spiesz, P., Hunger, M., 2017b. Durability of ultra-high performance concrete – Experiences from a real-scale application, in: *Proceedings of the 14th International Conference on Durability of*

- Building Materials and Components. pp. 1–12.
- Sujivorakul, C., Waas, A.M., Naaman, A.E., 2000. Pullout response of a smooth fiber with an end anchorage. *J. Eng. Mech.* 126, 986–993. [https://doi.org/10.1061/\(ASCE\)0733-9399\(2000\)126](https://doi.org/10.1061/(ASCE)0733-9399(2000)126)
- Tai, Y.S., 2009a. Uniaxial compression tests at various loading rates for reactive powder concrete. *Theor. Appl. Fract. Mech.* 52, 14–21. <https://doi.org/10.1016/j.tafmec.2009.06.001>
- Tai, Y.S., 2009b. Flat ended projectile penetrating ultra-high strength concrete plate target. *Theor. Appl. Fract. Mech.* 51, 117–128. <https://doi.org/10.1016/j.tafmec.2009.04.005>
- Tai, Y.S., El-Tawil, S., 2017. High loading-rate pullout behavior of inclined deformed steel fibers embedded in ultra-high performance concrete. *Constr. Build. Mater.* 148, 204–218. <https://doi.org/10.1016/j.conbuildmat.2017.05.018>
- Tai, Y.S., El-Tawil, S., Chung, T.H., 2016. Performance of deformed steel fibers embedded in ultra-high performance concrete subjected to various pullout rates. *Cem. Concr. Res.* 89, 1–13. <https://doi.org/10.1016/j.cemconres.2016.07.013>
- Teng, T.L., Chu, Y.A., Chang, F.A., Shen, B.C., Cheng, D.S., 2008. Development and validation of numerical model of steel fiber reinforced concrete for high-velocity impact. *Comput. Mater. Sci.* 42, 90–99. <https://doi.org/10.1016/j.commatsci.2007.06.013>
- Thai, H.T., Nguyen, T.K., Vo, T.P., Lee, J., 2014. Analysis of functionally graded sandwich plates using a new first-order shear deformation theory. *Eur. J. Mech. A/Solids* 45, 211–225. <https://doi.org/10.1016/j.euromechsol.2013.12.008>
- Thomas, R.J., Sorensen, A.D., 2017. Review of strain rate effects for UHPC in tension. *Constr. Build. Mater.* 153, 846–856. <https://doi.org/10.1016/j.conbuildmat.2017.07.168>
- Tran, N.T., Tran, T.K., Kim, D.J., 2015. High rate response of ultra-high-performance fiber-reinforced concretes under direct tension. *Cem. Concr. Res.* 69, 72–87. <https://doi.org/10.1016/j.cemconres.2014.12.008>
- Tran, T.K., Kim, D.J., 2014. High strain rate effects on direct tensile behavior of high performance fiber reinforced cementitious composites. *Cem. Concr. Compos.* 45, 186–200. <https://doi.org/10.1016/j.cemconcomp.2013.10.005>
- Ueno, H., Beppu, M., Ichino, H., Musha, H., Okamoto, S., 2018. A method for evaluating the local failure of ultra-high-performance short polyvinyl alcohol fiber-reinforced concrete panels subjected to a projectile impact. *Int. J. Prot. Struct.* 9, 289–312. <https://doi.org/10.1177/2041419618755158>
- Vegt, I., 2016. Concrete in dynamic tension: The fracture process. TU Delft Univ. Technische Universiteit Delft. <https://doi.org/10.4233/uuid>
- Wang, S., Le, H.T.N., Poh, L.H., Feng, H., Zhang, M.H., 2016. Resistance of high-performance fiber-reinforced cement composites against high-velocity projectile impact. *Int. J. Impact Eng.* 95, 89–104. <https://doi.org/10.1016/j.ijimpeng.2016.04.013>
- Wang, X., Wang, K., Taylor, P., Morcou, G., 2014. Assessing particle packing based self-consolidating concrete mix design method. *Constr. Build. Mater.* 70, 439–452. <https://doi.org/10.1016/j.conbuildmat.2014.08.002>
- Warren, T.L., Forrestal, M.J., 1998. Effects of strain hardening and strain-rate sensitivity on the penetration of aluminum targets with spherical-nosed rods. *Int. J. Solids Struct.* 35, 3737–3753. [https://doi.org/10.1016/S0020-7683\(97\)00211-4](https://doi.org/10.1016/S0020-7683(97)00211-4)
- Weerheijm, J., 2013. Understanding the tensile properties of concrete. Woodhead Publishing Limited. <https://doi.org/10.1533/9780857097538.1>

- Wille, K., 2012. Concrete strength dependent pull-out behavior of deformed steel fibers. 8th RILEM Int. Symp. Fiber Reinf. Concr. challenges Oppor. 123–135.
- Wille, K., El-Tawil, S., Naaman, A.E., 2014. Properties of strain hardening ultra high performance fiber reinforced concrete (UHP-FRC) under direct tensile loading. *Cem. Concr. Compos.* 48, 53–66. <https://doi.org/10.1016/j.cemconcomp.2013.12.015>
- Wille, K., Naaman, A.E., 2012. Pullout behavior of high-strength steel fibers embedded in ultra-high-performance concrete. *ACI Mater. J.* 109, 479–488. <https://doi.org/10.14359/51683923>
- Wille, K., Naaman, A.E., 2010. Bond stress-slip behavior of steel fibers embedded in ultra high performance concrete 99–111.
- Wille, K., Naman, A.E., Parra-Montesinos, G.J., 2011. Ultra-High Performance Concrete with compressive strength exceeding 150 MPa (22ksi) : a simpler way. *ACI Mater. J.* 108, 46–53. <https://doi.org/10.14359/51664215>
- Willey, J.A., 2013. Use of Ultra-High Performance Concrete to mitigate impact and explosive threats. Missouri University Of Science And Technology.
- Wu, H., Fang, Q., Chen, X.W., Gong, Z.M., Liu, J.Z., 2015a. Projectile penetration of ultra-high performance cement based composites at 510-1320 m/s. *Constr. Build. Mater.* 74, 188–200. <https://doi.org/10.1016/j.conbuildmat.2014.10.041>
- Wu, H., Fang, Q., Gong, J., Liu, J.Z., Zhang, J.H., Gong, Z.M., 2015b. Projectile impact resistance of corundum aggregated UHP-SFRC. *Int. J. Impact Eng.* 84, 38–53. <https://doi.org/10.1016/j.ijimpeng.2015.05.007>
- Wu, H., Li, Y.C., Fang, Q., Peng, Y., 2019. Scaling effect of rigid projectile penetration into concrete target: 3D mesoscopic analyses. *Constr. Build. Mater.* 208, 506–524. <https://doi.org/10.1016/j.conbuildmat.2019.03.040>
- Wu, M., Zhang, C., Chen, Z., 2015. Determining the impact behavior of concrete beams through experimental testing and meso-scale simulation: II. Particle element simulation and comparison. *Eng. Fract. Mech.* 135, 113–125. <https://doi.org/10.1016/j.engfracmech.2014.12.020>
- Wu, Z., Khayat, K.H., Shi, C., 2018. How do fiber shape and matrix composition affect fiber pullout behavior and flexural properties of UHPC? *Cem. Concr. Compos.* 90, 193–201. <https://doi.org/10.1016/j.cemconcomp.2018.03.021>
- Wu, Z., Shi, C., He, W., 2017a. Comparative study on flexural properties of ultra-high performance concrete with supplementary cementitious materials under different curing regimes. *Constr. Build. Mater.* 136, 307–313. <https://doi.org/10.1016/j.conbuildmat.2017.01.052>
- Wu, Z., Shi, C., He, W., Wang, D., 2017b. Static and dynamic compressive properties of ultra-high performance concrete (UHPC) with hybrid steel fiber reinforcements. *Cem. Concr. Compos.* 79, 148–157. <https://doi.org/10.1016/j.cemconcomp.2017.02.010>
- Wu, Z., Shi, C., He, W., Wu, L., 2016. Effects of steel fiber content and shape on mechanical properties of ultra high performance concrete. *Constr. Build. Mater.* 103, 8–14. <https://doi.org/10.1016/j.conbuildmat.2015.11.028>
- Xie, J., Elwi, A.E., MacGregor, J.G., 1995. Mechanical properties of three high-strength concretes containing silica fume. *ACI Mater. J.* 92, 135–145.
- Xu, B., Toutanji, H.A., Gilbert, J., 2010. Impact resistance of poly(vinyl alcohol) fiber reinforced high-performance organic aggregate cementitious material. *Cem. Concr. Res.* 40, 347–351. <https://doi.org/10.1016/j.cemconres.2009.09.006>
- Xu, H., Wen, H.M., 2016. A computational constitutive model for concrete subjected to dynamic

- loadings. *Int. J. Impact Eng.* 91, 116–125. <https://doi.org/10.1016/j.ijimpeng.2016.01.003>
- Xu, M., Hallinan, B., Wille, K., 2016. Effect of loading rates on pullout behavior of high strength steel fibers embedded in ultra-high performance concrete. *Cem. Concr. Compos.* 70, 98–109. <https://doi.org/10.1016/j.cemconcomp.2016.03.014>
- Xu, S.L., Wang, N., Zhang, X.F., 2012. Flexural behavior of plain concrete beams strengthened with ultra high toughness cementitious composites layer. *Mater. Struct.* 45, 851–859. <https://doi.org/10.1617/s11527-011-9803-0>
- Yang, E.-H., Wang, S., Yang, Y., Li, V.C., 2008. Fiber-bridging constitutive law of Engineered Cementitious Composites. *J. Adv. Concr. Technol.* 6, 181–193. <https://doi.org/10.3151/jact.6.181>
- Yang, J., Dong, Y., 2003. Effects of the component and fiber gradient distributions on the strength of cement-based composite materials. *J. Wuhan Univ. Technol. Sci. Ed.* 18, 61–64.
- Yang, J., Hai, R., Dong, yan ling, Wu, ke ru, 2003. Effects of the component and fiber gradient distributions on the strength of cement-based composite materials. *J. Wuhan Univ. Technol. Mater. Sci. Ed.* 18, 61–64.
- Yankelevsky, D.Z., 2017. Resistance of a concrete target to penetration of a rigid projectile - revisited. *Int. J. Impact Eng.* 106, 30–43. <https://doi.org/10.1016/j.ijimpeng.2017.02.021>
- Yoo, D.Y., Banthia, N., 2017a. Size-dependent impact resistance of ultra-high-performance fiber-reinforced concrete beams. *Constr. Build. Mater.* 142, 363–375. <https://doi.org/10.1016/j.conbuildmat.2017.03.080>
- Yoo, D.Y., Banthia, N., 2017b. Mechanical and structural behaviors of ultra-high-performance fiber-reinforced concrete subjected to impact and blast. *Constr. Build. Mater.* 149, 416–431. <https://doi.org/10.1016/j.conbuildmat.2017.05.136>
- Yoo, D.Y., Banthia, N., 2016. Mechanical properties of ultra-high-performance fiber-reinforced concrete: A review. *Cem. Concr. Compos.* 73, 267–280. <https://doi.org/10.1016/j.cemconcomp.2016.08.001>
- Yoo, D.Y., Banthia, N., Kim, S.W., Yoon, Y.S., 2015a. Response of ultra-high-performance fiber-reinforced concrete beams with continuous steel reinforcement subjected to low-velocity impact loading. *Compos. Struct.* 126, 233–245. <https://doi.org/10.1016/j.compstruct.2015.02.058>
- Yoo, D.Y., Banthia, N., Lee, J.Y., Yoon, Y.S., 2018. Effect of fiber geometric property on rate dependent flexural behavior of ultra-high-performance cementitious composite. *Cem. Concr. Compos.* 86, 57–71. <https://doi.org/10.1016/j.cemconcomp.2017.11.002>
- Yoo, D.Y., Banthia, N., Yoon, Y.-S., 2016. Impact resistance of Ultra-High Performance Fiber-Reinforced Concrete with different steel fibers. 9th RILEM Int. Symp. Fiber Reinf. Concr. 398–405.
- Yoo, D.Y., Kim, M.J., Kim, S.W., Park, J.J., 2017a. Development of cost effective ultra-high-performance fiber-reinforced concrete using single and hybrid steel fibers. *Constr. Build. Mater.* 150, 383–394. <https://doi.org/10.1016/j.conbuildmat.2017.06.018>
- Yoo, D.Y., Park, J.J., Kim, S.W., 2017b. Fiber pullout behavior of HPFRCC: Effects of matrix strength and fiber type. *Compos. Struct.* 174, 263–276. <https://doi.org/10.1016/j.compstruct.2017.04.064>
- Yoo, D.Y., Yoon, Y.S., Banthia, N., 2015b. Flexural response of steel-fiber-reinforced concrete beams: Effects of strength, fiber content, and strain-rate. *Cem. Concr. Compos.* 64, 84–92. <https://doi.org/10.1016/j.cemconcomp.2015.10.001>

- Yu, R., 2015. Development of sustainable protective Ultra-High Performance Fibre Reinforced Concrete (UHPFRC). Eindhoven University of Technology.
- Yu, R., Spiesz, P., Brouwers, H.J.H., 2016. Energy absorption capacity of a sustainable Ultra-High Performance Fibre Reinforced Concrete (UHPFRC) in quasi-static mode and under high velocity projectile impact. *Cem. Concr. Compos.* 68, 109–122. <https://doi.org/10.1016/j.cemconcomp.2016.02.012>
- Yu, R., Spiesz, P., Brouwers, H.J.H., 2014. Static properties and impact resistance of a green Ultra-High Performance Hybrid Fibre Reinforced Concrete (UHPHFRC): Experiments and modeling. *Constr. Build. Mater.* 68, 158–171. <https://doi.org/10.1016/j.conbuildmat.2014.06.033>
- Zanotti, C., Banthia, N., Plizzari, G., 2014. A study of some factors affecting bond in cementitious fiber reinforced repairs. *Cem. Concr. Res.* 63, 117–126. <https://doi.org/10.1016/j.cemconres.2014.05.008>
- Zhang, J., Leung, C.K.Y., Cheung, Y.N., 2006. Flexural performance of layered ECC-concrete composite beam. *Compos. Sci. Technol.* 66, 1501–1512. <https://doi.org/10.1016/j.compscitech.2005.11.024>
- Zhang, J., Li, V.C., 2002. Effect of inclination angle on fiber rupture load in fiber reinforced cementitious composites. *Compos. Sci. Technol.* 62, 775–781. [https://doi.org/10.1016/S0266-3538\(02\)00045-3](https://doi.org/10.1016/S0266-3538(02)00045-3)
- Zhang, J., Wang, Z., Ju, X., Shi, Z., 2014. Simulation of flexural performance of layered ECC-concrete composite beam with fracture mechanics model. *Eng. Fract. Mech.* 131, 419–438. <https://doi.org/10.1016/j.engfracmech.2014.08.016>
- Zhang, M.H., Sharif, M.S.H., Lu, G., 2007. Impact resistance of high-strength fibre-reinforced concrete. *Mag. Concr. Res.* 59, 199–210. <https://doi.org/10.1680/macr.2007.59.3.199>
- Zhang, M.H., Shim, V.P.W., Lu, G., Chew, C.W., 2005. Resistance of high-strength concrete to projectile impact. *Int. J. Impact Eng.* 31, 825–841. <https://doi.org/10.1016/j.ijimpeng.2004.04.009>
- Zhen, M., Jiang, Z.G., Song, D.Y., Liu, F., 2014. Analytical solutions for finite cylindrical dynamic cavity expansion in compressible elastic-plastic materials. *Appl. Math. Mech. (English Ed.)* 35, 1039–1050. <https://doi.org/10.1007/s10483-014-1842-7>
- Zile, E., Zile, O., 2013. Effect of the fiber geometry on the pullout response of mechanically deformed steel fibers. *Cem. Concr. Res.* 44, 18–24. <https://doi.org/10.1016/j.cemconres.2012.10.014>

List of notations

Abbreviations

AP	Armor-piercing
BA 1-3	Basalt aggregate with sizes of 1-3 mm
BA 2-5	Basalt aggregate with sizes of 2-5 mm
BA 5-8	Basalt aggregate with sizes of 5-8 mm
BA 8-11	Basalt aggregate with sizes of 8-11 mm
BA 8-16	Basalt aggregate with sizes of 8-16 mm
CEM	Portland cement
DIF	Dynamic increase factor
$DIF_{f,i}$	Dynamic increase factor of a single steel fiber in the i^{th} layer
DIF_m	Dynamic increase factor of UHPC
DOP	Depth of penetration
ECC	Engineered cementitious composite
EOS	Equation of state
HF	Hooked-end steel fiber
HJC	Holmquist Johnson Concrete
ITZ	Interfacial transition zones
LP	Limestone powder
mS	Micro-silica
NC	Normal strength concrete
S	Sand
SEM	Scanning electron microscopy
SF	Straight steel fiber
SP	Superplasticizer
UHPC	Ultra-High Performance Concrete
UHPFRC	Ultra-High Performance Fiber Reinforced Concrete
W	Water

Nomenclature		SI unit
A, B, C	Cavity expansion model parameters in Chapter 7 Eq. 7-42	-
A_c	Normalized cohesive strength parameter in HJC model	-
A_1	Cross-sectional area of beam top layer	[m ²]
A_2	Cross-sectional area of beam bottom layer	[m ²]
B_c	Normalized pressure hardening parameter in HJC model	-
b	Beam width	[m]
C_c	Strain rate parameter in HJC model	-
C_0	Parameter in Chapter 7 Eq. 7-25	[N]
C_1	Parameter in Chapter 7 Eq. 7-38	[N/m]
D	Damage	-
D_{eq}	Equivalent crater diameter	[m]
D_I	Parameters in Chapter 7 Eq. 7-50	[m]
D_{II}	Parameters in Chapter 7 Eq. 7-50	-
D_1, D_2	Damage parameters in HJC model	-
d	Projectile diameter	[m]
d_f	Fiber diameter	[m]
E	Elastic modulus	[Pa]
E_a	Total absorbed impact energy at multiple impacts	[N·m]
E_{a0}	Absorbed impact energy at a single impact	[N·m]
$E_{f,d,i}$	Impact energy consumed by fiber pullout in the i^{th} layer	[N·m]
E_i	Impact energy	[N·m]
$E_{m,d,i}$	Impact energy absorbed by UHPC matrix in the i^{th} layer	[N·m]
$E_{m,s,i}$	Flexural energy absorbed by UHPC matrix in the i^{th} layer	[N·m]
E_p	Pullout energy dissipation	[N·m]
E_s	Beam flexural energy	[N·m]
E_1	Elastic modulus of beam top layer	[Pa]
E_2	Elastic modulus of beam bottom layer	[Pa]
$eff_{f,s}$	Fiber efficiency under static flexural	[N·m/kg]
$eff_{f,d}$	Fiber efficiency under dynamic impact	[N·m/kg]
F	Axial force on the projectile head	[N]
$F_{critical}$	Critical load at the first stage of beam failure	[N]
$F_{c,bottom}$	Critical cracking load of beam bottom layer	[N]
$F_{c,top}$	Critical cracking load of beam top layer	[N]
$F_{d,shear}$	Critical debonding load by shear	[N]
$F_{d,tension}$	Critical debonding load by tension	[N]
F_{i+1}	Axial force at the i^{th} tunneling stage	[N]
$F_{s,max}$	Beam peak flexural load	[N]
F_1	Axial force at the cratering stage	[N]
f_p	Snubbing friction coefficient	-
$f_{ct,d}$	Dynamic tensile strength	[Pa]

f_{ctm}	Mean value of tensile strength	[Pa]
G	Shear modulus	[Pa]
G_n	Parameter in modified NDRC and UKAEA formula	-
g	Gravitational acceleration	[m/s ²]
H	Beam height	[m]
h	Length of the projectile nose	[m]
h_i	Thickness of the i^{th} layer	[m]
h_0	Height of beam neutral axis	[m]
I	Parameter in Li-Chen formula	-
I_0	Inertia moment	[m ⁴]
K	Bulk modulus	[Pa]
K_1, K_2, K_3	Pressure parameters in HJC model	[Pa]
k	Parameter associated with projectile shape	-
k_p	Spalling coefficient	-
L	Beam length	[m]
L_s	Beam span length	[m]
l	Actual fiber embedded length obtained from pullout load-slip curves	[m]
l_e	Fiber embedded length	[m]
l_f	Fiber length	[m]
M	Projectile mass	[kg]
m	Hoek-Brown parameter	-
N	Impact number	-
N_c	Pressure hardening exponent	-
N_I, N_{II}	Projectile nose shape coefficients	-
N_{l-c}	Projectile nose shape coefficient in Li-Chen formulae	-
$N_{(z),i}$	Fibers number in an unit area on the crack plane at the depth of z	-
N^*	Projectile nose shape coefficient in NDRC and UKAEA formulae	-
P_{crush}	Crushing pressure	[Pa]
P_f	Pullout load due to frictional bond	[N]
P_h	Pullout load due to anchorage part	[N]
P_{lock}	Locking pressure	[Pa]
P_{max}	Peak pullout load	[N]
P_n	Normalized pullout load	-
P^*	Normalized pressure	-
R	Reaction load under drop-weight impact	[N]
R_{peak}	Peak reaction force	[N]
$R_{\text{peak},1}$	Peak reaction force at the first impact	[N]
$R_{\text{peak},n}$	Peak reaction force at the last impact	[N]
r	Radius in spherical coordinate	[m]
r_c	Radius of cavity	[m]
r_p	Radius of the comminuted region	[m]
r_{cr}	Radius of the cracked region	[m]
r_e	Radius of the elastic region	[m]

r_t	Critical radius for response mode transfer	[m]
\dot{r}_c	Cavity expansion velocity	[m/s]
\dot{r}_i	Critical expansion velocity for response mode transfer	[m/s]
S_f	Parameter in Forrestal semi-empirical formula	-
S_{l-c}	Parameter in Li-Chen formula	-
s	Projectile head surface	[m ²]
T	Maximum tensile pressure	[Pa]
T^*	Normalized maximum tensile hydrostatic pressure	-
t_i	Time at the end of the $i-1^{\text{th}}$ tunneling stage	[s]
u	Particle displacement at time t	[m]
V	Penetration velocity at time t	[m/s]
V_b	Beam velocity under impact	[m/s]
V_f	Fiber volume fraction	[%]
$V_{f,i}$	Fiber volume fraction in the i^{th} layer	[%]
$V_{m,i}$	Matrix volume fraction in the i^{th} layer	[%]
V_i	Initial penetration velocity at the i^{th} tunneling stage	[m/s]
V_0	Initial penetration velocity at the cratering stage	[m/s]
v	Particle velocity in the radial direction	[m/s]
w_h	Crack width at beam bottom	[m]
x	Penetration depth at time t	[m]

<i>Greek letters</i>		SI unit
σ_b	Layer bond strength	[Pa]
$\sigma_{c,s}$	Static compressive strength	[Pa]
$\sigma_{c,s,i}$	Static compressive strength of UHPFRC in the i^{th} layer	[Pa]
$\sigma_{c,d}$	Dynamic compressive strength	[Pa]
$\sigma_{c,eq}$	Equivalent compressive strength of layered target	[Pa]
σ_{max}	Maximum fiber stress	[Pa]
σ_n	Normal stress on projectile head	[Pa]
σ_r	Radial Cauchy stress component	[Pa]
$\sigma_{t,s}$	Static tensile strength	[Pa]
$\sigma_{t,d}$	Dynamic tensile strength	[Pa]
$\sigma_{t,1}$	Tensile strength of beam top layer	[Pa]
$\sigma_{t,2}$	Tensile strength of beam bottom layer	[Pa]
σ_y	Fiber strength	[Pa]
σ_θ	Circumferential Cauchy stress component	[Pa]
σ_1	Major principal stress	[Pa]
σ_3	Minor principal stress	[Pa]
σ^*	Normalized equivalent stress	-
τ	Interfacial shear strength	[Pa]
τ_{eq}	Equivalent bond strength	[Pa]
$\tau_{eq,d}$	Equivalent bond strength under dynamic pullout	[Pa]
$\tau_{eq,s}$	Equivalent bond strength under static pullout	[Pa]
$\tau_{f,d}$	Dynamic frictional shear stress	[Pa]
$\tau_{f,s}$	Quasi-static frictional shear stress	[Pa]
τ_{max}	Maximum bond strength	[Pa]
τ_1	Shear stress in beam top layer	[Pa]
τ_2	Shear stress in beam bottom layer	[Pa]
ε_p	Equivalent plastic strain	-
ε_r	Radial strain	-
ε_θ	Circumferential strain	-
$\dot{\varepsilon}_c$	Compressive strain rate	[s ⁻¹]
$\dot{\varepsilon}_{c,0}$	Static reference rate	[s ⁻¹]
$\dot{\varepsilon}_d$	Beam strain rate	[s ⁻¹]
$\dot{\varepsilon}_t$	Tensile strain rate	[s ⁻¹]
$\dot{\varepsilon}_{t,0}$	Static reference rate	[s ⁻¹]
$\dot{\varepsilon}_r$	Radial strain rate	[s ⁻¹]
$\dot{\varepsilon}_\theta$	Circumferential strain rate	[s ⁻¹]
$\dot{\varepsilon}^*$	Dimensionless strain rate	-
ρ	Density	[kg/m ³]
ρ_f	Fiber density	[kg/m ³]

ρ_i	Density of the i^{th} layer	[kg/m ³]
ρ_0	Material density in the un-deformed state	[kg/m ³]
μ	Poisson's ratio	-
μ_{crush}	Crushing volumetric strain	-
μ_f	Friction coefficient	-
μ_{lock}	Locking volumetric strain	-
μ_p	Plastic volumetric strain	-
α	Angle of fiber hook	[°]
β	Angle between pullout force and reaction force	[°]
β_E	Layer elastic modulus ratio	-
β_h	Layer thickness ratio	-
β_t	Rate effect relevant parameter	-
γ_t	Rate effect relevant parameter	-
γ_c	Critical layer tensile strength ratio	-
δ	Beam deflection	[m]
δ_t	Rate effect relevant parameter	-
ζ	Rate effect reduction factor	-
η_g	Fiber group effect coefficient	-
η_θ	Fiber orientation coefficient	-
θ	Fiber inclination angle	[°]
ψ	Projectile head geometry factor, CRH for an ogive head	-
φ	Projectile angle	[°]

List of publications

Peer-reviewed journals

- [1] Y.Y.Y. Cao, Q.L. Yu, Effect of inclination angle on hooked-end steel fiber pullout behavior in ultra-high performance concrete, *Composite Structures* 201 (2018) 151–160.
- [2] Y.Y.Y. Cao, Q.L. Yu, H.J.H. Brouwers, W. Chen, Predicting the rate effects on hooked-end fiber pullout performance from UHPC, *Cement and Concrete Research* 120 (2019) 164–175.
- [3] Y.Y.Y. Cao¹, P.P. Li¹, H.J.H. Brouwers, M. Sluijsmans, Q.L. Yu, Enhancing flexural performance of ultra-high performance concrete by an optimized layered-structure concept, *Composites Part B* 171 (2019) 154–165 (¹ Equivalent first authors).
- [4] P.P. Li¹, Y.Y.Y. Cao¹, H.J.H. Brouwers, W. Chen, Q.L. Yu, Development and properties evaluation of sustainable ultra-high performance pastes with quaternary blends, *Journal of Cleaner Production* 240 (2019) 118124 (¹ Equivalent first authors).
- [5] Y.Y.Y. Cao, Q.H. Tan, Z.G. Jiang, H.J.H. Brouwers, Q.L. Yu, A nonlinear rate-dependent model for predicting the penetration depth in UHPFRC, *Cement and Concrete Composites* 106 (2020) 103451.
- [6] Y.Y.Y. Cao, G. Liu, P.P. Li, H.J.H. Brouwers, Q.L. Yu, Enhancing the low-velocity impact resistance of Ultra-High Performance Concrete by an optimized layered-structure concept (Submitted).
- [7] Y.Y.Y. Cao, P.P. Li, H.J.H. Brouwers, Q.L. Yu, Resistance of Multi-Layered UHPFRC against in-service projectile: Experimental Investigation and Modelling Prediction (Submitted).
- [8] Y.Y.Y. Cao, Q.L. Yu, H.J.H. Brouwers, Numerical investigation on ballistic performance of coarse-aggregated layered UHPFRC (Submitted).
- [9] P.P. Li, Y.Y.Y. Cao, M. Sluijsmans, H.J.H. Brouwers, Q.L. Yu, Synergistic effect of steel fibers and coarse aggregates on impact properties of ultra-high performance fiber reinforced concrete (Submitted).
- [10] Y.Y.Y. Cao, Q.L. Yu, H.J.H. Brouwers, Fibers effects on the rate dependent flexural performance of ultra-high performance concrete (In preparation).

Conference proceedings

- [1] Y.Y.Y. Cao, Q.L. Yu, H.J.H. Brouwers, 2017. Mesoscale modelling of concrete damage under dynamic loading, in *Non-Traditional Cement and Concrete VI*. Bílek, V., Keršner, Z. & Šimonová, H. (eds.). Brno University of Technology, p. 80-88
- [2] Y.Y.Y. Cao, Q.L. Yu, 2017. Numerical Investigation of Fibers Effects in SFRC under Dynamic Tension, in: *The 9th International Symposium on Cement and Concrete (ISCC 2017)*. Wuhan, China, pp. 1–7.
- [3] Y.Y.Y. Cao, Q.L. Yu, H.J.H. Brouwers, 2018. Effects of inclination angle on pullout performance of hooked end fiber embedded in UHPC, in: *AuxDefense 2018*. Zurich: Trans Tech Publications, p. 60-65 6 p. (Key Engineering Materials; vol. 812)
- [4] Y.Y.Y. Cao, Q.L. Yu, H.J.H. Brouwers, 2019. Experimental and modeling study of double-

- layered UHPFRC under bending, in: 2nd International Interactive Symposium on UHPC. 8 p. 38
- [5] Y.Y.Y. Cao, Q.L. Yu, P.P. Li, H.J.H. Brouwers, 2019. Effects of fiber content on mechanical properties of UHPFRC with coarse aggregates, in: 2nd International Interactive Symposium on UHPC. 8 p.
- [6] Y.Y.Y. Cao, M. Sluijsmans, H.J.H. Brouwers, Q.L. Yu, 2019. Ballistic performances of multi-layered Ultra-high Performance Fiber Reinforced Concrete, in: 2nd International Conference of Sustainable Building Materials (ICSBM 2019), Eindhoven, the Netherlands. 9 p.

Curriculum Vitae

Yangyueye Cao was born on 31 March 1991 in Hunan, China. She studied at Tianjin University, China, from September 2009 to July 2013, and received her Bachelor's degree in Civil Engineering. She continued her graduate study at National University of Defense Technology, China, during September 2013 to September 2015. The research topic of her master study was *Investigation on the Mechanisms and Engineering Modeling of Confined Concrete against Penetration*. In March 2017, she began her PhD study under the supervision of prof.dr.ir. H.J.H. Brouwers and prof.dr. Qingliang Yu at Eindhoven University of Technology, the Netherlands. Her PhD research involved the static and dynamic properties of Ultra-High Performance Concrete, of which the results are presented in this dissertation.

Bouwstenen is een publicatiereeks van de Faculteit Bouwkunde, Technische Universiteit Eindhoven. Zij presenteert resultaten van onderzoek en andere activiteiten op het vakgebied der Bouwkunde, uitgevoerd in het kader van deze Faculteit.

Bouwstenen en andere proefschriften van de TU/e zijn online beschikbaar via:
<https://research.tue.nl/>

Reeds verschenen in de serie

Bouwstenen

nr 1

Elan: A Computer Model for Building Energy Design: Theory and Validation

Martin H. de Wit

H.H. Driessen

R.M.M. van der Velden

nr 2

Kwaliteit, Keuzevrijheid en Kosten: Evaluatie van Experiment Klarendal, Arnhem

J. Smeets

C. le Nobel

M. Broos

J. Frenken

A. v.d. Sanden

nr 3

Crooswijk: Van 'Bijzonder' naar 'Gewoon'

Vincent Smit

Kees Noort

nr 4

Staal in de Woningbouw

Edwin J.F. Delsing

nr 5

Mathematical Theory of Stressed Skin Action in Profiled Sheeting with Various Edge Conditions

Andre W.A.M.J. van den Bogaard

nr 6

Hoe Berekenbaar en Betrouwbaar is de Coëfficiënt k in x -ksigma en x -ks?

K.B. Lub

A.J. Bosch

nr 7

Het Typologisch Gereedschap: Een Verkennende Studie Omtrent Typologie en Omtrent de Aanpak van Typologisch Onderzoek

J.H. Luiten

nr 8

Informatievoorziening en Beheerprocessen

A. Nauta

Jos Smeets (red.)

Helga Fassbinder (projectleider)

Adrie Proveniers

J. v.d. Moosdijk

nr 9

Strukturering en Verwerking van Tijdgegevens voor de Uitvoering van Bouwwerken

ir. W.F. Schaefer

P.A. Erkelens

nr 10

Stedebouw en de Vorming van een Speciale Wetenschap

K. Doevendans

nr 11

Informatica en Ondersteuning van Ruimtelijke Besluitvorming

G.G. van der Meulen

nr 12

Staal in de Woningbouw, Korrosie-Bescherming van de Begane Grondvloer

Edwin J.F. Delsing

nr 13

Een Thermisch Model voor de Berekening van Staalplaatbetonvloeren onder Brandomstandigheden

A.F. Hamerlinck

nr 14

De Wijkgedachte in Nederland: Gemeenschapsstreven in een Stedebouwkundige Context

K. Doevendans

R. Stolzenburg

nr 15

Diaphragm Effect of Trapezoidally Profiled Steel Sheets:

Experimental Research into the Influence of Force Application

Andre W.A.M.J. van den Bogaard

nr 16

Versterken met Spuit-Ferrocement: Het Mechanische Gedrag van met Spuit-Ferrocement Versterkte Gewapend Betonbalken

K.B. Lubir

M.C.G. van Wanroy

nr 17

**De Tractaten van
Jean Nicolas Louis Durand**
G. van Zeyl

nr 18

**Wonen onder een Plat Dak:
Drie Opstellen over Enkele
Vooronderstellingen van de
Stedebouw**
K. Doevendans

nr 19

**Supporting Decision Making Processes:
A Graphical and Interactive Analysis of
Multivariate Data**
W. Adams

nr 20

**Self-Help Building Productivity:
A Method for Improving House Building
by Low-Income Groups Applied to Kenya
1990-2000**
P. A. Erkelens

nr 21

**De Verdeling van Woningen:
Een Kwestie van Onderhandelen**
Vincent Smit

nr 22

**Flexibiliteit en Kosten in het Ontwerpproces:
Een Besluitvormingondersteunend Model**
M. Prins

nr 23

**Spontane Nederzettingen Begeleid:
Voorwaarden en Criteria in Sri Lanka**
Po Hin Thung

nr 24

**Fundamentals of the Design of
Bamboo Structures**
Oscar Arce-Villalobos

nr 25

Concepten van de Bouwkunde
M.F.Th. Bax (red.)
H.M.G.J. Trum (red.)

nr 26

Meaning of the Site
Xiaodong Li

nr 27

**Het Woonmilieu op Begrip Gebracht:
Een Speurtocht naar de Betekenis van het
Begrip 'Woonmilieu'**
Jaap Ketelaar

nr 28

Urban Environment in Developing Countries
editors: Peter A. Erkelens
George G. van der Meulen (red.)

nr 29

**Stategische Plannen voor de Stad:
Onderzoek en Planning in Drie Steden**
prof.dr. H. Fassbinder (red.)
H. Rikhof (red.)

nr 30

Stedebouwkunde en Stadsbestuur
Piet Beekman

nr 31

**De Architectuur van Djenné:
Een Onderzoek naar de Historische Stad**
P.C.M. Maas

nr 32

Conjoint Experiments and Retail Planning
Harmen Oppewal

nr 33

**Strukturformen Indonesischer Bautechnik:
Entwicklung Methodischer Grundlagen
für eine 'Konstruktive Pattern Language'
in Indonesien**
Heinz Frick arch. SIA

nr 34

**Styles of Architectural Designing:
Empirical Research on Working Styles
and Personality Dispositions**
Anton P.M. van Bakel

nr 35

**Conjoint Choice Models for Urban
Tourism Planning and Marketing**
Benedict Dellaert

nr 36

Stedelijke Planvorming als Co-Productie
Helga Fassbinder (red.)

nr 37

Design Research in the Netherlands

editors: R.M. Oxman
M.F.Th. Bax
H.H. Achten

nr 38

Communication in the Building Industry

Bauke de Vries

nr 39

**Optimaal Dimensioneren van
Gelaste Plaatliggers**

J.B.W. Stark
F. van Pelt
L.F.M. van Gorp
B.W.E.M. van Hove

nr 40

Huisvesting en Overwinning van Armoede

P.H. Thung
P. Beekman (red.)

nr 41

**Urban Habitat:
The Environment of Tomorrow**

George G. van der Meulen
Peter A. Erkelens

nr 42

A Typology of Joints

John C.M. Olie

nr 43

**Modeling Constraints-Based Choices
for Leisure Mobility Planning**

Marcus P. Stemerding

nr 44

Activity-Based Travel Demand Modeling

Dick Ettema

nr 45

**Wind-Induced Pressure Fluctuations
on Building Facades**

Chris Geurts

nr 46

Generic Representations

Henri Achten

nr 47

**Johann Santini Aichel:
Architectuur en Ambiguiteit**

Dirk De Meyer

nr 48

**Concrete Behaviour in Multiaxial
Compression**

Erik van Geel

nr 49

Modelling Site Selection

Frank Witlox

nr 50

Ecolemma Model

Ferdinand Beetstra

nr 51

**Conjoint Approaches to Developing
Activity-Based Models**

Donggen Wang

nr 52

On the Effectiveness of Ventilation

Ad Roos

nr 53

**Conjoint Modeling Approaches for
Residential Group preferences**

Eric Molin

nr 54

**Modelling Architectural Design
Information by Features**

Jos van Leeuwen

nr 55

**A Spatial Decision Support System for
the Planning of Retail and Service Facilities**

Theo Arentze

nr 56

Integrated Lighting System Assistant

Ellie de Groot

nr 57

Ontwerpend Leren, Leren Ontwerpen

J.T. Boekholt

nr 58

**Temporal Aspects of Theme Park Choice
Behavior**

Astrid Kemperman

nr 59

**Ontwerp van een Geïndustrialiseerde
Funderingswijze**

Faas Moonen

nr 60

Merlin: A Decision Support System for Outdoor Leisure Planning

Manon van Middelkoop

nr 61

The Aura of Modernity

Jos Bosman

nr 62

Urban Form and Activity-Travel Patterns

Daniëlle Snellen

nr 63

Design Research in the Netherlands 2000

Henri Achten

nr 64

Computer Aided Dimensional Control in Building Construction

Rui Wu

nr 65

Beyond Sustainable Building

editors: Peter A. Erkelens
Sander de Jonge
August A.M. van Vliet

co-editor: Ruth J.G. Verhagen

nr 66

Das Globalrecyclingfähige Haus

Hans Löfflad

nr 67

Cool Schools for Hot Suburbs

René J. Dierkx

nr 68

A Bamboo Building Design Decision Support Tool

Fitri Mardjono

nr 69

Driving Rain on Building Envelopes

Fabien van Mook

nr 70

Heating Monumental Churches

Henk Schellen

nr 71

Van Woningverhuurder naar Aanbieder van Woongenot

Patrick Dogge

nr 72

Moisture Transfer Properties of Coated Gypsum

Emile Goossens

nr 73

Plybamboo Wall-Panels for Housing

Guillermo E. González-Beltrán

nr 74

The Future Site-Proceedings

Ger Maas

Frans van Gassel

nr 75

Radon transport in Autoclaved Aerated Concrete

Michel van der Pal

nr 76

The Reliability and Validity of Interactive Virtual Reality Computer Experiments

Amy Tan

nr 77

Measuring Housing Preferences Using Virtual Reality and Belief Networks

Maciej A. Orzechowski

nr 78

Computational Representations of Words and Associations in Architectural Design

Nicole Segers

nr 79

Measuring and Predicting Adaptation in Multidimensional Activity-Travel Patterns

Chang-Hyeon Joh

nr 80

Strategic Briefing

Fayez Al Hassan

nr 81

Well Being in Hospitals

Simona Di Cicco

nr 82

Solares Bauen: Implementierungs- und Umsetzungs-Aspekte in der Hochschulausbildung in Österreich

Gerhard Schuster

nr 83

Supporting Strategic Design of Workplace Environments with Case-Based Reasoning

Shauna Mallory-Hill

nr 84

ACCEL: A Tool for Supporting Concept Generation in the Early Design Phase

Maxim Ivashkov

nr 85

Brick-Mortar Interaction in Masonry under Compression

Ad Vermeltfoort

nr 86

Zelfredzaam Wonen

Guus van Vliet

nr 87

Een Ensemble met Grootstedelijke Allure

Jos Bosman

Hans Schippers

nr 88

On the Computation of Well-Structured Graphic Representations in Architectural Design

Henri Achten

nr 89

De Evolutie van een West-Afrikaanse Vernaculaire Architectuur

Wolf Schijns

nr 90

ROMBO Tactiek

Christoph Maria Ravesloot

nr 91

External Coupling between Building Energy Simulation and Computational Fluid Dynamics

Ery Djunaedy

nr 92

Design Research in the Netherlands 2005

editors: Henri Achten

Kees Dorst

Pieter Jan Stappers

Bauke de Vries

nr 93

Ein Modell zur Baulichen Transformation

Jalil H. Saber Zaimian

nr 94

Human Lighting Demands: Healthy Lighting in an Office Environment

Myriam Aries

nr 95

A Spatial Decision Support System for the Provision and Monitoring of Urban Greenspace

Claudia Pelizaro

nr 96

Leren Creëren

Adri Proveniers

nr 97

Simlandscape

Rob de Waard

nr 98

Design Team Communication

Ad den Otter

nr 99

Humaan-Ecologisch Georiënteerde Woningbouw

Juri Czabanowski

nr 100

Hambase

Martin de Wit

nr 101

Sound Transmission through Pipe Systems and into Building Structures

Susanne Bron-van der Jagt

nr 102

Het Bouwkundig Contrapunt

Jan Francis Boelen

nr 103

A Framework for a Multi-Agent Planning Support System

Dick Saarloos

nr 104

Bracing Steel Frames with Calcium Silicate Element Walls

Bright Mweene Ng'andu

nr 105

Naar een Nieuwe Houtskeletbouw

F.N.G. De Medts

nr 106 and 107
Niet gepubliceerd

nr 108
Geborgenheid
T.E.L. van Pinxteren

nr 109
Modelling Strategic Behaviour in Anticipation of Congestion
Qi Han

nr 110
Reflecties op het Woondomein
Fred Sanders

nr 111
On Assessment of Wind Comfort by Sand Erosion
Gábor Dezsö

nr 112
Bench Heating in Monumental Churches
Dionne Limpens-Neilen

nr 113
RE. Architecture
Ana Pereira Roders

nr 114
Toward Applicable Green Architecture
Usama El Fiky

nr 115
Knowledge Representation under Inherent Uncertainty in a Multi-Agent System for Land Use Planning
Liyang Ma

nr 116
Integrated Heat Air and Moisture Modeling and Simulation
Jos van Schijndel

nr 117
Concrete Behaviour in Multiaxial Compression
J.P.W. Bongers

nr 118
The Image of the Urban Landscape
Ana Moya Pellitero

nr 119
The Self-Organizing City in Vietnam
Stephanie Geertman

nr 120
A Multi-Agent Planning Support System for Assessing Externalities of Urban Form Scenarios
Rachel Katoshevski-Cavari

nr 121
Den Schulbau Neu Denken, Fühlen und Wollen
Urs Christian Maurer-Dietrich

nr 122
Peter Eisenman Theories and Practices
Bernhard Kormoss

nr 123
User Simulation of Space Utilisation
Vincent Tabak

nr 125
In Search of a Complex System Model
Oswald Devisch

nr 126
Lighting at Work: Environmental Study of Direct Effects of Lighting Level and Spectrum on Psycho-Physiological Variables
Grazyna Górnicka

nr 127
Flanking Sound Transmission through Lightweight Framed Double Leaf Walls
Stefan Schoenwald

nr 128
Bounded Rationality and Spatio-Temporal Pedestrian Shopping Behavior
Wei Zhu

nr 129
Travel Information: Impact on Activity Travel Pattern
Zhongwei Sun

nr 130
Co-Simulation for Performance Prediction of Innovative Integrated Mechanical Energy Systems in Buildings
Marija Trčka

nr 131
Niet gepubliceerd

nr 132

Architectural Cue Model in Evacuation Simulation for Underground Space Design

Chengyu Sun

nr 133

Uncertainty and Sensitivity Analysis in Building Performance Simulation for Decision Support and Design Optimization

Christina Hopfe

nr 134

Facilitating Distributed Collaboration in the AEC/FM Sector Using Semantic Web Technologies

Jacob Beetz

nr 135

Circumferentially Adhesive Bonded Glass Panes for Bracing Steel Frame in Façades

Edwin Huveners

nr 136

Influence of Temperature on Concrete Beams Strengthened in Flexure with CFRP

Ernst-Lucas Klamer

nr 137

Sturen op Klantwaarde

Jos Smeets

nr 139

Lateral Behavior of Steel Frames with Discretely Connected Precast Concrete Infill Panels

Paul Teewen

nr 140

Integral Design Method in the Context of Sustainable Building Design

Perica Savanović

nr 141

Household Activity-Travel Behavior: Implementation of Within-Household Interactions

Renni Anggraini

nr 142

Design Research in the Netherlands 2010

Henri Achten

nr 143

Modelling Life Trajectories and Transport Mode Choice Using Bayesian Belief Networks

Marloes Verhoeven

nr 144

Assessing Construction Project Performance in Ghana

William Gyadu-Asiedu

nr 145

Empowering Seniors through Domotic Homes

Masi Mohammadi

nr 146

An Integral Design Concept for Ecological Self-Compacting Concrete

Martin Hunger

nr 147

Governing Multi-Actor Decision Processes in Dutch Industrial Area Redevelopment

Erik Blokhuis

nr 148

A Multifunctional Design Approach for Sustainable Concrete

Götz Hüsken

nr 149

Quality Monitoring in Infrastructural Design-Build Projects

Ruben Favié

nr 150

Assessment Matrix for Conservation of Valuable Timber Structures

Michael Abels

nr 151

Co-simulation of Building Energy Simulation and Computational Fluid Dynamics for Whole-Building Heat, Air and Moisture Engineering

Mohammad Mirsadeghi

nr 152

External Coupling of Building Energy Simulation and Building Element Heat, Air and Moisture Simulation

Daniel Cóstola

nr 153

**Adaptive Decision Making In
Multi-Stakeholder Retail Planning**

Ingrid Janssen

nr 154

Landscape Generator

Kymo Slager

nr 155

Constraint Specification in Architecture

Remco Niemeijer

nr 156

**A Need-Based Approach to
Dynamic Activity Generation**

Linda Nijland

nr 157

**Modeling Office Firm Dynamics in an
Agent-Based Micro Simulation Framework**

Gustavo Garcia Manzato

nr 158

**Lightweight Floor System for
Vibration Comfort**

Sander Zegers

nr 159

Aanpasbaarheid van de Draagstructuur

Roel Gijsbers

nr 160

'Village in the City' in Guangzhou, China

Yanliu Lin

nr 161

Climate Risk Assessment in Museums

Marco Martens

nr 162

Social Activity-Travel Patterns

Pauline van den Berg

nr 163

**Sound Concentration Caused by
Curved Surfaces**

Martijn Vercammen

nr 164

**Design of Environmentally Friendly
Calcium Sulfate-Based Building Materials:
Towards an Improved Indoor Air Quality**

Qingliang Yu

nr 165

**Beyond Uniform Thermal Comfort
on the Effects of Non-Uniformity and
Individual Physiology**

Lisje Schellen

nr 166

Sustainable Residential Districts

Gaby Abdalla

nr 167

**Towards a Performance Assessment
Methodology using Computational
Simulation for Air Distribution System
Designs in Operating Rooms**

Mônica do Amaral Melhado

nr 168

**Strategic Decision Modeling in
Brownfield Redevelopment**

Brano Glumac

nr 169

**Pamela: A Parking Analysis Model
for Predicting Effects in Local Areas**

Peter van der Waerden

nr 170

**A Vision Driven Wayfinding Simulation-System
Based on the Architectural Features Perceived
in the Office Environment**

Qunli Chen

nr 171

**Measuring Mental Representations
Underlying Activity-Travel Choices**

Oliver Horeni

nr 172

**Modelling the Effects of Social Networks
on Activity and Travel Behaviour**

Nicole Ronald

nr 173

**Uncertainty Propagation and Sensitivity
Analysis Techniques in Building Performance
Simulation to Support Conceptual Building
and System Design**

Christian Struck

nr 174

**Numerical Modeling of Micro-Scale
Wind-Induced Pollutant Dispersion
in the Built Environment**

Pierre Gousseau

nr 175

**Modeling Recreation Choices
over the Family Lifecycle**

Anna Beatriz Grigolon

nr 176

**Experimental and Numerical Analysis of
Mixing Ventilation at Laminar, Transitional
and Turbulent Slot Reynolds Numbers**

Twan van Hooff

nr 177

**Collaborative Design Support:
Workshops to Stimulate Interaction and
Knowledge Exchange Between Practitioners**

Emile M.C.J. Quanjel

nr 178

Future-Proof Platforms for Aging-in-Place

Michiel Brink

nr 179

**Motivate:
A Context-Aware Mobile Application for
Physical Activity Promotion**

Yuzhong Lin

nr 180

**Experience the City:
Analysis of Space-Time Behaviour and
Spatial Learning**

Anastasia Moiseeva

nr 181

**Unbonded Post-Tensioned Shear Walls of
Calcium Silicate Element Masonry**

Lex van der Meer

nr 182

**Construction and Demolition Waste
Recycling into Innovative Building Materials
for Sustainable Construction in Tanzania**

Mwita M. Sabai

nr 183

**Durability of Concrete
with Emphasis on Chloride Migration**

Przemysław Spiesz

nr 184

**Computational Modeling of Urban
Wind Flow and Natural Ventilation Potential
of Buildings**

Rubina Ramponi

nr 185

**A Distributed Dynamic Simulation
Mechanism for Buildings Automation
and Control Systems**

Azzedine Yahiaoui

nr 186

**Modeling Cognitive Learning of Urban
Networks in Daily Activity-Travel Behavior**

Şehnaz Cenani Durmazoğlu

nr 187

**Functionality and Adaptability of Design
Solutions for Public Apartment Buildings
in Ghana**

Stephen Agyefi-Mensah

nr 188

**A Construction Waste Generation Model
for Developing Countries**

Lilliana Abarca-Guerrero

nr 189

**Synchronizing Networks:
The Modeling of Supernetworks for
Activity-Travel Behavior**

Feixiong Liao

nr 190

**Time and Money Allocation Decisions
in Out-of-Home Leisure Activity Choices**

Gamze Zeynep Dane

nr 191

**How to Measure Added Value of CRE and
Building Design**

Rianne Appel-Meulenbroek

nr 192

**Secondary Materials in Cement-Based
Products:
Treatment, Modeling and Environmental
Interaction**

Miruna Florea

nr 193

**Concepts for the Robustness Improvement
of Self-Compacting Concrete:**

**Effects of Admixtures and Mixture
Components on the Rheology and Early
Hydration at Varying Temperatures**

Wolfram Schmidt

nr 194

Modelling and Simulation of Virtual Natural Lighting Solutions in Buildings

Rizki A. Mangkuto

nr 195

Nano-Silica Production at Low Temperatures from the Dissolution of Olivine - Synthesis, Tailoring and Modelling

Alberto Lazaro Garcia

nr 196

Building Energy Simulation Based Assessment of Industrial Halls for Design Support

Bruno Lee

nr 197

Computational Performance Prediction of the Potential of Hybrid Adaptable Thermal Storage Concepts for Lightweight Low-Energy Houses

Pieter-Jan Hoes

nr 198

Application of Nano-Silica in Concrete

George Quercia Bianchi

nr 199

Dynamics of Social Networks and Activity Travel Behaviour

Fariya Sharmeen

nr 200

Building Structural Design Generation and Optimisation including Spatial Modification

Juan Manuel Davila Delgado

nr 201

Hydration and Thermal Decomposition of Cement/Calcium-Sulphate Based Materials

Ariën de Korte

nr 202

Republiek van Beelden: De Politieke Werkingen van het Ontwerp in Regionale Planvorming

Bart de Zwart

nr 203

Effects of Energy Price Increases on Individual Activity-Travel Repertoires and Energy Consumption

Dujuan Yang

nr 204

Geometry and Ventilation: Evaluation of the Leeward Sawtooth Roof Potential in the Natural Ventilation of Buildings

Jorge Isaac Perén Montero

nr 205

Computational Modelling of Evaporative Cooling as a Climate Change Adaptation Measure at the Spatial Scale of Buildings and Streets

Hamid Montazeri

nr 206

Local Buckling of Aluminium Beams in Fire Conditions

Ronald van der Meulen

nr 207

Historic Urban Landscapes: Framing the Integration of Urban and Heritage Planning in Multilevel Governance

Loes Veldpaus

nr 208

Sustainable Transformation of the Cities: Urban Design Pragmatics to Achieve a Sustainable City

Ernesto Antonio Zumelzu Scheel

nr 209

Development of Sustainable Protective Ultra-High Performance Fibre Reinforced Concrete (UHPFRC): Design, Assessment and Modeling

Rui Yu

nr 210

Uncertainty in Modeling Activity-Travel Demand in Complex Urban Systems

Soora Rasouli

nr 211

Simulation-based Performance Assessment of Climate Adaptive Greenhouse Shells

Chul-sung Lee

nr 212

Green Cities: Modelling the Spatial Transformation of the Urban Environment using Renewable Energy Technologies

Saleh Mohammadi

nr 213

A Bounded Rationality Model of Short and Long-Term Dynamics of Activity-Travel Behavior

Ifigeneia Psarra

nr 214

Effects of Pricing Strategies on Dynamic Repertoires of Activity-Travel Behaviour

Elaheh Khademi

nr 215

Handstorm Principles for Creative and Collaborative Working

Frans van Gassel

nr 216

Light Conditions in Nursing Homes: Visual Comfort and Visual Functioning of Residents

Marianne M. Sinoo

nr 217

**Woonsporen:
De Sociale en Ruimtelijke Biografie van een Stedelijk Bouwblok in de Amsterdamse Transvaalbuurt**

Hüseyin Hüsnu Yegenoglu

nr 218

Studies on User Control in Ambient Intelligent Systems

Berent Willem Meerbeek

nr 219

Daily Livings in a Smart Home: Users' Living Preference Modeling of Smart Homes

Erfaneh Allameh

nr 220

Smart Home Design: Spatial Preference Modeling of Smart Homes

Mohammadali Heidari Jozam

nr 221

**Wonen:
Discoursen, Praktijken, Perspectieven**

Jos Smeets

nr 222

Personal Control over Indoor Climate in Offices:

Impact on Comfort, Health and Productivity

Atze Christiaan Boerstra

nr 223

Personalized Route Finding in Multimodal Transportation Networks

Jianwe Zhang

nr 224

The Design of an Adaptive Healing Room for Stroke Patients

Elke Daemen

nr 225

Experimental and Numerical Analysis of Climate Change Induced Risks to Historic Buildings and Collections

Zara Huijbregts

nr 226

Wind Flow Modeling in Urban Areas Through Experimental and Numerical Techniques

Alessio Ricci

nr 227

Clever Climate Control for Culture: Energy Efficient Indoor Climate Control Strategies for Museums Respecting Collection Preservation and Thermal Comfort of Visitors

Rick Kramer

nr 228

Fatigue Life Estimation of Metal Structures Based on Damage Modeling

Sarmediran Silitonga

nr 229

A multi-agents and occupancy based strategy for energy management and process control on the room-level

Timilehin Moses Labeodan

nr 230

Environmental assessment of Building Integrated Photovoltaics: Numerical and Experimental Carrying Capacity Based Approach

Michiel Ritzen

nr 231

Performance of Admixture and Secondary Minerals in Alkali Activated Concrete: Sustaining a Concrete Future

Arno Keulen

nr 232

World Heritage Cities and Sustainable Urban Development: Bridging Global and Local Levels in Monitoring the Sustainable Urban Development of World Heritage Cities

Paloma C. Guzman Molina

nr 233

Stage Acoustics and Sound Exposure in Performance and Rehearsal Spaces for Orchestras: Methods for Physical Measurements

Remy Wenmaekers

nr 234

Municipal Solid Waste Incineration (MSWI) Bottom Ash: From Waste to Value Characterization, Treatments and Application

Pei Tang

nr 235

Large Eddy Simulations Applied to Wind Loading and Pollutant Dispersion

Mattia Ricci

nr 236

Alkali Activated Slag-Fly Ash Binders: Design, Modeling and Application

Xu Gao

nr 237

Sodium Carbonate Activated Slag: Reaction Analysis, Microstructural Modification & Engineering Application

Bo Yuan

nr 238

Shopping Behavior in Malls

Widiyani

nr 239

Smart Grid-Building Energy Interactions: Demand Side Power Flexibility in Office Buildings

Kennedy Otieno Aduda

nr 240

Modeling Taxis Dynamic Behavior in Uncertain Urban Environments

Zheng Zhong

nr 241

Gap-Theoretical Analyses of Residential Satisfaction and Intention to Move

Wen Jiang

nr 242

Travel Satisfaction and Subjective Well-Being: A Behavioral Modeling Perspective

Yanan Gao

nr 243

Building Energy Modelling to Support the Commissioning of Holistic Data Centre Operation

Vojtech Zavrel

nr 244

Regret-Based Travel Behavior Modeling: An Extended Framework

Sunghoon Jang

nr 245

Towards Robust Low-Energy Houses: A Computational Approach for Performance Robustness Assessment using Scenario Analysis

Rajesh Reddy Kotireddy

nr 246

Development of sustainable and functionalized inorganic binder-biofiber composites

Guillaume Doudart de la Grée

nr 247

A Multiscale Analysis of the Urban Heat Island Effect: From City Averaged Temperatures to the Energy Demand of Individual Buildings

Yasin Toparlar

nr 248

Design Method for Adaptive Daylight Systems for buildings covered by large (span) roofs

Florian Heinzelmann

nr 249

Hardening, high-temperature resistance and acid resistance of one-part geopolymers

Patrick Sturm

nr 250

Effects of the built environment on dynamic repertoires of activity-travel behaviour

Aida Pontes de Aquino

nr 251

Modeling for auralization of urban environments: Incorporation of directivity in sound propagation and analysis of a framework for auralizing a car pass-by

Fotis Georgiou

nr 252

Wind Loads on Heliostats and Photovoltaic Trackers

Andreas Pfahl

nr 253

Approaches for computational performance optimization of innovative adaptive façade concepts

Roel Loonen

nr 254

Multi-scale FEM-DEM Model for Granular Materials: Micro-scale boundary conditions, Statics, and Dynamics

Jiadun Liu

nr 255

Bending Moment - Shear Force Interaction of Rolled I-Shaped Steel Sections

Rianne Willie Adriana Dekker

nr 256

Paralympic tandem cycling and hand-cycling: Computational and wind tunnel analysis of aerodynamic performance

Paul Fionn Mannion

nr 257

Experimental characterization and numerical modelling of 3D printed concrete: Controlling structural behaviour in the fresh and hardened state

Robert Johannes Maria Wolfs

nr 258

Requirement checking in the building industry: Enabling modularized and extensible requirement checking systems based on semantic web technologies

Chi Zhang

nr 259

A Sustainable Industrial Site Redevelopment Planning Support System

Tong Wang

nr 260

Efficient storage and retrieval of detailed building models: Multi-disciplinary and long-term use of geometric and semantic construction information

Thomas Ferdinand Krijnen

nr 261

The users' value of business center concepts for knowledge sharing and networking behavior within and between organizations

Minou Weijs-Perrée

nr 262

Characterization and improvement of aerodynamic performance of vertical axis wind turbines using computational fluid dynamics (CFD)

Abdolrahim Rezaeiha

nr 263

In-situ characterization of the acoustic impedance of vegetated roofs

Chang Liu

nr 264

Occupancy-based lighting control: Developing an energy saving strategy that ensures office workers' comfort

Christel de Bakker

nr 265

Stakeholders-Oriented Spatial Decision Support System

Cahyono Susetyo

nr 266

Climate-induced damage in oak museum objects

Rianne Aleida Luimes

nr 267

Towards individual thermal comfort: Model predictive personalized control of heating systems

Katarina Katic

nr 268

Modelling and Measuring Quality of Urban Life: Housing, Neighborhood, Transport and Job

Lida Aminian

nr 269

Optimization of an aquifer thermal energy storage system through integrated modeling of aquifer, HVAC systems and building

Basar Bozkaya

nr 270

Numerical modeling for urban sound propagation: developments in wave-based and energy-based methods

Raúl Pagán Muñoz

nr 271

Lighting in multi-user office environments: improving employee wellbeing through personal control

Sanae van der Vleuten-Chraibi

nr 272

A strategy for fit-for-purpose occupant behavior modelling in building energy and comfort performance simulation

Isabella I. Gaetani dell'Aquila d'Aragona

nr 273

Een architectuurhistorische waardestelling van naoorlogse woonwijken in Nederland: Het voorbeeld van de Westelijke Tuinsteden in Amsterdam

Eleonore Henriette Marie Mens

nr 274

Job-Housing Co-Dependent Mobility Decisions in Life Trajectories

Jia Guo

nr 275

A user-oriented focus to create healthcare facilities: decision making on strategic values

Emilia Rosalia Catharina Maria Huisman

nr 276

Dynamics of plane impinging jets at moderate Reynolds numbers – with applications to air curtains

Adelya Khayrullina

nr 277

Valorization of Municipal Solid Waste Incineration Bottom Ash - Chemical Nature, Leachability and Treatments of Hazardous Elements

Qadeer Alam

nr 278

Treatments and valorization of MSWI bottom ash - application in cement-based materials

Veronica Caprai

nr 279

Personal lighting conditions of office workers - input for intelligent systems to optimize subjective alertness

Juliëtte van Duijnhoven

nr 280

Social influence effects in tourism travel: air trip itinerary and destination choices

Xiaofeng Pan

nr 281

Advancing Post-War Housing: Integrating Heritage Impact, Environmental Impact, Hygrothermal Risk and Costs in Renovation Design Decisions

Lisanne Claartje Havinga

nr 282

Impact resistant ultra-high performance fibre reinforced concrete: materials, components and properties

Peipeng Li

nr 283

Demand-driven Science Parks: The Perceived Benefits and Trade-offs of Tenant Firms with regard to Science Park Attributes

Wei Keat Benny Ng

nr 284

Raise the lantern; how light can help to maintain a healthy and safe hospital environment focusing on nurses

Maria Petronella Johanna Aarts

nr 285

Modelling Learning and Dynamic Route and Parking Choice Behaviour under Uncertainty

Elaine Cristina Schneider de Carvalho

nr 286

Identifying indoor local microclimates for safekeeping of cultural heritage

Karin Kompatscher

nr 287

Probabilistic modeling of fatigue resistance for welded and riveted bridge details. Resistance models and estimation of uncertainty.

Davide Leonetti

Ultra-High Performance Fiber Reinforced Concrete (UHPFRC) is one of the most advanced and promising cementitious materials developed to date. It can be used to improve the static and dynamic performances of specialized structures, e.g. nuclear power plants and high rising buildings. Coarse basalt aggregates are utilized to partially replace the expensive fine particles in UHPFRC in the present research, which reduces the production cost and enhances the impact resistance of the UHPFRC. Moreover, the steel fibers in UHPFRC play an important role. To achieve a more effective fiber amount distribution, an optimized layered-structure concept is applied, i.e. designing UHPFRC with multi-layers. This thesis investigates the fibers effects on the coarse-aggregated layered UHPFRC subjected to static and dynamic loads, with special attention to the fiber pullout performance at mesoscale and the fiber amount distribution over the layered UHPFRC at macroscale.

DEPARTMENT OF THE BUILT ENVIRONMENT